

Ultracold Yb Gases with Control over Spin and Orbital Degrees of Freedom

Dissertation
zur Erlangung des Doktorgrades
des Department Physik
der Universität Hamburg

vorgelegt von
Alexander Thobe
aus Hannover

Hamburg
2014

Gutachter der Dissertation:	Prof. Dr. Klaus Sengstock Prof. Dr. Henning Moritz Prof. Dr. Thomas C. Killian
Gutachter der Disputation:	Prof. Dr. Klaus Sengstock Prof. Dr. Andreas Hemmerich
Datum der Disputation:	24. April 2014
Vorsitzender des Prüfungsausschusses:	Prof. Dr. Peter Schmelcher
Vorsitzende des Promotionsausschusses:	Prof. Dr. Daniela Pfannkuche
Dekan der Fakultät für Mathematik, Informatik und Naturwissenschaften:	Prof. Dr. Heinrich Graener

Abstract

Ultracold quantum degenerate gases of alkaline-earth-like atoms open up new perspectives for the investigation of strongly-correlated many-body physics. Long-lived metastable states in combination with a decoupled nuclear spin enable the realization of intriguing Hamiltonians beyond the possibilities of current alkali-based experiments, ranging from the Kondo lattice model to $SU(N)$ -symmetric magnetic systems. Among the alkaline-earth-like elements, Yb is particularly versatile due to its large number of bosonic and fermionic isotopes with a wide range of interaction strengths. This thesis describes a newly-built setup for the study of quantum many-body physics with ultracold Yb, demonstrating the preparation of Bose-Einstein condensates and multi-component degenerate Fermi gases in an optical lattice with coherent control over the electronic state.

Within this work we have implemented for the first time a two-dimensional magneto-optical trap (2D-MOT) for the initial laser cooling of Yb. The slow atoms from the 2D-MOT can directly be loaded into a 3D-MOT operating on a narrow intercombination transition, and loading rates comparable with Zeeman slower setups are achieved. The flexibility and the compact setup of the 2D-MOT makes our setup well suited for the production of multi-element quantum gas mixtures in the future.

Via evaporative cooling in a crossed optical dipole trap Bose-Einstein condensates of ^{174}Yb with up to $2 \cdot 10^5$ atoms are produced. Loading the condensate into a triangular optical lattice, we observe the superfluid to Mott-insulator transition with Yb. Using the fermionic isotope ^{173}Yb , quantum degenerate, multi-component Fermi gases with one to six spin components are obtained with up to $8 \cdot 10^4$ atoms at $0.15T_F$.

In order to coherently prepare Yb quantum gases in the metastable 3P_0 state, an ultrastable laser addressing the $^1S_0 \rightarrow ^3P_0$ clock transition at 578 nm has been developed as a major part of this thesis. Exhibiting a short-term stability at the 1Hz-level, this laser will serve as an important tool for the manipulation and probing of strongly-correlated many-body systems of ultracold Yb.

Control over the electronic state is demonstrated by Rabi spectroscopy on the $^1S_0 \rightarrow ^3P_0$ transition of quantum degenerate ^{173}Yb in a three-dimensional optical lattice. In a spin-polarized sample more than 90% of the atoms can be prepared in the metastable 3P_0 state. Driving a vibrational sideband transition, the atoms can also be coherently excited to higher bands in the optical lattice. Moreover, first experiments towards the electronic state control of interacting spin mixtures are performed, exhibiting signatures of interaction-induced lineshifts.

The preparation and manipulation techniques presented in this thesis constitute an important step towards the exploration of novel quantum many-body physics with ultracold Yb.

Zusammenfassung

Ultrakalte Quantengase aus Erdalkali-ähnlichen Atomen eröffnen neue Möglichkeiten zur Untersuchung stark korrelierter Quantenvielteilchensysteme. Langlebige metastabile Zustände kombiniert mit einem entkoppelten Kernspin ermöglichen es faszinierende Vielteilchensysteme zu realisieren, die über die Möglichkeiten heutiger Alkali-basierter Experimente hinausgehen: Vom Kondo-Gitter-Modell bis hin zu $SU(N)$ -symmetrischen magnetischen Systemen. Von allen Erdalkali-ähnlichen Elementen besticht vor allem Ytterbium (Yb) durch die Vielzahl von fermionischen und bosonischen Isotopen mit unterschiedlichen Wechselwirkungsstärken. Im Rahmen der vorliegenden Arbeit wurde ein neuer experimenteller Aufbau zur Erforschung von Quantenvielteilchensystemen aus ultrakalten Yb-Atomen realisiert. Mit diesem Aufbau wurden sowohl Bose-Einstein Kondensate, als auch mehrkomponentige Fermigase in einem optischen Gitter präpariert. Ferner wurde die kohärente Kontrolle des elektronischen Zustands ultrakalter Atome demonstriert.

In dem hier vorgestellten Aufbau wurde zum ersten Mal eine zweidimensionale magneto-optische Falle (2D-MOT) zur Erzeugung langsamer Yb-Atome implementiert. Die Atome aus der 2D-MOT können direkt in eine 3D-MOT auf einer schmalen Interkombinationslinie geladen werden. Die erzielten Laderaten sind mit denen von Zeeman slowern vergleichbar. Durch die Flexibilität und den kompakten Aufbau der 2D-MOT ist unsere Apparatur besonders gut für die Erzeugung mehrelementiger Quantengasmischungen in zukünftigen Experimenten geeignet. Mittels evaporativer Kühlung in einer gekreuzten Dipolfalle wurden reine ^{174}Yb Bose-Einstein Kondensate mit bis zu $2 \cdot 10^5$ Atomen realisiert. Anhand dieser Kondensate konnte der Mott-Isolator Übergang in einem optischen Dreiecksgitter demonstriert werden. Des Weiteren wurden unter Verwendung des fermionischen Isotops ^{173}Yb ein- bis sechskomponentige quantenentartete Fermigase mit bis zu $8 \cdot 10^4$ Atomen bei $0.15T_F$ erzeugt.

Zur kohärenten Präparation von Yb-Quantengasen im metastabilen 3P_0 -Zustand wurde als wichtiger Teil dieser Arbeit ein hochstabiler Laser für die Anregung des $^1S_0 \rightarrow ^3P_0$ Uhrenübergangs bei 578 nm entwickelt. Mit einer Kurzzeitstabilität von etwa 1 Hz eröffnet dieser Laser vielfältige Möglichkeiten der gezielten Manipulation und Detektion von ultrakalten Yb-Vielteilchensystemen.

Die Kontrolle des elektronischen Zustands wurde anhand von Rabi-Spektroskopie auf dem $^1S_0 \rightarrow ^3P_0$ Übergang von quantenentartetem ^{173}Yb in einem dreidimensionalen optischen Gitter gezeigt. In einem Spin-polarisierten Ensemble können mehr als 90% der Atome im metastabilen 3P_0 präpariert werden. Die kohärente Anregung in höhere Bänder des optischen Gitters ist durch die Adressierung von Vibrationsseitenbändern möglich. Schließlich wurden erste Experimente zur Kontrolle des elektronischen Zustands in wechselwirkenden Spin-Mischungen durchgeführt. Diese weisen Anzeichen von wechselwirkungsinduzierten Linienverschiebungen auf.

Die in dieser Arbeit vorgestellten Präparations- und Manipulationstechniken stellen einen guten Ausgangspunkt dar, um die neuartige Physik von Yb-Quantengasen zu untersuchen.

Publikationen

Im Rahmen der vorliegenden Arbeit ist die folgende wissenschaftliche Veröffentlichung entstanden.

Publications

The following research article has been published in the course of this thesis.

- [1] S. Dörscher, A. Thobe, B. Hundt, A. Kochanke, R. LeTargat, P. Windpassinger, C. Becker, and K. Sengstock, *Creation of quantum-degenerate gases of ytterbium in a compact 2D-/3D-magneto-optical trap setup*, *Review of Scientific Instruments* **84**, 043109 (2013)

Contents

Introduction - Many-body physics with ultracold Ytterbium	1
1 A 2D/3D-MOT Setup for Laser Cooling of Yb	7
1.1 Cooling Transitions of Yb	7
1.2 The MOT setup	12
1.3 The Cooling Laser Systems	14
1.4 Characterization of the 2D/3D-MOT Setup	17
1.4.1 Bosonic ^{174}Yb	18
1.4.2 Fermionic ^{173}Yb	20
1.5 Comparison to Zeeman Slowers	21
2 Quantum Degenerate Yb	23
2.1 Collisional Properties of Yb	23
2.2 Polarizability of the 1S_0 and 3P_0 states	26
2.3 The Crossed Dipole Trap Setup	28
2.4 Bose Einstein Condensates of ^{174}Yb	30
2.4.1 Evaporative Cooling	30
2.4.2 ^{174}Yb in a Triangular Optical Lattice	35
2.5 Quantum Degenerate Fermi Gases of ^{173}Yb	41
2.5.1 Evaporative Cooling	42
2.5.2 Production and Detection of Spin-Mixtures	45
2.5.3 ^{173}Yb in the Optical Lattice	49
3 Control of the Electronic State	57
3.1 The 578nm Spectroscopy Lasersystem	58
3.1.1 Laser and Stabilization Cavity	58
3.1.2 Linewidth Narrowing via a Fast Pound-Drever-Hall Lock	63
3.1.3 Evaluation of the Laser Stability	72
3.1.4 The Spectroscopy Setup	79
3.2 Lattice Spectroscopy of Single Component Fermions	80
3.3 Spectroscopy of a Two-Component Gas	87
3.3.1 Theoretical Description of the Spectroscopy of Spin Mixtures	87
3.3.2 Spectroscopy of a Two-Component Gas	94
Outlook	97

Appendix A Spectroscopic Excitation of Motional States	99
Appendix B Derivation of the Spectroscopy Hamiltonian	105
Appendix C Yb Term Diagram	111
Bibliography	113

List of Figures

0.1	Level scheme of Yb and Sketch of the Kondo Lattice	3
0.2	Artificial Magnetic Fields for Yb in a State-Dependent Optical Lattice	4
1.1	Level Scheme of the Lowest Energy States of Yb	8
1.2	Hyperfine Structure of the 3P_1 and 1P_1 States of Yb	10
1.3	MOT Loading Process at Large Differential Zeeman Shift	11
1.4	The 2D/3D-MOT Vacuum Setup	13
1.5	Schematic of the 556 nm Laser System	14
1.6	Schematic of the 399 nm Laser System	16
1.7	3D-MOT Loading Rate for ^{174}Yb	17
1.8	3D-MOT Loading Rate versus Push Beam Power and Frequency Broadening	19
1.9	3D-MOT Loading Rate for ^{173}Yb	20
2.1	Polarizability of the 1S_0 and 3P_0 states of Yb	27
2.2	Setup of the Crossed Optical Dipole Trap	29
2.3	Atom Number and Temperature During Evaporative Cooling of ^{174}Yb	31
2.4	BEC Phase Transition and Trap Frequencies	32
2.5	Influence of Dipole Trap Adjustment on Atom Number	33
2.6	Equipotential Contours of the Crossed Dipole Trap	34
2.7	Atom Number Decay of the ^{174}Yb BEC	35
2.8	BEC Size versus MOT Loading Time	35
2.9	Schematic of the Optical Lattice Setup	36
2.10	Laser Setup of the Optical Lattice	37
2.11	Calibration of the Three-Beam Lattice	38
2.12	Superfluid to Mott-Insulator Transition of ^{174}Yb	40
2.13	Evaporation Ramp for ^{173}Yb	42
2.14	T/T_F -Thermometry	43
2.15	Atom Number Decay of a Degenerate Fermi Gas of ^{174}Yb	44
2.16	The Optical Stern-Gerlach Setup	46
2.17	Polarizability and Scattering Rate Near the $^1S_0 \rightarrow ^3P_1$ Transition	47
2.18	Preparation of Different Spin Mixtures of ^{173}Yb	48
2.19	Band Mapping out of the 1D-Lattice	50
2.20	Bandstructure of a 1D-Lattice and Brillouin zones of a Square Lattice	51
2.21	Eigenstates of a Harmonic+Lattice Potential	52
2.22	Fraction of Harmonic Oscillator States above E_r	53

2.23	Band Mapping out of the 3D-Lattice	54
2.24	Band Mapping out of the 2D-Lattice	55
3.1	Setup of the Ultrastable Cavity	60
3.2	Long-Term Stability of the Cavity Temperature Controller	61
3.3	Measurement of the Linewidth of the Ultrastable Cavity	62
3.4	Schematic Layout of a Laser Frequency Stabilization Loop	63
3.5	Noise Density and Power Spectral Density of a Locked Laser	65
3.6	Pound-Drever-Hall Setup and Error Signal	66
3.7	Current-FM Transfer Function of the 1156nm Laser Diodes	67
3.8	Spectral Analysis of the PDH Error Signal	70
3.9	Bode Diagram of the Fast Frequency Stabilization Loop	71
3.10	Setup for the Beat Note Measurement of the Clock Laser	73
3.11	Clock Laser Beat Signal (Logarithmic Scale)	74
3.12	Clock Laser Beat Signal (Linear Scale)	75
3.13	Sensitivity of the Ultrastable Cavities to Power Fluctuations	76
3.14	Thermal Expansion of the ULE Cavity	77
3.15	Longterm Measurement of the Clock Laser Beat Signal	78
3.16	Setup for the Spectroscopy on the $^1S_0 \rightarrow ^3P_0$ transition	79
3.17	Sideband Spectrum of a Spin-Polarized Gas in an Optical Lattice	82
3.18	Measured Rabi Oscillations on the $^1S_0 \rightarrow ^3P_0$ transition	83
3.19	Rabi Oscillations with an Inhomogeneous Rabi Frequency	84
3.20	Rabi Spectra of a Spin-Polarized Fermi Gas	85
3.21	Rabi Oscillations on the First Blue Sideband	86
3.22	Illustration of Two Spectroscopy Configurations	88
3.23	Level Diagram of an Interacting Two-Atom System	90
3.24	Calculated Rabi Spectra in the $\pm 5/2$ -Configuration Without Double Excitation	91
3.25	Calculated Rabi Spectra in the $\pm 5/2$ -Configuration With Double Excitation	93
3.26	Rabi Spectra Measured in the $(3/2)(5/2)$ -Configuration	94
3.27	Rabi Spectrum Measured in the $\pm 5/2$ -Configuration	95
4.1	Phase Diagram of the 1D Kondo Lattice Model	98
A.1	Calculated Franck-Condon Factors for Optical Spectroscopy of Lattice-Confined Atoms	101
A.2	Calculated Rabi Spectra of Lattice-Confined Atoms	101
C.1	Yb Term Diagram	112

Introduction - Many-body physics with ultracold Ytterbium

For a very long time, the work of physicists has been to take the world to pieces in order to find the elementary constituents of all things in nature. While this work has not come to an end as can be seen in the exciting research in current elementary particle physics, it can already be considered extremely successful: The physics of single electrons, neutrons and protons, which make up the matter we find on earth, can be quantitatively described with enormous accuracy. Interestingly, one of the main challenges for today's physicists is putting all these particles back together and understand how the collective properties of nuclei, molecules or solid state materials emerge from the physics of their microscopic constituents. One outstanding problem of this kind is the mechanism of the high-temperature superconductivity of cuprate materials [2], which is still barely understood. But there are many more questions in condensed matter and general many-body physics which are equally puzzling and have withstood their solution for many years, such as the existence of spin-liquid states in frustrated magnets [3] or Majorana bound-states in hybrid superconductors [4].

The fact that the size of the Hilbert spaces of quantum many-body systems grows exponentially with the number of particles makes them computationally intractable and therefore extremely difficult to analyze theoretically. Consequently, tackling many-body physics problems requires reducing their complexity to the minimum. To this end, strongly simplified theoretical models have been developed, such as the Hubbard model or the Kondo lattice model in condensed matter physics, which are hoped to capture the essence of the physics behind the phenomena to be studied. However, even these simplified models cannot be solved entirely and it is unclear whether they really contain the answers to the open questions. The idea of simplification can, however, also be transferred to the experimental domain: One can try to engineer an artificial material, which is free from all features that unnecessarily complicate the physical understanding. Such an artificial material should ideally allow to tune all relevant physical parameters over a wide range, the particle spacings should be large enough to directly look at the microscopic structure, and the relevant timescales should be slow enough to study dynamic effects without extreme effort. It can then be investigated, whether this simplified toy-material exhibits the same phenomena as the original condensed matter sample. One can test, how the material responds to changes in the physical parameters, and in which way the macroscopic properties are connected to the microscopic states of the particles. In other words, one can directly look at a physical realization of a simplified model instead of solving it computationally. This would circumvent the computational limitations encountered in the theoretical study of many-body physics problems.

In 1998 Jaksch and Zoller [5] were the first to realize that ultracold, neutral atoms constitute

wonderful building blocks of such toy-materials. Although interacting only via weak van-der-Waals forces, neutral atoms cooled to nK-temperatures can be brought into the regime where interactions dominate over all other energy scales and strong quantum-correlations govern the many-particle physics. This can be done in two ways: Feshbach-resonances can be used to strongly increase the interactions after the atoms have been cooled down [6]. Alternatively, the kinetic energy, which still dominates over the interaction energy in bare, trapped gases of ultracold atoms, can further be reduced by applying an optical lattice potential to the atoms [7]. In a deep enough lattice, the on-site interaction of two atoms on the same lattice site becomes much larger than the kinetic tunneling energy, and the sample enters the interaction-dominated regime.

In the past years, considerable progress has been made on experiments with strongly correlated many-body systems of ultracold atoms. The Mott-insulator state has been realized with bosonic [8] as well as fermionic atoms [9, 10], the BEC-BCS crossover has been intensely studied in many experiments ([11, 12] and references therein), and the equation of state of a unitary Fermi gas has been measured [13], to name only a few. While these experiments demonstrate the potential of ultracold atoms as model systems for many-body physics, a lot of effort is still necessary to reach the regimes that allow to address the cutting-edge problems of condensed matter physics. Many of these efforts today are devoted to establishing new experimental tools for the manipulation and probing of the atomic samples in order to step-by-step increase the complexity of the many-body Hamiltonians which can be realized: Novel optical lattice geometries are implemented [14, 15], probing and manipulation techniques with high spatial resolution are developed [16, 17], strong artificial magnetic fields for cold atoms are engineered [18]. Since the internal structure of the atoms crucially determines how they can be manipulated and what kinds of many-body Hamiltonians can be studied with them, extending the experimental trapping and cooling techniques to more and more atomic species is an important part of this work. Most cold-atoms-experiments today work with alkali atoms, which possess many desirable properties: Their strong D1- and D2-spectral lines in the red to near-infrared spectral range offer strong cycling transitions well suited for laser cooling. They comprise bosonic as well as fermionic isotopes with various ground-state spin configurations. Several isotopes exhibit broad Feshbach-resonances that can be used for tuning of the ground-state interaction. However, two other classes of atoms receive growing attention. The first one consists of atoms with a sizable magnetic dipole moment in the ground state. Three elements belonging to this class have been cooled to quantum degeneracy: Chromium [19], Dysprosium [20], and Erbium [21]. The rich physics connected to the anisotropic, long-range dipole-dipole interactions of these elements is attracting great interest [22]. The second class is that of alkaline-earth-like atoms, consisting of the alkaline-earth elements and Ytterbium (Yb), which exhibits a very similar electronic structure. These elements have been used already for several years in the field of frequency metrology, because they exhibit ultranarrow optical transitions which are very insensitive to environmental perturbations, making them excellent frequency references [23]. Their potential for the field of quantum many-body physics has only been realized a few years ago, when a series of theoretical proposals showed how the characteristic properties of these atoms could be used to engineer fascinating Hamiltonians [24, 25] and establish powerful tools for quantum

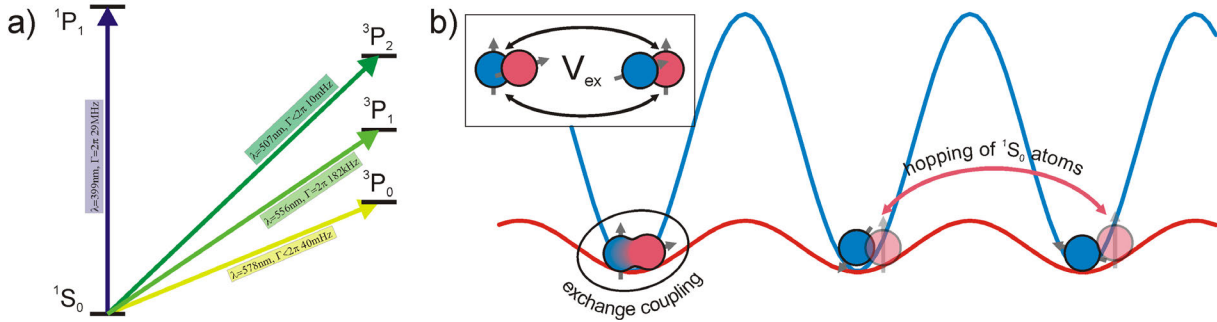


Figure 0.1: Panel a): The five lowest energy electronic states of Yb. The spectrum is split between singlet- and triplet-states of the combined electron spin. The three 3P -states couple to the ground state only via narrow intercombination transitions. While the transition to the 3P_1 state is still broad enough to be used for laser cooling, the ${}^3P_{0,2}$ are true metastable states with lifetimes of tens of seconds and can be used for the study of quantum many-body physics. Panel b): Illustration of the Kondo lattice model realized with ultracold Yb. A mixture of ground- and metastable state atoms is loaded into a state dependent optical lattice, where only the ground-state atoms can hop between lattice sites. A difference in the interaction between symmetric and anti-symmetric superpositions of ground- and metastable state atoms leads to a direct spin-exchange interaction between the two species.

information processing [26–28]. Motivated by these exciting prospects, the goal of the work presented in this thesis has been to build an apparatus for the investigation of quantum many-body physics with ultracold Yb, allowing experiments beyond what is presently possible with alkali atoms.

The most interesting aspect of alkaline-earth-like atoms is the existence of low-lying metastable electronic states. Because of their two valence-electrons, the energy spectrum of these atoms resembles that of Helium, being split into singlet ($S = 0$) and triplet states ($S = 1$) of the combined electron spin S . The selection rule $\Delta S = 0$ for electric dipole transitions forbids transitions between singlet and triplet states. However, imperfect LS-coupling leads to very weak so-called *intercombination* transitions connecting these states. Figure 0.1 a) depicts the five lowest lying electronic states of Yb. The ground state is a 1S_0 -state with no angular momentum $L = S = J = 0$. It is connected to the next higher singlet state 1P_1 via a strong dipole-allowed transition in the blue. Energetically in between these two states lie three 3P states. The 3P_1 is coupled to the ground state via a relatively broad intercombination transition in the green. The other two states 3P_0 and 3P_2 are true metastable states with lifetimes of tens of seconds. The corresponding dipole transitions to the ground state exhibit extremely narrow linewidths of only a few mHz.

These metastable states differ strongly from the ground state in their interactions as well as their ac-polarizability, which has intriguing consequences for experiments with mixtures of ground- and metastable-state atoms. For the fermionic alkaline-earth and Yb isotopes, which exhibit nuclear spin, mixtures of the 1S_0 ground state with the 3P_0 metastable state are of special interest, because both states have a vanishing electronic angular momentum $J = 0$. Thus, in such a mixture the electronic state and nuclear spin constitute independent degrees of freedom. In ref. [24] it has been pointed out that two alkaline-earth-like atoms on the same site of an optical

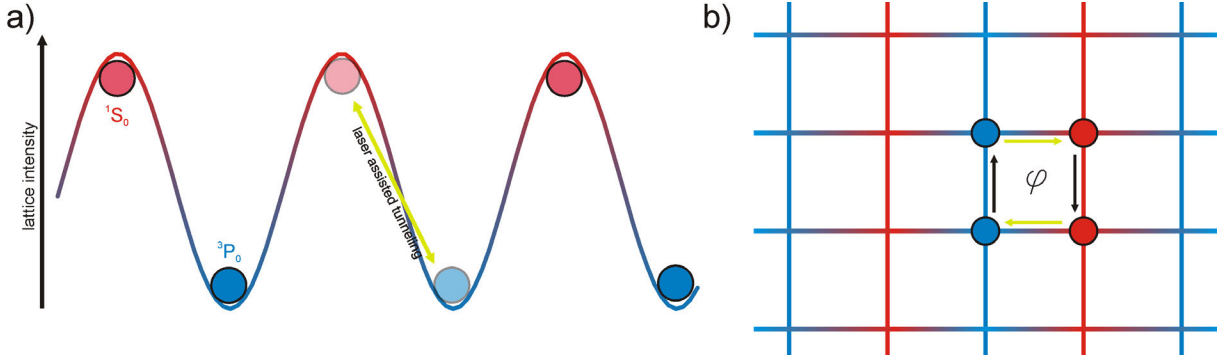


Figure 0.2: Panel a) depicts ground- and metastable state Yb-atoms in a state-dependent optical lattice, which is red-detuned for the ground-state and blue-detuned for the excited state. The two species thus occupy individual sub-lattices shifted by half a lattice spacing. Coupling the two electronic states by laser radiation leads to laser-assisted tunneling between the two sub-lattices. This can be used for the generation of strong artificial magnetic fields as illustrated in panel b). The atoms are placed on a two-dimensional square lattice, where along one direction normal tunneling occurs (indicated by black arrows) and laser assisted tunneling is active along the other direction (indicated by yellow arrows). Due to the spatially varying phase of the coupling laser, a net phase is imprinted on the atomic wavefunction, when moving around a lattice plaquette. This phase ϕ is equivalent to a vector potential acting on the atoms.

lattice, each in a different electronic state 1S_0 or 3P_0 , are subject to a direct spin-exchange interaction. If this spin-exchange interaction is combined with a state-dependent optical lattice that allows tunneling 1S_0 atoms between neighboring sites but freezes out the motion of 3P_0 atoms, the system is described by the Kondo lattice model, one of the most important models in current condensed matter physics [24, 29]. Such a state-dependent lattice is easily realized for ground- and metastable-state atoms. The ac-polarizability of the 1S_0 ground state is mostly determined by strong transitions to other singlet states, while the polarizability of the 3P_0 state is dominated by transitions to other triplet states. Therefore, the relative size of the polarizabilities of the two states varies strongly with wavelength. Choosing the right wavelength for the optical lattice thus allows to realize almost any state dependence. The Kondo lattice scenario with ultracold Yb-atoms is illustrated in fig. 0.1 b). 3P_0 atoms experience a deep optical lattice and are pinned to the individual lattice sites. 1S_0 atoms are allowed to hop between neighboring sites, where they couple to the localized 3P_0 atoms via the spin-exchange interaction. Up to now experiments of ultracold atoms in optical lattices have mostly been restricted to the Hubbard model. Therefore, the realization of the Kondo lattice would constitute an important step in the study of condensed matter problems with cold atoms.

Mixtures of 1S_0 and 3P_0 atoms in state-dependent optical lattices have, however, many more interesting applications. Consider for example atoms in an optical lattice, which is red-detuned for the ground state and blue-detuned for the metastable state. Since the ground-state atoms are drawn to the intensity maxima and the metastable states to the intensity minima, the two species occupy individual sub-lattices, shifted by half a lattice site with respect to each other as shown in fig. 0.2 a). If in such a lattice the two states are coupled by means of laser radiation, transitions between the ground- and metastable state are accompanied by laser-assisted tunneling

from one sub-lattice to the other. In such a laser-assisted tunneling process the spatially varying, complex-valued phase of the coupling laser is imprinted on the atomic wavefunction. This phase can be used to generate artificial magnetic fields for Yb-atoms moving on a two-dimensional optical lattice as depicted in fig. 0.2 b). The lattice must be implemented such that along one direction the atoms move by regular spontaneous tunneling, while laser-assisted tunneling occurs along the second direction [30]. It can be shown that in this scenario the atomic wavefunction acquires a net phase when moving around a lattice plaquette, equivalent to the Aharonov-Bohm phase of electrons moving in a magnetic field [31]. The system is then described by the Harper Hamiltonian, which contains important aspects of the integer quantum Hall effect [32] and is still subject of intense theoretical study. While similar schemes can be implemented for alkali atoms [33, 34], they require near resonant optical lattices and Raman coupling, which both induce significant heating of the atoms. The facts that for Yb the lattice can be far detuned from any transition and spontaneous emission from the metastable state is negligible constitute two important advantages, which make the implementation of strong synthetic magnetic fields for ultracold Yb very promising.

These are only two examples, which illustrate the possibilities that ultracold alkaline-earth-like atoms offer for the field of strongly correlated quantum many-body physics. Other interesting research directions using specific features of these atoms include high-spin quantum magnetism [35] and dipolar open-shell molecules [36].

Experiments with ultracold Yb have been pioneered by the research group of Y. Takahashi in Kyoto, who produced the first Bose-Einstein-condensate of ^{174}Yb already in 2003 [37]. By the time we started the Yb-experiment in Hamburg, his group had cooled five of the seven stable Yb-isotopes into the quantum degenerate regime. Since then they have also performed first interesting experiments with Yb in optical lattices [38, 39]. In contrast, none of the alkaline-earth-elements had been cooled to quantum degeneracy when we started our work. This happened, however, shortly afterwards when first ^{40}Ca [40] and later ^{84}Sr [41] were Bose-condensed. While especially Sr has now been demonstrated to be an extremely versatile atom, Yb captivates with its large number of stable isotopes, especially the two fermionic ones each with very interesting characteristics, as well as its favorable laser cooling properties. These two aspects as well as the successful experiments in the Kyoto group were our main motivation to choose Yb for our experiments.

This thesis comprises three chapters. The first chapter describes the experimental setup for the laser cooling of Yb. We demonstrate for the first time a two-dimensional magneto-optical trap (2D-MOT) as a source of slow Yb atoms, providing an alternative to the commonly used Zeeman slower. After discussing the characteristics of the two cooling transitions used for the 2D- and 3D-MOT, the cooling and trapping performance is characterized and compared to that of Zeeman slower setups.

Chapter 2 presents the production of quantum degenerate gases of bosonic ^{174}Yb and fermionic ^{173}Yb . Following a discussion of the evaporative cooling to quantum degeneracy in a crossed optical dipole trap for each isotope, their behavior in a triangular optical lattice is examined. For ^{174}Yb a measurement of the superfluid to Mott-insulator transition is presented. For ^{173}Yb

special attention is paid to the process of loading the optical lattice, revealing that due to the high mass of Yb higher Bloch-bands of the lattice are easily populated. Moreover, techniques for the preparation and detection of the nuclear spin states of ^{173}Yb are demonstrated.

Chapter 3 finally deals with the control of the electronic state of ultracold Yb. In section 3.1 a stable laser system for addressing the ultranarrow $^1S_0 \rightarrow ^3P_0$ transition is presented, which has also been built in the course of this thesis. With this system a linewidth at the few-Hz level could be demonstrated. The remaining two sections cover the spectroscopy on the $^1S_0 \rightarrow ^3P_0$ transition of fermionic ^{173}Yb in an optical lattice. First the spectroscopy is characterized experimentally using a spin-polarized sample. Finally, the spectroscopy Hamiltonian of an interacting two-component spin-mixture is discussed in detail and first spectroscopy experiments on such an interacting sample are presented.

1 A 2D/3D-MOT Setup for Laser Cooling of Yb

Every cold atoms experiment starts with an initial laser cooling and trapping stage, taking the atoms evaporated from a solid piece of material at a few hundred K to a dilute gas in the μK -regime. In this chapter I present our laser cooling setup for Yb, demonstrating for the first time a 2D-MOT as a source of cold Yb atoms, providing an alternative to the commonly used Zeeman slower.

The arguments in favor of a 2D-MOT can be summarized as follows: The 2D-MOT has become well established as a reliable, bright, and flexible source of cold atoms in the past years. Compared to a Zeeman slower it is more compact and in principle easier to build. Moreover, it can be used for cooling multiple elements for the investigation of heteronuclear quantum gas mixtures, while Zeeman slower setups often require two separate slowers for this purpose. Finally, a 2D-MOT does not require a slowing laser beam from the direction of the 3D-MOT. Therefore, 2D-MOT setups typically have better optical access to the 3D-MOT chamber than Zeeman slower setups. An important argument for our team was the fact that all other experiments in our group use 2D-MOTs. Doing so also for Yb allowed us to adopt for the most part the design of the other experiments in our group.

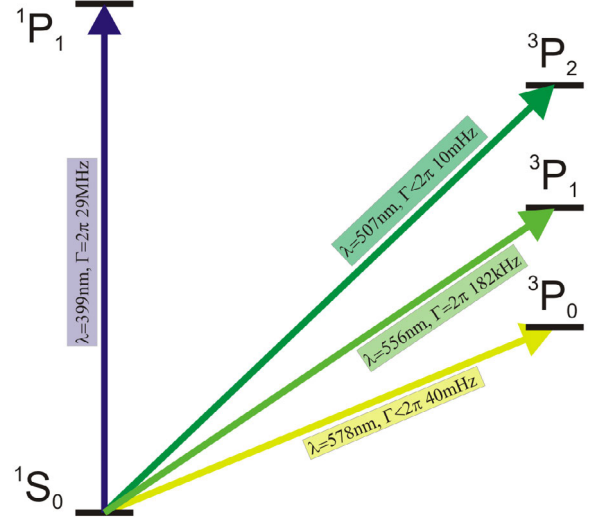
Until 2009 2D-MOTs were exclusively used for elements with comparatively high vapor pressure at room temperature, such as Rb, K, or Hg [42–44], where the 2D-MOT can be loaded from background vapor. Yb however, exhibits an extremely low vapor pressure at room temperature and the 2D-MOT needs to be loaded from a thermal beam emitted from an oven or a dispenser. In ref. [45] the authors showed that this is indeed feasible by demonstrating a 2D-MOT for Li, which was loaded from a thermal atom beam emitted from an oven located at the side of the 2D-MOT.

This chapter presents the implementation of such a side-loaded 2D-MOT for Yb. It is organized as follows: After summarizing the details of the relevant cooling transitions in section 1.1, the vacuum chamber and the geometry of the 2D/3D-MOT setup, as well as the cooling laser systems are described in sections 1.2 and 1.3. The setup is then characterized in section 1.4. Finally, the advantages and disadvantages of a 2D-MOT compared to a Zeeman slower are discussed in section 1.5.

1.1 Cooling Transitions of Yb

The most important parameter of an optical transition used for laser cooling and magneto-optical trapping is the linewidth Γ . It determines both the radiation pressure and thus the capture velocity of a MOT, as well as the Doppler temperature, which is approximately the temperature

Figure 1.1: Diagram of the lowest lying energy levels of Yb. Two transitions are well suited for laser cooling: The $^1S_0 \rightarrow ^1P_1$ with its large linewidth yields a large capture velocity but also a large Doppler temperature. It is thus ideal for pre-cooling thermal atoms to sub-mK temperatures. The narrower $^1S_0 \rightarrow ^3P_1$ intercombination transition with a Doppler temperature of $4.4 \mu\text{K}$ can then be used to cool the atoms further.



limit in a MOT. The Doppler temperature T_D is given by

$$T_D = \frac{\hbar\Gamma}{2k_B} \approx 24 \mu\text{K}/\text{MHz} \cdot \frac{\Gamma}{2\pi}, \quad (1.1)$$

where \hbar denotes Planck's constant and k_B the Boltzmann constant. An upper bound for the MOT capture velocity v_c can be estimated by taking the slowing force to be at its maximum of $\hbar k\Gamma/2$ over the whole MOT volume, with k denoting the wavenumber of the cooling light. From energy conservation one obtains

$$v_c = \sqrt{\frac{\hbar k\Gamma d}{M}}, \quad (1.2)$$

where d is the MOT diameter and M the mass of the atom. For Yb with a mass of ~ 174 u and a cooling transition in the visible spectral range ($\lambda \approx 500$ nm) the capture velocity amounts to

$$v_{c,\text{Yb}} \approx 17 \text{ m/s} \cdot \sqrt{\frac{d \cdot \Gamma}{\text{cm} \cdot \text{MHz}}} \quad (1.3)$$

Using these estimates, one can identify two useful cooling transitions in the energy spectrum of Yb, which is depicted in fig. 1.1: The $^1S_0 \rightarrow ^1P_1$ transition at 399 nm and the $^1S_0 \rightarrow ^3P_1$ transition at 556 nm. The 399 nm transition, with a linewidth of $\Gamma = 2\pi \cdot 29$ MHz results in a Doppler temperature of $700 \mu\text{K}$ and a capture velocity of $102 \text{ m/s} \cdot \sqrt{d/\text{cm}}$. Thus it is well suited for initially cooling the atoms from a few hundred K to sub-mK temperatures. Due to its high Doppler temperature, it is however rather impractical for a final laser cooling stage prior to evaporation. For alkali atoms, which can be sub-Doppler cooled, the Doppler temperature is basically irrelevant. However, all known sub-Doppler cooling mechanisms rely on redistribution of population between different m_F -ground-states. Hence, they do not work for the bosonic isotopes of Yb, which all have $F = 0$ in the ground-state. Thus, the temperature

of a MOT on the $^1S_0 \rightarrow ^1P_1$ transition will really be limited to $T_D = 700 \mu\text{K}$, which is a rather bad starting point for evaporation into the quantum degenerate regime. Luckily, the $^1S_0 \rightarrow ^3P_1$ intercombination transition provides a much lower Doppler temperature of $4.4 \mu\text{K}$ due to its narrow linewidth of $\Gamma = 2\pi \cdot 182 \text{ kHz}$. At the same time, the capture velocity on this transition of $7 \text{ m/s} \cdot \sqrt{d/\text{cm}}$ is still sufficient to capture atoms from a Zeeman slower or a 2D-MOT. The Doppler temperature of $4.4 \mu\text{K}$ is comparable to the sub-Doppler temperatures achieved with alkali atoms and presents a good starting point for evaporative cooling. This suggests a two stage cooling procedure, where the atoms are initially cooled in a Zeeman-slower or a 2D-MOT on the broad $^1S_0 \rightarrow ^1P_1$ transition. The resulting beam of pre-cooled atoms is then directly loaded into a 3D-MOT on the narrower $^1S_0 \rightarrow ^3P_1$ intercombination transition. This two-color cooling scheme has been pioneered by the group of Y. Takahashi [46] and to my knowledge is currently used by all Yb-quantum gas experiments worldwide.

Since the maximum capture velocity of the intercombination MOT is rather small, it is desirable to fully reach this maximum in the experiment. This is complicated by the fact that the Doppler shift is independent of the transition linewidth. For narrow line transitions it thus exceeds the natural linewidth already for very low velocities and easily shifts the atoms out of resonance with the cooling light. Our intercombination MOT has a diameter of $d = 2 \text{ cm}$ (cf. section 1.2), resulting in a maximal capture velocity of 10 m/s according to eq. (1.3). The Doppler shift at this velocity is

$$\Delta\nu_D = \frac{kv_c}{2\pi} = 18 \text{ MHz}, \quad (1.4)$$

which is about a 100 times the natural linewidth of the transition. Consequently, an atom that traverses the MOT will most of the time scatter no photons, because it is Doppler-shifted out of resonance with the cooling light. Part of this Doppler shift is compensated by the Zeeman shift as the atoms move through the magnetic field gradient of the MOT. For our geometry with a MOT diameter of 2 cm and a gradient field of 2 G/cm the Zeeman shift across the MOT amounts to $\Delta\nu_Z \approx 8 \text{ MHz}$, leaving an uncompensated Doppler shift of about 10 MHz . In order to keep the scattering rate, and thus the slowing force, at its maximum during the entire capture process, light with a spectral width of about 10 MHz is required. This is still 50 times the natural linewidth. The required broadening can either be achieved by saturation broadening or by actively modulating the laser frequency itself. The latter method is more economic, because saturating the transition implies a reduction of the scattering rate per photon.

For the fermionic isotopes ^{171}Yb and ^{173}Yb , which carry a nuclear spin of $I = 1/2$ and $I = 5/2$ respectively, the hyperfine structure of the cooling transitions needs to be taken into account. It is shown in fig. 1.2. The hyperfine splitting of the 3P_1 -manifold is on the order of a few GHz, much larger than the relevant detunings in the intercombination-MOT. Consequently, neighboring hyperfine transitions that are not used for the MOT can be neglected. The hyperfine splittings of the 1P_1 -manifold are about a factor of ten smaller and amount to a few hundred MHz. A rather small splitting compared to the linewidth of $\Gamma = 2\pi \cdot 29 \text{ MHz}$. For ^{171}Yb this is not problematic, because the $F = 3/2$ -state used for cooling is the lowest hyperfine state. The cooling laser can thus be red-detuned from the whole hyperfine manifold, which is ideal for Doppler cooling. For ^{173}Yb the hyperfine structure is however extremely problematic:

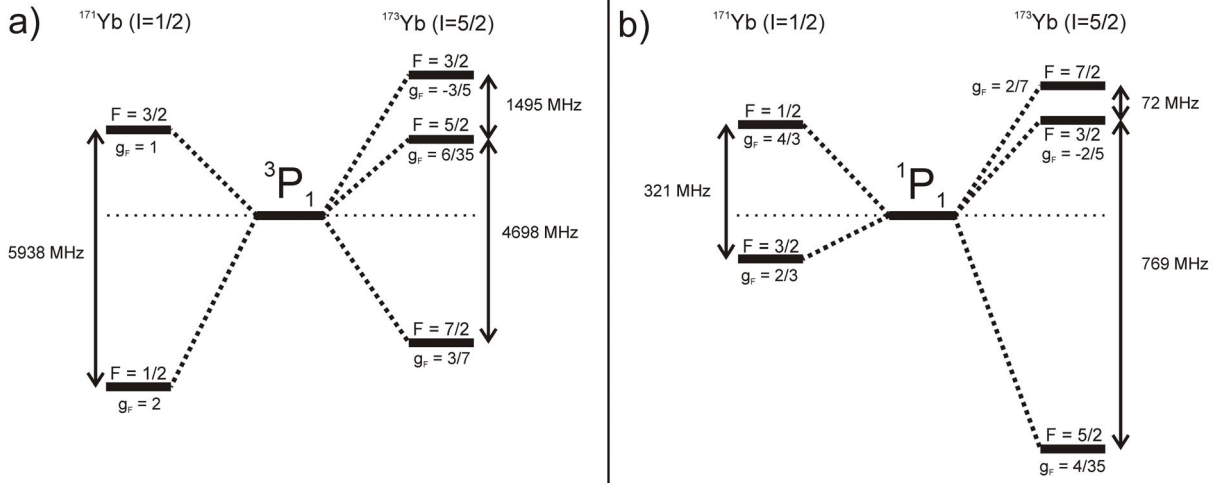


Figure 1.2: Hyperfine structure of the 3P_1 and 1P_1 states of Yb. For the 3P_1 -state shown in panel a), the hyperfine splitting is in the GHz-range and thus negligible compared to the detunings in a MOT. The splittings in the 1P_1 manifold are however only a few hundred MHz, corresponding only to a few linewidths of the $^1S_0 \rightarrow ^1P_1$ transition. Especially the $F = 3/2$ and $F = 7/2$ states in ^{173}Yb are only 2.5Γ apart. This narrow hyperfine structure is a serious problem for a MOT on this transition. The hyperfine Landé-factors g_F are indicated next to each level.

The $F = 7/2$ -state that must be used for Doppler cooling is the highest energy hyperfine level. And only 2.5Γ below lies the $F = 3/2$ -state. Thus, for MOT detunings of $\Delta < 2.5\Gamma$ the cooling laser will be closely blue-detuned from that state, resulting in Doppler heating. Tuning the cooling laser below the $F = 3/2$ -state is also problematic, because the g_F -factors of the $F = 3/2$ - and $F = 7/2$ -states have opposite sign. Thus, the $F = 3/2$ -state causes a *deconfining* position-dependent force acting against the desired confining force exerted by the $F = 7/2$ -transition. Already in early experiments on magneto-optical trapping of Yb on the 399 nm-transition, a strongly suppressed loading rate for ^{173}Yb has been observed and was attributed to the narrow hyperfine structure [47–49]. This problem applies of course also to a 2D-MOT and presents a major disadvantage of a 2D-MOT for Yb compared to a Zeeman slower. Unfortunately, we realized this too late. Still, we managed to tweak the 2D-MOT such that we can reasonably work with ^{173}Yb in our experiment, as will be described in section 1.4.

Another peculiarity of the laser cooling and trapping of fermionic Yb- and alkaline-earth isotopes, which must be shortly mentioned here, comes from the large difference of the ground- and excited-state magnetic moments of the cooling transitions. Since the ground state of Yb has a purely nuclear spin, its magnetic moment is ~ 2000 times smaller than those of the excited 1P_1 and 3P_1 states, which are on the order of the Bohr-magneton. Therefore, in the magnetic field gradient of the MOT the cooling transitions split up according to the magnetic quantum number of the excited state m'_F as shown in fig. 1.3 a). This is in stark contrast to alkali atoms, where the differential magnetic moment is small and the transition splits up according to the difference of the initial- and final-state magnetic quantum numbers Δm_F . This is shown in panel b) of the same figure. The consequences of this m'_F -dependent splitting for the magneto-optical trapping

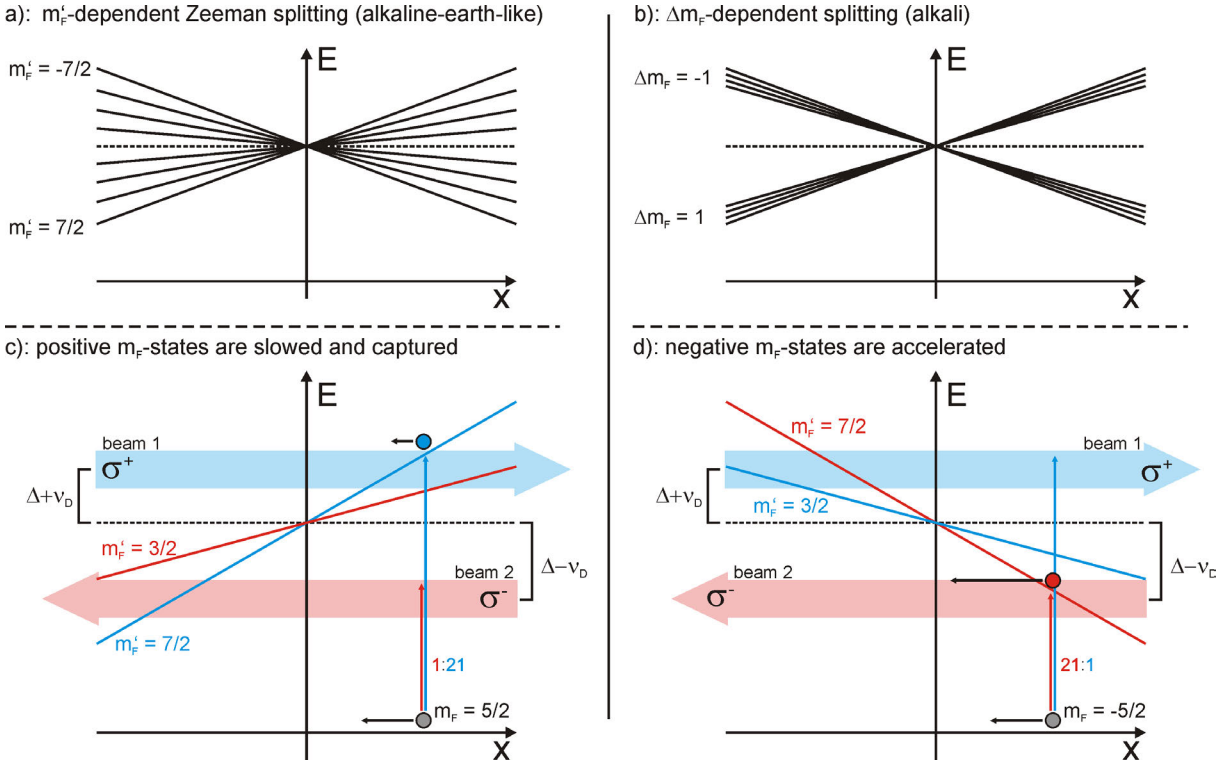


Figure 1.3: Illustration of the capture process in a MOT using a transition with a large differential Zeeman shift as in Yb. In the magnetic field gradient of a MOT, such a transition splits up according to the magnetic quantum number of the final state m'_F , as shown in panel a). In contrast, when the differential Zeeman shift is low as in the case of alkalis, the transition splits up according to the Δm_F of the transition, as shown in panel b). In the case of a large differential Zeeman shift, only half of the m_F -ground states can be efficiently captured as shown in panels c) and d) for the $(^1S_0, F = 5/2) \rightarrow (^3P_1, F = 7/2)$ of ^{173}Yb . For positive m_F shown in c), the magnetic field shifts both transitions σ^+ and σ^- to higher frequencies. Thus, the Doppler-blue-shifted σ^+ -polarized beam is in resonance and slows down the atom. For negative m_F shown in d), both transitions exhibit a negative Zeeman shift, bringing them into resonance with the Doppler-red-shifted σ^- -polarized beam, which accelerates the atom. For the stretched states $m_F = \pm 5/2$ shown here, the large ratio between the Clebsch-Gordan coefficients of 1:21 further favors the slowing of the $m_F = +5/2$ -state and the acceleration of the $m_F = -5/2$ -state.

of alkaline-earth-like atoms have first been noticed by the Tokyo group [50] and are nicely explained in ref. [51]. Essentially, it can be summarized by saying that in the steady state the MOT only works well for one half of the m_F -ground-states, while being ineffective on the other half. As long as enough MOT-photons are scattered to continuously randomize the ground-state m_F -population, this is more or less irrelevant. Only the average restoring force is reduced. During the MOT capture process, when the Doppler shift ν_D is large compared to the Zeeman shift, the consequences are more drastic, as can be seen from the following discussion: Consider an atom in the $m_F = +5/2$ ground-state, entering the MOT from the direction of positive x , shown in fig. 1.3 c). It can be excited to the $m'_F = +7/2$ -state by absorbing a σ^+ -polarized photon from MOT-beam 1, slowing down the atom, or it can be excited to the $m'_F = +3/2$ -state

by absorbing a σ^- -polarized photon from MOT-beam 2, accelerating the atom. The magnetic field gradient shifts both states to higher energies in the region of $x > 0$. Due to the Doppler shift, beam 1 is blue shifted into resonance with the $m'_F = +7/2$ -transition, while beam 2 is red-shifted, out of resonance. This strongly favors the desired scattering of σ^+ -photons from beam 1 that slows down the atom. The Clebsch-Gordan coefficients further suppress the unwanted scattering of σ^- -photons. Thus, atoms entering the MOT in the $m_F = +5/2$ -state can be efficiently captured. These arguments also hold for the other states with $m_F > 0$. Only the lower Zeeman shift slightly reduces the suppression of unwanted σ^- -scattering. The situation is, however, completely reversed for states with $m_F < 0$: Consider now an atom in the $m_F = -5/2$ ground-state entering the MOT again from the direction of positive x . This atom can be excited to the $m'_F = -7/2$ -state by absorbing σ^- -photons from beam 2, accelerating the atom. Or it can be excited to the $m'_F = -3/2$ -state by absorbing σ^+ -photons from beam 1, slowing down the atom. Contrary to the $+5/2$ -case, the combination of Zeeman- and Doppler shift brings the undesired σ^- -transition into resonance, while shifting the desired σ^+ -transition out of resonance. The Clebsch-Gordan coefficients further worsen the situation, as they suppress the σ^+ - compared to the σ^- -transition. Consequently, atoms in the $m_F = -5/2$ -state are hardly captured by the MOT at all. This effect is less pronounced but qualitatively the same for the other states with $m_F < 0$. This discussion shows that due to the large differential Zeeman shift between the ground- and excited m_F -states only half of the m_F -states can be captured in a MOT.

1.2 The MOT setup

The vacuum setup we use is similar to those used in the other experiments in our group. It is presented in great detail in the PhD thesis of Sören Dörscher [52], who did the CAD design. Figure 1.4 depicts the essential parts of our MOT setup. The vacuum chamber consists of two glass cells connected to a small stainless steel chamber. The steel chamber provides separate connections to two 50 l/s ion pumps, one for each glass cell, and connects the two cells via a differential pumping tube. The 2D-MOT is operated in the upper glass cell. From there, the slowed atoms propagate through the differential pumping tube into the lower glass cell, called *science cell*, where they are eventually cooled to quantum degeneracy. A close-up of the 2D-MOT cell is shown in panel b) of fig. 1.4. Two dispensers¹ are mounted upright in the corners of the glass cell. The slit-shaped openings are facing the center of the cell that corresponds to the position of the 2D-MOT. Expectedly, the dispensers emit almost into the full half space in front of the opening. Thus, in order to avoid coating the glass cell with Yb, we have installed additional slit apertures in front of the dispensers that limit the coating of the glass cell to the corners, where no laser beams pass through.

The magnetic field gradient for the 2D-MOT is generated by four coils of rectangular shape, which can be seen in fig. 1.4 a) and b), generating a gradient of $4.6 \text{ G/cm} \cdot \text{A}^{-1}$. Each coil consists of 84 turns of copper wire with a diameter of 1.25 mm. In order to reach gradients as

¹Alvatec, AS-4-Yb-500-S

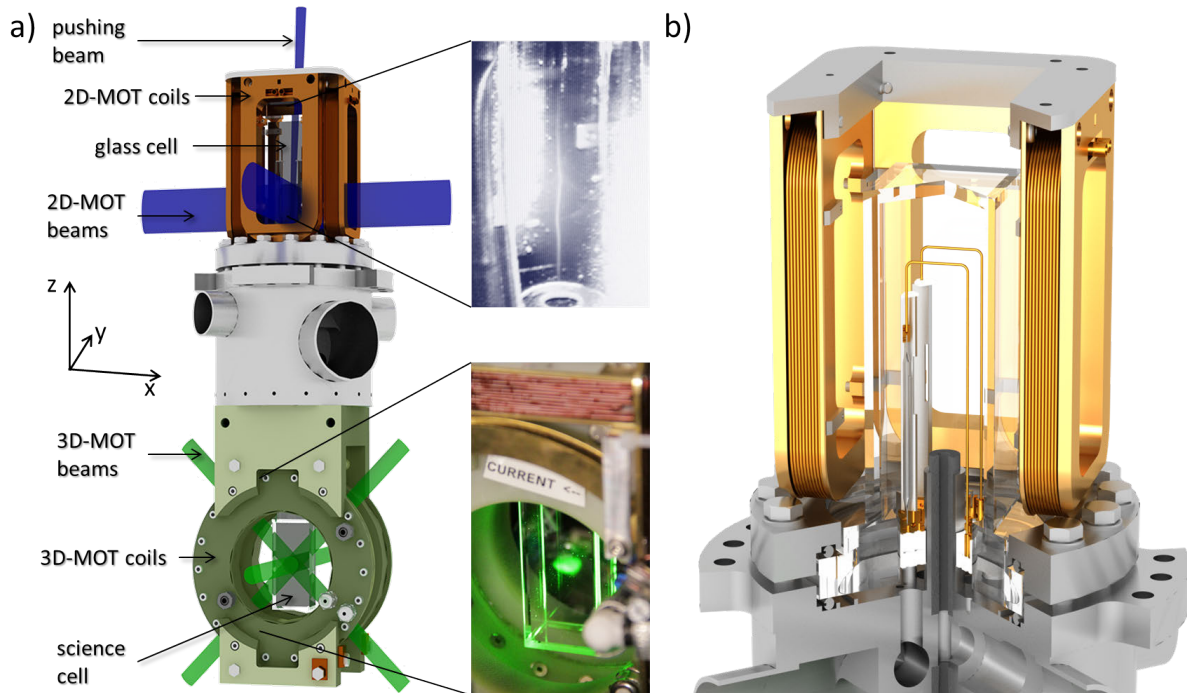


Figure 1.4: Schematic of the vacuum setup and the 2D-/3D-MOT geometry. Panel a) depicts a three-dimensional drawing of the vacuum chamber and the MOT beams. The 2D-MOT glass cell is connected to the science cell via a narrow differential pumping tube located inside the stainless steel chamber. A push-beam enhances the flux of atoms reaching the science cell. For the bosonic ^{174}Yb the fluorescence of the 2D-MOT can well be observed on a ccd-camera as a thin long line. Hundreds of millions of atoms in the 3D-MOT fluoresce in bright green. Panel b) depicts a close-up of the 2D-MOT cell. Two dispensers are mounted upright in the corners of the glass cell, emitting Yb vapor through ~ 2 cm long slits. Additional apertures carefully positioned in front of the dispensers protect the glass cell from being coated with Yb.

high as 60 G/cm necessary for the Yb-2D-MOT, the brass reels on which the coils are wound are water-cooled. Some other groups use permanent magnets to generate the 2D-MOT field. While this is a good option for a single-element 2D-MOT, it cannot be done when using the 2D-MOT for cooling multiple elements, since this usually requires changing the gradient during the experimental cycle. The 2D-MOT beams are elliptical with diameters of $(1 \text{ cm} \times 4 \text{ cm})$. The long axis is oriented vertically to match the emission characteristics of the dispenser and the slit aperture in front of it.

The 3D-MOT gradient is generated by a pair of Helmholtz coils, which shall also serve as a quadrupole trap for RF-evaporation of Rb, when producing ultracold Yb-Rb-mixtures in the future. Therefore, they have been designed for the generation of high field gradients of $\sim 160 \text{ G/cm}$. The coils consist of 48 turns of copper wire with a diameter of 2.15 mm , producing a gradient of $1.3 \text{ G/cm} \cdot \text{A}^{-1}$ along their axis of symmetry. They are placed in a hermetically sealed housing made of fiber enforced epoxy to avoid eddy-currents. Cooling water is sent

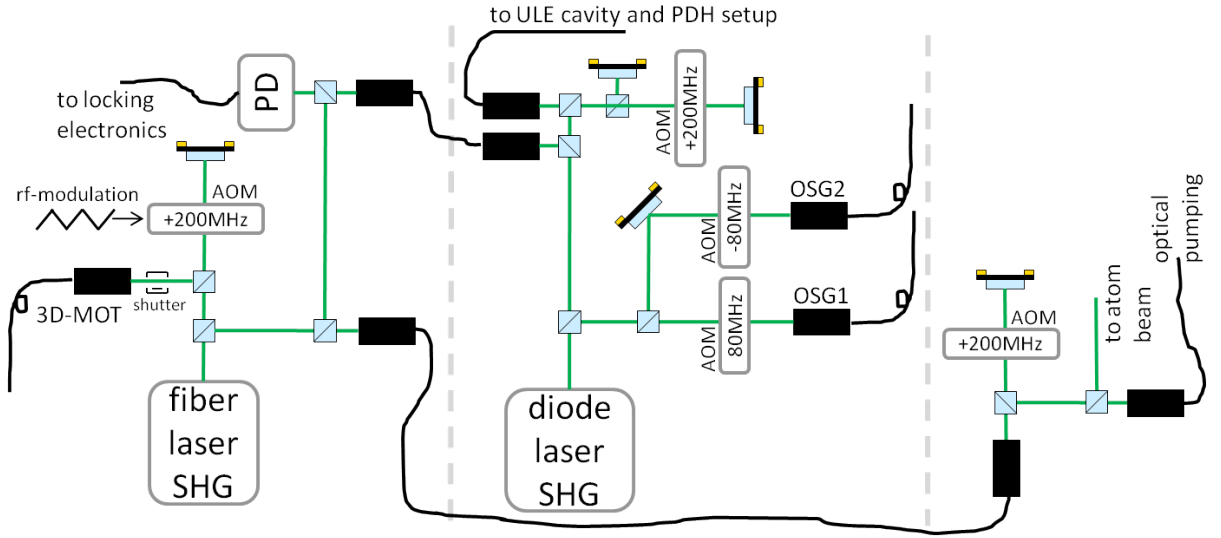


Figure 1.5: Simplified schematic of the 556 nm laser system. We have two commercial frequency-doubled laser sources at our disposal, a diode laser-based and a fiber laser-based system. The diode laser-based system is locked to an ultrastable ULE cavity via the Pound-Drever-Hall (PDH) technique and is used for the optical Stern-Gerlach separation described in section 2.5.2. The MOT light is derived from the fiber laser-based system, which is stabilized to the fluorescence of an Yb atomic beam in the case of ^{174}Yb and offset locked to the cavity-locked diode laser for ^{173}Yb . The 200 MHz acousto-optic modulator (AOM) in the MOT arm is used to broaden the frequency spectrum of the cooling light as described in the main text. A mechanical shutter completely shuts off the cooling light after the MOT phase.

through the housing, flowing directly around the wire. This results in a very compact design with high cooling efficiency. The large inner diameter of the coil housings provides an opening angle of 90° at which the atoms can be accessed through the coil openings. The distance of 3.4 cm between the two coil housings provides very good optical access to the atoms from the side of the coils as well. The coils have been tested up to a current of 140 A, producing a gradient of 182 G/cm or alternatively a homogeneous field of 890 G. The Yb 3D-MOT needs of course only a very small magnetic field gradient of a few G/cm, due to the narrow linewidth of the $^1S_0 \rightarrow ^3P_1$ transition.

The 3D-MOT beams have a circular cross section with a $1/e^2$ -diameter of 2 cm, one propagating along y and the other two in the x - z -plane under $\pm 45^\circ$ with respect to the horizontal as can be seen in fig. 1.4 a). Initially, we used six independent beams for the 3D-MOT. Recognizing later that laser power is more important than perfect balancing of the radiation pressure, we switched to a three beam configuration, where each beam is retro-reflected in a cat's-eye configuration.

1.3 The Cooling Laser Systems

The choice of available laser sources for the two cooling transitions at 399 nm and 556 nm are rather limited. Light at 556 nm can in principle be obtained from dye lasers, which are however

experimentally rather inconvenient. The only alternatives are frequency-doubled diode or fiber lasers. We have two laser systems at this wavelength: A diode laser-based system² with an output power of ≈ 200 mW and a frequency-doubled fiber laser³ with an output power of ≈ 290 mW. The whole laser system is depicted in fig. 1.5. Because of its higher output power, the fiber laser is employed for the 3D-MOT. A 200 MHz acousto-optic modulator (AOM) in double-pass configuration in the 3D-MOT beamline is used to broaden the spectrum of the cooling laser and thereby increase the capture velocity. This is done by modulating the RF-frequency driving the AOM over several MHz using a triangular modulation signal as indicated in fig. 1.5. The diode laser system is used for the optical Stern-Gerlach separation of ^{173}Yb (cf. section 2.5.2) and might be used in the future for a double-isotope MOT. We use two different locking schemes for ^{173}Yb and ^{174}Yb . For ^{174}Yb only the fiber laser providing the MOT light is needed. In this case we stabilize the laser to the Doppler-free fluorescence signal obtained from spectroscopy on an Yb atomic beam. For ^{173}Yb the Doppler-free signal from the atomic beam spectroscopy is rather weak, due to the lower isotope abundance and the large number of magnetic substates, each resulting in its own lamb-dip, shifted by stray magnetic fields. Moreover, we need a far-detuned laser for the spin separation via the optical Stern-Gerlach effect. In this case we stabilize the lasers as follows: The diode laser-based system is locked to a stable high-finesse Fabry-Perot cavity and is used for the optical Stern-Gerlach pulse. A small portion of this stabilized laser light is overlapped with light from the fiber laser and the resulting beat note is used for offset-locking the fiber laser to the diode laser system such that it is resonant with the $(^1S_0, F = 5/2) \rightarrow (^3P_1, F = 7/2)$ transition and can be used for the MOT. The offset-lock and the optical Stern-Gerlach setup has in large part been implemented by my colleague André Kochanke.

The 399 nm-light can be generated either via frequency-doubled diode lasers or directly via blue laser diodes. Since using directly the blue laser diodes is in principle easier and cheaper than using a frequency-doubled laser, we started with a laser setup based purely on blue laser diodes. This setup is described in the Diplomarbeit of Hans Kessler [53], which I supervised within my time in the lab. After first running the 2D-MOT with this setup, we realized that the MOT loading rate was limited by the 399 nm laser power. Therefore we added a frequency-doubled laser system⁴ (SHG-system), used exclusively for the 2D-MOT light.

Figure 1.6 depicts the complete 399 nm setup in the current configuration. The central part of the system is a home-built external cavity diode laser (ECDL), using a Nichia laser diode⁵ and a diffraction grating⁶ with 3600 lines/mm and 50% diffraction efficiency for s-polarized light. Although the bare laser diode delivers up to 120 mW output power, it only exhibits single-frequency operation in the external cavity up to a power of 12 mW. The single-frequency output power could be significantly increased, when the feedback from the grating was reduced by intentionally misaligning the grating. Of course, for reliable operation the grating needs to be

²TOPTICA: DL-FA SHG

³Menlo Systems: Orange one-SHG

⁴Toptica: DL-TA SHG

⁵NDV4313, selected for a central wavelength of 400 nm

⁶Optometrics: 3-4361

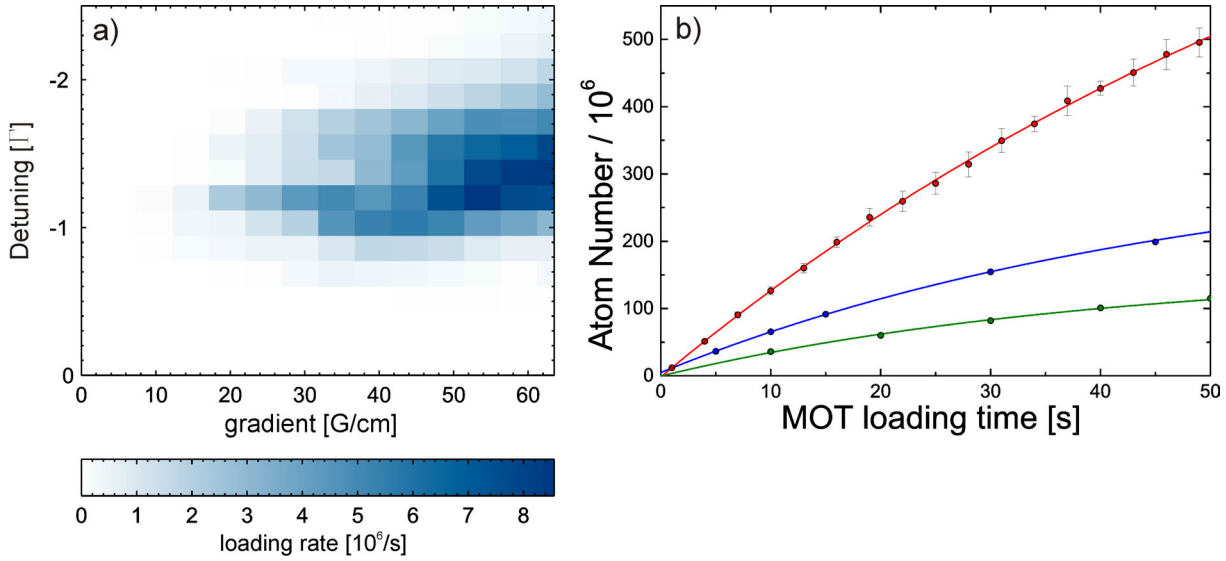


Figure 1.7: Panel a): 3D-MOT loading rate for ^{174}Yb measured as a function of 2D-MOT magnetic field gradient and detuning in units of the 2D-MOT linewidth Γ . The best loading rate is obtained at a gradient of 60 G/cm and a detuning of -1.2Γ . Panel b): Number of ^{174}Yb atoms trapped in the 3D-MOT as a function of loading time for the optimum 2D-MOT parameters. The red data points correspond to the current setup. The green data points were obtained, using the fiber-coupled injection locked diode lasers slave 2 and 3 for the 2D-MOT and a six-beam 3D-MOT configuration. The blue data points were obtained by replacing the diode lasers with the frequency-doubled system, still using optical fibers and a six-beam 3D-MOT.

changing the reference frequency of the offset-lock. This has two important advantages: First, no AOMs are needed to adjust the detuning. Thus, the typical 15 to 20% loss of an AOM are avoided. Moreover, the detuning can be changed quickly over a wide range of several GHz, limited by the bandwidth of the reference input of the locking electronics of 7 GHz. This might be useful in the future for the production of Yb isotope mixtures. During the MOT-loading cycle, the frequency could be changed from one isotope to another to sequentially load the two isotopes into a two-color 3D-MOT. The offset-lock electronics we use have been designed by Jürgen Appel et al. and are described in ref. [54]. This setup provides us with a power of 180 mW in each of the 2D-MOT beams. For the elliptical 2D-MOT beams with diameters of (1 cm \times 4 cm) the resulting peak saturation parameter is $s_0 = I/I_{\text{sat}} \approx 1.9$.

1.4 Characterization of the 2D/3D-MOT Setup

In order to characterize the 2D/3D-MOT-setup described above, the dependence of the 3D-MOT loading rate on the various parameters of the 2D- and 3D-MOT has been analyzed for the bosonic isotope ^{174}Yb and the fermionic ^{173}Yb .

1.4.1 Bosonic ^{174}Yb

After initial optimization, we studied the influence of the most important MOT parameters on the 3D-MOT loading rate $R_{3\text{D}}$. Figure 1.7 a) depicts $R_{3\text{D}}$ as a function of the 2D-MOT magnetic field gradient and the 2D-MOT detuning $\Delta_{2\text{D}}$ in units of the $^1S_0 \rightarrow ^1P_1$ linewidth Γ . The loading rate is maximized for a gradient of about 60 G/cm and a detuning of $\Delta_{2\text{D}} = -2\pi \cdot 35 \text{ MHz} = -1.2 \Gamma$. These parameters are immediately plausible, considering the available 2D-MOT power and beam geometry: For the transverse 2D-MOT diameter of 1 cm, the maximum capture velocity is 102 m/s as explained in section 1.1. Due to the low saturation parameter of $s_0 = 1.9$, at most $s_0/(s_0 + 1) \approx 65\%$ of this capture velocity can be achieved. Considering further imperfections such as the Gaussian intensity profile of the MOT beams, a capture velocity of $\sim 50 \text{ m/s}$ can be considered realistic. The resulting Doppler shift at this velocity is $\nu_D = 125 \text{ MHz}$. At our optimum field gradient of 60 G/cm, the Zeeman shift across the MOT amounts to 84 MHz. The remaining 40 MHz are within the saturation broadened linewidth of $\Gamma\sqrt{1 + s_0} = 48 \text{ MHz}$. The detuning of $\Delta_{2\text{D}} = -2\pi \cdot 35 \text{ MHz}$ corresponds to the MOT light being in resonance with atoms at rest near the edge of the MOT, as should be the case for optimum capture.

A detailed understanding of fig. 1.7 a) can be obtained by numerically integrating the trajectories of a thermal distribution of particles cooled by the 2D-MOT. This calculation was performed in our team by Sören Dörscher and is in detail presented in his PhD thesis [52]. The predicted optimum detuning and gradient agree very well with our measured optimum values. The simulation also reveals that the observed maximum is indeed the global optimum. For larger gradient fields, the loading rate starts to decrease again.

Having found the optimum detuning and gradient, the third important 2D-MOT parameter is the power of the push beam. The relative increase of the loading rate with push beam power is shown in fig. 1.8 a). For push beam powers above 300 μW , the loading rate saturates at about three times the loading rate without push beam. For the Rb 2D-MOTs in other experiments in our group the push beam increases the loading rate by more than a factor of 10. The fact that the increase is lower in our case may partly be explained by the rather low capture velocity of the 3D-MOT. Besides pushing more atoms down, the push beam may also accelerate atoms to velocities outside of the capture range of the 3D-MOT. Another reason might be an asymmetric emission profile of the dispenser. The push beam being about 20 MHz red-detuned works by pushing atoms down that were initially traveling slowly upward in the 2D-MOT. If most of the atoms were already emitted downwards by the dispenser, there would be little to be gained by the push beam.

The most important parameter of the 3D-MOT is the magnitude of the spectral broadening. As explained in the previous section, the spectrum of the cooling light is broadened by modulation via a double-pass AOM. We use a triangular modulation signal with a modulation frequency of 200 kHz and a modulation amplitude of up to several MHz. $R_{3\text{D}}$ as a function of the spectral width of the cooling laser is plotted in fig. 1.8 b). In this measurement the center frequency of the cooling light was adjusted such that the highest frequency component was kept at a constant detuning of -3.2 MHz . As the broadening is increased, the loading rate increases almost lin-

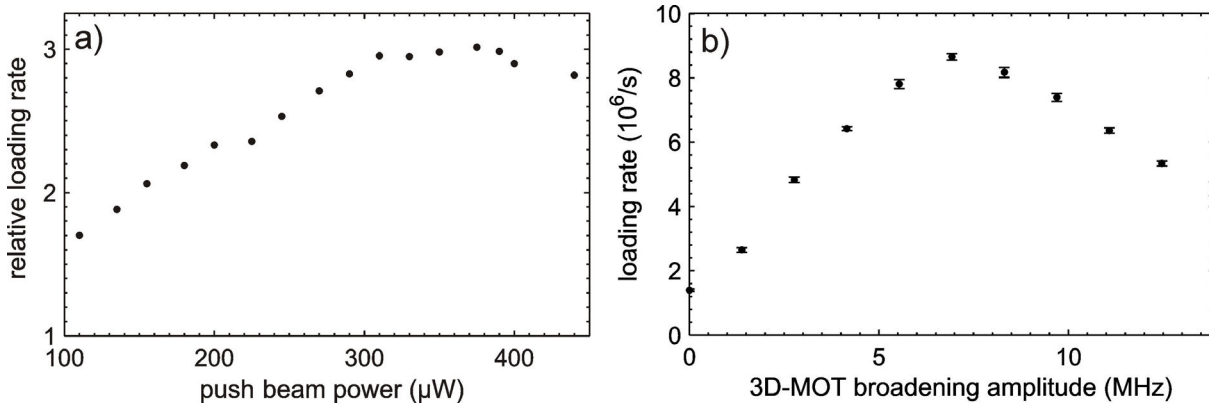


Figure 1.8: Panel a): Relative increase of the 3D-MOT loading rate due to the push beam as a function of push beam power. Initially the loading rate increases linearly. For push-beam powers above 300 μW it saturates at about three times the bare loading rate. Panel b): 3D-MOT loading rate as a function of the spectral broadening of the 3D-MOT cooling light. For broadening amplitudes up to 7 MHz, the loading rate decreases linearly, because the capture velocity of the 3D-MOT increases. For larger broadening, the spectral power density becomes too low and compromises the capture efficiency.

early up to a spectral width of 7 MHz. This indicates that the beam of atoms produced by the 2D-MOT exhibits a rather flat velocity distribution, with the consequence that an increase in the capture velocity due to the spectral broadening causes a proportional increase of the loading rate. For spectral widths above 7 MHz, the loading rate decreases again. This can be understood as follows: In section 1.1 it was estimated that the maximum capture velocity of our 3D-MOT of 10 m/s is achieved for a spectral width of the cooling laser of 10 MHz. Realistically, the maximum capture velocity is below this value, because part of the atoms hit the MOT off-center and the effective cooling volume might be reduced by imperfect overlap of the cooling beams at the edges of the MOT. Therefore, the capture velocity is probably close to its maximum for a spectral width of 7 MHz. Broadening the light further will take power from the frequency components that contribute to the cooling. Since the average intensity per natural linewidth is already down to $\sim 2I_{\text{sat}}$ for a broadening of 7 MHz, the capture rate will decrease for further broadening.

Figure 1.7 b) shows measured 3D-MOT loading curves for different experimental configurations. The green curve was recorded in the initial configuration using the injection locked laser diodes for the 2D-MOT resulting in a power of 50 mW per 2D-MOT beam. Changing from the diode lasers to the SHG-system increased the 2D-MOT power by a factor of two to 100 mW per 2D-MOT beam, resulting in a two times larger loading rate, shown in blue. Finally, bringing the blue SHG system from the laser table to the vacuum table and removing the optical fibers, increased the 2D-MOT power to 180 mW per beam. Moreover, we changed from a six-beam- to a retroreflected three-beam 3D-MOT and improved the push beam configuration. These changes resulted in another factor of two improvement in the loading rate, shown in red. In this final configuration we achieve loading rates of about $13 \cdot 10^6 \text{ s}^{-1}$, yielding more than 10^8 atoms after 10 s loading. This is comparable to Zeeman slower setups and a good starting point for

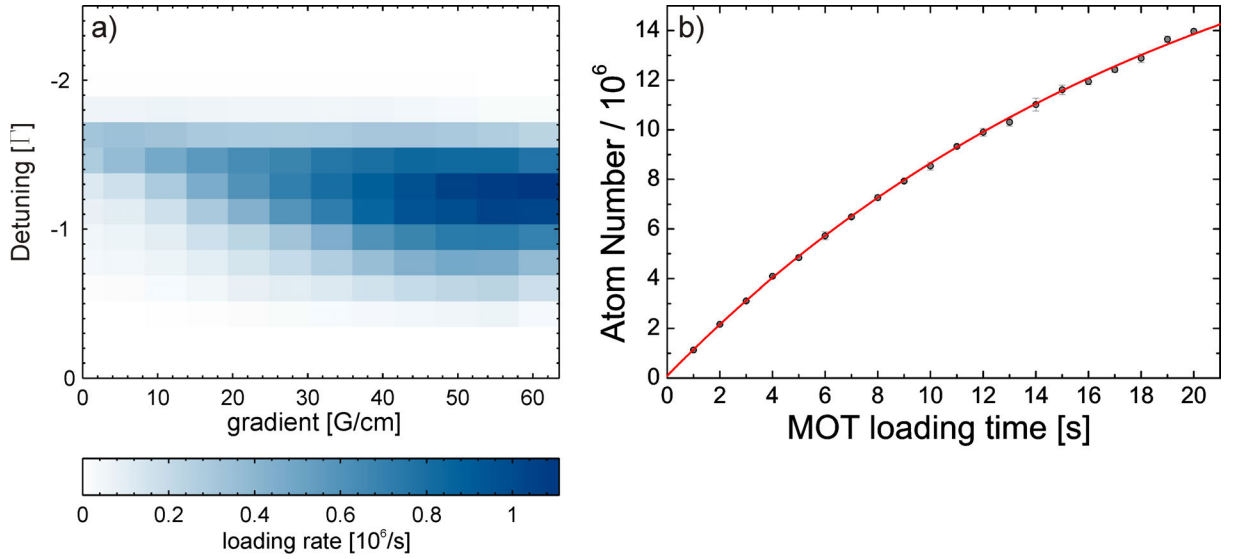


Figure 1.9: Panel a): 3D-MOT loading rate for ^{173}Yb measured as a function of 2D-MOT magnetic field gradient and detuning in units of the 2D-MOT linewidth Γ . This measurement is analogous to that presented in fig. 1.7 for ^{174}Yb . The loading rate exhibits a sharp cut-off at a detuning of -1.5Γ , which is attributed to the resonance of the ($^1P_1, F = 3/2$)-hyperfine state at $\sim -2.5\Gamma$. The optimum loading rate is however achieved for similar parameters as for ^{174}Yb , i.e. a gradient of 60 G/cm and a detuning of -1.2Γ . Note that for this measurement, the 2D-MOT polarization has been adjusted for an optimal loading rate and deviates considerably from the usual circular polarization. Panel b): Number of ^{173}Yb atoms trapped in the 3D-MOT as a function of loading time for the optimum 2D-MOT parameters.

evaporative cooling.

1.4.2 Fermionic ^{173}Yb

For the fermionic isotope ^{173}Yb , laser cooling on the $^1S_0 \rightarrow ^1P_1$ transition is disturbed by the narrow hyperfine splitting between the $F = 7/2$ - and $F = 3/2$ -states. This effect is so severe that the 3D-MOT loading rate reaches only a few 10^4 s^{-1} , if only the laser detunings are changed from ^{174}Yb to ^{173}Yb . The most important adjustment that needs to be made to improve the loading rate is the polarization of the 2D-MOT cooling beams. The change of the polarization has to be accompanied by a realignment of the cooling beams, probably because of a different overall radiation pressure compared to the bosons. Iteratively adjusting alignment and polarization of the 2D-MOT beams yields loading rates between $1.1 \cdot 10^6 \text{ s}^{-1}$ and $1.5 \cdot 10^6 \text{ s}^{-1}$. Accounting for the two times lower natural abundance of ^{173}Yb compared to ^{174}Yb the 3D-MOT loading rate is still a factor of five lower. This must be attributed in large part to the large differential Zeeman shift between the ground- and excited states of the MOT transitions. As detailed in section 1.1, this has the effect that only half the m_F -ground states can be efficiently captured by the MOT. The atoms emitted from the dispenser can be assumed to be randomly distributed among the different m_F -states. Consequently, only half of the atoms whose velocities lie within

the 2D-MOT capture range can indeed be captured, reducing the 2D-MOT flux by a factor of two, compared to the bosons. The atoms emitted from the 2D-MOT towards the 3D-MOT are again randomly distributed among the six ground-state m_F -levels, due to optical pumping in the 2D-MOT and the absence of a guiding magnetic field in the differential pumping stage. Thus, only 50% of the atoms reaching the 3D-MOT can be captured. As a result of this reduction of the loading rates of both MOT stages by a factor of two, the 3D-MOT loading rate is reduced by a factor of four compared to the bosons. In the light of these considerations, the factor of five reduction observed in our setup is astonishingly good given the hyperfine structure problems. In section 1.5 it will be argued that this problem should not arise in Zeeman slower setups.

The 3D-MOT loading rate as a function of the 2D-MOT gradient and detuning is depicted in fig. 1.9 a). Apart from the overall lower loading rate, the qualitative behavior of R_{3D} is also different compared to the bosonic ^{174}Yb . Towards lower gradients it falls off more slowly than for the bosons. A possible explanation for this effect could be that the change of the light polarization away from perfect circular polarization reduces the position-dependent force for the sake of better transverse cooling. Another difference to the boson 2D-MOT is the sharp cut-off of the loading rate at a detuning of about -1.5Γ . This can be attributed to the $m_F = 3/2$ -state located at a detuning of $-72\text{ MHz} \approx 2.5\Gamma$. The behavior of the loading rate with the push beam power and the spectral broadening of the 3D-MOT laser is similar to the case of ^{174}Yb .

1.5 Comparison to Zeeman Slowers

Having presented our 2D-MOT setup for Yb and characterized its performance, I want to compare it to the common Zeeman slower-based setups and discuss its advantages and disadvantages.

In the previous section it has been shown that the performance of the 2D/3D-MOT system differs significantly between bosonic ^{174}Yb and fermionic ^{173}Yb . Therefore, these two cases must be discussed separately. Considering bosonic ^{174}Yb , the loading rate achieved in our setup can compete with existing Zeeman slower setups. It even significantly surpasses the loading rates published by the Tokyo and Seattle groups [37, 55]. Those experiments work, however, with significantly lower cooling laser powers. Zeeman slower-based Yb-setups built in Munich and Florence approximately at the same time as our project seem to surpass our numbers. The performance of our setup is, however, more than sufficient for a fast and reliable production of ^{174}Yb -Bose-Einstein condensates as will be shown in section 2.4.

It has been mentioned above that the production of ultracold mixtures of Yb and Rb atoms is one of the long-term perspectives for our setup. For this purpose, a 2D-MOT provides a significantly better optical access to the 3D-MOT chamber as can be seen by looking at the dual Zeeman slower setups of the Yb-Rb-experiment in Düsseldorf [56] or the Yb-Li-experiment in Seattle [57]. This limitation of the Zeeman slower setups can in principle be circumvented by transporting the atoms from the 3D-MOT chamber into a glass cell with good optical access. While it has been shown that this can work reliably [58], it is certainly an additional complication of the experiment, which one might want to avoid.

In section 1.4.2 it has been shown that for fermionic ^{173}Yb the performance of our 2D/3D-MOT system is a factor of five worse than for the boson ^{174}Yb . The two effects that lead to this degradation of the MOT-performance for ^{173}Yb are the hyperfine structure and the large differential Zeeman shift. There are strong arguments that the problems connected to these effects are intrinsically circumvented when a Zeeman slower of the increasing-field-type, also called σ^- -type, is used [59]. In this configuration, the atoms exit from the oven at zero magnetic field so that all m_F -states are initially resonant with the slowing laser. The first few scattering photons from the σ^- -polarized slowing laser then pump all atoms into the $m_F = -5/2$ -state. Once the atoms have reached the outermost m_F -level, the slowing laser only couples to the desired ($^1P_1, F = 7/2, m_F = -7/2$)-state. Consequently, the $F = 5/2$ and $F = 3/2$ states have no influence on the slowing process. Being slowed on the $|m_F = -5/2\rangle \rightarrow |m_F = -7/2\rangle$ cycling transition, they obviously exit the Zeeman slower in the $m_F = -5/2$ -state. If the orientation of the magnetic field gradient and the light polarization of the 3D-MOT are chosen such that the $m_F = -5/2$ -state is efficiently captured [46], all of the slowed atoms can be loaded into the MOT. Therefore, the performance of the Zeeman slower/3D-MOT combination should be independent of the isotope used and the loading rates are solely determined by the isotope abundances. This is confirmed by experiments in the Kyoto group [60].

In section 1.4.2 it has further been mentioned that the ^{173}Yb -2D-MOT requires a polarization and an alignment, which significantly differ from the optimum configuration for the bosons. This is problematic for the production of mixtures of ^{173}Yb and one of the other Yb-isotopes. The easiest way to load a double isotope 3D-MOT would be to simply change the 2D-MOT detuning from one isotope to the other within the experimental sequence and in this way load the two isotopes sequentially. For this to work, an alignment of the 2D-MOT beams needs to be found which results in reasonable loading rates for both isotopes. For ^{173}Yb and the bosonic Yb-isotopes, we have not been able to find such an alignment.

In summary, a 2D-MOT is a good alternative to a Zeeman slower for the bosonic Yb-isotopes, resulting in comparable 3D-MOT loading rates. It has the technical advantage that it can be used for multiple elements, providing better optical access to the 3D-MOT chamber in multi-element experiments than setups with multiple Zeeman slowers. In the case of ^{173}Yb , the 2D-MOT performance is however compromised due to fundamental problems related to the internal structure of ^{173}Yb , namely the narrow hyperfine structure of the 1P_1 -state and the large differential Zeeman shift of the cooling transitions. These lead to a significantly reduced 3D-MOT loading rate and pose substantial problems for the production of isotope mixtures comprising ^{173}Yb . Thus, for ^{173}Yb a Zeeman slower, which most probably avoids these problems, would be preferable.

2 Quantum Degenerate Yb

This chapter describes the preparation and manipulation of ultracold, quantum degenerate samples of bosonic ^{174}Yb and fermionic ^{173}Yb in our setup. It begins with a discussion of the collisional properties and AC-polarizability of Yb in sections 2.1 and 2.2, since these two properties are of crucial importance for the evaporative cooling and many-body physics of ultracold atomic gases. Following the description of our crossed dipole trap in section 2.3, the preparation and manipulation of the bosonic and fermionic isotopes is in detail presented in the final two sections 2.4 and 2.5, including details on our optical lattice and the preparation and detection of nuclear spin states.

2.1 Collisional Properties of Yb

Once an atomic gas has been laser cooled to μK temperatures and is loaded at high density into a conservative trap, its physics is solely determined by the elastic and inelastic collision properties, as well as the quantum statistics of the atoms. At ultracold temperatures only the lowest partial wave collisions are relevant. Below a few tens of μK even p-wave collisions are more and more suppressed. The only relevant collision parameter is then the s-wave scattering length a . The interaction potentials that determine a are the Born-Oppenheimer potentials of the various molecular orbitals that at large distance connect to the relevant two-atom scattering states. A detailed, comprehensive discussion of ultracold temperature scattering is hard to find. The basic theory of low energy scattering is reviewed e.g. in [61]. A more detailed overview, also covering the collisional coupling of the hyperfine states of alkali atoms, can be found in [62].

For atomic states with non-zero electronic, as well as nuclear angular momentum and hyperfine coupling, the total angular momenta F_1 and F_2 of the individual atoms are in general not conserved in an s-wave collision. This is because the spin-exchange coupling and the coupling between the electronic angular momentum to the internuclear axis dominates over the hyperfine interaction at short internuclear distances [62]. Consequently, different hyperfine states have different scattering lengths, depending on the combined two-atom spin $f = F_1 + F_2$, which must be conserved in an elastic s-wave collision. This is the case for alkali atoms and lies at the heart of spin-dynamics, which have been observed in many experiments [63].

For 1S_0 ground-state Yb- or alkaline-earth atoms the scattering is much simplified, because the electronic orbital angular momentum, as well as the electronic spin are zero. Consequently, there is no hyperfine interaction and the $|^1S_0, ^1S_0\rangle$ scattering state couples only to a single molecular orbital, the $^1\Sigma_g^+$ state, independent of the nuclear spin [62, 64]. Therefore, the nu-

s-wave scattering lengths of Yb in units of a_0							
Isotope:	^{168}Yb	^{170}Yb	^{171}Yb	^{172}Yb	^{173}Yb	^{174}Yb	^{176}Yb
^{168}Yb	252	117	89	65	38	2	-358
^{170}Yb		64	36	-2	-81	-517	209
^{171}Yb			-3	-8	-577	428	141
^{172}Yb				-598	417	200	106
^{173}Yb					199	138	80
^{174}Yb						105	54
^{176}Yb							-24

Table 2.1: Inter- and intra-species s-wave scattering lengths of all Yb isotopes, given in units of the Bohr radius a_0 . The data is taken from ref. [65] and has been obtained from two-color photoassociation spectra.

clear spins of two colliding 1S_0 atoms are individually conserved. On the one hand, this implies that ground-state Yb gases will not exhibit any spin dynamics. On the other hand, it gives rise to $SU(N)$ symmetry of the many-body Hamiltonians of N -component nuclear spin mixtures. This symmetry has been predicted to lead to exotic magnetic phases which have never been observed experimentally [24].

The ground-state s-wave scattering lengths have been measured for all combinations of Yb-isotopes via photo-association spectroscopy in the Kyoto group [65]. Their results are shown in table 2.1. The various scattering lengths cover a wide range from strongly attractive to strongly repulsive. This is especially interesting because the ground state of Yb does not exhibit magnetic Feshbach resonances that allow tuning of the interaction. By choosing suitable isotope mixtures, at least a limited range of different interactions can be realized. Stable quantum degenerate gases have been produced in the Kyoto group for all isotopes, except for the strongly attractive boson ^{172}Yb [37, 66–69].

As pointed out in the introduction, quantum many-body experiments with Yb are not a priori restricted to the electronic ground state. The spontaneous decay rates of the metastable $^3P_{0,2}$ -states on the order of 0.1 s^{-1} are small enough to be neglected on typical experimental timescales of $< 1\text{ s}$. Studying the many-body physics of 1S_0 - $^3P_{0,2}$ -mixtures depends, however, also on the collisional stability of these states. In contrast to ground-state collisions, scattering involving the metastable states is far more complicated.

In collisions between ground- and metastable-state atoms, the various $|^1S_0, ^3P_J\rangle$ scattering states connect to four different molecular orbitals, two of which are attractive ($^3\Sigma_u^+$ and $^3\Pi_g$), and two repulsive ($^3\Sigma_g^+$ and $^3\Pi_u$) [64, 70]. Coupling between these orbitals can lead to fine structure changing collisions, as well as principle quantum number changing collisions. Fine structure changing collisions are energetically impossible for the 3P_0 -state at ultralow temperatures, because it is the energetically lowest in the 3P_J fine-structure triplet. Principle quantum number changing collisions are however possible. In such a collision, the 3P_0 -state decays to the 1S_0 ground state, releasing the excitation-energy as kinetic energy, which causes the colliding atoms to escape from the trap. Collisions between two 3P_0 atoms are even more complicated.

Since both atoms can change their electronic configurations, the number of inelastic collision channels is much larger than for 1S_0 - 3P_0 -collisions.

Elastic collisions between 1S_0 and 3P_0 atoms are again simplified due to the zero net electronic angular momentum in both states. As a consequence of the absence of hyperfine coupling the molecular orbitals maintain their *geradelungerade* symmetry also at large internuclear distance in the separated atom limit [71, 72]. The two orbitals connecting to the $|^1S_0, ^3P_0\rangle$ limit are the Hund's case (c) orbitals 0_u^- and 0_g^- [70]. They connect to the separated atom states:

$$0_g^- \longrightarrow |^1S_0\rangle |^3P_0\rangle + |^3P_0\rangle |^1S_0\rangle = |eg\rangle^+ \quad (2.1)$$

$$0_u^- \longrightarrow |^1S_0\rangle |^3P_0\rangle - |^3P_0\rangle |^1S_0\rangle = |eg\rangle^- \quad (2.2)$$

The difference of the 0_u^- and 0_g^- molecular potentials leads to different scattering lengths a_{eg+} and a_{eg-} for the $|eg\rangle^-$ and $|eg\rangle^+$ states, which are thus the eigenstates of the s-wave interaction between 1S_0 and 3P_0 atoms.

For atoms in the lowest band of an optical lattice s-wave collisions shift the energy of two atoms occupying the same site by the energy [73]

$$U = \frac{2\pi\hbar^2 a}{M} \int d^3r |w(\mathbf{r})|^4, \quad (2.3)$$

where $w(\mathbf{r})$ is the lowest band Wannier function and M is the mass of the atom. Thus, the on-site (elastic) interaction Hamiltonian for two atoms with two possible electronic states $|^1S_0\rangle = |g\rangle$ and $|^3P_0\rangle = |e\rangle$ reads:

$$\begin{aligned} \hat{\mathcal{H}}_{\text{int}} = & (U_{ee} |ee\rangle \langle ee| + U_{eg}^+ |eg\rangle^+ \langle eg|^+ + U_{eg}^- |eg\rangle^- \langle eg|^- + U_{gg} |gg\rangle \langle gg|) \\ & \otimes \mathbb{1}_{\uparrow\downarrow}^{(1)} \otimes \mathbb{1}_{\uparrow\downarrow}^{(2)}. \end{aligned} \quad (2.4)$$

For the sake of clarity, also the nuclear-spin part of the Hamiltonian is explicitly written here. It is simply given by the identity operators in the spin subspaces of the two atoms $\mathbb{1}_{\uparrow\downarrow}^{(1,2)}$, because the interaction is spin-independent owing to the lack of hyperfine coupling. Resolving the differences between the four interaction energies U_{gg} , U_{eg+} , U_{eg-} , and U_{ee} with a stable laser on the $^1S_0 \rightarrow ^3P_0$ transition will be a valuable tool allowing occupation number dependent probing and manipulation of ultracold mixtures of these states as will be detailed in chapter 3.

Until very recently, the only available data on the 1S_0 - 3P_0 scattering lengths were those obtained from precision spectroscopy in optical lattice clock setups, probing density shifts of the $^1S_0 \rightarrow ^3P_0$ transition in low-density thermal atomic samples [74–78]. However, when finishing this manuscript, the Munich group published the first direct spectroscopic measurements of the 1S_0 - 3P_0 interaction shifts of a quantum degenerate gas of ^{173}Yb in a three-dimensional optical lattice [79]. We have performed similar measurements also showing a signature of 1S_0 - 3P_0 interaction, which are presented in section 3.3.2 of this thesis. Table 2.2 summarizes the currently most accurate values of the scattering lengths for the fermionic Sr and Yb isotopes taken from the above mentioned publications. For the bosonic Yb isotopes there is no available data.

1S_0 - 3P_0 s-wave scattering lengths and inelastic loss coefficients			
Isotope:	^{173}Yb	^{171}Yb	^{87}Sr
a_{gg}	199 ± 2 [65]	-3 [65]	96.2 ± 0.1 [80]
a_{eg+}	219.5 ± 2 [79]	~ 25 [76]	169 ± 8 [75]
a_{eg-}	2170 ± 190 [79]	-	68 ± 22 [75]
a_{ee}	306.2 ± 10.4 [79]	-	176 ± 11 [75]
β_{eg}	6 ± 1.4 [79]	-	-
β_{ee}	220 ± 50 [79]	-	140 ± 80 [77]

Table 2.2: S-wave scattering lengths and inelastic loss coefficients for 1S_0 - 3P_0 -mixtures of the fermionic Sr and Yb isotopes. Scattering lengths are given in units of the Bohr radius a_0 . Inelastic loss coefficients for 1S_0 - 3P_0 -collisions (β_{eg}) and 3P_0 - 3P_0 -collisions (β_{ee}) are given in $10^{-13} \text{ cm}^3/\text{s}$. The values for ^{173}Yb have been obtained via clock spectroscopy on a quantum degenerate two-component mixture in a three-dimensional optical lattice [79]. For ^{87}Sr ([75] and references therein) as well as ^{171}Yb [76] the scattering lengths are deduced from density shifts in an optical lattice clock. The ground state scattering lengths measured via photo-association spectroscopy are given for reference [65, 80].

The fact that fermionic 1S_0 - 3P_0 -mixtures are characterized by two scattering lengths a_{ge+} and a_{ge-} makes them especially interesting candidates for quantum-many-body experiments. For example, it has been shown that the difference of the singlet and triplet scattering lengths $\Delta a_{eg} = (a_{ge+} - a_{ge-})$ gives rise to a Kondo-exchange coupling, allowing to realize the Kondo lattice Hamiltonian with ultracold fermionic Yb [25, 81]. The extremely large Δa_{eg} of ^{173}Yb as well as the moderate inelastic loss rate of 1S_0 - 3P_0 collision (β_{eg}) deduced from the Munich experiments make this isotope a very promising candidate for experiments along these lines. While so far little is known about the collisional properties of ^{171}Yb , it may also be of special interest. Its extremely small ground-state interaction could result in an even larger ratio between ground-state and exchange interaction leading to a purely exchange-dominated system.

2.2 Polarizability of the 1S_0 and 3P_0 states

The way in which atoms can be manipulated with off-resonant light is determined by their polarizability $\alpha(\lambda)$, its real part $\text{Re}(\alpha)$ being the proportionality constant between the dipole potential U_{dip} generated by a light-field at wavelength λ and the intensity I of that field [84]:

$$U_{\text{dip}} = -\text{Re}(\alpha) \cdot I \quad (2.5)$$

Figure 2.1 depicts $\text{Re}(\alpha)$ for the 1S_0 ground state and the 3P_0 metastable state of Yb, calculated by summing up the two-level-contributions of all known transitions involving these states. The polarizability of the ground state is dominated by the strong $^1S_0 \rightarrow ^1P_1$ transition at 399 nm. The only lower lying transition of significant strength is the $^1S_0 \rightarrow ^3P_1$ at 556 nm. Thus, for wavelengths above 556 nm the dipole potential is always attractive and varies only weakly,

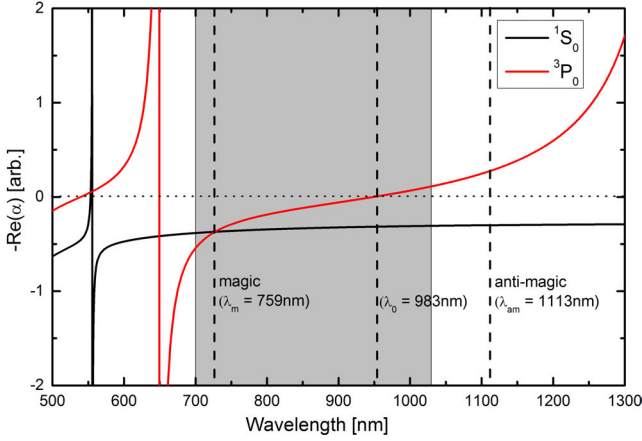


Figure 2.1: Real part of the AC-polarizabilities of the 1S_0 (black) and 3P_0 (red) states of Yb. The polarizabilities are calculated by summing over the two-level-contributions of all known transitions. Characteristic frequencies, such as the magic and anti-magic wavelengths, as well as the zero crossing of the 3P_0 polarizability are reproduced by this calculation only with $\sim 10\%$ inaccuracy. More accurate values for these frequencies based on a measurement of the magic wavelength [82] and a relativistic many-body calculation of α [83] are written next to the dashed lines in the figure. The gray-shaded region indicates the wavelength tuning range of a Ti:Sapph laser. Tuning its wavelength allows the realization of different state dependent lattices.

decreasing for larger wavelengths. For the metastable 3P_0 state, $\text{Re}(\alpha)$ exhibits a qualitatively different shape: The dominant resonances are the $^3P_0 \rightarrow ^3S_1$ transition at 649 nm and the $^3P_0 \rightarrow ^3D_1$ transition¹ at 1388 nm, leading to an almost linearly shaped polarizability between 800 nm and 1100 nm, changing its sign near ~ 950 nm. When working with mixtures of 1S_0 and 3P_0 atoms, this qualitative difference between the polarizabilities makes the wavelength of a far off-resonant dipole potential a new tunable parameter. Mixtures of ground-state alkali atoms exhibit such a state dependent polarizability only very close to the D1- and D2-lines. It is thus accompanied by a significant inelastic photon-scattering rate, causing appreciable heating of the ultracold sample. Tuning of the differential polarizability is especially interesting, when working with optical lattices. By tuning the wavelength of the lattice laser, qualitatively different state dependent lattices can be generated: For lattice wavelengths between ~ 700 nm and ~ 900 nm, the 1S_0 and 3P_0 polarizabilities are both attractive. Therefore, a lattice potential at these wavelengths has the same geometry for both states. However, the lattice depths are generally different. Only at a single, so-called *magic* wavelength the polarizabilities are exactly equal and the two states experience the exact same lattice potential. For wavelengths above ~ 950 nm the polarizabilities have opposite sign, attractive for the ground state and repulsive for the metastable state. Thus, the lattice potentials for the two states are displaced by half a lattice spacing, creating an overall checkerboard lattice, with each state living on its individual sub-lattice. The relative depth of the two sub-lattices varies with wavelength, being exactly equal at the so-called *anti-magic* wavelength slightly above 1100 nm. Due to the shallow slope of the polarizabilities, the simple calculation shown in fig. 2.1 does not accurately reproduce the exact values for the magic and anti-magic wavelengths, as well as the zero crossing of the 3P_0 polarizability. The magic wavelength has however been determined experimentally to be located at $\lambda_{\text{magic}} = 759$ nm [82]. Moreover, a relativistic many-body calculation of the polarizabilities of the 1S_0 and 3P_0 states has been carried out in ref. [83], which reproduces

¹For an extended level scheme of Yb including these transitions see appendix C.

the measured magic wavelength up to an inaccuracy of 1.3%. From the plot presented therein, values for the anti-magic wavelength (1113 nm), as well as the zero-crossing (983 nm) can be extracted. These values are also given in fig. 2.1.

In order to exploit the differential polarizability between the 1S_0 and 3P_0 states as a tuning parameter in our experiments, we have chosen to use a titanium-sapphire (Ti:Sapph) laser for our optical lattice, as described in section 2.4.2. It would be ideal, to also use a Ti:Sapph for the dipole trap. However, in contrast to optical lattices, a dipole trap for all optical evaporation requires rather high powers of > 10 W, which are not regularly available from a Ti:Sapph laser. Therefore, we decided to use a dipole trap laser at 532 nm, strongly attractive for the 1S_0 and weakly attractive for the 3P_0 state. When working with Yb only, 1064 nm would be the better choice. The higher available power at that wavelength roughly compensates the lower polarizability of the ground state, but the photon scattering rate would be significantly lower. However, our machine is supposed to also produce ultracold mixtures of Yb and Rb at a later stage. The large differential polarizability of these two elements might necessitate the use of a bichromatic dipole trap using both 532 nm and 1064 nm light in order to equalize the dipole potential for both species [85]. Therefore, we decided to start with a 532 nm trap for Yb.

2.3 The Crossed Dipole Trap Setup

Three different criteria are important for an optical dipole trap that is used both for evaporation as well as confining the atoms during the actual experiment: First, the trap should have a large effective trap volume in order to maximize the transfer efficiency from the MOT into the dipole trap. Second, it should have large trap frequencies during evaporation, in order to speed up the evaporation. Third, it should have low trap frequencies after evaporation has been completed, which are ideally the same in all three directions, such that an isotropic and homogeneous sample is obtained. Meeting all of these criteria at the same time is generally difficult. We decided to plan our trap similar to the dipole traps used successfully in the Kyoto group, with a tightly focused strong horizontal beam (from here on called DT1) and a larger and weaker beam (from here on called DT2) for confinement along the propagation axis of the horizontal beam. In order to achieve lower trapping frequencies in the final trap, we left the option to implement an additional horizontal beam with a larger beam diameter the atoms could be transferred to, if desired.

The geometric configuration of the trap is shown in fig. 2.2 a). The horizontal beam DT1 is oriented along y , while the weak beam DT2 propagates in the x - z -plane, tilted by 19° with respect to the horizontal in order to leave room for the imaging setup along x . DT1 has a maximum power of about 9 W at the location of the atoms and an elliptical beam profile with $1/e^2$ -radii of $w_{0x} = 29 \mu\text{m}$ and $w_{0z} = 18 \mu\text{m}$. At full power, this results in a trap depth of $623 \mu\text{K}$. For DT2 a round beam with a $1/e^2$ -radius of $w_0 = 79 \mu\text{m}$ and a maximum power of 3.2 W at the location of the atoms is used. This results in a maximum potential depth of $18.5 \mu\text{K}$.

Initially, we used a vertical beam for DT2 with an elliptical cross-section of $w_{0x} = 85 \mu\text{m}$ and

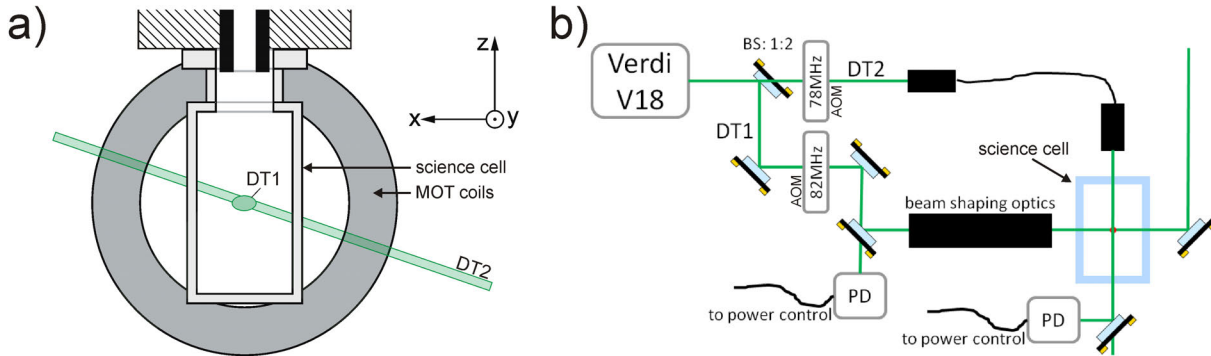


Figure 2.2: a): Geometry of the dipole trap. The strong beam (DT1) propagates horizontally along the y -direction. The weak beam (DT2) is running in the x - z -plane, tilted by 19° with respect to the horizontal. b): Simplified schematic of the laser system used for the crossed optical dipole trap. 18 W of 532 nm-light generated by a frequency-doubled solid state laser (Coherent Verdi V18) is split into two beams with a splitting ratio of 1:2. Their power is controlled with two acousto optic modulators. The stronger beam (DT1) is guided to the vacuum chamber via free space. Rigidly mounted beam-shaping optics focus the beam to the position of the MOT. The weaker beam (DT2) is brought to the vacuum chamber via a single mode fiber. A small portion of each beam is detected on a photodiode for active power stabilization.

$w_{0y} = 28 \mu\text{m}$, the short axis oriented along y , i.e. the direction of DT1. The advantage of this configuration is that the trapping frequency along the z -direction can be adjusted independent of the other two trapping frequencies [1, 52]. When realizing that the size of our ultracold gases was limited by the effective volume of the crossed trap, we changed DT2 to the tilted configuration described above. All data presented in this thesis has been obtained using this configuration.

The beam-shaping optics for the horizontal and the initial vertical beam have been designed and built by my colleague Sören Dörscher and are described in detail in his PhD thesis [52]. The modified, round DT2 beam is produced simply by a standard commercial $f = 12 \text{ mm}$ fiber collimator² and a $f = 500 \text{ mm}$ achromatic doublet lens. The weak beam with a maximum power of 3.2 W can still be conveniently fiber coupled. For the strong beam with 9 W the fiber is easily damaged when the beam is not well coupled into the fiber. Therefore, DT1 is guided to the experiment via free space. The power of the two beams is adjusted via two AOMs³, which are made of quartz to avoid thermal lensing. The voltage controlled oscillators driving the AOMs are detuned by a few MHz in order to avoid interference of the two dipole trap beams. For active power control, a portion of the light is split off and detected on a photodiode. The photodiode signal is fed to a home-built proportional-integral-controller that regulates the power via the AOMs with a servo-bandwidth of a few tens of kHz. In order to measure the power of the horizontal beam over a range of three orders of magnitude, we use a home-built logarithmically amplified photodiode. The whole laser setup of the crossed optical dipole trap is shown in fig. 2.2 a).

²Schäfter und Kirchhoff

³Crystal Technologies MODEL 3080-292

Loading of the dipole trap is achieved by simply overlapping it with the MOT. Atoms whose energy is reduced below the trap depth after entering the trapping volume get caught in the dipole trap. In order to optimize the loading, the MOT has to be compressed and cooled as much as possible. We do so in a MOT cooling and compression stage directly after loading the MOT. During this stage, all three MOT parameters are changed over a period of 400 ms: The frequency broadening of the cooling light, needed to maximize the capture velocity, is no longer necessary after the MOT loading phase and is therefore reduced to zero. At the same time the power of the cooling light is lowered to only a few % of the loading power, significantly reducing the Doppler-limited temperature. Moreover, the detuning is reduced to $\sim \Gamma$ helping both to further cool and to compress the MOT. The magnetic field gradient is increased from 2 G/cm to 7 G/cm enhancing the MOT compression. In order to precisely overlap the compressed MOT with the dipole trap, we finely adjust the MOT position by applying a small homogeneous magnetic field offset, which is slowly ramped up during the cooling and compression stage.

2.4 Bose Einstein Condensates of ^{174}Yb

Due to its high natural abundance of 32% and its moderately repulsive scattering length of $105a_0$, the bosonic isotope ^{174}Yb is the easiest to cool to ultralow temperatures. Thus, we used this isotope to optimize and characterize our setup. In section 2.4.1 the evaporative cooling to Bose-Einstein-condensation is characterized. Section 2.4.2 describes our three-beam optical lattice and presents a measurement of the bosonic Mott-insulator transition of ^{174}Yb in a triangular lattice geometry.

2.4.1 Evaporative Cooling

Once the atoms have been loaded into the dipole trap as described in the previous section, evaporation is forced by continuously ramping down the dipole trap power. Our evaporation ramp consists of two steps. In the first step the power of DT1 is exponentially ramped down from its maximum power of 9 W to a power of about 300 mW within 5 s, while the power of DT2 is kept constant. During this first step the atoms concentrate in the crossed dipole trap region, as the temperature drops below the potential depth of DT2. At the end of the first evaporation step, the potential depths of the two trapping beams are almost equal, and most of the atoms are trapped in the crossed region. In the second evaporation step the powers of both beams are simultaneously decreased over 1.5 s until they reach their final values of 25 mW and 1.9 W and an almost pure Bose-Einstein condensate (BEC) has formed. As for the first step, we use exponential ramps. The evaporation procedure has been optimized by varying the duration as well as the final trap powers for each of the two evaporation steps. Dividing the second evaporation step into two with different ramp speeds did not further improve the cooling efficiency.

The evolution of the temperature and the number of trapped atoms during evaporative cooling is shown in fig. 2.3. The temperature has been determined from the expansion of the thermal fraction of the gas, fitted with a Gaussian. Note the different time-scales used for the two evapo-

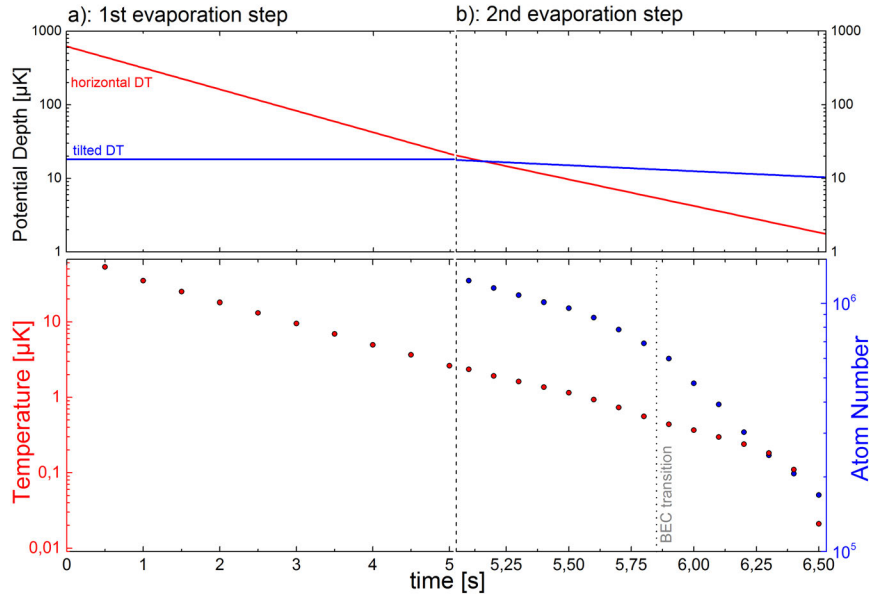


Figure 2.3: Evolution of potential depth, particle number and temperature during the evaporative cooling procedure. During the first step (a) only the power of DT1 is decreased until its potential depth roughly equals that of DT2 and nearly all atoms are concentrated in the crossed trapping region. During the first step the extension of the gas is still too large to determine the total atom number. In the second step (b) both dipole trap beams, DT1 and DT2, are simultaneously decreased until an almost pure BEC has formed in the trap. Temperatures are extracted from the expansion of the thermal fraction of the gas. The potential depths given correspond to the AC-Stark shift at the peak of the Gaussian beam profiles and are not to be confused with the actual depth of the overall trap.

ration steps a) and b). The evaporation speed is significantly higher in the second step. This can be explained by the higher density in the crossed region compared to the extremely elongated horizontal trap. Due to the correspondingly higher elastic scattering rate, the atoms thermalize faster, allowing a faster power rampdown. The sharp drop in temperature at the end of the evaporation must be attributed to problems with the temperature determination, when the thermal fraction of the atoms becomes too small for the Gaussian fit to work reliably.

During evaporative cooling, the atom number decreases exponentially together with temperature. Interestingly, the loss rate increases in the final stage of evaporation near the BEC phase transition. This might be explained by the potential tilt due to gravity becoming important at very low trap depths. This tilt makes the trapping barrier increasingly asymmetric with its lowest region at the bottom of the trap. Thus, not the total kinetic energy of the atoms is decisive for evaporation, but the kinetic energy along the vertical direction. This reduced dimensionality of evaporation makes the cooling significantly less efficient [86, 87].

The phase transition from a thermal gas to a BEC is shown in fig. 2.4 a). We cross the phase transition at a critical temperature of ~ 500 nK with about $6 \cdot 10^5$ atoms in the trap. At the end of the evaporation stage we end up with a little below $2 \cdot 10^5$ atoms in an almost pure condensate. We measure the trapping frequencies of the final trap configuration by observing center of mass oscillation of the BEC, which are induced by pulsing on one of the optical lattice beams (see

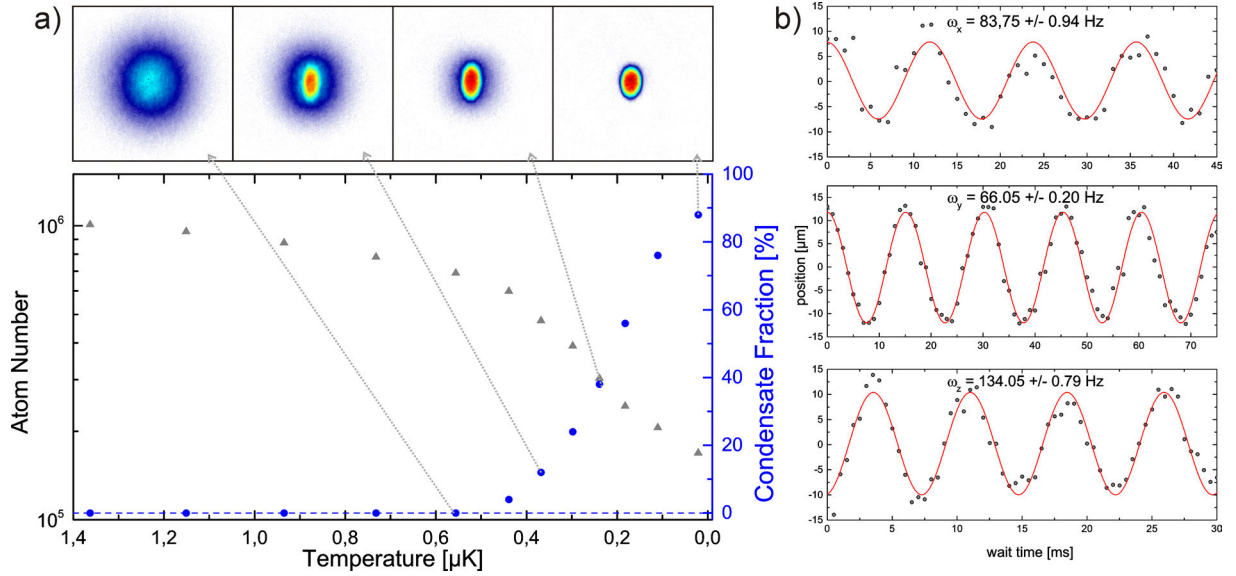


Figure 2.4: a): Particle number and condensate fraction as a function of temperature, as the gas is evaporatively cooled across the BEC phase transition. The absorption images, taken 17.5 ms after release from the trap, exhibit the characteristic transition from a Gaussian- to a Thomas-Fermi profile. The condensate fraction is determined from a two-dimensional bimodal fit to the image data. For large condensate fractions small variations of the image background disturb the fit, resulting in an underestimation of the condensate fraction. b) Center of mass oscillations of the BEC along the principal axes of the dipole trap at the end of evaporation, revealing trapping frequencies of $(\omega_x, \omega_y, \omega_z) \approx (84, 66, 134)$ Hz.

section 2.4.2) that has been intentionally misaligned from the center of the trap. From these oscillations shown in fig. 2.4 b) we deduce trapping frequencies along the principal axes of the trap of $(\omega_x, \omega_y, \omega_z) \approx (84, 66, 134)$ Hz.

Our dipole trap configuration with the tightly focused DT1 beam and the rather large, nearly horizontal beam DT2, allows to partially compensate gravity by adjusting the transverse displacement d between the two beams (see fig. 2.5 b)): Figure 2.5 a) demonstrates the effect of the transverse displacement d on the final atom number in the BEC for different final potential depths of DT2. For a shallow DT2 potential, the atom number exhibits a maximum as the beam position is moved across the horizontal beam axis, whereas for a deep DT2 potential the situation is inverted and the maximum is turned into a minimum. This can qualitatively be explained by looking at the effective trap depth and volume. In fig. 2.6 the equipotential contours of the total trapping potential in the x - z -plane including gravity are plotted for different beam displacements for a shallow and a deep DT2 potential. Clearly, for the shallow DT2 (fig. 2.6 a)) trap depth and volume are maximized at intermediate displacements d , where gravity is best canceled, maximizing the size of the BEC. If the displacement is too large or too small, the slope of the tilted beam potential is too small to compensate gravity and the trap opens at the bottom. For a strong DT2 (fig. 2.6 b)), the maximum slope of the DT2 potential is so strong, that it pulls the atoms out of the trap, causing the BEC size to be decreased compared to the low power case. Since the beam is tilted this happens to one side of the trap. For larger or smaller

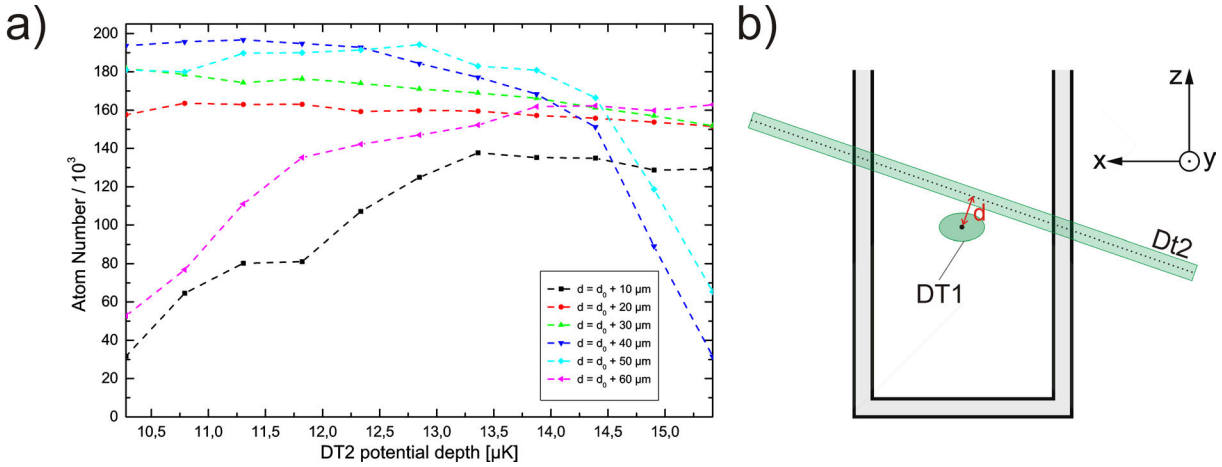


Figure 2.5: a): Atom number in the BEC at the end of evaporation as a function of the final potential depth of DT2. The different curves correspond to different transverse displacements d of DT2 with respect to the center of DT1 as indicated in panel b). The absolute value of d could not be determined. Consequently, the values for d given in panel a) are written with an unknown offset d_0 . For a discussion of this measurement see the main text.

displacements, the slope is weakened and effectively cancels gravity. To understand quantitatively, why the configuration of low DT2 potential and intermediate displacement results in the largest BEC sizes, one would have to calculate the total trapping volume for the different configurations. However, not only the volume of the trap is important for the final BEC size, but also the shape of the trap barrier, which influences the evaporation process. As mentioned above, a strongly asymmetric barrier which is significantly lower in one direction than in the other two, reduces the dimensionality of evaporation and decreases the cooling efficiency. For our final trap configuration, the potential depth produced by DT2 is much larger than that of DT1. Therefore, the most symmetric barrier is achieved by reducing the power of DT2 as far as possible and placing the steepest slope of the beam at the trap center to still cancel gravity. Indeed this results in the largest BECs as can be seen from fig. 2.5 a).

The decay of the atom number after the BEC has been prepared is shown in fig. 2.7. For times above 4 s it is exponential with a decay time constant of 5.7 s, equivalent to a decay rate of $\Gamma_{\text{dec}} = 0.174 \text{ s}^{-1}$. The scattering rate of dipole trap photons in the final trap configuration including the displacement of the tilted beam amounts to $\Gamma_{\text{scat,DT}} = 0.137 \text{ s}^{-1}$. The remaining loss rate of 0.037 s^{-1} or $(27 \text{ s})^{-1}$ could either be due to background gas collisions or photon scattering of residual light from the 2D-MOT laser located near the vacuum chamber. Although we have shielded and shuttered the 2D-MOT laser with great care, leaking of photons at this low rate cannot be excluded.

During the first seconds after the end of evaporation, the atoms decay non-exponentially. In order to check, whether three-body loss is responsible for this decay, a model containing three-body and one-body loss taken from ref. [88] has been fitted to the data. For this fit the single particle loss rate Γ_1 , as well as an offset in the detected atom number have been fixed to the values obtained from the exponential decay at large times. The best fit is shown as solid blue

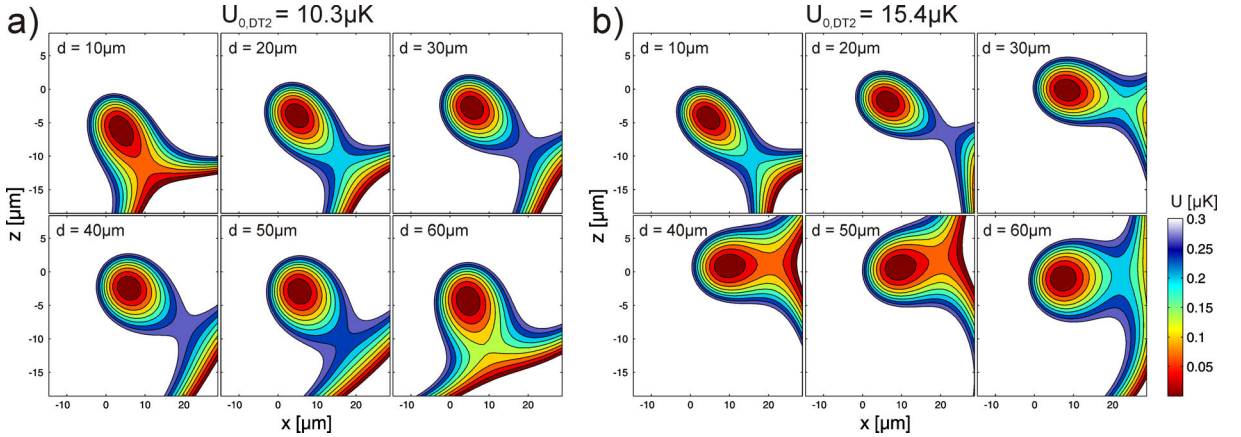


Figure 2.6: Equipotential contours of the total trapping potential of the crossed dipole trap in the x - z -plane at the end of the evaporation ramp for different transverse displacements d of DT2 with respect to the center of DT1 (cf. fig. 2.5 b)). The peak potential depth of DT2 is $10.3 \mu\text{K}$ in panel a) and $15.4 \mu\text{K}$ in panel b), corresponding to the minimum and maximum potential depths in fig. 2.5 a). The variation of the trap volume for the different configurations qualitatively explains the behavior of the BEC size in fig. 2.5 a)

line in fig. 2.7. It clearly does not agree with the data. When the single particle decay rate and atom number offset are left as a free parameters, the fit results in $\Gamma_1 \sim 10^{-10} \text{ s}^{-1}$, which is clearly not reasonable. Therefore, we conclude that three-body loss is not responsible for the non-exponential decay of the condensate.

Most likely this decay is caused by further lowering of the trap depth during the first seconds after the end of evaporation, occurring due to a focus shift of the horizontal beam. Such a focus shift can be caused by the modulator crystal of the dipole trap AOM cooling down: The RF-power driving the AOM heats the modulator crystal causing a slight change in the diffraction angle. Due to the imaging properties of our beam shaping optics, this temperature-induced tilt is translated into a focus shift. The shift changes whenever the RF-power is significantly increased or lowered as is the case during the evaporation ramp. If the lowering of the power during the evaporation happens too fast for the modulator to thermalize, the focus will shift further even after the final power has been reached. Such a residual focus shift away from the trap center would cause further unwanted lowering of the potential, forcing further evaporation. Since this has not bothered us so far, we have not investigated the decay further. Such problems will be eliminated once we set up a third dipole trap beam, the atoms are transferred to, after evaporative cooling has been stopped. Such a third beam would be fiber coupled, which would eliminate any focus drifts.

In terms of stability, the dependence of the BEC size on the MOT atom number is of interest. Figure 2.8 depicts BEC atom number and condensate fraction as a function of the MOT loading time. For the short loading times used here, the MOT atom number depends almost linearly on the loading time (cf. fig. 1.7). Condensate fraction and atom number increase nearly exponentially, but with different time constants. The condensate fraction already saturates for loading times above 3 s. The atom number increases more slowly, with a $1/e$ -time of 1.9 s. At

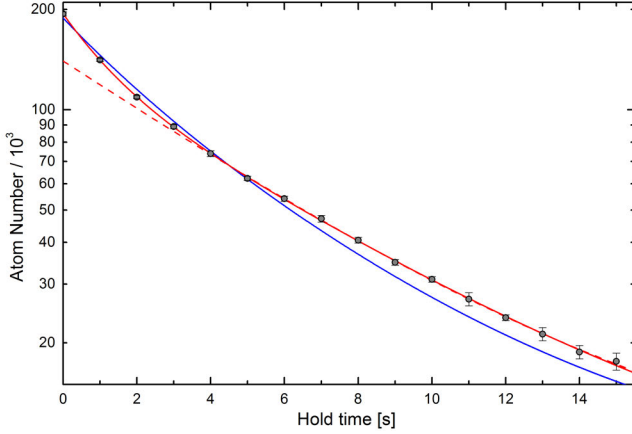


Figure 2.7: Atom number decay of the BEC in the crossed dipole trap directly following the evaporative cooling. The decay is clearly non-exponential. The solid red line is a double exponential fit to the data, while the dashed red line has been obtained with an exponential fit to the data starting from $t = 4$ s. The solid blue line corresponds to the best fit of inelastic three-body losses according to the model from [88], with the single particle lifetime and atom number offset fixed to the values obtained from the exponential fit at large times. It clearly does not fit the data. A detailed discussion is given in the main text.

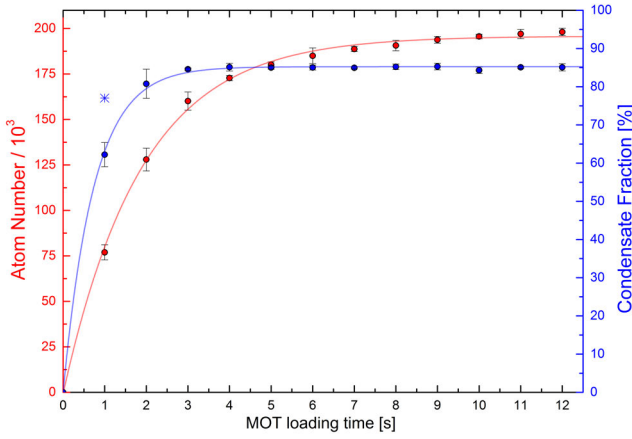


Figure 2.8: Atom number and condensate fraction at the end of evaporation as a function of the MOT loading time. The condensate fraction already saturates for MOT loading times above 3 s. The atom number grows more slowly. Imperfections of the image background disturb the bimodal fit and limit the *detectable* condensate fraction to $\sim 85\%$. For long MOT loading times of 10 s, $\pm 10\%$ fluctuation of the MOT atom number only results in $\pm 1\%$ fluctuation in the BEC atom number. For short MOT loading times the condensate fraction can be significantly increased by adapting the evaporative cooling ramp (blue star).

a MOT loading time of 10 s, $\pm 10\%$ fluctuation of the MOT atom number only results in $\pm 1\%$ fluctuation in the BEC atom number.

2.4.2 ^{174}Yb in a Triangular Optical Lattice

As discussed in the introduction, the most interesting regime of quantum-many-body physics is the regime, where the interactions between the particles dominate over all other energy scales. The extremely weak interactions between neutral atoms therefore require cooling to ultralow temperatures in order to reduce the kinetic energy until it is comparable to the interaction energy. However, even at temperatures of 100 nK and densities of 10^{14} cm^{-3} , the interactions are still so weak that they can be described by a mean-field potential completely neglecting quantum correlations between the particles. In order to reach the strongly-correlated, interaction-dominated regime, either the interaction has to be significantly increased by the use of Feshbach resonances. Alternatively, if no Feshbach resonances exist as for Yb, the atoms can be placed into an optical lattice potential. Instead of increasing the interaction, an optical lattice reduces the kinetic energy of the atoms, which can move in the lattice only by tunneling between adjacent

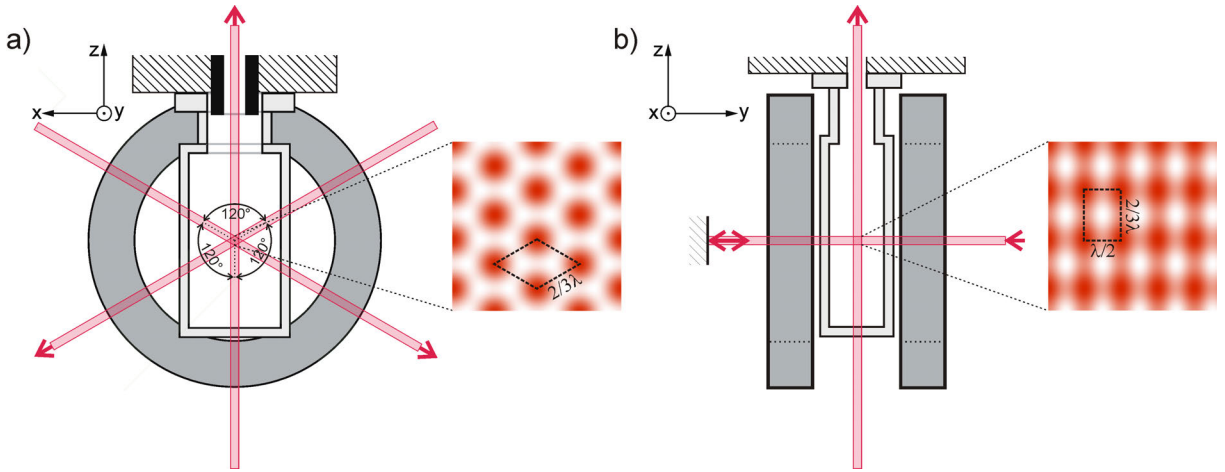


Figure 2.9: Schematic view of the geometry of the optical lattice. a): Three beams of equal frequencies propagating in the x - z -plane and intersecting under angles of 120° generate a 2D optical lattice. If the beams are polarized along y , perpendicular to their plane of propagation, they produce a triangular lattice with a lattice spacing of $2/3\lambda$, as indicated in the figure. Rotating the polarization into the plane of propagation changes the lattice geometry to a honeycomb lattice. b): An additional retro-reflected beam along y is detuned from the 2D-lattice by 160 MHz, adding a sinusoidal 1D-lattice with a lattice spacing of $\lambda/2$ perpendicular to the 2D-lattice resulting in an overall 3D lattice.

sites. In deep lattices, the kinetic energy can easily be reduced below 1% of the onsite interaction, taking the atomic ensemble into the strongly correlated regime.

The configuration of our optical lattice is shown in fig. 2.9. It consists of three beams propagating in the vertical x - z -plane intersecting at an angle of 120° , as well as one retro-reflected horizontal beam along y . The three beams in the x - z -plane all have the same frequency so that they all interfere and generate a two-dimensional (2D) optical lattice potential. The horizontal beam along y is 160 MHz detuned from the 2D-lattice and its intensity incoherently adds to that of the other beams. Thus, it generates a regular sinusoidal one-dimensional (1D) lattice along y , whose only tunable parameter is the lattice depth. The three-beam lattice in the x - z -plane offers significantly more flexibility: Depending on the polarization of the beams the lattice geometry can be changed from triangular (also called hexagonal) for y -polarization to a honeycomb geometry for the beams polarized in the lattice plane. Moreover, by modulating the phase difference between the three beams, the whole lattice can be shaken. This technique allows to imprint arbitrary phases on the tunneling matrix elements, and thereby realize artificial vector potentials for the atoms. The Rb experiment in our group was the first to use such a three-beam lattice and successfully realize artificial vector potentials by lattice shaking. Their success inspired us to also implement this kind of optical lattice in our setup. More details about the three beam lattice and the generation of artificial vector potentials by phase modulation can be found in references [89–92].

The laser system for our optical lattice is schematically depicted in fig. 2.10. The most important aspect to notice is the use of fiber noise cancellation for the three-beam lattice. While for retro-reflected optical lattices the phase of the lattice potential is solely determined by the

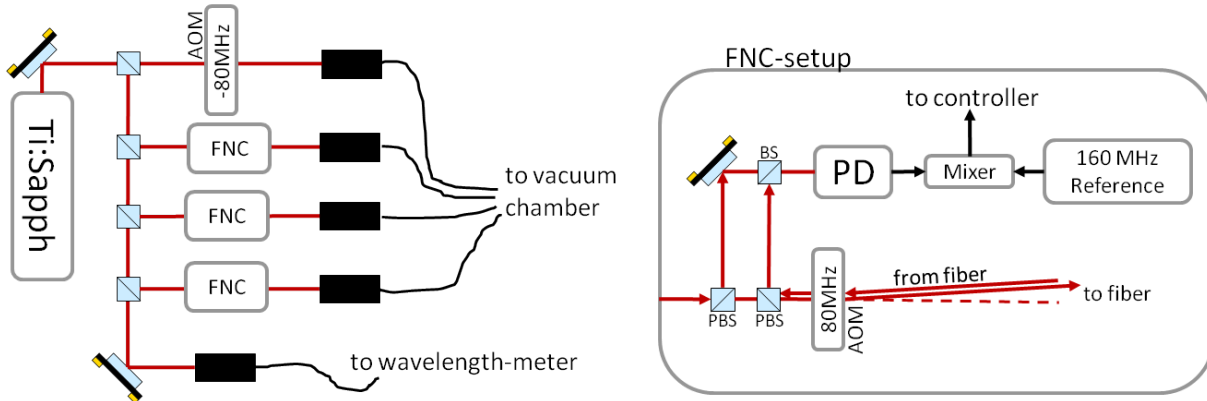


Figure 2.10: Schematic view of the laser system used for the optical lattice. The output of a Ti:Sapph laser (Coherent MBR) is split into four beams, one for the 1D-lattice along y and three for the 2D-lattice. In order to achieve a stable interference pattern of the three 2D-lattice beams, we use a fiber-noise-cancellation (FNC) setup, that stabilizes the phase of the fiber output relative to a laser beam picked off in front of the fiber. Details on the FNC setup can be found in ref. [89].

position of the retro-reflecting mirror, the phase of the three-beam lattice is given by the total path-length difference between the individual beams, which can fluctuate due to vibrations, thermal drifts and air currents. The most important source of phase noise are vibration-induced changes of the optical path length in the 5 m-long fibers. Therefore, the phases of the 2D-lattice beams at the fiber outputs are stabilized relative to the phase of local oscillator beams picked-off somewhere in front of the fibers. This is done by detecting the beat note between the light retro-reflected from the plane-cut output facet of the fiber and the local oscillator and locking it to a stable RF source as shown in fig. 2.10. As laser source for the lattice we use a Ti:Sapph laser because of its wide wavelength tuning range, allowing significant tuning of the differential polarizability between the 1S_0 and 3P_0 states (cf. section 2.2). For experiments where this differential polarizability has to be controlled with high precision, the frequency of the Ti:Sapph can be stabilized to a precision wavelength meter⁴ with a longterm stability of ~ 10 MHz. The laser system has been setup by my colleague Bastian Hundt and it will be presented in more detail in his PhD thesis.

Pumped with 18.5 W at 532 nm the Ti:Sapph delivers a maximum output power of 5 W at the magic wavelength 759 nm. Considering this maximum output power, the sizes of the lattice beams are chosen such that we can reach the Mott-insulator regime in the triangular as well as the honeycomb geometry. The measured $1/e^2$ -diameters at the waists of our lattice beams are $((92.1, 92.2, 92.1) \pm 0.2) \mu\text{m}$ for the three-beam lattice and $(83 \pm 0.2) \mu\text{m}$ for the 1D-lattice. The beam-shaping optics for the lattice beams have been built by Niels Petersen and will be described in his Master thesis.

The alignment of the lattice beams is done in the same way as in ref. [89]: After careful geometrical pre-alignment, the final adjustment is done by minimizing the center-of-mass oscillations

⁴High-Finesse WS-U

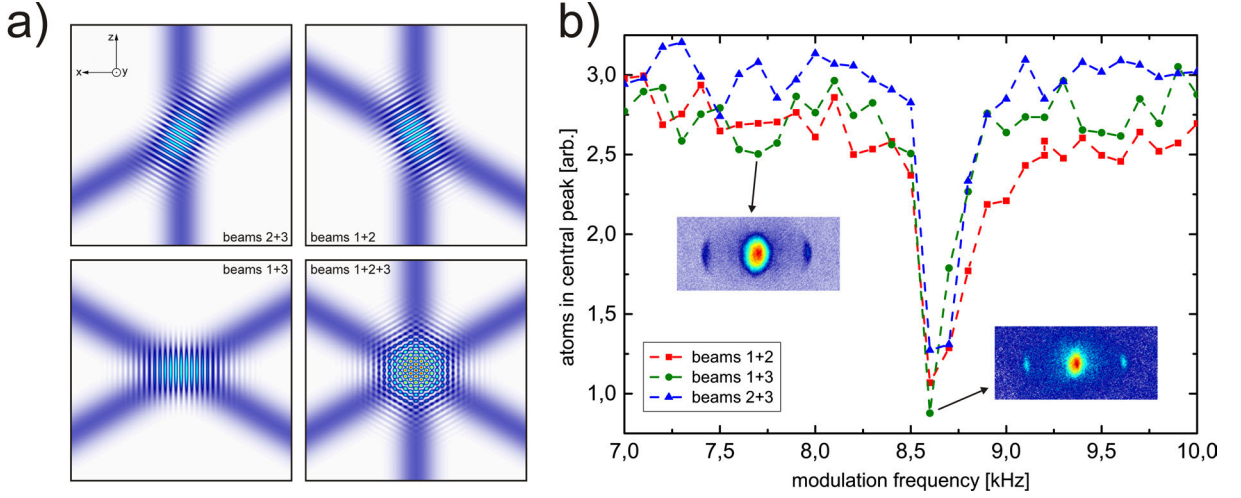


Figure 2.11: a): Intensity distribution in the x - z -plane for different combinations of 2D-lattice beams switched on (not to scale). The three possible combinations of 2D-lattice beams produce 3 different 1D-lattices, rotated by 60° with respect to each other. When all three 1D-lattices are equally deep, all three beams together produce a symmetric triangular lattice. In order to calibrate the lattice, the intensities of the three beams are adjusted such that the parametric excitation to the second excited band occurs at the same modulation frequency for all three 1D-lattices. Panel b) depicts the measured excitation spectra for a 1D-lattice depth of $6.2 E_r$ after the lattice has been calibrated. The parametric heating results in a depletion of the central BEC peak in the time-of-flight image.

induced by pulsing on the lattice beam that is to be aligned. We apply the lattice beam for typically 2 ms. If the beam is not perfectly pointing at the trap center, the additional dipole potential of the lattice beam displaces the trap minimum, causing oscillations of the BEC⁵. These oscillations vanish once the beam has been aligned perfectly to the trap minimum. We estimate the alignment uncertainty achieved with this method to be $\pm 2 \mu\text{m}$, corresponding to $\sim 2\%$ of the beam radius. The longitudinal alignment of the focus to the trap center is done by evaporating into a crossed dipole trap consisting of the horizontal dipole trap beam DT1 and the lattice beam under consideration. For evaporation, only DT1 is ramped down, while the power of the lattice beam is held constant. The final power of DT1 is chosen such that the temperature of the gas is slightly below the critical temperature for Bose-Einstein-condensation. For the given temperature and DT1 potential at this point, the critical temperature and thus the condensate fraction are solely determined by the confinement produced by the lattice beam, which depends on its alignment. The critical temperature is highest when the lattice beam intersects with the dipole trap at its focus, maximizing the confinement and consequently the critical temperature. We thus adjust the focus position such that for a given final power of DT1, the condensate fraction is maximized. We estimate the uncertainty of the focus position found with this technique to be $\pm 3 \text{ mm}$ corresponding to 10 % of the beams Rayleigh range z_R .

For all experiments performed within this thesis the three-beam lattice has been set to the triangular configuration. This is done by adjusting the polarization of all three beams along y ,

⁵These oscillations allow to determine the trapping frequencies of the dipole trap as shown in fig. 2.4

i.e. perpendicular to the lattice plane. For a precise adjustment of the polarization, we exploit the fact that the 1D-lattice propagates perpendicular to the 2D-lattice and thus along the direction of the desired 2D-lattice polarization. Consequently, if the 2D-lattice beams are perfectly y -polarized, they do not interfere with the 1D-lattice. In order to probe the interference between the 1D- and 2D-lattices, we set them to the same frequency and block the retro-reflection of the 1D-lattice beam. Moreover, we coarsely set the polarization of the 1D-lattice perpendicular to the k -vector of the 2D-lattice beam, whose polarization is to be adjusted. This maximizes the interference contrast between the 1D-lattice and the in-plane polarization component of the 2D-lattice beam. We then observe Kapitza-Dirac diffraction off the 1D-lattice generated by the interference between the 1D-lattice beam and the 2D-lattice beam. When the polarization of the 2D-lattice beam is aligned perfectly parallel to the k -vector of the 1D-lattice, the two beams do not interfere and no Kapitza-Dirac diffraction peaks are observed. The sensitivity of this technique can be enhanced by using a sequence of multiple Kapitza-Dirac pulses. The uncertainty of the polarization angle adjusted with this method is $\pm 1^\circ$, corresponding to a maximum of 0.03% of the power having the wrong polarization. Having optimized the polarization of the 2D-lattice beam in this way, we can cross-check for the perpendicularity of the 1D- and 2D-lattice beams. To that end we rotate the polarization of the 1D-lattice such that it points along the k -vector of the 2D-lattice beam. In this configuration the two beams can only interfere, if the angle between them deviates from 90° . From Kapitza-Dirac diffraction in this configuration we deduce an upper limit of $\pm 1.5^\circ$ for the deviation of the angle between the 2D-lattice beams and the 1D-lattice from 90° .

The lattice depth has been calibrated by the standard technique of parametric heating: If the lattice intensity is modulated, parametric excitation causes severe heating and particle loss, when the modulation frequency equals the energy difference between the lowest and the second excited band of the lattice. This loss and heating cause a depletion of the central BEC peak in the time-of-flight image. Measuring the atom number in the central peak versus modulation frequency thus allows to determine the energy difference between these bands for a given lattice intensity. Comparing the measured resonance frequency to the calculated band structure then allows to extract the lattice depth. For the three-beam lattice, there is an additional complication: In order to achieve a fully symmetric triangular lattice, all three beams should have the same intensity. The symmetry of the lattice can however not be extracted from a simple parametric heating spectrum. In order to calibrate all three beams individually, we use the fact that the triangular lattice is in fact a superposition of three 1D-lattices intersecting at an angle of 60° as shown in fig. 2.11 a). Each of these 1D-lattices is generated by one of three possible pairs of 2D-lattice beams. The triangular lattice is symmetric when all three of these 1D-lattices are equally deep. Thus, we adjust the intensities of the three beams until the parametric heating resonances of all three 1D-lattices occur at the same modulation frequency. Figure 2.11 b) shows the parametric excitation spectra of the three 1D-lattices after they have been calibrated.

Having aligned and calibrated the lattice, we checked whether we can drive our ultracold bosonic gas into the Mott-insulator regime. To this end, we used the following experimental sequence: After producing a BEC in the crossed dipole trap, the horizontal 1D-lattice is ramped to $25 E_T$ within 50 ms, dividing the gas into an array of decoupled quasi-2D condensates. Once

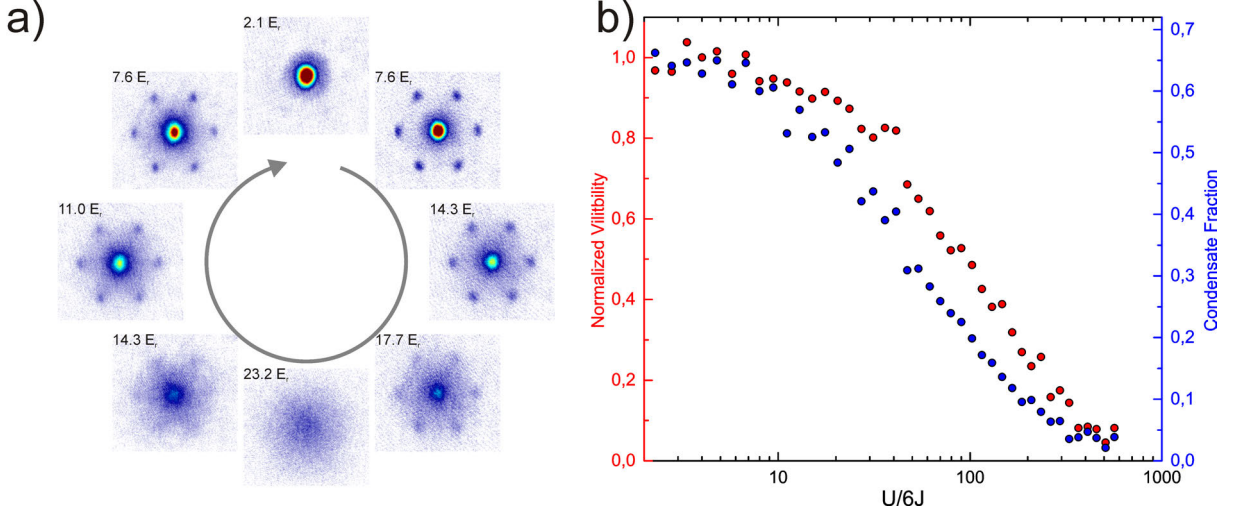


Figure 2.12: Measurement of the superfluid to Mott-insulator transition in an array of quasi-2D condensates of ^{174}Yb in a triangular optical lattice. Details on the experimental sequence are given in the main text. Panel a) depicts a series of time-of-flight images, exhibiting the characteristic loss and revival of coherence as the lattice depth is first increased and then decreased again. In panel b) visibility of the interference pattern and condensate fraction are plotted versus ratio of onsite interaction U and hopping J . The fact that the condensate fraction drops faster than the visibility is attributed to particle-hole excitations in the Mott-insulating state. The supposedly rather high density in the lattice is expected to significantly influence the transition (see main text).

the 1D-lattice has reached its final value, the 2D-lattice beams are ramped to depths between 1 and $23 E_r$. Subsequently, all potentials are abruptly switched off and the sample is imaged after 33 ms time-of-flight. As the lattice depth increases, the characteristic loss of coherence in the momentum distribution is observed as shown in fig. 2.12. The coherence revives as the lattice depth is lowered again and the phase transition is reversed, bringing the atomic ensemble back into the superfluid regime. The parameter that determines the phase of the system is the ratio of the onsite interaction U and the hopping zJ . z is the number of nearest neighbors, which is $z = 6$ for a 2D triangular lattice. We have compared the dependence of visibility and condensate fraction on $U/6J$ measured in our setup to the same measurement performed on the Rb-experiment in our group. This Rb-measurement is in detail described in ref. [89]. The trapping frequencies and lattice parameters are similar to our setup. As in ref. [89], we find that the condensate fraction drops at significantly lower $U/6J$ than the visibility. And similarly we attribute this effect to a small amount of particle-hole excitations in the Mott-insulator phase. However, the overall drop in the visibility as well as in the condensate fraction occurs at considerably larger $U/6J$ values than in the Rb-experiment. Possibly, this observation is related to the two times higher mass of Yb compared to Rb, as explained in the following: While the lattice parameters U and J depend on the mass only via the recoil energy, the harmonic potential in units of E_r is proportional to the squared product of the mass m and mean trap frequency $\bar{\omega}$:

$$V_{\text{trap}}/E_r \propto m^2 \bar{\omega}^2 \quad (2.6)$$

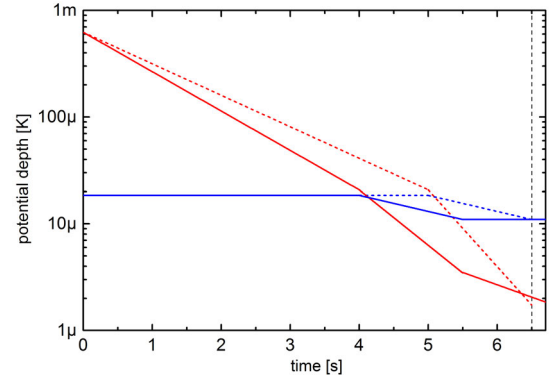
Consequently, in order to achieve the same confinement for Yb and Rb, the trapping frequencies for Yb must be a factor of two lower than for Rb to compensate the mass difference. Or from a different point of view: For the same trapping frequencies, the density, being roughly proportional to $m\bar{\omega}$, is twice as large for Yb. Evaluating the shell structure for 1D- and 2D-lattice depths of 25 and 22.5 E_r , neglecting tunneling ($J = 0$) [93] and using the parameters of the measurement shown in fig. 2.12, one finds a maximum site occupation of $n_{\text{max}} = 7$. In contrast, the same calculation for the experimental parameters from ref. [89] yields $n_{\text{max}} = 4$. As a consequence of the high site occupation in our experiment, the thickness of the outer Mott-shells obtained from the $J = 0$ -calculation is only two to three lattice sites. For such narrow shells, the fluid regions expected between the shells can be assumed to significantly disturb the Mott-state, leading to an increased visibility. Moreover, for the high expected occupation numbers of up to seven, bond-charge interactions can significantly enhance the tunnel-coupling between adjacent sites, shifting the critical $U/6J$ to larger values [94].

The measurement of the bosonic Mott-insulator transition was mainly performed to check the reliability of our lattice setup, which we had just installed. Therefore, after convincing ourselves that we could reliably ramp into and out of the Mott-state, we decided to pursue our main goal and prepare the setup for the investigation of the clock transition on the fermionic isotope ^{173}Yb . Now being fully aware of the high densities in our setup and the physics this is most probably connected to, it would be interesting to evaluate, whether our setup allows e.g. to quantitatively investigate the bond-charge coupling for high occupation numbers. The supposedly very small three-body loss rate of Yb should be very favorable for experiments along these lines. For studies of Hubbard-physics, however, the density would need to be significantly reduced. As mentioned already in section 2.3, this will be possible in the near future with the help of a third dipole trap beam allowing to considerably lower the trapping frequencies.

2.5 Quantum Degenerate Fermi Gases of ^{173}Yb

The main interest in ultracold gases of alkaline-earth-like elements comes from their fermionic isotopes which in contrast to their bosonic counterparts exhibit nuclear spin. It is the interplay between the nuclear spin and the electronic degree of freedom that allows to realize many-body Hamiltonians which are difficult to implement with alkali atoms [24]. The two fermionic isotopes of Yb both have interesting properties: ^{173}Yb carries a large nuclear spin of 5/2 with six different m_I -states, opening up many possibilities for the study of multi-component fermi-mixtures. ^{171}Yb in contrast only has a nuclear spin of 1/2. Its main feature, however, is the small s-wave scattering length of $-3a_0$. Consequently, the importance of the 1S_0 - 3P_0 interaction relative to the ground-state interaction is significantly increased for this isotope, as explained in section 2.1. Still, the small ground-state interaction also requires a second species for efficient sympathetic cooling during evaporation. Since this increases the experimental complexity significantly, we have decided to begin our fermion experiments with ^{173}Yb .

Figure 2.13: Evolution of the potential depths of the two dipole trap beams DT1 (solid red line) and DT2 (solid blue line) during the forced evaporation of ^{173}Yb . In a first step only DT1 is reduced until most of the atoms are concentrated in the crossed trap. In a second step, both beams are ramped down, bringing the gas into the quantum degenerate regime. In a third step, DT1 is slowly reduced further, until $T/T_F = 0.15$ is reached. For comparison the ramps used for the bosonic isotope ^{174}Yb are plotted as dashed lines for DT1 (red) and DT2 (blue).



2.5.1 Evaporative Cooling

Evaporative cooling of fermionic atoms to ultra-low temperatures is complicated by the Pauli principle, which states that identical fermions do not undergo s-wave collisions. Consequently, thermalization in a gas of identical fermions becomes extremely slow once the temperature drops below the threshold for p-wave collisions. Efficient evaporative cooling of fermions is only possible either in a mixture of different internal states or sympathetically in a heteronuclear mixture, ideally with a bosonic species as coolant. ^{173}Yb with its scattering length of $199 a_0$ and large nuclear spin of $I = 5/2$ is well suited for direct evaporation in a spin mixture. The experimental procedure for the preparation of a quantum degenerate fermi gas of ^{173}Yb is basically the same as for the production of BECs described above: Within 20 s we load about $14 \cdot 10^6$ atoms into the 3D-MOT. After the loading phase the MOT is cooled and compressed as described in section 2.3. Interestingly, the lowest light power that can be used before the atoms start to fall out of the MOT is slightly higher than for the bosons. This might be explained by the lower average restoring force due to the small Zeeman shift of the ground state (cf. section 1.1). The final temperature in the MOT is however between 10 and 15 μK , similar to the bosons. After the compression phase we end up with about $2 \cdot 10^6$ atoms in the dipole trap at a few tens of μK .

For forced evaporative cooling we use a power ramp which is slightly different from the one used for the bosons: We start by ramping down DT1 within 4 s to a power of 300 mW until nearly all atoms are confined in the crossed region, keeping the power of DT2 constant. This first step is 1 s faster than for the bosons, which can be attributed to the twice as large scattering length speeding up thermalization. In the second step, both beams are ramped down within 1.5 s to powers of 50 mW for DT1 and 1.9 W for DT2. At the end of the second step the gas has just entered the quantum degenerate regime with $\sim 2 \cdot 10^5$ atoms at 40% of T_F . In the third evaporation step, the gas is brought deeper into the quantum degenerate regime by slowly reducing the power of DT1 further to its final value of 25 mW within 1.3 s. Slowing down the forced evaporation is necessary, because in the quantum degenerate regime only atoms near the Fermi surface contribute to the thermalization, slowing it down considerably [95]. The evolution of the potential depth of the two dipole trap beams during the forced evaporation phase is shown

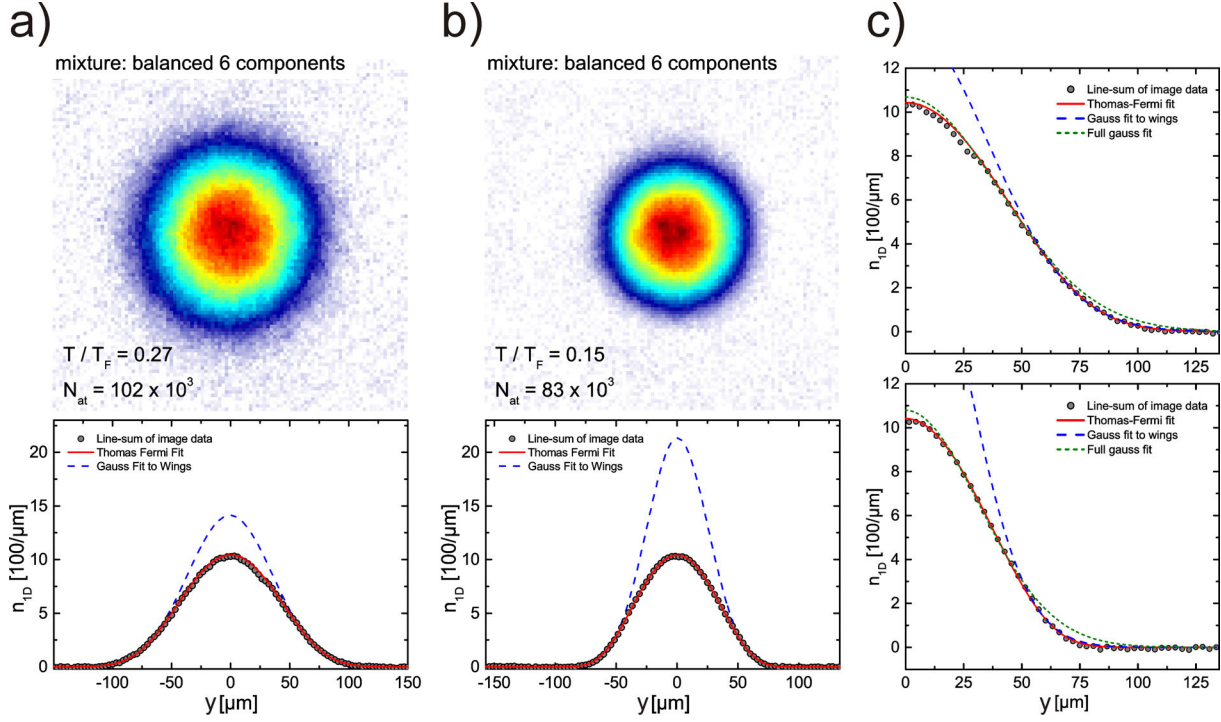


Figure 2.14: Evaluation of time-of-flight images of the ultracold Fermi gas. A two-dimensional fit of a Thomas-Fermi profile (solid red line) allows to extract T/T_F . Quantum-degeneracy can be clearly observed by comparing the data to a 2D Gaussian fit to the wings of the time-of-flight distribution (dashed blue line), which significantly overestimates the density in the center of the distribution. The data in panel b) is taken at the end of the forced evaporation phase. For the image in panel a), the final trap depth was set to a larger value in order to obtain a less degenerate sample. Panel c) depicts close-ups of the line-sums from a) and b), including a 2D Gaussian fit to the whole distribution (dashed green line). While the deviation is much smaller than for the fit to the wings only, it can clearly be observed.

in fig. 2.13. As for the bosons, all ramps are of exponential shape. At the end of this three-step evaporation we end up with a balanced spin mixture of $70 \dots 80 \cdot 10^3$ atoms at 15% of the Fermi temperature. The temperature is determined by fitting a two-dimensional Thomas-Fermi profile to the density distribution after time of flight, leaving the fugacity z , the peak density and the Thomas-Fermi radii as free parameters. The temperature relative to the Fermi temperature is then obtained from the fugacity via:

$$6 \cdot Li_3(z) = - \left(\frac{T_F}{T} \right)^3, \quad (2.7)$$

where $Li_3(z)$ is the third order poly-logarithmic function [96]. The signature of Fermi degeneracy in the time-of-flight distribution is a flattening at the center compared to the slope at the edges of the distribution. It is due to Pauli pressure pushing the atoms to the edges of the momentum distribution, when the occupation of the lowest energy states becomes on the order of unity. This flattening can be most clearly observed when fitting a Maxwell-Boltzmann distri-

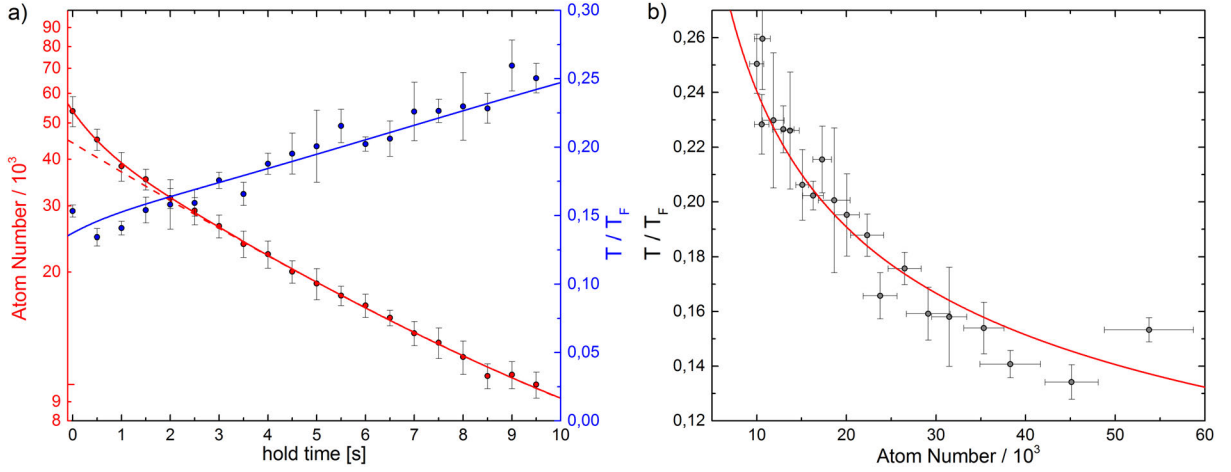


Figure 2.15: a): Decay of the degenerate Fermi gas held in the crossed dipole trap. As for the bosons, the lifetime is limited by photon scattering from the dipole trap. For short hold-times a slight non-exponential decay is observed, attributed to a focus shift of DT1. The solid red line is a double exponential fit to the data. The dashed red line is an exponential fit to the data for $t \geq 4$ s. The increase of T/T_F over time, can be explained by a reduction of T_F due to the loss of particles. Panel b) shows T/T_F vs. the particle number N , together with a fit of the expected $N^{-1/3}$ dependence. From this fit and the fit to $N(t)$ in a), the time dependence of T/T_F is calculated and shown as solid blue line in panel a).

bution, i.e. a 2D-Gaussian, to the wings of the momentum distribution, as shown in fig. 2.14 a) and b). Comparing this Gaussian 'wing-fit' to the measured data and the Thomas-Fermi fit, the increase in Fermi degeneracy at a lower T/T_F can clearly be observed. When fitting a 2D-Gaussian to the whole time-of-flight distribution, the deviations from the Thomas-Fermi profile are much smaller, as can be seen in the close-up of the line profiles in panel c) of fig. 2.14. At moderate $T/T_F \approx 0.3$, the deviation is hardly visible. At $T/T_F \approx 0.15$, however, the deviation can clearly be observed.

Figure 2.15 a) shows the decay of our degenerate Fermi gas in the crossed dipole trap. The decay rate of $(0.19 \pm 0.04) \text{ s}^{-1}$ for hold times longer than 4 s is compatible with that measured for the bosons. During the first four seconds we observe again a slight non-exponential decay, however much less than for the bosons. This strengthens the assumption that a focus shift of the horizontal dipole trap beam resulting in unwanted lowering of the trap is responsible for this non-exponential decay: The third evaporation step, lasting for 1.2 s, provides more time for the AOM to thermalize, compared to the bosons, where this third step is not used. Thus, the unwanted focus shift following the evaporation is smaller. Moreover, since we regularly adjust the dipole trap focus position for optimal evaporation performance, the overall focus position might be slightly different in this measurement compared to the BEC measurements presented in section 2.4.1, changing the influence of the thermal focus shift.

As the ultracold gas decays, the ratio T/T_F slowly increases from 15% to 25% over a hold-time of 10 s. This can for the most part be explained by the decay of the atom number resulting in a decrease of the Fermi temperature proportional to $N^{-1/3}$. In fig. 2.15 b) T/T_F is plotted

versus the number of atoms N . The $N^{-1/3}$ dependence fits the data reasonably well. The solid blue line combines the fitted curves for $N(t)$ and $T/T_F(N)$ to yield the time dependence of $T/T_F(t)$. Comparing this curve to the measured temperatures, one can extract a heating rate of about 2% of T_F over 10 s or $2 \cdot 10^{-3} T_F \text{ s}^{-1}$.

2.5.2 Production and Detection of Spin-Mixtures

In contrast to their bosonic counterparts, the fermionic Yb-isotopes exhibit nuclear spin. In order to fully exploit this additional degree of freedom, controlled preparation and readout of the nuclear-spin magnetic quantum number m_I are required. For electronic states with non-zero angular momentum J , the electronic and nuclear spins couple to a total hyperfine spin F , which can be controlled conveniently via direct coherent coupling of different spin states using microwave- and RF-radiation. This is the case for the ground states of alkali atoms, or the 3P_2 -state of Yb. For the $J = 0$ states of Yb such as the 1S_0 ground state and the metastable 3P_0 state, this is hardly feasible for two reasons: First, the nuclear magnetic moment is ~ 2000 times smaller than that of the electron. Consequently, ~ 2000 times higher fields are required in order to achieve a coupling to the nuclear spin on the same order of magnitude as for the electron spin. Producing such high fields is hardly feasible experimentally. Secondly, the nuclear spin states do not exhibit a quadratic Zeeman shift. Thus, all m_I -states are equally separated and cannot be individually addressed. While both problems can in principle be overcome by using Raman-instead of direct coupling and inducing a nonlinear splitting between the m_I -states by means of near resonant light-shifts, the most straightforward way to control the spin composition of the ultracold gas is to perform optical pumping prior to evaporation.

In our experiment, optical pumping proceeds as follows: After the dipole trap has been loaded and the MOT light is switched off, we apply a homogeneous magnetic field of 67 G along the axis of the horizontal dipole trap. This splits neighboring m_F -levels of the ($^3P_1, F = 7/2$) hyperfine state by 40 MHz, far enough to address them individually despite the Doppler- and light-shift broadening in the dipole trap. We are then able to depopulate individual ground-state m_I -levels by shining in pulses of σ^+ -polarized 556 nm light at the right detuning along the direction of the magnetic field. Subsequently, we perform evaporative cooling.

In order to probe the spin distribution of the ultracold gas, we use the so-called optical Stern-Gerlach (OSG) technique [97–99]: After releasing the atoms from the trap, we pulse on a laser beam tuned in between the hyperfine states of the $^1S_0 \rightarrow ^3P_1$ transition, resulting in an m_I -dependent light-shift. With the slope of the Gaussian beam profile positioned at the center of the atom cloud, the atoms experience an m_I -dependent force that spatially separates the different spin components after time-of-flight. Figure 2.16 a) and b) show the geometry of the OSG setup. The beam enters the glass cell under an angle of 11° with respect to the horizontal, its center located half its $1/e^2$ -radius above the atoms. The spin components thus separate perpendicular to the axis of the beam, i.e. almost vertically, as shown in fig. 2.16 b). Splitting the cloud vertically instead of horizontally has the advantage that the splitting can be seen from both imaging directions (x and y). The OSG beam has a $1/e^2$ -diameter of $200 \mu\text{m}$, a power of 40 mW and a detuning of 1.27 GHz to the blue of the ($^3P_1, F = 7/2$)-state. The light is derived

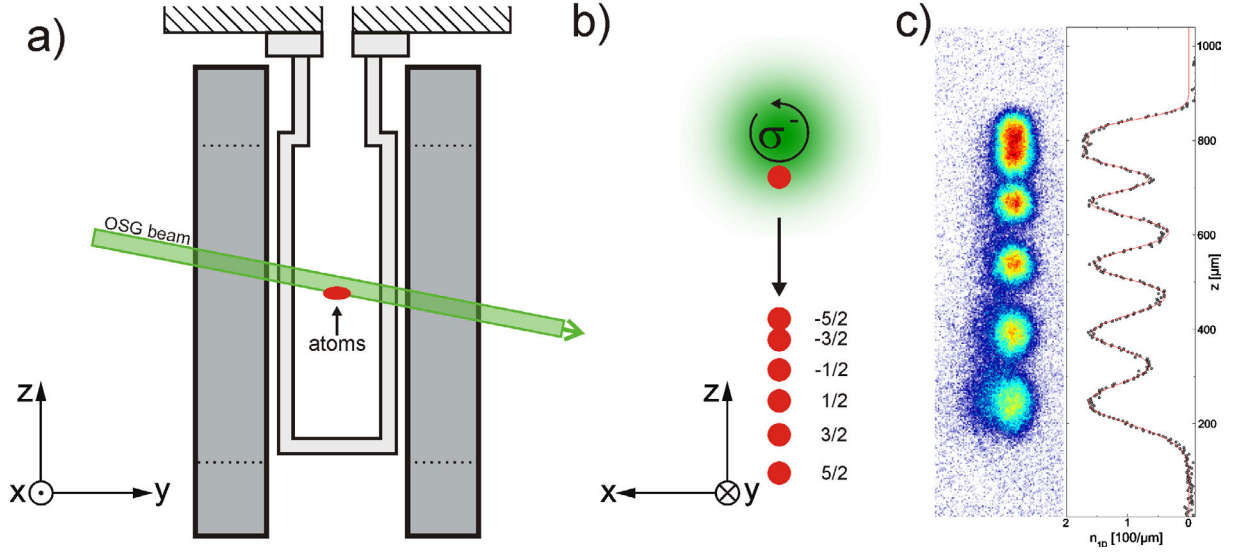


Figure 2.16: Geometry of the optical Stern-Gerlach (OSG) setup. Panel a): The OSG beam propagates in the y - z plane at an angle of 11° with respect to the horizontal. Panel b): The beam is adjusted half the $1/e^2$ -radius above the atoms, such that the largest intensity gradient is located at the position of the atom cloud. Due to the differential light-shift between the different spin components, the cloud splits up perpendicular to the OSG beam. The almost vertical separation can be seen from both imaging directions x and y . Panel c): Absorption image of a degenerate gas of ^{173}Yb after OSG separation without optical pumping prior to evaporation. The gas is a balanced mixture of all six spin components. The OSG beam has been aligned slightly further away from the atoms to reduce photon scattering.

from the frequency-doubled diode laser-based system, locked to the ULE cavity (cf. fig. 1.5). The OSG setup has in large part been implemented by my colleague André Kochanke and will be described in more detail elsewhere.

Figure 2.17 shows the polarizability and scattering rate close to the $^1S_0 \rightarrow ^3P_1$ transition. The dashed lines indicate the detuning used in the experiments described here. The differences between the polarizabilities of neighboring m_I -states are rather asymmetric, such that a good separation of all six components is hardly possible without significant photon scattering. By adjusting the power or the alignment of the OSG beam, we can choose between good separation of all six spin components or low photon scattering. Minimizing photon scattering is especially important when a precise quantitative measurement of the spin composition is desired. The OSG performance could be improved by the use of two OSG beams of opposite circular polarization, as has been demonstrated for ^{87}Sr [100]. This should allow to well separate all six spin components without significant photon scattering.

With optical pumping and OSG spin separation at hand, we can evaluate the production of different spin mixtures of quantum degenerate ^{173}Yb . Without optical pumping prior to evaporation, we end up with a balanced mixture of all six spin states as shown in fig. 2.16 c). By subsequently depopulating one or more m_I -states, we prepare degenerate Fermi gases with one to six spin components. This is shown in fig. 2.18. Here, the OSG beam is applied for a time of

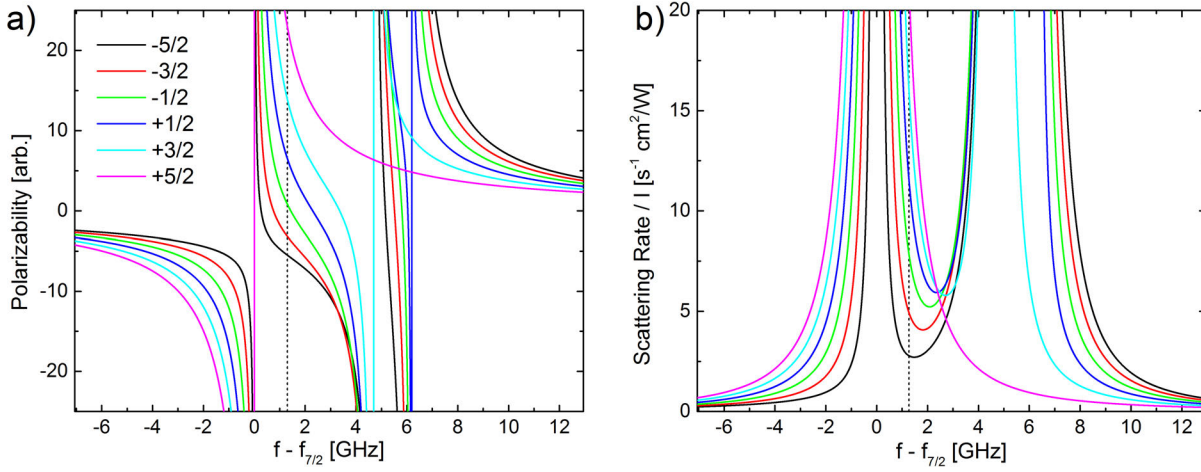


Figure 2.17: Polarizability and scattering rate for the different m_I states of ^{173}Yb for σ^+ -polarized light. The frequency is given with respect to the $(^1S_0, I = 5/2) \rightarrow (^3P_1, F = 7/2)$ -transition. In the experiments described here, a detuning of 1.27 GHz to the blue of that transition has been used (marked by dashed line). The asymmetric splitting of the polarizability makes it difficult to separate all spin components without significant photon scattering.

1 ms directly after switching off the trap, resulting in a good separation of all six spin components. The spin distribution is however distorted due to photon scattering and the corresponding optical pumping. Quantitative evaluation of the spin composition can be performed with reduced OSG duration. Images without spin separation, shown to the right of the respective OSG images, are used to extract T/T_F for the different mixtures.

Let us first consider only the cases of multi-component spin mixtures with two to six components. For all of these spin mixtures the same evaporation ramp is used. In the measurements, the total atom number decreases with the number of spin components, while the degeneracy T/T_F slightly increases. Going from six to four components hardly changes the degeneracy. For three and two components T/T_F then increases by 1...2%.

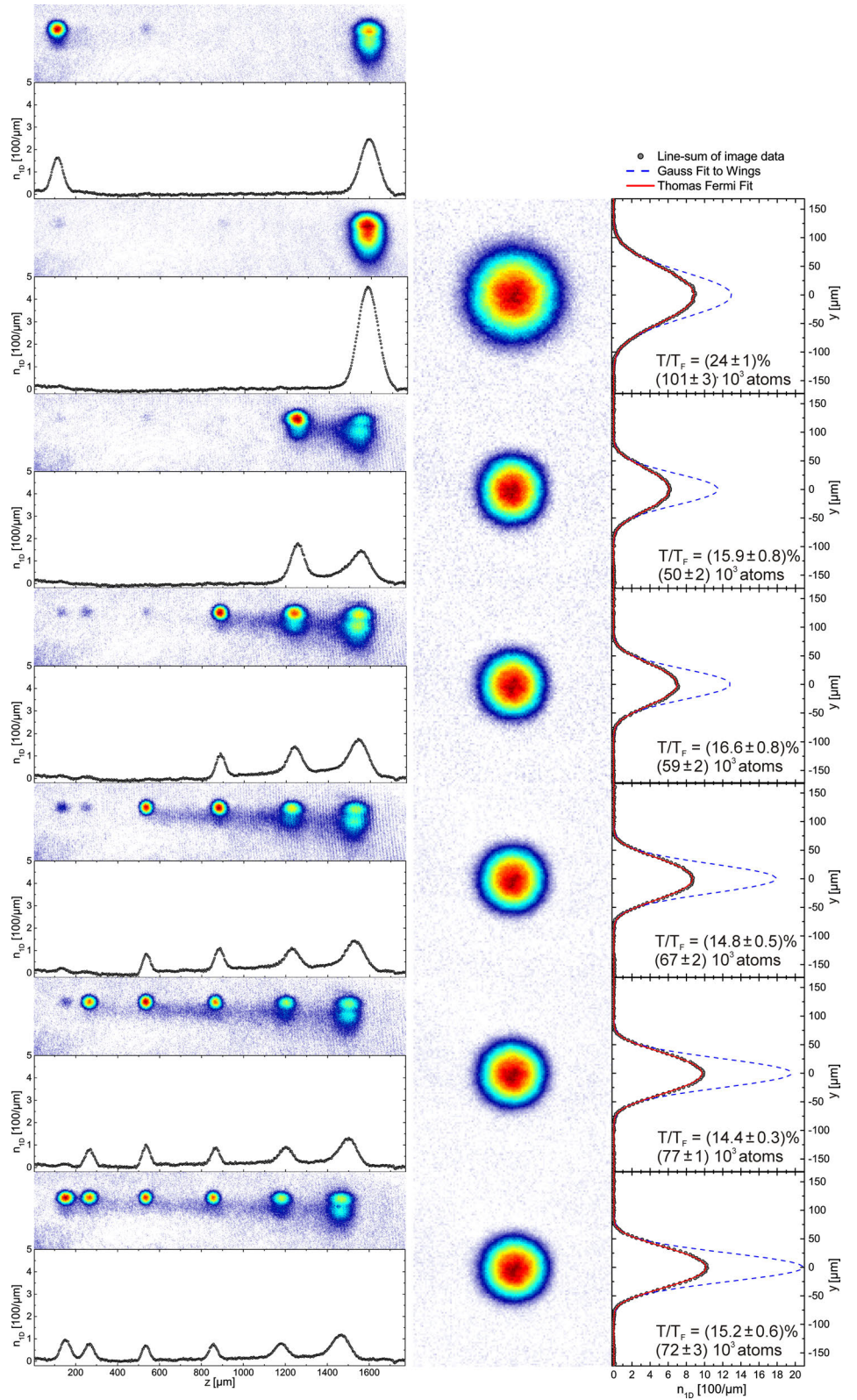
Three different effects influence the dependence of T/T_F on the number of spin components. First, the optical pumping heats the sample in the dipole trap. This heating amounts however only to a few photon recoils, which is negligible compared to the initial temperature in the dipole trap of a few tens of μK . Second, the evaporative cooling efficiency decreases with the number of spin components present, because the evaporation depends on elastic collisions between different spin states. Third, as atoms are transferred from one spin component to another, the number of atoms per component is increased, resulting in an increase of T_F , which at constant temperature reduces the degeneracy parameter T/T_F .

The reduced evaporation efficiency directly manifests itself in the decrease of the total atom number as the number of m_I -states is reduced. The fact that T/T_F only decreases very little indicates that the increase in the Fermi temperature nearly balances the reduced evaporation efficiency.

The spin polarized gas constitutes a special case. Because of the Pauli exclusion of s-wave collisions, a spin polarized gas can hardly be evaporatively cooled into the quantum degenerate

Figure 2.18:

Different spin mixtures of degenerate ^{173}Yb . Different mixtures are produced by depopulating unwanted spin components by optical pumping prior to evaporation. As the number of components is reduced from six to two, a slight increase of the degeneracy parameter T/T_F can be observed, which is attributed to a reduced evaporation efficiency. A spin-polarized sample is produced via sympathetic cooling by minority spin components, which are completely eliminated during evaporation. Details are given in the main text.



regime without a second species as sympathetic coolant. In order to provide such a coolant, we adjust the duration of the optical pumping pulses such that a small but equal fraction of the unwanted spin components is still present at the beginning of the evaporation. We then force evaporation by ramping down the dipole trap until all unwanted spin components are removed from the trap. The degeneracy that can be achieved without having unwanted spin components present at the end of evaporation is limited to $T/T_F \approx 0.25$, because the forced evaporation is not spin-selective. In order to optimize the final T/T_F , both the initial spin distribution as well as the evaporation ramp have to be adjusted iteratively. The final trap depth for the case of a spin-polarized gas is larger than for the multi-component spin mixtures. Another way to produce a spin-polarized gas, which we have not yet explored, is the removal of unwanted spin components after evaporating a multi-component mixture.

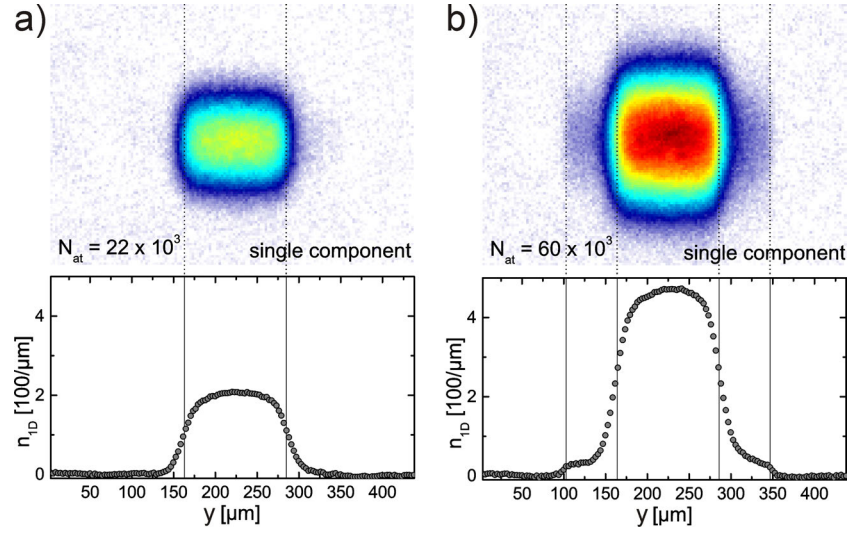
In section 2.1 it has been pointed out that for the ($J = 0$)-states the scattering length is independent of the nuclear spin. Thus, as long as only ground-state spin mixtures are to be studied, only the number of components in a given spin mixture matters. Which m_I -states are used exactly is irrelevant. However, when the ground state is optically coupled to the 3P_0 metastable state, the exact choice of spin components is indeed important, because of the m_I -dependent Clebsch-Gordan coefficients of the $^1S_0 \rightarrow ^3P_0$ transition. In this context a two-component spin mixture of the two stretched states $m_I = \pm 5/2$ is of special interest, as will be explained in section 3.3.1. We prepare this mixture in the following way: We use the σ^- -polarized imaging beam along the y direction on the 399 nm transition to pump nearly all atoms to the $m_I = -5/2$ state. Subsequently, the desired amount of population is transferred back to $m_I = +5/2$ state with the optical pumping beam on the 556 nm transition. The uppermost panel of fig. 2.18 shows a 1:2 mixture of these two components.

2.5.3 ^{173}Yb in the Optical Lattice

Like electrons in a solid state crystal, fermionic atoms in an optical lattice fill up the reciprocal lattice from $q = 0$ in the first Brillouin zone up to the fermi surface. Thus, their momentum distribution after abruptly switching off the lattice does not exhibit the discrete peaks observed for bosons. Instead, the presence of the lattice potential is best observed by so-called *band mapping*. This is done by ramping down the lattice on a time-scale that is slow compared to the band-gap of the lattice and fast with respect to the trapping frequency [101, 102]. If the correct ramp speed is chosen, quasi-momentum is conserved and adiabatically mapped onto real momentum in the limit of vanishing lattice depth. The momentum distribution can then be observed in the density distribution after time-of-flight. If the lattice is decreased too fast, atoms are excited to higher bands and the band population is not conserved. If the lattice is decreased too slowly, the quasi-momentum states of the lattice ultimately transform back to the harmonic oscillator eigenstates of the trap. Both, ramping too slowly or too fast, will smear out sharp features in the momentum distribution, such as the edges of the first Brillouin zone.

Figure 2.19 depicts the time-of-flight distribution after band mapping out of the horizontal 1D-lattice for a spin-polarized gas at $T/T_F = 0.3$ for two different atom numbers. After evaporative cooling has been completed, the 1D-lattice is ramped up linearly within 50 ms to a depth of

Figure 2.19: Time-of-flight images obtained after band mapping of a spin-polarized gas at $T/T_F = 0.3$ out of a 1D-lattice with a depth of $20E_r$, averaged over 15 individual measurements. The lattice is oriented horizontally. Best mapping is achieved, by linearly ramping down the lattice within 2 ms. For $22 \cdot 10^3$ atoms, the lowest band is completely filled with no observable higher band population. For an increased atom number of $60 \cdot 10^3$ about 10% of the atoms occupy the second band.



$20E_r$. The atoms are then held in the lattice for 20 ms, before band mapping is performed by ramping down the lattice linearly within 2 ms. In the direction of the lattice, the distribution is flattened in the center and falling off steeply at the edges of the first Brillouin zone, marked by dashed lines in fig. 2.19. The edges of the distribution are smoothed out due to the finite ramp-down time of the lattice. For $2 \cdot 10^4$ atoms in panel a) the 1st Brillouin zone is homogeneously filled and no higher band population is observed. In panel b) however, where the atom number is increased by a factor of three, about 10% of the atoms homogeneously populate the second band, or the second Brillouin zone of the lattice. Observing atoms in the second band at these moderate atom numbers is rather unusual. In order to understand how this comes about, it is worthwhile to consider the process of loading the lattice in some detail.

The most simple approach to the problem is to consider particles in a box potential, on top of which a lattice is slowly increased. The eigenstates of the box potential without the lattice are plane waves, linearly spaced in momentum space. When the lattice is slowly increased, these momentum states are adiabatically transformed into the corresponding quasi-momentum states of the lattice potential. Thus, all states occupying the first Brillouin zone before the lattice is applied will be loaded into the first band, states initially in the second Brillouin zone will be loaded into the second band, and so on.

In one dimension, the energy at the edge of the N th Brillouin zone is

$$E_N = N^2 \frac{\hbar^2 k_L^2}{2M} = N^2 E_r, \quad (2.8)$$

where k_L is the wavenumber of the lattice laser. Therefore, the criterion that all states with momenta in the N th Brillouin zone are mapped into the N th band can equivalently be expressed in terms of energy: All states with energies below E_r will form the first band. All states with energies between E_r and $4E_r$ will form the second band, and so on. This can immediately be seen by looking at the band structure of a 1D-lattice shown in fig. 2.20 a).

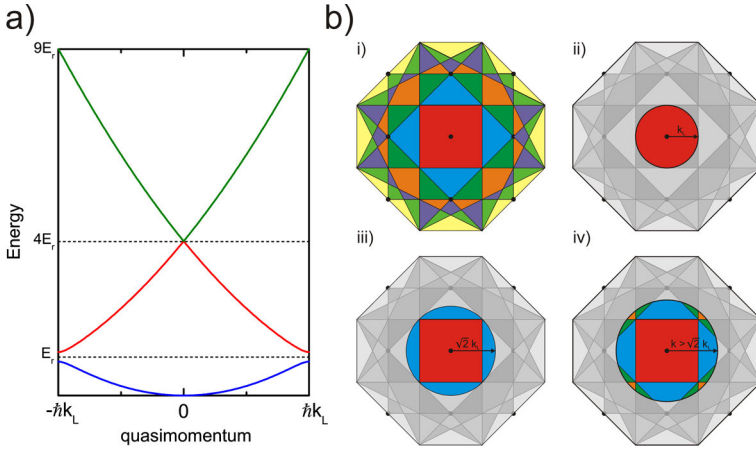


Figure 2.20: a) Band structure of a 1D-lattice with a depth of $0.5E_r$. The band gaps between the N th and $(N+1)$ th band appear at energies N^2E_r . b) i): Brillouin zones of a square lattice. ii) If initially momentum states up to $\hbar|\vec{k}| = \hbar k_L$ are occupied, only the first band is populated but cannot be completely filled. iii): The first band is completely filled if initially all states up to $\hbar|\vec{k}| = \hbar\sqrt{2}k_L$ are occupied. This also leads to population in the second band. iv): If the maximum initial momentum exceeds $\hbar\sqrt{2}k_L$, even the third and fourth band will be populated.

The situation changes when higher dimensions are considered, because the energy is no longer constant along the borders of the Brillouin zones. E.g. in two dimensions, the first Brillouin zone of a square lattice is a square of size $2k_L$. The free momentum states below E_r lie however on a disk of radius k_L . Consequently, the first band of the lattice cannot be completely filled, without populating higher bands. The highest possible filling factor of the first band is the ratio between the area of the first Brillouin zone and the area of a disk of radius k_L , which is $\pi/4 \approx 0.8$. If states above E_r are occupied, they will partly be loaded into higher bands, although the lowest band is not yet full, as illustrated in fig. 2.20 b). This problem can also be formulated in position- instead of momentum-space by considering that the density of a 2D-Fermi gas is given by

$$n_{0,2d} = \frac{\pi}{4a^2} \cdot \frac{E_F}{E_r}, \quad (2.9)$$

where a is the lattice spacing. If all states up to $E_F = E_r$ are occupied, the number of atoms per unit cell is only $a^2 \cdot n_{0,2d} = \pi/4 \approx 0.8$. Similar arguments hold for three dimensions: Here, the volume of the Brillouin zone of a cubic lattice has to be compared to that of a sphere with radius k_L , resulting in the highest possible filling of $\pi/6 \approx 0.5$. Thus, in order to fill up the first band completely, the gas needs to be adiabatically compressed after the lattice has been applied. In experiments with ultracold atoms in optical lattices, this adiabatic compression is intrinsically taken care of by the harmonic trapping potential. The underlying mechanism can be understood by solving the single particle Hamiltonian of a combined harmonic+lattice potential as has been done in one dimension in refs. [103–105]. The probability distribution $|\Psi(x)|^2$ of the corresponding eigenstates in position space is shown in fig. 2.21 for two different lattice depths. In panel a) the lattice depth is $0.5E_r$, in panel b) $2E_r$. Comparing the two plots reveals that as the lattice depth is increased, the highest energy states start to localize in the outer regions of the trap. This happens as soon as the potential energy difference between neighboring sites due to the harmonic confinement exceeds the nearest neighbor tunneling. As a consequence of the localization, the energies of the eigenstates are more and more determined by the local value of the trapping potential, pushing the states towards the center of the trap and compressing the

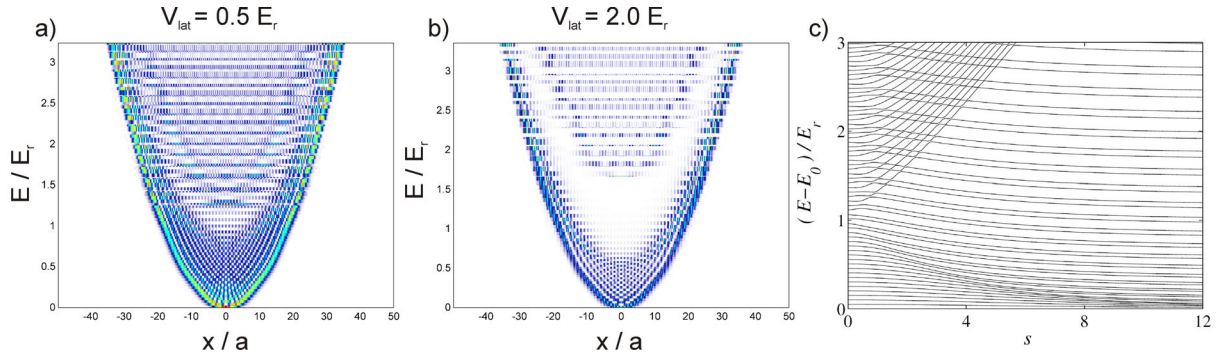


Figure 2.21: Panels a) and b) show the spatial distribution of the lowest energy eigenstates of a combined harmonic+lattice potential for lattice depths of $0.5E_r$ and $2E_r$, respectively. The x -axis denotes the position in units of the lattice spacing a . The energy in units of E_r is given on the y -axis. The harmonic trapping frequency is 66 Hz, corresponding to ω_y in our experiment. As the lattice depth increases, the states start to localize in the outer regions of the trap, leading to the appearance of a bandgap in the center. Panel c): Energy spectrum of a combined harmonic+lattice potential. Reprinted figure with permission from Viverit et al., Phys. Rev. Lett. **93**, 110401 (2004). Copyright (2004) by the American Physical Society. s is the lattice depth in units of the recoil energy. The level spacing changes from linear for the initial harmonic oscillator states to quadratic for the localized states. About one third of the states above E_r steeply bend upwards as the lattice is increased, forming the second band.

sample. The appearance of localized states is also responsible for the formation of a bandgap in the trap center, spreading towards the edges as the lattice depth increases. The first band is filled as soon as the highest energy states have tightly localized at the edges of the trap and a homogeneous density of one atom per lattice site is reached in the occupied central trapping region. Depending on the initial number of atoms and the harmonic confinement, this happens at different lattice depths.

Remarkably, the criterion found for the homogeneous lattice, stating that all states with energies below E_r are loaded into the lowest band, remains valid also for the harmonically confined lattice. This can be seen in fig. 2.21 a) and b) as well as in panel c) of the same figure. The latter has been taken from ref. [104] and depicts the energy spectrum of a 1D harmonic+lattice potential as a function of lattice depth for a harmonic confinement of $\hbar\omega_{trap} = 0.05E_r$. All states with initial energies below E_r transform smoothly from the linearly-spaced harmonic oscillator states to the quadratically-spaced localized states. States above E_r behave differently: One set of states strongly bends upwards in energy as the lattice depth increases. Those are the states eventually forming the second band. The second set of states exhibits the same smooth behavior as the states below E_r . Those states finally end up as localized states in the first band. Looking closely at the spectrum, it can be seen that all the crossings between the localized and second-band states are in fact avoided crossings with extremely narrow splittings. This can be understood as follows: Because of the spatial separation between the first- and second-band states, the tunnel-coupling responsible for the avoided crossing becomes very small. Consequently, if the lattice were ramped up perfectly adiabatically such that all atoms in the second band had enough time to tunnel to lower lying localized states, none of the avoided crossings would be crossed and all states would finally end up in the first band. However, the tunnel-

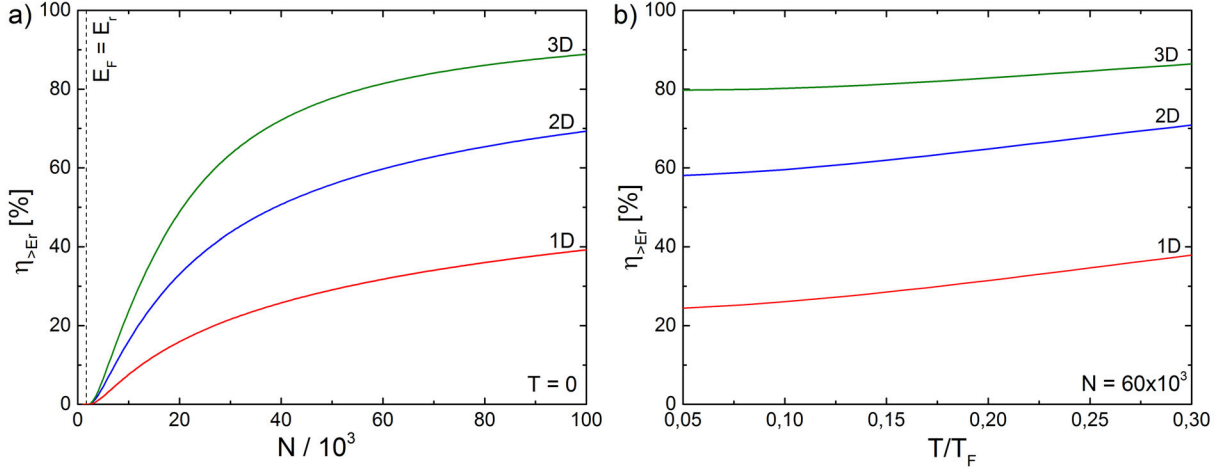


Figure 2.22: Panel a): Fraction $\eta_{>E_r}$ of atoms fulfilling the conditions of eqs. (2.10) and (2.11) versus the total atom number N . The red line corresponds to the case of a 1D-lattice (red line). For the case of a 2D- and 3D-lattice the condition of eq. (2.11) is applied along all lattice directions, resulting in the blue line for a 2D-lattice and the green line for a 3D-lattice. All harmonic oscillator states below the Fermi energy are assumed to be populated, corresponding to zero temperature. Panel b) depicts $\eta_{>E_r}$ as a function of T/T_F for a fixed atom number of $N = 6 \cdot 10^4$. Temperature is taken into account by populating the harmonic oscillator states according to the Fermi-Dirac distribution. The different lines are again corresponding to the different dimensionalities.

coupling and thus the avoided crossings quickly become negligibly small, such that adiabaticity can hardly be achieved experimentally. Thus, it is reasonable to expect that all of the steeply upward bending states will be transferred to the second band. Looking at fig. 2.21 c), one finds that roughly one third of the states above E_r are loaded into the second band.

These considerations now allow to perform a simple estimate of the number of atoms transferred to higher bands during the loading of the lattice. First, let us consider the case of an ensemble of atoms trapped in a 3D-harmonic trap, loaded into a 1D-lattice along the y -direction as has been done in the measurements of fig. 2.19. Since the lattice is oriented along one of the principle axes of the trap, the Hamiltonian separates for the three directions x , y , and z and the condition $E < E_r$ applies separately to the direction of the 1D-lattice. Therefore, out of all harmonic oscillator states with energies

$$E(n_x, n_y, n_z) = \left(n_x + \frac{1}{2}\right) \hbar\omega_x + \left(n_y + \frac{1}{2}\right) \hbar\omega_y + \left(n_z + \frac{1}{2}\right) \hbar\omega_z < E_F. \quad (2.10)$$

those states with

$$\left(n_y + \frac{1}{2}\right) \hbar\omega_y > E_r \quad (2.11)$$

cannot all be loaded into the first band. The red line in fig. 2.22 a) depicts the fraction of atoms $\eta_{>E_r}$ that fulfill eqs. (2.10) and (2.11) for the case of a 1D-lattice. For a quadratic 2D- or a cubic 3D-lattice, the condition of eq. (2.11) has to be applied analogously to all lattice directions, leading to correspondingly higher values of $\eta_{>E_r}$, shown in blue and green in the same plot.

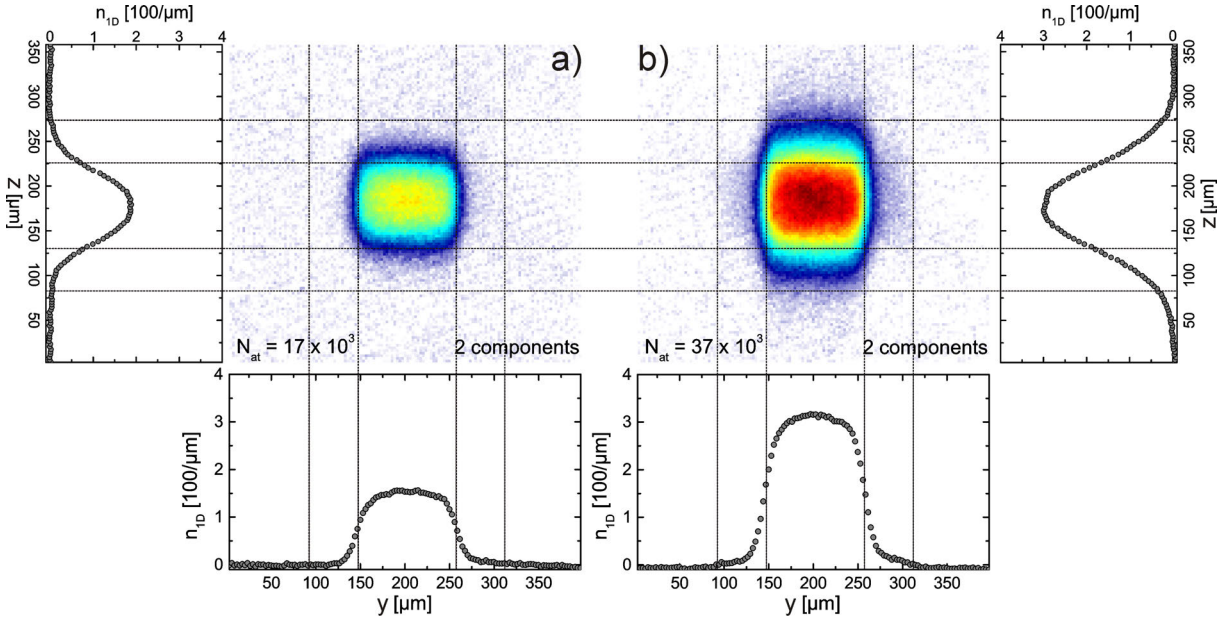


Figure 2.23: Time-of-flight distribution of a two-component mixture at $T/T_F = 0.2$ after band mapping out of the full 3D-lattice, averaged over 20 runs. The lattice depth is $13.7E_r$ for the triangular lattice and $14.5E_r$ for the 1D-lattice, in order to achieve approximately equal tunneling in all three directions. The images are taken along x , in the plane of the triangular lattice and perpendicular to the 1D-lattice. Correspondingly, only the horizontal momentum distribution exhibits the sharp edges of the first Brillouin zone. In the vertical direction, the image integrates over the hexagonal volume of the Brillouin zone, leading to a more peaked line-profile. The projected edges of the first and second Brillouin zone are marked by dashed lines. In panel a) at a filling of $8.5 \cdot 10^3$ per spin component only very little population is observed in higher bands, while for a filling of $18.5 \cdot 10^3$ per component as in b), significant population in higher bands can be observed.

The lattice and trapping parameters used for this calculation correspond to the parameters from our experiment⁶. $\eta_{>E_r}$ stays zero, until the Fermi energy crosses the recoil energy. Above this threshold, marked by the dashed line in fig. 2.22, $\eta_{>E_r}$ initially increases almost linearly with atom number and also linearly with the lattice dimension. This changes for larger atom numbers: At some point the first Brillouin zone of the 3d-lattice is completely filled, implying that all further atoms will increase $\eta_{>E_r}$. For the 2D- and 1D-lattice, the lowest band can accommodate an infinite number of atoms, because there is no limit on the momentum in the directions that are not confined by the lattice. In the case of a triangular lattice, the situation is more complicated, since the lattice is not oriented along the principal axes of the harmonic potential and the Hamiltonian does not separate for the three directions x , y , and z . The qualitative behavior of $\eta_{>E_r}$ can however be expected to be very similar to the case of a square lattice. Temperature can be included in the estimate by taking the population of the initial harmonic oscillator states according to the Fermi-Dirac distribution. Figure 2.22 b) depicts $\eta_{>E_r}$ as a function of T/T_F for $n = 6 \cdot 10^4$ atoms. In the range between $T/T_F = 0.05 \dots 0.3$ it increases almost linearly.

These values can now be compared to the measurements in fig. 2.19. As discussed above, one

⁶ $(\omega_x, \omega_y, \omega_z) = (84, 66, 134)$ Hz, $E_r = 2$ kHz

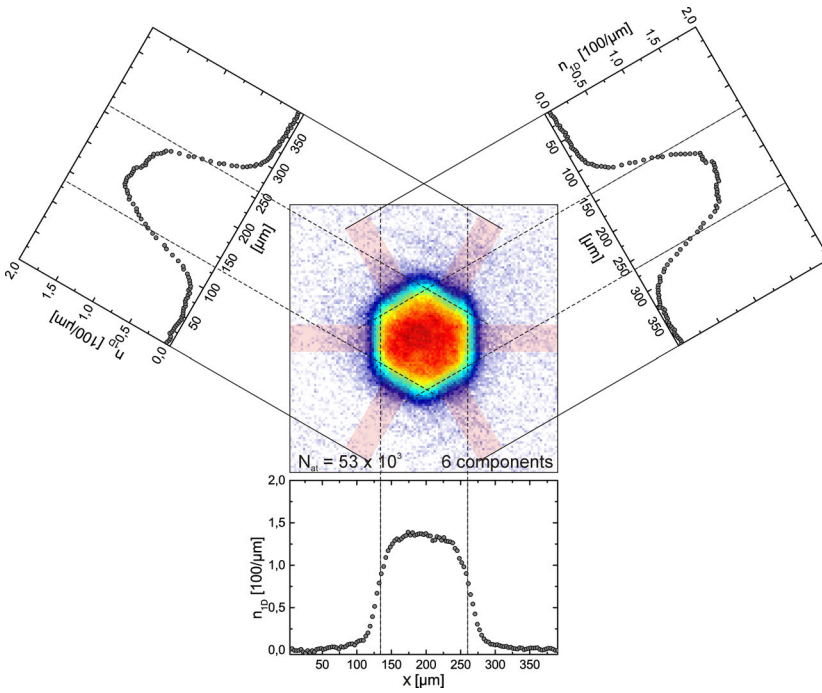


Figure 2.24: Time-of-flight distribution after band mapping of a six-component mixture at $0.15 T/T_F$ out of a 2D triangular lattice with a depth of $15.2 E_T$, averaged over 15 runs. Line sums taken of the colored regions in the image reveal a homogeneous population of the first Brillouin zone. Also in this case, some higher band population is observed as expected from fig. 2.22.

can crudely estimate from fig. 2.21 c) the fraction of atoms transferred to the second band to be $\eta_{>E_T}/3$. Thus, for a sample of $6 \cdot 10^4$ spin polarized fermions at $T/T_F = 0.3$ as in fig. 2.19 c), we expect from fig. 2.22 b) about 13% of the atoms in the second band, which agrees rather well with our measurement. For $2.2 \cdot 10^4$ as in fig. 2.19 b), the estimate still yields $\eta_{>E_T}/3 \approx 9\%$ in the second band. This does not fit to the image in fig. 2.19 a), which is compatible with no second band population. This might be explained by the fact that the avoided crossings between the first and second band states seen in fig. 2.21 c) are still rather large for the states just above E_T . Therefore, one might assume that some of the lowest energy states above E_T can be adiabatically transferred over the crossings into the first band, reducing the second band population. A reliable calculation of the second band population can only be obtained from a full simulation of the loading process, which is beyond the scope of this thesis.

Figure 2.23 shows a two-component mixture after band mapping out of the full 3d-lattice for two different fillings. The image is taken along x , in the plane of the triangular lattice. Thus, along the horizontal direction we observe the sharp edges of the Brillouin zone. Along the vertical direction the imaging process integrates over the hexagonal Brillouin zone of the triangular lattice, causing a rather peaked density distribution. For a filling of $8.5 \cdot 10^3$ atoms per spin component as in panel a), hardly any population of higher bands is observed. However, already for a filling of $18.5 \cdot 10^3$ atoms per spin component there is a significant population in higher bands. Since the higher band population distributes over several Brillouin zones, no sharp edges of individual higher zones can be observed.

The hexagonal shape of the first Brillouin zone of the triangular lattice is best observed with a six-component mixture in a 2D triangular lattice. A corresponding image is shown in fig. 2.24.

Also in this case, some higher band population is observed in correspondence with fig. 2.22. These measurements as well as the discussion of the loading process reveal that a band insulator in the lowest band can only be achieved in our current setup for rather low atoms numbers. As soon as the Fermi energy exceeds the recoil energy, higher bands are populated. For our parameters of $\bar{\omega} \approx 2\pi \cdot 90$ Hz and $E_r = 2$ kHz this happens already for an atom number of 1800 per spin component. In the measurements presented in this section, we observe significant higher band population in the 3D-lattice for atom numbers exceeding ~ 8000 per spin component. As in the case of the bosonic Mott-insulator, the problematic parameter here is the large mass of Yb. The ratio of the Fermi- and the recoil energy, which determines the number of atoms that can be loaded into the lowest band, is proportional to the product of mass and trapping frequency. In three dimensions:

$$\frac{E_F}{E_r} = \frac{\sqrt[3]{48N_{\text{at}}}}{\hbar k_L^2} \cdot m\bar{\omega} \quad (2.12)$$

Thus, at the same trapping frequency, a factor of two lower mass allows to load eight times more atoms into the lowest band. If we used e.g. ^{40}K in our experiment, we could load $150 \cdot 10^3$ atoms into the lowest band of our lattice instead of 1800. This once more stresses the need for very low trapping frequencies, when working with Yb in optical lattices.

3 Control of the Electronic State

In the introduction I argued that an important motivation to use ultracold Yb for the study of quantum many-body physics is the existence of the two long lived electronically excited states 3P_0 and 3P_2 . Due to the long lifetime of these states on the order of seconds, the electronic state can be used as a second internal degree of freedom in addition to the nuclear spin. This is an important difference to alkali elements, where the magnetic quantum number m_F of the ground-state spin F is the only internal degree of freedom. Using different electronic states is especially interesting, because the s-wave scattering length of an atom generally depends strongly on its electronic wavefunction as discussed in section 2.1. In contrast, the scattering lengths of the different hyperfine-states of alkali atoms differ only by a few percent. Thus, mixtures of ground- and metastable state Yb atoms may exhibit new interesting physics, which are not present in ultracold alkali quantum gases. Moreover, the polarizabilities of the ground and metastable electronic states of Yb are largely different, because they couple to different excited states (see section 2.2). This allows to achieve far off-resonant state-dependent optical lattices, which is again impossible with alkalis. I find two ideas particularly interesting that exploit these features of the electronic degree of freedom: The generation of homogeneous artificial magnetic fields for ultracold atoms in an optical lattice [30, 31], and the realization of the Kondo lattice Hamiltonian with ultracold atoms [24, 25, 81], which have briefly been described in the introduction. These proposals, however, depend strongly on the details of the elastic and inelastic interaction properties of the metastable states. While the interaction properties of the 3P_2 state have been determined for two bosonic isotopes from spectroscopy experiments in the Kyoto group [106], they were largely unknown for the 3P_0 -state when this work was performed. Thus, before being able to use the 3P_0 -state for the study of quantum many-body physics, the interaction properties of this state needed to be measured. The most direct way to measure the excited state interactions is to spectroscopically probe the interaction induced shift of the $^1S_0 \rightarrow ^3P_0$ transition in an optical lattice. In this chapter, I describe our efforts towards such spectroscopic measurements of the interaction properties of the 3P_0 -state. Section 3.1 describes the laser system used to drive the ultranarrow $^1S_0 \rightarrow ^3P_0$ transition. Sections 3.2 and 3.3 present our experiments on Rabi spectroscopy of single- and two-component quantum gases in a magic optical lattice. When finishing this manuscript, the Munich group published the first measurement of the 3P_0 -interaction of ^{173}Yb , using techniques similar to those described here [79]. The scattering lengths resulting from these measurements have already been discussed in section 2.1.

3.1 The 578nm Spectroscopy Lasersystem

In order to take full advantage of the possibilities that coherent control of the electronic state offers, a laser system of sufficient coherence time and power is indispensable. High power is necessary, in order to homogeneously excite an atomic ensemble that suffers from inhomogeneous broadening due to interactions or differential light shifts. Interactions of ultracold atoms in optical lattices are on the order of a few kHz. Thus, exciting atoms independent of their interacting environment requires Rabi frequencies of about 100kHz. With a Rabi frequency of $77\text{Hz} \cdot I / (\text{mW}/\text{cm}^2)$ for ^{173}Yb measured at NIST [107] and a beam diameter of $2w_0 = 200\mu\text{m}$, a power of 200mW is required. On the other hand, in order to selectively excite atoms dependent on the interaction with their environment or some externally applied field gradient, the laser should exhibit a large coherence time sufficient to resolve the respective line shifts. With the above assumption of interactions on the order of kHz, it seems reasonable to aim at a resolution of $\sim 100\text{Hz}$. However, obtaining high contrast Rabi oscillation at this resolution, requires a laser linewidth significantly below this resolution limit. Thus, a linewidth of $\sim 10\text{Hz}$ is desirable.

Fortunately, it is well known from the field of optical atomic clocks, how laser linewidths at the Hz-level can be achieved (see e.g. [108–111]). In all of these systems, linewidth narrowing is achieved by fast frequency stabilization to an ultrastable high finesse fabry-perot resonator. Directly stabilizing the free-running laser to the atomic transition of interest is not feasible, because the spectroscopy signals obtained from the necessarily narrow transitions in standard vapor cells are too weak to be detected with a good signal to noise ratio. If a fast stabilization loop with sufficient gain is realized, the laser noise is completely eliminated except for a noise pedestal 40 to 50dB below the carrier. The laser frequency stability is then solely determined by the stability of the reference cavity, being the decisive part of an ultrastable laser system. Therefore, I start by describing our ultrastable cavity setup as well as the laser we use in section 3.1.1. Section 3.1.2 explains the technical details of the stabilization loop. The stability we achieve with our system is evaluated in section 3.1.3.

3.1.1 Laser and Stabilization Cavity

As a laser source for the $^1S_0 \rightarrow ^3P_0$ transition of Yb at 578 nm we use an amplified frequency-doubled diode laser¹ at 1156 nm with a total output power of 300 mW. Let me briefly discuss the arguments for this choice. The only available scientific lasers directly emitting at 578 nm are dye lasers [111]. These are, however, experimentally rather inconvenient and are basically not used anymore. The second, preferable method to generate 578 nm light is to upconvert infrared lasers via second harmonic generation (SHG) or sum frequency generation (SFG) in a nonlinear crystal. Suitable infrared lasers are either diode lasers at 1156 nm, which can be frequency-doubled, or an Yb fiber laser at 1030 nm and an Nd:YAG laser at 1319 nm, which

¹Toptica DL-SHG pro

can be combined in SFG to reach 578 nm [107]. While the latter option profits from inherently lower frequency noise of the solid state lasers compared to diode lasers, the SFG is technically somewhat more complicated. For frequency doubling, the infrared light can easily be enhanced in a build-up cavity to boost the conversion efficiency. SFG, on the other hand, is usually done in a single pass through a crystal waveguide, resulting in significantly lower efficiencies. Of course, the total visible output power is still higher for the solid state laser SFG compared to the SHG power of a bare diode laser, because the infrared power to start with is a lot higher. However, since 2012 tapered amplifiers at 1156 nm have become available, allowing powers of > 300 mW at the doubled wavelength. Moreover, the two solid state lasers significantly exceed the price of a diode laser and a tapered amplifier. Thus, a frequency-doubled diode laser seems to be a good choice.

The second important component for the spectroscopy laser system is the reference cavity, used to stabilize the laser and narrow down its linewidth as far as possible. Since linewidths of < 1 Hz of state-of-the-art stable laser seems to be more than sufficient for our purposes, our team decided to simply buy the best commercially available cavity, rather than going for a home-built solution. The cavity we use has been developed in the group of John Hall in Boulder [109] and is commercially available from the company *Advanced Thin Films* for many years now. Its main feature is the vertical, midplane-mounted design. The high symmetry makes the cavity length robust against mechanical perturbations. Moreover, the cavity spacer as well as the mirror substrates are made of ULE, a glass that exhibits a zero crossing of the thermal expansion coefficient near room temperature. Apart from the cavity geometry and material one has to decide, whether the infrared or the frequency-doubled light is stabilized to the cavity and choose the mirror coatings correspondingly. In our team, it has been decided to use the 578 nm light for the stabilization. This provides the flexibility to change the laser source and use e.g. the SFG solution described above, if this proves useful at a later stage.

The cavity setup: Although the cavity is designed to be as robust as possible against external perturbations, it has to be extremely well shielded from mechanical and thermal fluctuations. Our cavity setup, realizing this shielding, has been designed by Thomas Rützel. It is based on the setup described in [108] and is in detail explained in his Diplomarbeit [112], which was supervised as part of this PhD thesis. Here, I will only present the most important features of the setup. A sketch and a photograph of the complete system is shown in fig. 3.1. The cavity is mounted vertically on three teflon rods fixed to a ring of Zerodur glass. It is situated inside of two heat shields made of gold-coated copper. This whole ensemble is placed inside a home-built stainless steel vacuum chamber, which is held at a pressure of a few times 10^{-7} mbar. All the materials have been carefully selected to minimize the thermal coupling between the cavity, the heat shields and the vacuum chamber. The outer heat shield is sitting on a ring-shaped thermoelectric cooler (TEC) that is used for active temperature stabilization. The vacuum chamber together with the optical setup for the frequency stabilization is mounted on a breadboard that is placed on a passive vibration isolation system². The whole setup rests on a standard optical table and is surrounded by a box shielded with acoustic insulation foam.

²MinusK 150BM-1

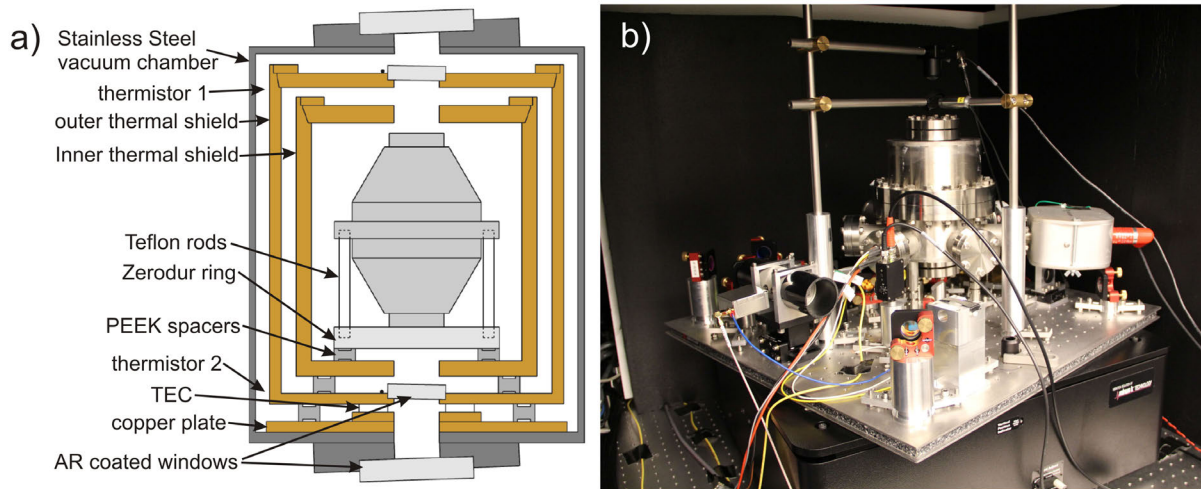


Figure 3.1: Panel a) schematically depicts the mounting of the ultra stable cavity in the vacuum chamber. Held at its midplane, the ULE cavity is supported by three rods made of Teflon. The Teflon rods are mounted in a Zerodur ring that is fixed to the inner thermal shield. Three PEEK spacers between the Zerodur ring and the thermal shield minimize the thermal contact. Spacers of the same kind are used to insulate the two thermal shields from each other. For active temperature control the outer shield is directly placed on a TEC, using low outgassing thermal paste to maximize the heat conductance. Two thermistors on the top and the bottom of the thermal shield are used for temperature sensing. For optimal thermal contact between the bottom of the TEC and the vacuum chamber, a large copper plate is installed in between. Panel b) shows a photo of the whole cavity assembly.

Temperature control: Active temperature control of the cavity is necessary for two reasons. First, thermal drifts that determine the longterm frequency stability of the cavity need to be canceled. Second, the cavity temperature needs to be tuned away from room temperature in order to reach the zero crossing of the thermal expansion coefficient. We have chosen to actively control the temperature of the outer copper heat shield for two reasons. First, we can cool the heat shield to temperatures far below room temperature without suffering from water condensation, because the shield is in vacuum. Second, we have the inner heat shield as a passive insulation layer to damp residual temperature fluctuations that cannot be eliminated by the temperature servo. As temperature sensors, we use two $10\text{ k}\Omega$ -thermistors placed at the top and the bottom of the outer heat shield. The temperature controller measures their series resistance, which is apart from small imperfections a measure of the mean temperature of the shield. This is important, because the TEC, being the heat sink/source, is situated on the bottom of the shield. When the TEC heats or cools, heat flows to the bottom of the shield and leads to a vertical temperature gradient, due to its finite thermal resistance. Consequently, if only one sensor at the top or at the bottom of the shield is used, this gradient causes the average temperature of the shield to vary as the cooling power of the TEC changes. And since the thermalization between the heat shields is much slower than within each individual shield, the inner shield will follow the average temperature of the outer shield. This effect becomes more pronounced as the set temperature is tuned away from room temperature and the required cooling power increases. The controller used for the temperature stabilization is a home-built proportional-integral-controller.

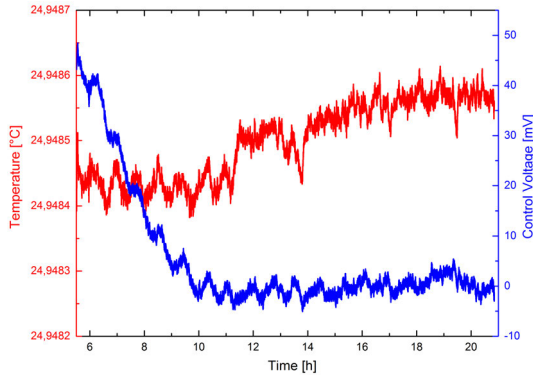


Figure 3.2: 24 hour trace of the temperature of the self stabilized temperature control circuit. The temperature, shown in red, is measured with a 10 k Ω thermistor connected to a precision multi-meter. The peak to peak temperature variation is below 200 μ K over the whole measurement cycle. The blue curve depicts the control voltage, which is proportional to the TEC drive current.

The circuit is in large part taken from ref. [113]. For the pc-board layout I have taken special care to minimize thermoelectric voltages, leading to variations of the temperature setpoint and errors in the measured temperature. Still, the controller is temperature-stabilized itself by a second identical circuit on the same board, to reduce thermoelectric voltages to a minimum. Before implementing the controller at the cavity setup it was evaluated by monitoring the temperature of the pc-board with an extra thermistor connected to a precision multimeter, while the temperature stabilization of the board was active. The temperature measured with the separate thermistor was stable to better than 200 μ K over 24 hours as shown in fig. 3.2.

The high-finesse mirrors: The relevant characteristics of the cavity mirrors are the finesse, which is a measure of the mirror reflectivity, and the cavity transmission, which is a measure of the mirror's losses. The cavity finesse is measured via the decay of the intracavity field: Light is coupled into the cavity after passing through an AOM. A photodetector behind the cavity output mirror monitors the transmission, which is proportional to the intracavity intensity. The laser frequency is then tuned near the cavity resonance such that from time to time, light is coupled into the cavity mode and is detected on the transmission photodetector. As soon as the detected transmission rises above a certain threshold, the AOM is switched off and no more light is coupled into the cavity. Once the incoming light has been switched off, the exponential decay of the intracavity field is measured by the transmission photodetector. This kind of measurement is often referred to as cavity ringdown measurement. The decay signal observed with our cavity is shown in fig. 3.3 a). From the time constant of the exponential decay, the cavity finesse \mathcal{F} is calculated via [114]

$$\mathcal{F} = \frac{c\pi}{L} \cdot \tau, \quad (3.1)$$

where L is the cavity length (in our case 7.75 cm), c is the speed of light and τ is the $1/e$ -decay time of the intracavity intensity. The measured decay time of 12.2 μ s corresponds to a finesse of $\mathcal{F} = 148120$ and a full width at half maximum (FWHM) of the cavity resonance of $\Delta\nu_{\text{FWHM}} = 13.03$ kHz. This was verified by locking the laser to a second high finesse cavity as described in section 3.1.2 and monitoring the transmission while slowly scanning the locked laser across the cavity resonance. This direct linewidth measurement is shown in fig. 3.3 b). The measured linewidth of 13.13 kHz agrees well with the ringdown measurement. The measurements shown in fig. 3.3 were performed a few days after evacuating the cavity

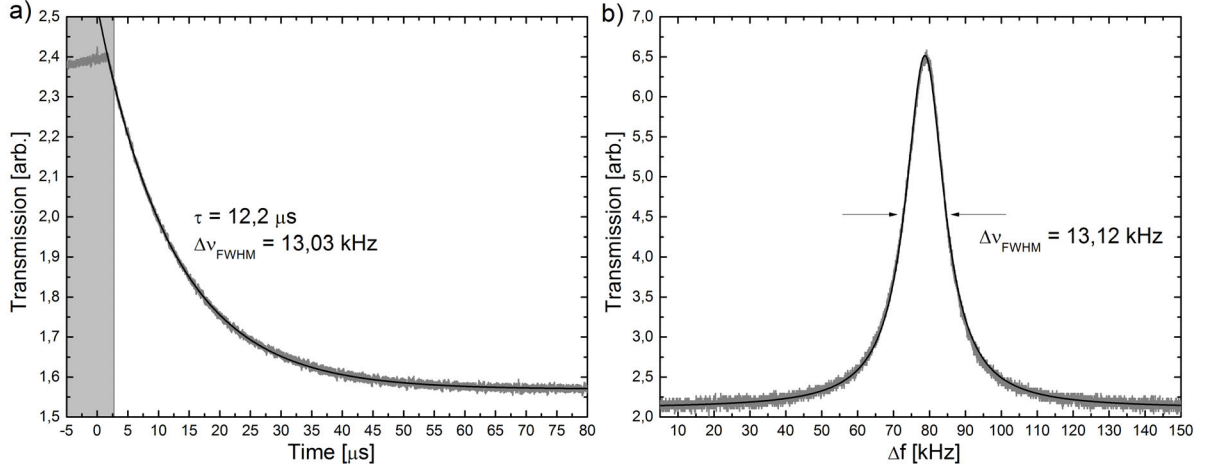


Figure 3.3: Panel a) depicts the decay of the cavity transmission after coupling light into the cavity and suddenly switching off the input light. The exponential fit yields a decay constant of $\tau = 12.2 \mu\text{s}$ corresponding to cavity linewidth $\Delta\nu_{\text{FWHM}} = 13.03 \text{ kHz}$. The shaded region has been excluded from the fit, in order to be insensitive to the switching characteristics. The 3 dB-bandwidth of the detector is 20 MHz. In panel b) the cavity transmission is plotted as the laser is scanned across the resonance. The laser has been locked to a second ULE cavity, to make the linewidth sufficiently narrow. The observed FWHM agrees well with that extracted from the ringdown measurement.

chamber. After some time in the vacuum, the finesse slightly increased resulting in a narrower linewidth of 12.09 kHz (cf. fig. 3.6).

In order to determine the mirror losses, the transmission and reflection coefficients of the cavity were measured for the locked laser on resonance with a power meter, resulting in

$$\mathcal{T} = P_{\text{T}}/P_{\text{in}} = (19 \pm 1) \% ; \quad \mathcal{R} = P_{\text{R}}/P_{\text{in}} = (39 \pm 2) \% \quad (3.2)$$

Here, P_{in} is the power sent to the cavity. P_{R} and P_{T} denote the reflected and transmitted power, respectively. From these numbers together with the finesse one can calculate the mirror transmission and loss coefficients T and A , as well as the mode-matching coefficient ϵ via simple formulas derived in [115]:

$$\alpha = \frac{\mathcal{T}}{1 - \mathcal{R}} = 0.31 \pm 0.02 \quad (3.3)$$

$$T = \frac{\pi}{\mathcal{F}} \frac{2\alpha}{1 + \alpha} = (10.1 \pm 0.5) \text{ ppm} \quad (3.4)$$

$$A = \frac{\pi}{\mathcal{F}} \frac{1 - \alpha}{1 + \alpha} = (11.1 \pm 0.5) \text{ ppm} \quad (3.5)$$

$$\epsilon = \mathcal{T} \left(\frac{T + A}{T} \right)^2 = (84 \pm 7) \% \quad (3.6)$$

These calculations rely on the assumption that the two mirrors are identical. Differences between the mirrors cannot be deduced from the cavity properties. Equation (3.2) implies that

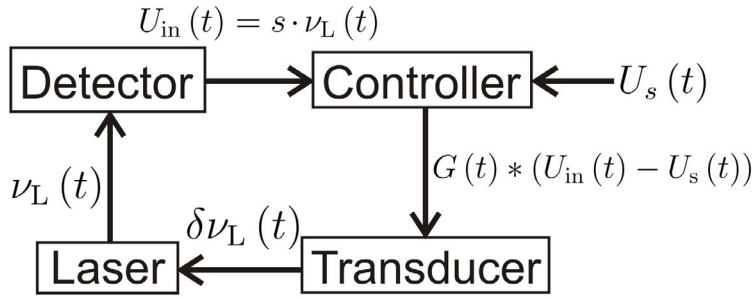


Figure 3.4: Schematic layout of a laser frequency stabilization loop. A frequency detector produces a voltage $U_{in}(t)$ proportional to the laser frequency. This voltage is filtered and amplified by an electronic control circuit and fed to a transducer, which affects a change in the laser frequency.

$1 - \mathcal{T} - \mathcal{R} = 42\%$ of the power incident on the cavity is absorbed by the cavity mirrors. This absorption loss heats the mirror coatings and thereby shifts the resonance frequency. The importance of this effect will be discussed in section 3.1.3. The excellent mode matching of more than 80% is important in order to minimize the laser shot noise, which is the dominant noise source in our Pound-Drever-Hall detector as described in the following section.

3.1.2 Linewidth Narrowing via a Fast Pound-Drever-Hall Lock

While frequency stabilization setups belong to the standard tools in almost every atomic physics lab, the requirements on frequency stability are usually quite moderate. Laser cooling of atoms, as well as imaging, is typically done on transitions that are a few hundred kHz to several MHz wide. A frequency stability of a few percent of these linewidths works well for most experiments. Thus, the inherent short term stability of typical diode lasers of a few hundred kHz is usually sufficient and frequency stabilization loops only need to compensate slow drifts of the laser frequency. If, however, the laser linewidth is to be reduced to the Hz-level, the demands on gain and bandwidth of the control loop become much higher and one has to worry about details that most of the time do not matter.

Before presenting the actual implementation of the linewidth narrowing loop, I will try to clarify the requirements the setup has to meet to reduce the laser linewidth to the Hz-level. These requirements concern three quantities: The detector's frequency resolution, the low frequency gain of the controller and the bandwidth of the control loop.

The basic layout of a laser frequency control loop is shown in fig. 3.4. A frequency detector generates a voltage proportional to the laser frequency $U_{in}(t) = s \cdot \nu_L(t)$, where s is the sensitivity of the detector. This voltage is then compared to some set value $U_s(t)$. The deviation from the set value is filtered and amplified by the controller before being fed to a transducer affecting a change of the laser frequency, which in turn leads to a change in the detector voltage $U_{in}(t + dt)$. The Fourier transform of $U_{in}(t)$ per square root of unit bandwidth is called the noise spectral density of $U_{in}(t)$, which has units $V/\sqrt{\text{Hz}}$ and is denoted as $\rho_U(\nu)$. Multiplying $\rho_U(\nu)$ by the detector slope s , one finds the frequency noise spectral density of the laser in units $\text{Hz}/\sqrt{\text{Hz}}$:

$$\rho_\nu(\nu) = s \cdot \rho_U(\nu) = s \cdot \mathfrak{F}(U_{in}(t)) \quad (3.7)$$

The frequency noise spectral density, being immediately linked to the signals in a frequency

control loop, seems to be a good quantity to analyze such a control loop. In everyday lab work, however, one often thinks in terms of the linewidth of a laser, which is strictly speaking the width of the power spectral density (PSD) of the lasers electric field. PSD and noise spectral density are related via [116]:

$$\text{PSD}_E(\nu) = 2E_0^2 \int_{-\infty}^{\infty} e^{i2\pi(\nu_0-\nu)\tau} \exp\left(-2 \cdot \int_0^{\infty} |\rho_\nu(f)|^2 \frac{\sin^2(\pi f \tau)}{f^2} df\right) d\tau \quad (3.8)$$

This rather non-trivial dependence underlines that the linewidth is indeed not a very practical measure of laser frequency noise. In fact, since the PSD contains the integral over the whole noise spectrum, it can hardly be used to extract information about the spectral composition of the laser noise. Still, it is the PSD and thus the linewidth that eventually determines the resolution in a spectroscopy experiment. An intuitive connection between the two quantities can be made by evaluating eq. (3.8) for a flat noise density $\rho_\nu(\nu) = \rho_0$. For this special case one finds a Lorentzian power spectral density with a FWHM of

$$\Delta\nu = \pi \cdot |\rho_0|^2. \quad (3.9)$$

In order to achieve a Lorentzian linewidth of $\Delta\nu = 1$ Hz, the noise density of the laser would thus need to be reduced below $\rho_{1\text{Hz}} = 0.56 \text{ Hz}/\sqrt{\text{Hz}}$ across the whole spectrum. Due to the finite bandwidth of the feedback loop, this is of course impossible. The general shape of a realistic noise spectrum of a locked laser is depicted by the blue line in fig. 3.5 a). At low Fourier frequencies the noise is reduced to the detector noise level, if a sufficiently high gain is achieved. Towards higher Fourier frequencies the loop gain decreases. Consequently, the noise increases and reaches that of the free-running laser a little above the control bandwidth.

Ref. [116] analyzes the PSD, belonging to such a noise density that is truncated at low frequencies: The authors show that the noise density can be divided into two regions that affect the power spectral density in qualitatively different ways: In the first region, above the dashed green line in fig. 3.5, the noise amplitude is higher than the noise frequency. In other words, the modulation index of the noise is > 1 . The noise in this region contributes to the central part around the carrier of the PSD. In the region below the green line, the noise frequency is larger than the noise amplitude and the modulation index is thus < 1 . Noise in this region only contributes to the wings of the power spectral density, leaving the central part unchanged. Accordingly, a truncated noise density as shown in fig. 3.5 a) results in a narrow central carrier with a linewidth determined by the low-frequency noise level and small additional peaks at some distance from the carrier, stemming from the unaltered high-frequency part of the noise density. This is schematically shown in fig. 3.5 b). If these side peaks are far enough from the carrier as to not interfere with the spectral features that are to be addressed with the laser, they can be neglected.

With this understanding it is now possible to quantify the requirements for achieving a 1Hz-linewidth of the locked laser. Since the linewidth is determined by the low frequency noise level, which for high enough gain is limited by the detector noise, the maximum allowable detector noise ρ_{det} is directly given by the white noise level from eq. (3.9) corresponding to the

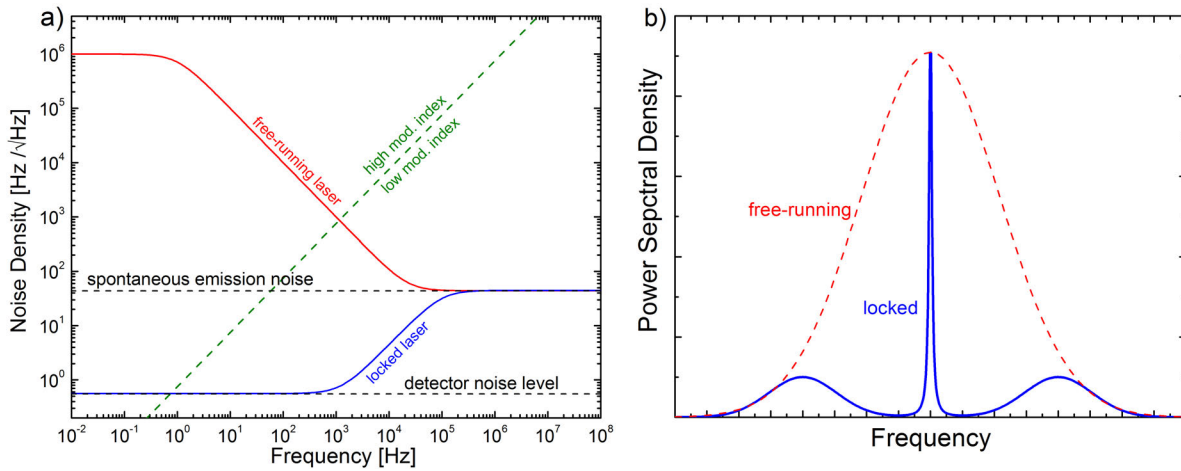


Figure 3.5: a) Schematic plot of the noise density of a free-running (red solid line) and locked (blue solid line) diode laser. The green dashed line separates regions of high and low modulation index of the noise according to ref. [116]. b) Schematic plot of the power spectral densities of a free-running (dashed red line) and locked (solid blue line) laser. The technical low frequency noise of the free-running laser results in a broad gaussian power spectral density. The frequency lock suppresses the low frequency noise ideally down to the detector noise level ρ_{det} , leading to a narrow central carrier in the power spectral density. The unsuppressed high frequency noise appears in the power spectral density as small side peaks.

desired linewidth. For a linewidth of 1 Hz this amounts to $0.56 \text{ Hz}/\sqrt{\text{Hz}}$ as stated above. To understand how much gain is needed in the control loop, the noise density of the free-running laser has to be analyzed. It is schematically depicted by the red line in fig. 3.5 a) and is composed of two contributions: First, the noise due to spontaneous emission that is fundamentally connected to the lasing process and leads to the Schawlow-Townes linewidth limit [117]. It has a flat frequency spectrum and for typical external cavity diode lasers (ECDL) is on the order of a few tens of $\text{Hz}/\sqrt{\text{Hz}}$ corresponding to a Lorentzian Schawlow-Townes linewidth of a few kHz. The second, more important contribution is technical noise, which dominates at low Fourier frequencies. The most relevant technical noise sources are fluctuations of the laser diode pump current, acoustic and mechanical vibrations, as well as temperature fluctuations. The spectral density of the technical noise typically increases strongly towards lower Fourier frequencies and can easily reach levels of up to $1 \text{ MHz}/\sqrt{\text{Hz}}$ as shown in fig. 3.5 a). Reducing this noise below the $0.56 \text{ Hz}/\sqrt{\text{Hz}}$ needed for a 1 Hz-linewidth, thus requires a loop gain of more than 120 dB. This demand on the gain also puts a lower limit on the required control loop bandwidth. The maximum possible servo bandwidth is determined by the phase of the loop transfer function. At some Fourier frequency this phase reaches -180° , making the loop unstable if the gain at this frequency is larger than unity. Thus, the gain has to be reduced from about 120 dB at 1 Hz to 0 dB before the phase reaches -180° . This cannot be done arbitrarily fast, because a n th order low pass reducing the gain by $n \cdot 20 \text{ dB/decade}$ also introduces a phase lag of $-n \cdot 90^\circ$ into the transfer function. Conservatively assuming a first order low pass characteristic for the loop filter a loop gain of 120 dB at 1 Hz can be reduced to 0 dB at 1 MHz. Thus, a control bandwidth of

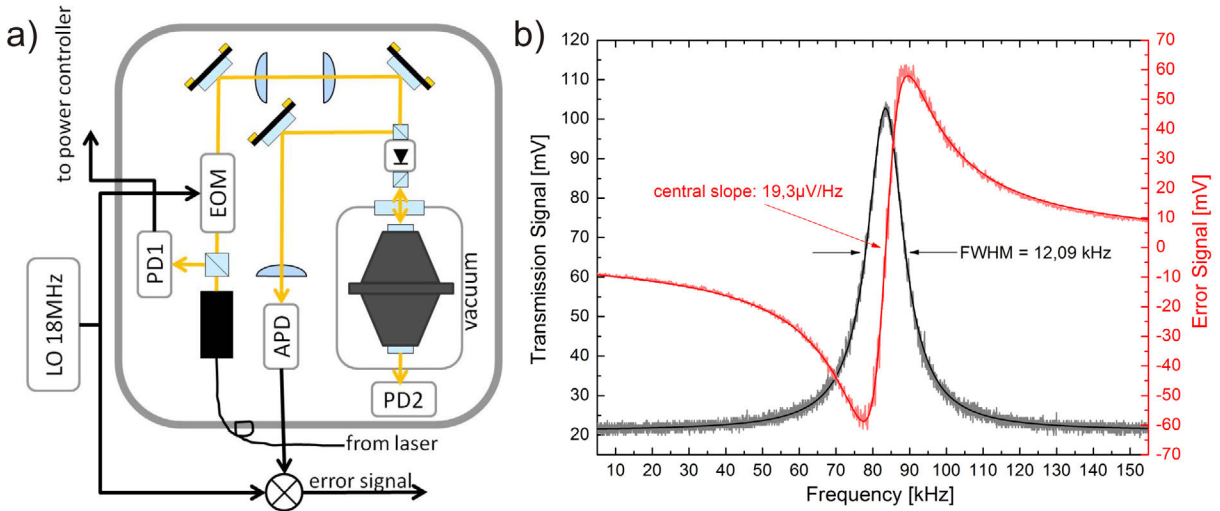


Figure 3.6: a): Sketch of the PDH setup. A few tens of μW of probe light are brought to the setup via an optical fiber. 50% of this light is split off by a non-polarizing beam splitter and directed to the photodiode PD1 used for active stabilization of the probe power. The other half of the light is phase modulated at 18 MHz by the electro optic modulator (EOM) after passing through a high quality glan-polarizer for polarization cleaning. The spatial mode of the beam is matched to the cavity with three lenses. An optical isolator is used to separate the reflected from the incoming light and reduce etaloning between the cavity and the various optical elements. The light reflected from the cavity is detected with a fast, low noise avalanche photodiode (APD). The error signal is then obtained by mixing the APD signal with the local oscillator (LO) driving the EOM. The light transmitted through the cavity is monitored by the photodiode PD2. b): Measured error- and transmission signals of the PDH detector. The error signal is shown in light red together with a fit of the ideal PDH signal shape in deep red. The transmission signal plotted in gray exhibits a perfect Lorentzian shape with a FWHM of 12.09 kHz. The black line is a Lorentzian fit to the transmission signal. Note that the linewidth in this measurement, performed after the cavity had been under vacuum for some weeks, is slightly lower than that in fig. 3.3, measured right after evacuation of the cavity chamber.

roughly 1 MHz will be necessary to reach the high gain, required for the narrow linewidth. It is interesting to compare this bandwidth estimate to the intersection of the modulation index separation line with the noise density of the free-running laser in fig. 3.5 a), which occurs already at ~ 1 kHz. According to the model from ref. [116] it would suffice to eliminate the noise below this intersection point. Thus, the control bandwidth is in fact determined by the required gain at low frequencies rather than by the bandwidth of the noise that must be eliminated. This implies that the bandwidth requirements can be relaxed, if the technical laser noise at low frequencies is reduced leading to a lower required gain.

Having clarified the requirements on the frequency control loop, I will now describe the three main components of the loop: The detector, the controller and the transducer. As already mentioned above, we detect the laser-cavity frequency difference by means of the Pound-Drever-Hall (PDH) technique, which has been described in great detail in many publications, e.g. [118, 119]. It can be summarized as follows: The light sent to the cavity is phase modulated at some RF-frequency ω_m , resulting in two symmetric sidebands in the frequency spectrum of

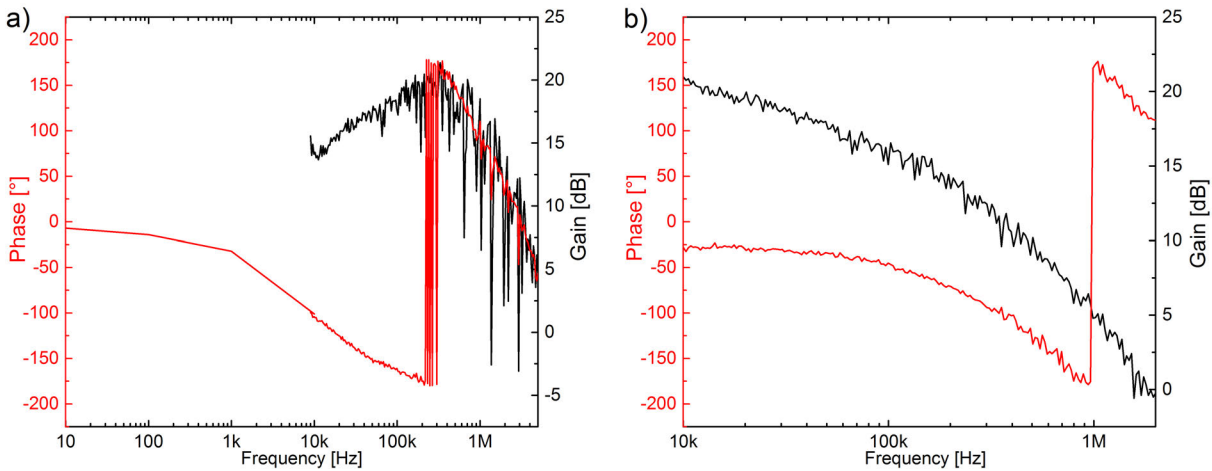


Figure 3.7: Current-FM transfer function of the 1156nm laser diodes of the 578nm laser system. The initially installed diode shown in panel a) exhibits a strong roll-off of the phase already in the low kHz-range, accompanied by an increasing FM gain. This transfer function makes frequency feedback via the injection current nearly impossible. The replaced diode shown in panel b) displays a better current-FM behavior. The phase rolls off in the high kHz-range and at the same time the gain decreases. With this diode a loop bandwidth of 300 kHz has been achieved.

the light. Near a cavity resonance, the light reflected off the cavity experiences a frequency-dependent phase shift, resulting in a phase difference between the carrier and the sidebands. In the time domain, this phase shift appears as an amplitude modulation of the reflected light at the frequency ω_m , which is detected with a suitable photodetector. Mixing the detected signal at the right phase with the RF-source used for the initial modulation results in a DC output voltage that near resonance depends linearly on the frequency difference between the light field and the cavity resonance. The details of our PDH setup are depicted in fig. 3.6 a). Its key components apart from the cavity are the electro-optic modulator (EOM), the Faraday isolator and the PDH photodetector. The EOM³ uses two brewster-cut electro optic crystals to minimize birefringence induced polarization modulation and the resulting unwanted residual amplitude modulation (see below). The Faraday isolator minimizes etaloning between the cavity input mirror and the photodetector as well as the other optical elements. Again this is important to minimize residual amplitude modulation of the probe light. The photodetector's bandwidth and noise have been chosen such that neither limit the performance of the PDH lock. We use a custom made avalanche photo diode⁴ (APD) with a 3 dB bandwidth of 80 MHz, a gain of 100 mV/ μ W and a noise density of < 0.5 pW/ $\sqrt{\text{Hz}}$ corresponding to the shot noise of 0.8 μ W. The error signal, obtained with this setup is shown in fig. 3.6 b). It exhibits the dispersive shape typical of an error signal obtained from a resonance. On resonance it has a linear slope of $s = 19.3$ μ V/Hz, which is the detector sensitivity.

The transducer used for the frequency feedback turned out to be the difficult part in our sys-

³LINOS PM-25

⁴FEMTO Messtechnik

tem. Using a diode laser, the idea in the beginning had been to use the diode pump current for fast frequency changes, which is commonly done in diode laser locking setups. However, the current-to-frequency modulation (current-FM) response of laser diodes differs strongly between different types of diodes. The current-FM transfer function of the diode initially built into our SHG system is shown in fig. 3.7 a). For modulation frequencies above 10 kHz the measurement was done with a network analyzer as follows: The laser was weakly locked to a Fabry-Perot resonator with a 1 MHz linewidth via the ECDL piezo in a slow feedback loop with a servo bandwidth of ~ 100 Hz. Thereby the laser is loosely held on the central slope of the PDH error signal. This error signal is then fed to the network analyzer which measures the frequency response of the laser to a fast current modulation. Due to the low locking bandwidth, the fast frequency modulation is unaffected by the lock. For lower frequencies, where the network analyzer cannot be used, the laser was not locked to the cavity. Instead, the laser was modulated with an amplitude of 2 to 3 linewidths around the cavity resonance and the phase-shift of the cavity transmission signal with respect to the modulation signal was measured. The obtained transfer function shows that a stable servo loop using current feedback is hardly possible with this diode. The phase of the transfer function already starts to roll off at about 1 kHz reaching -90° at 10 kHz. At the same time the gain increases up to a peak at about 200 kHz. Thus, the requirement of a gain below unity as the phase exceeds -180° can hardly be met.

The unfortunate behavior of this diode's transfer function can be explained by the interplay of temperature and charge carrier density modulation in the diode as described in ref. [120]. When the current through the laser diode changes, also the density of the charge carriers in the laser diode changes. The charge carrier density influences the index of refraction in the laser diode and thus the laser frequency. The transfer function of this carrier induced frequency modulation is approximately flat up to modulation frequencies of ~ 1 GHz, which is far beyond the requirements of laser locking. However, at low frequencies the current modulation also affects the temperature of the diode, which leads to a change in the laser cavity length and thus to a frequency change. At low frequencies the two effects have opposite sign: An increase in current causes a temperature increase, leading to a decrease in frequency. In contrast, an increased carrier density, corresponding to an increase in current, causes a decrease of the refractive index leading to a frequency increase. Thus, the two effects partly cancel each other at low frequencies when they are of similar size. This seems to be the case in our laser diode. At low frequencies, thermal FM dominates and the phase of the transfer function is zero. As the modulation frequency increases, the thermal FM falls off, leading to an increase of the gain, because thermal FM no longer cancels carrier-FM. Simultaneously, the phase changes from 0 to -180° , because the dominating effect changes from thermal to carrier-FM.

In 2012 the company that built our diode laser system was able to offer us a different diode, with a much more well behaved current-FM transfer function, shown in fig. 3.7 b). As the phase rolls off at high frequencies also the FM gain decreases, which allows to achieve a stable feedback loop with this diode. However, the phase reaches -180° already at 1 MHz, such that only a control bandwidth of 300 kHz could be achieved with this diode in our setup. This bandwidth was just enough to achieve stable locking of the laser, but the lock was very sensitive to small changes of the loop gain. Therefore, also this second diode did not seem suitable for a reliable

operation of the stabilization loop. Apart from current modulation there are two other possibilities to achieve fast frequency feedback with an ECDL: An EOM inside the external cavity, or an AOM behind the laser. The intra-cavity EOM would probably have been the ideal solution. In [110] a servo bandwidth of 3 MHz has been achieved with this technique. However, implementing the EOM into the laser would have required building a new ECDL, which seemed much more complicated than simply inserting an additional AOM into the setup. Therefore, I decided to implement a fast AOM as frequency transducer. The feedback bandwidth that can be achieved with an AOM is determined by the delay, the radio frequency wave experiences when travelling from the bonded electrodes through the transducer and the acousto optic crystal to the position of the laser beam. The sound velocity in TeO_2 crystals used in most modulators is 4200 m/s. Thus, already a distance of 1 mm between the transducer and the laser beam causes a delay of 235 ns, equivalent to the delay of 47 m of RG58 coaxial cable. In order to keep this delay as small as possible, we use a modulator designed for a small beam waist⁵ of $2w_0 = 80 \mu\text{m}$. Moreover, mounting the AOM on a translation stage, we transversely position the modulator such that the distance between the transducer and the laser beam is minimized. A sharp cutoff of the diffraction efficiency can be observed when getting too close to the transducer. The AOM position is adjusted right to this cutoff point.

In order to fully exploit the delay limited bandwidth of the AOM it is important that the modulation bandwidth of the RF-source driving the AOM is much larger than the desired loop bandwidth. We use a voltage-controlled oscillator⁶ (VCO) with a specified modulation bandwidth of 50 MHz. The control input is driven with a fast op-amp⁷, resulting in a measured 3dB FM-bandwidth of 30 MHz. Using the AOM as frequency transducer in the feedback loop, a servo bandwidth of nearly 1 MHz is achieved, about three times above the bandwidth reached with current feedback to the second laser diode.

The last component to be discussed is the electronic control circuit, used for properly filtering and amplifying the error signal. We use a commercial circuit⁸ that is based on a controller developed at MPQ in Munich [108]. It consists of two independent amplifier branches. A fast branch with a bandwidth of up to 10 MHz and a maximum gain of 80 dB, meant to drive a fast transducer, i.e. the AOM in our case. A slow branch with a DC-gain of 120 dB is connected to the piezo of the ECDL. The piezo has a much higher voltage-to-frequency conversion gain and frequency adjustment range than the AOM. Thus, with the slow branch connected to the piezo the low frequency gain can be boosted and longterm drifts of the laser over hundreds of MHz can be compensated without the laser falling out of lock. The fast branch features several lead and lag filters, whose corner frequencies can be adjusted in discrete steps to obtain the desired transfer function.

For the optimization of the control parameters, a small portion of the PDH photodetector signal is split off and analyzed with a spectrum analyzer. Figure 3.8 a) shows the obtained signal, which is the PDH error signal before being mixed with the local oscillator. The carrier at the

⁵Crystal Technology 3200-121

⁶minicircuits ROS-244+

⁷THS-4011

⁸Toptica FALC110

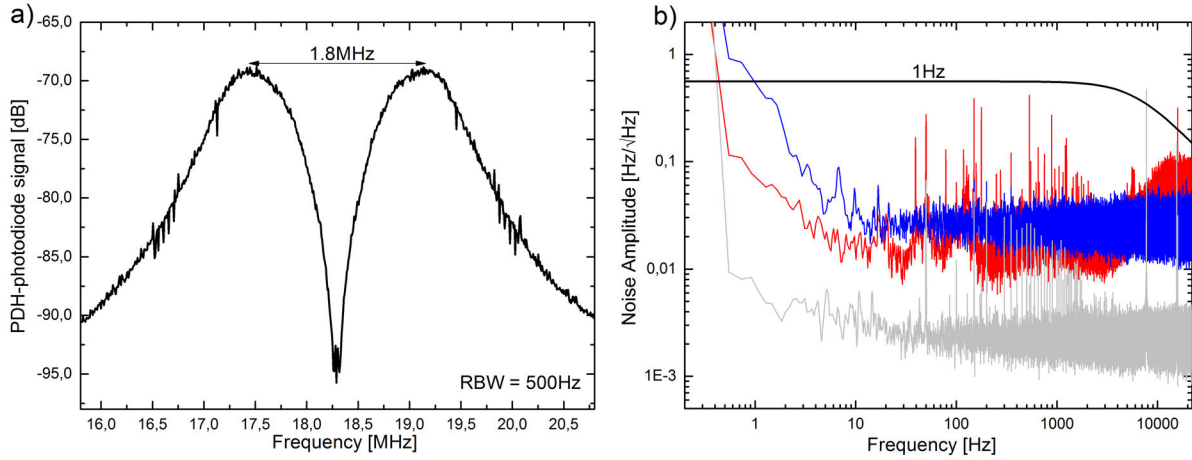


Figure 3.8: Panel a) depicts the power spectral density of the PDH photodetector signal, when the laser is locked to the cavity. This corresponds to the PDH error signal shifted to the PDH modulation frequency $\omega_m = 18.2$ MHz. The carrier at ω_m is suppressed when the laser is on resonance. The servo bumps are separated by 1.8 MHz, indicating a servo bandwidth of 900 kHz. Panel b) depicts the actual PDH error signal, as observed at the intermediate frequency output of the mixer. It has been converted to a frequency noise density by multiplying with the detector sensitivity s . The solid black line marks the white noise level corresponding to Lorentzian linewidth of 1 Hz. The gray signal is the detector noise without any light incident on the cavity (dark noise). The blue signal is the detector noise with light sent to the cavity, but tuned away from resonance (bright noise). This bright noise being significantly above the dark noise indicates that the detector noise is limited by the shot noise of the light. The red signal is the error signal measured when the laser is locked to the cavity. It lies well below the 1 Hz threshold.

PDH modulation frequency of 18.2 MHz is strongly suppressed when the laser is on resonance with the cavity. The setpoint of the controller is adjusted such that the carrier amplitude is minimized. Away from the carrier the detected frequency noise increases due to the phase delay and the decreasing gain in the feedback loop. These noise peaks are referred to as servo bumps and have their maximum approximately at the servo bandwidth. Figure 3.8 thus indicates a servo bandwidth of 900 kHz. The loop filter parameters are adjusted for minimum noise near the carrier and a well behaved roll-off of the servo bumps at high frequencies. The overall gain is set well below the oscillation threshold. A maximum bandwidth of 1.1 MHz could be achieved. However, for these settings the noise level at low frequencies was significantly higher than for the settings used in fig. 3.8 a). Therefore, the slightly lower bandwidth settings seem to be preferable.

An estimate of the full Bode plot of the control loop transfer function is shown in fig. 3.9 a) and b). The transfer function of the fast branch is given by the product of the transfer functions of the individual filter stages in the control circuit and the transfer function of the PDH detector. The transfer functions of the control circuit filter stages have been plotted according to their specifications, which have been checked with the help of a network analyzer. The transfer function of the PDH detector has been taken to be a first order low pass with a corner frequency of half the cavity linewidth. The overall gain of the fast branch has been scaled such that at the measured servo bandwidth of 900 kHz it reaches the 0 dB threshold. The voltage-frequency

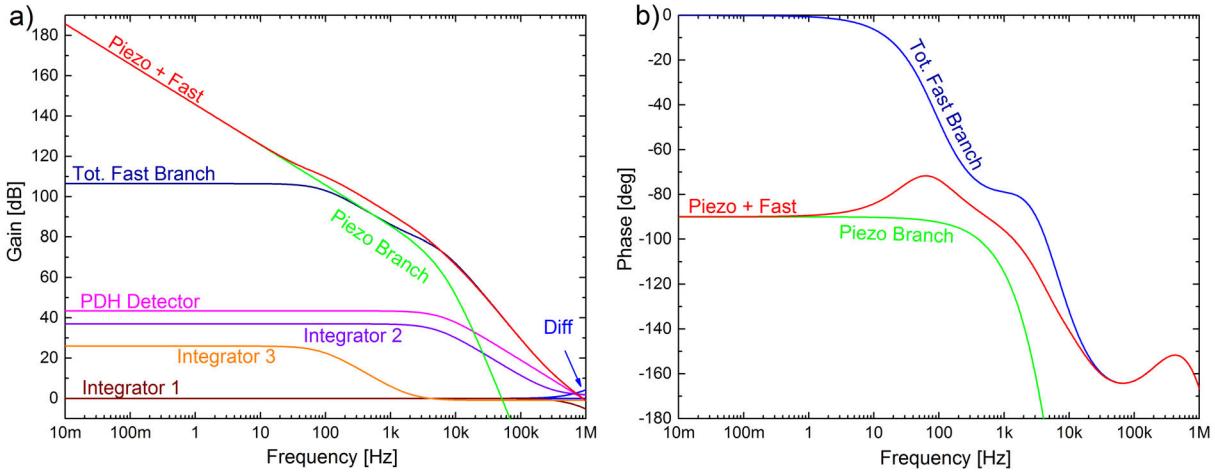


Figure 3.9: Schematic Bode diagram of the frequency stabilization feedback loop. Panel a) depicts the gain, panel b) the phase. The transfer function of the fast branch is the product of the transfer functions of the individual filter stages in the control circuit (Integrators 1-3 and a differentiator (Diff.)) and the transfer function of the PDH detector. The total transfer function is the sum of the fast branch and the piezo branch. See main text for detailed explanations.

conversion gain of the VCO and the PDH detector has been included into the PDH detector gain. For calculating the transfer function of the AOM, I assumed that the step response of the diffracted light frequency to a sudden change of the drive frequency is given by a delayed error function $\text{erf}(t - t_d)$. From this step response, the transfer function is obtained via a Laplace transformation. For a waist of $w_0 = 45 \mu\text{m}$ the resulting -3 dB bandwidth is 25 MHz. The loop bandwidth is of course limited by the delay t_d in the AOM step response, which was adjusted such that the phase of the total loop transfer function reaches -180° at 1.3 MHz, which corresponds to the measured oscillation frequency of the feedback loop. The resulting value for the delay is $t_d = 100 \text{ ns}$. Using the sound velocity of the TeO_2 crystal, this would correspond to a delay line of $426 \mu\text{m}$. However, by inspection it can be seen that the beam is much closer to the edge of the crystal. Thus, I conclude that the delay mainly occurs in the AOM transducer. This transducer is even a little thicker than $426 \mu\text{m}$, but the sound velocity is presumably larger than in the crystal. The phase lag due to the AOM at the measured oscillation frequency of 1.3 MHz is -47° . Apart from the AOM delay also the delay of 3.5 m of cable and 2 m of free space beam line has been included in the phase of the transfer function. For the piezo branch the overall gain was calculated from the voltage-to-frequency conversion gains of the piezo and the PDH detector, which were measured independently, and the specified voltage gain of the electronics. A mechanical resonance of the piezo is expected somewhere between 1.5 kHz – 4 kHz, which is not included in this Bode plot.

In the low frequency regime below 100 Hz the piezo branch dominates the loop gain. At intermediate frequencies between 100 Hz and 10 kHz, both the piezo- and the fast branch are relevant. Above 10 kHz the piezo gain drops quickly and the fast branch takes over up to the servo bandwidth of 900 kHz. Note that the piezo feedback branch alone is not stable at this high

gain. Only the fast branch taking over with enough phase margin at high frequencies stabilized the loop.

In order to characterize the lock, the noise density of the PDH error signal in the closed feedback loop is analyzed as shown in fig. 3.8 b). It has been converted to frequency noise density by multiplying with the detector slope s . The white noise, corresponding to a 1 Hz-linewidth according to eq. (3.9) seen through the 6 kHz low pass of our PDH detector is plotted as a black line. The detector noise, plotted in blue, is measured with the laser out of lock and far away from the cavity resonance. For Fourier frequencies above 10 Hz it is limited by the laser intensity noise around the PDH modulation frequency of 18.2 MHz. It has been checked independently that the laser intensity is shot noise limited at this high frequency. This flat noise level is far below the 1 Hz white noise, showing that the detector resolution is sufficient to achieve a laser linewidth below 1 Hz. The electronic dark noise, shown in gray, lies well below the shot noise and can thus be neglected. For Fourier frequencies below 10 Hz, the detector noise rises above the shot noise level. We attribute this to residual amplitude modulation at the PDH modulation frequency. The in-loop noise, shown in red, lies below the 1 Hz-threshold between 0.5 Hz and 20 kHz. At the lower end of the spectrum this is limited by the resolution bandwidth of the FFT-analyzer. At the high frequency end, the noise increases due to the decreasing gain of the feedback loop. This is, however, irrelevant for the central laser linewidth as discussed above. In the regions where the in-loop noise lies below the detector noise, the detector noise is partly converted to frequency noise due to the high gain of the feedback loop, limiting the locking accuracy. This is especially relevant at low Fourier frequencies where the residual amplitude modulation noise becomes large and even rises above the 1 Hz white noise. The conversion of this RAM noise into frequency noise will limit the linewidth of the locked laser most probably to a few Hz. Apart from the detector noise, also the electronic noise at the controller input stage is in principle relevant. However, it is specified to $12 \text{ nV}/\sqrt{\text{Hz}}$, corresponding to $0.6 \text{ mHz}/\sqrt{\text{Hz}}$, which is negligible compared to the detector noise.

This analysis of the in-loop error signal and the detector noise shows that we stabilize our laser to the cavity resonance with an accuracy close to 1 Hz, limited by residual amplitude modulation of the locking light. It does, however, not give any information about the overall stability of the locked laser, which is largely determined by the stability of the reference cavity. The only way to measure the overall frequency stability of the locked laser is to compare it to a second independently stabilized laser, which has similar or better noise characteristics. This analysis is described in the next section.

3.1.3 Evaluation of the Laser Stability

For the evaluation of the laser's stability, a second PDH setup was built with a similar cavity of a slightly different finesse ($\mathcal{F} = 103000$). The only difference in the lock setup is the PDH photodetector, which is a home-built photodiode with a bandwidth of $\sim 25 \text{ MHz}$. The modulation frequency of the second PDH setup is set to 15.8 MHz, about 2.4 MHz away from the modulation frequency of cavity 1, in order to avoid interference between the two setups. The setup for the beat note analysis is sketched in fig. 3.10. The laser light is split up into two

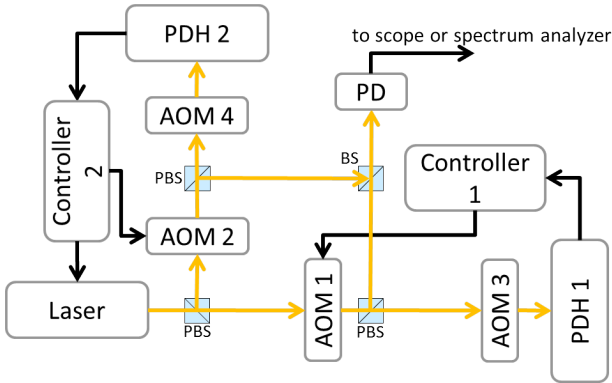


Figure 3.10: Schematic of the beat note measurement setup for the stability evaluation of the locked laser. The laser output is split up and each part is sent through its individual fast feedback AOM (AOM 1 and AOM 2). A small portion of the light in each arm is sent to two similar PDH setups using similar ultra stable cavities as described in the main text. AOM 3 and AOM 4 are used in double- and quadruple-pass configurations respectively to bridge the frequency difference between the two cavity modes. The ECDL piezo is locked to the PDH 1 error signal. The large part of the light, which is not sent to the cavities, is overlapped on a beam splitter and the resulting beat note is analyzed using an oscilloscope or a spectrum analyzer.

paths before passing the feedback AOMs. The light in the two paths is individually stabilized to the two cavities, each arm having its own fast feedback AOM. In order to bridge the frequency difference between the two cavities, the light stabilized to cavity 2 is sent through an AOM in quadruple-pass configuration. Since the slow branch of the control circuit acts back on the piezo of the ECDL, it can only be used in one of the control loops. For the measurements shown here it has been used in the lock to cavity 1.

With only one PDH lock active, the beat signal between the two arms exhibits the spectrum of the unstabilized laser with a width of ~ 100 kHz. When both locks are active, the beat signal is narrowed down to a carrier with a width of a few Hz about 50 dB above a noise plateau extending to the servo bandwidth of 1 MHz. This is shown in fig. 3.11 a). Looking at the beat signal with higher resolution as in fig. 3.11 b), one can see the low frequency noise due to vibrations, residual amplitude modulation, and light power fluctuations, as well as small peaks 50 Hz from the carrier coming from residual power line noise in the electronics.

For short observation times of ~ 2 s a narrow linewidth of down to 1 Hz of the beat signal can be observed as shown in fig. 3.12 a). There is, however, still significant low frequency noise that limits the linewidth to values between 10 Hz and 20 Hz for averaging times of up to 1 min, which is shown in fig. 3.12 b). The analysis of the in-loop error signal noise in the previous section has shown that residual amplitude modulation at the PDH frequency contributes a significant part of this low frequency noise. Moreover, also vibrations of the cavity setup, as well as fluctuations of the intra-cavity power are possible sources of such low frequency noise. While the influence of cavity vibrations is difficult to quantify, the contribution of intra-cavity power fluctuations to the frequency noise can readily be determined. The corresponding measurement has been performed in the same way as in [121]: The set voltage of the power controller of one of the cavities is repeatedly changed by 5%, while the power in the second cavity is held constant. The applied power change corresponds to a change in the transmitted light power of 99 nW for cavity 1 and 409 nW for cavity 2. The beat frequency of the two independently stabilized arms is monitored with a frequency counter during the power changes. The recorded frequency traces

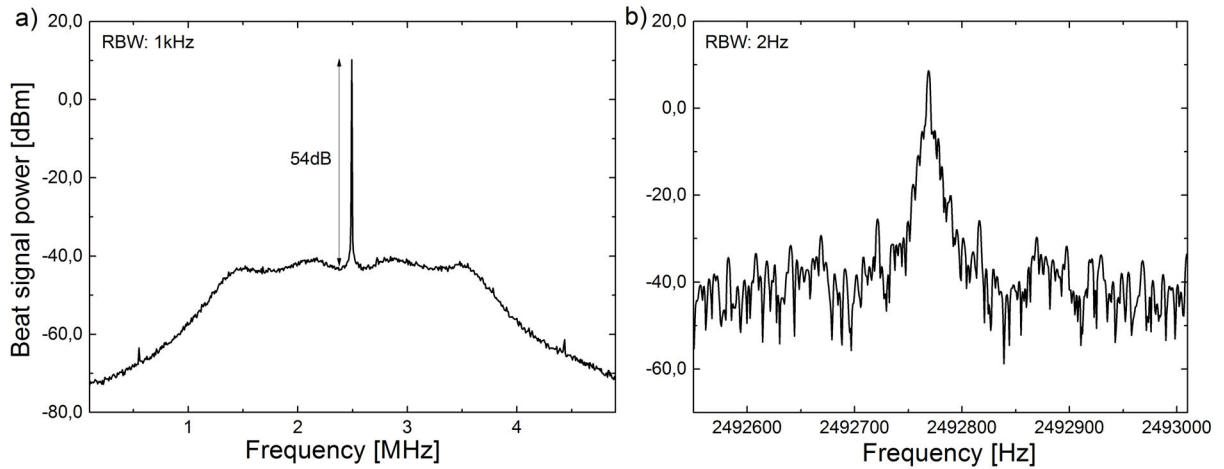


Figure 3.11: Beat signal between two laser beams that are independently stabilized to two identical ultra-stable cavity PDH setups, recorded with an RF-spectrum analyzer. In panel a) the frequency span is large enough to see the residual noise plateau about 54 dB below the narrow carrier signal. The noise is peaked at the servo bandwidth of ~ 1 MHz. Reducing the resolution bandwidth (RBW) to 2 Hz as in panel b), the dominant low frequency noise can be observed.

are shown in fig. 3.13 a) and c). After the rapid change of the power sent to the cavity, the beat frequency settles nearly exponentially to the new frequency as the mirror coatings thermalize to a new equilibrium temperature. The thermalization time constant is ~ 1.5 s for both cavities. In [121] the author observes a sudden step in the beat frequency preceding the exponential thermalization. It is attributed to an electronic offset of the error signal, causing the locking point to change with the amplitude of the error signal. In our measurements no such sudden step is observed. However, the low time resolution of our frequency counter of only 1 s might make it difficult to see such a jump even if it is there. Therefore, the electronic offsets were carefully measured to be below 1 mV. At our error signal slope of $19.3 \mu\text{V}/\text{Hz}$, a 1 mV voltage offset corresponds to a frequency offset of 52 Hz. A 5% change in the light power changes the error signal slope by 5% and thus results in a change of the frequency offset of 2.6 Hz. This is clearly negligible compared to the few hundred Hz frequency shift observed after the power change. In [121] the influence of the electronic offset is much larger, because the power is changed by more than 400% rather than 5% as in our case.

The overall power-dependent frequency shift extracted from the traces in fig. 3.13 a) and c) is $(3.45 \pm 0.38) \text{ kHz}/\mu\text{W}$ for cavity 1 and $(623 \pm 31) \text{ Hz}/\mu\text{W}$ for cavity 2. These values are extremely large compared to those reported by the PTB group [121] ($(10 \pm 2) \text{ Hz}/\mu\text{W}$) and by the NIST group [107] ($65 \text{ Hz}/\mu\text{W}$). Since the absorption of our cavity mirrors is similar to that of other high-finesse cavities, the large sensitivity to the intra-cavity power must be due to an extremely large coefficient of thermal expansion (CTE) of our mirror coatings. The reason for this large thermal expansion is not known right now. The sign of the frequency shift has been measured to be positive, i.e. a larger intra-cavity power causes an increase of the cavity frequency. This implies a positive CTE of the coatings, meaning that they expand

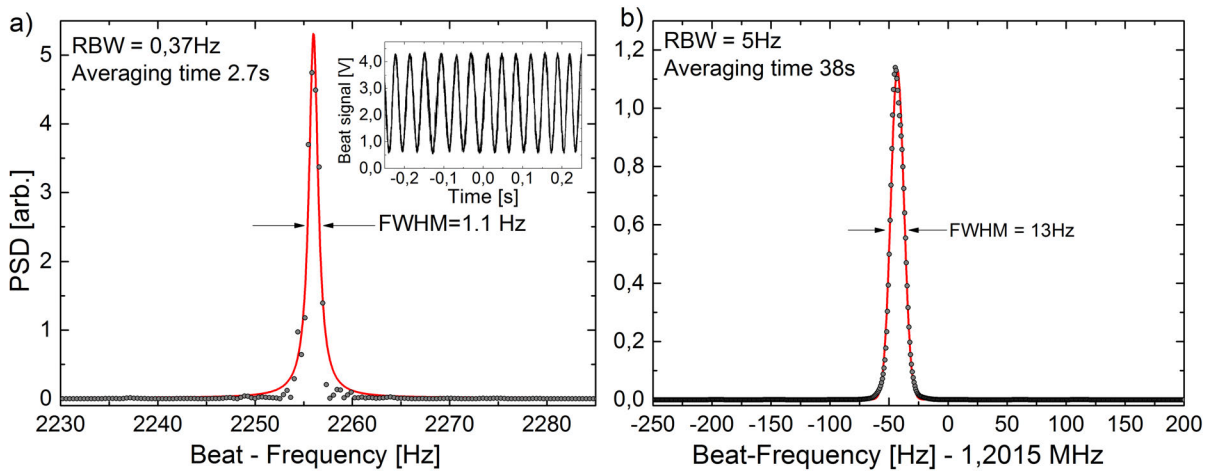


Figure 3.12: Beat signal between two laser beams that are independently stabilized to two identical ultra-stable cavity PDH setups. Panel a) depicts a single spectrum recorded with an audio analyzer, revealing a narrow Lorentzian spectrum with a width of 1 Hz. The inset shows the beat signal in the time domain at a beat frequency of 26 Hz. For longer averaging times, low frequency noise broadens the signal to a gaussian with a FWHM of 13 Hz. In these measurements a linear drift of ~ 2 Hz has been compensated by sweeping the RF-frequency of AOM 4 with a computer controlled DDS chip.

and shorten the cavity when heated. In order to obtain the contribution of the intra-cavity power fluctuations to the frequency noise of the locked laser, the noise density of the cavity transmission is multiplied with the observed power-dependent frequency shifts. The observed thermalization time of 1.5 s is accounted for by multiplying with the transfer function of a first order low pass with a corner frequency given by the inverse of the thermalization time. The resulting frequency noise densities are shown in fig. 3.13 b) and d). They lie below the 1 Hz-white noise density of $0.56 \text{ Hz}/\sqrt{\text{Hz}}$ across the whole spectrum. Consequently, fluctuations of the intra-cavity power cannot explain the observed 10 Hz linewidth of the beat signal. Still, the large CTE of our cavity mirrors might be a reason for a rather large CTE of the cavities as a whole (mirrors and spacer) as will be discussed below.

Apart from the linewidth of the laser on the timescale of a few seconds to one minute, also the longterm drift of the laser frequency is of great importance. It is limited by drifts of the cavity temperature. To minimize the sensitivity of the cavity frequency to thermal drifts, the cavity temperature should be tuned to the zero-crossing of the coefficient of thermal expansion (CTE), which according to the ULE specification lies between 5°C and 35°C .

In order to find the CTE zero crossing of cavity 1, the cavity frequency was measured at three different cavity temperatures. For this measurement, the cavity frequency was monitored via the beat note of the locked laser with a frequency comb⁹, while the cavity temperature was changed in two steps from 18.9°C to 13°C and finally to 7°C . The time evolution of the cavity frequency is shown in fig. 3.14. The first thing to observe is the long thermalization time-constant of $\tau_c \approx 36 \text{ h}$, indicating very good thermal insulation of the cavity from the

⁹Menlo Systems: FC-1500

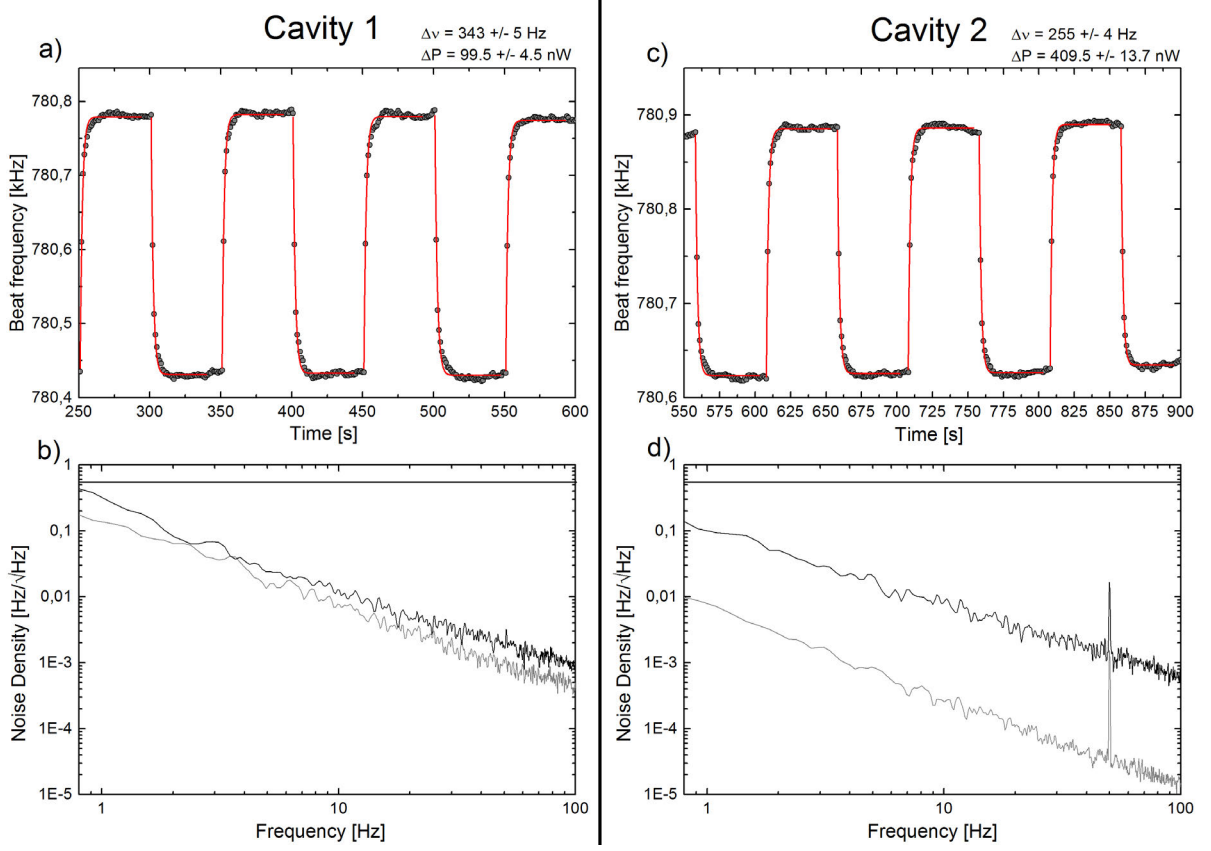


Figure 3.13: Influence of intra-cavity power fluctuations on the frequency stability of the locked laser for the two ultra-stable cavities. Panels a) and c): Frequency of the beat note between the two independently locked laser beams, while the power sent to one of the cavities is repeatedly changed by 5%. The absolute power change ΔP and the resulting frequency change $\Delta\nu$ are indicated at the top of the graphs. They result in power sensitivities of (3.45 ± 0.38) kHz/ μ W for cavity 1 and (623 ± 31) Hz/ μ W for cavity 2. The measured sensitivities and thermalization times can be used to convert the noise of the cavity transmission into frequency noise of the locked laser. The corresponding noise densities are plotted in black in panels b) and d). The gray curves show the detector noise with no light sent to the cavities.

outer thermal shield. The equilibrium cavity frequency corresponding to the set temperature was found by extrapolating a fit to the data. The exact thermalization curve is difficult to find analytically. Thus for simplicity, an exponential temperature evolution was assumed for the fit. Since the temperature was assumed to be near the zero crossing of the CTE, the temperature dependence of the CTE itself was taken to be linear:

$$\text{CTE} = \alpha \cdot (T(t) - T_0), \quad (3.10)$$

where T_0 is the zero-CTE temperature. With this, the cavity frequency is calculated as:

$$\Delta\nu(t) = \nu_0 \cdot \text{CTE} \cdot (T(t) - T_0) = \nu_0 \cdot \alpha \cdot (T(t) - T_0)^2 \quad (3.11)$$

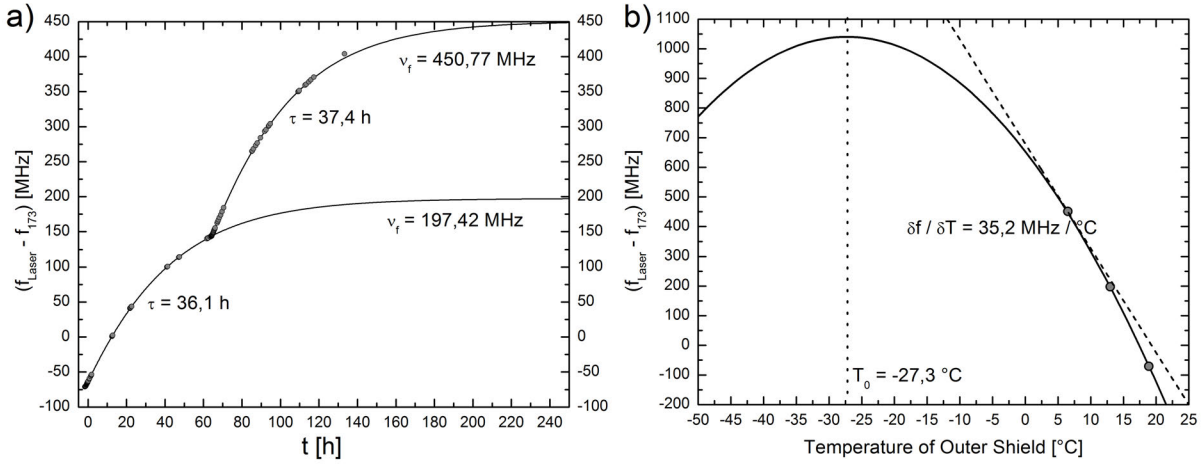


Figure 3.14: Measurement of the thermal expansion of the ULE cavity. Panel a) displays the evolution of the cavity frequency after two subsequent changes of the set temperature of the outer thermal shield. Equation (3.12) is fitted to the measured evolution to extrapolate to the longterm equilibrium frequency. The three equilibrium frequencies obtained from a) are plotted versus temperature in panel b). The three data points define a parabola with its vertex at the zero-CTE temperature.

Assuming an exponential temperature evolution $T(t) = T_i + \Delta T \exp(-t/\tau)$ one finds:

$$\Delta\nu(t) = \nu_0 \cdot \alpha \cdot \left((T_i - T_0)^2 + 2\Delta T (T_i - T_0) \exp(-t/\tau) + \Delta T^2 \exp(-2t/\tau) \right) \quad (3.12)$$

The equilibrium frequencies extracted from the fits of eq. (3.12) to the measured frequency evolution are plotted versus the set temperature in fig. 3.14 b). The three data points define a parabola, whose vertex is at the zero-CTE temperature. This measurement results in an extremely low T_0 of -27.3°C . At the lowest set temperature of 7°C the temperature sensitivity of the cavity is $-35.2 \text{ Hz}/\mu\text{K}$. This corresponds to a CTE of 58 ppb, which is about two times above the specified maximum CTE of ULE for temperatures between 5°C and 35°C . The same measurement was performed also for cavity 2, yielding $T_0 = -31.7^\circ\text{C}$. For the beat measurements shown in this thesis the temperature of cavity 2 was set to 18.3°C , resulting in a sensitivity of $-40.2 \text{ Hz}/\mu\text{K}$. One might be led to thinking that the anomalously low CTE of the whole cavity has to do with the anomalously large CTE of the mirror coatings. However, the expansion of the cavity spacer and mirror coatings affect the cavity frequency in opposite directions. While the expansion of the spacer leads to an increase in the cavity length, the mirror coatings can expand only away from the substrates into the cavity, leading to a shortening of the cavity. Consequently, a large positive CTE of the coatings would need to be canceled also by a large positive CTE of the cavity spacer, shifting the CTE zero-crossing to higher temperatures. Given this extremely low T_0 , we have decided to try working at a cavity temperature of 7°C . While water condensation is not a problem inside the vacuum chamber, reaching the -27°C would most probably not be possible with the cooling power of our TEC. Moreover, tuning the cavity so far away from room temperature will lead to a rather strong temperature gradient on the outer thermal shield, making the setup sensitive to variations of the room temperature as

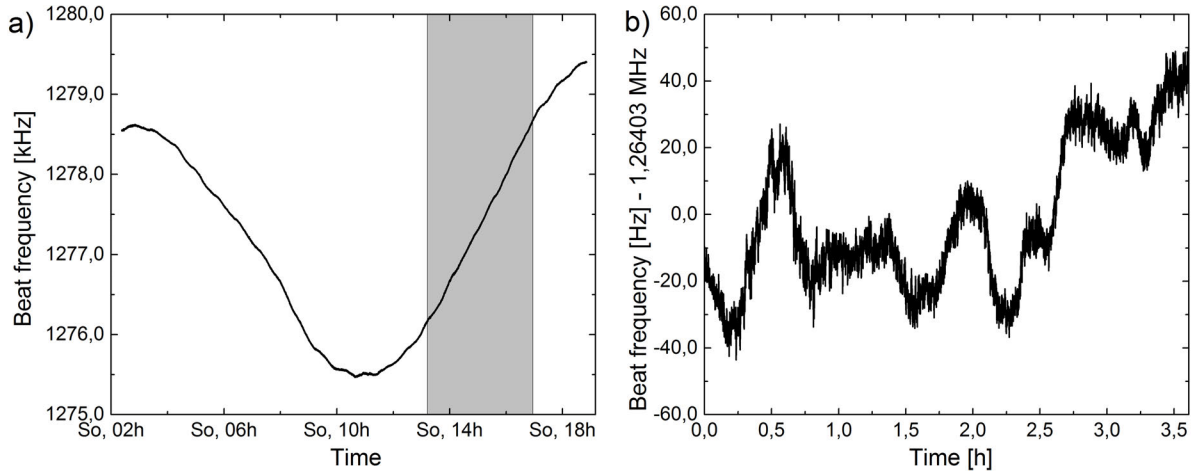


Figure 3.15: Panel a): Longterm measurement of the beat signals of the two independently stabilized laser beams, recorded with a frequency counter at 1s intervals. An overall linear drift of -2.43 Hz/s has been subtracted. The beat signal slowly oscillates over a few kHz during 16 hours, most probably due to variations of the environmental temperature. Panel b) shows a close-up of the gray-shaded region in panel a). A residual linear drift of 0.19 Hz/s has been subtracted. In this region, the beat frequency is stable within 100 Hz during 3.5 hours.

explained above.

Due to the large CTE of our cavities, thermal drifts of the cavity frequency are not negligible. Figure 3.15 shows a longterm trace of the beat note between the two cavities. Typically, the beat note drifts with a few Hz/s, most probably due to slow changes of the environmental temperature. This drift has been subtracted in fig. 3.15 a). The remaining nonlinear drift amounts to slow oscillations over a few kHz during one day. Zooming in at the linear regions of this slow oscillation and subtracting also the residual linear drift, a frequency instability of 100 Hz over a period of several hours is obtained as shown in fig. 3.15 a). When performing spectroscopy on the atomic sample, we actively compensate the linear drift by applying a frequency ramp to the AOM in front of cavity 1 (AOM 3 in fig. 3.10). During the measurement in fig. 3.15, cavity 1 was temperature controlled using the home-built controller described in section 3.1.1, which should provide 200 μ K instability. This would correspond to a frequency instability of 7 kHz at the measured temperature sensitivity of cavity 1 of 35.2 Hz/ μ K. Cavity 2 exhibiting a temperature sensitivity of 40.2 Hz/ μ K was, however, controlled with a standard laser diode temperature controller with a specified instability of only 2 mK. Thus, the drift of the beat frequency in this measurement might be limited by the temperature controller of cavity 2. However, during spectroscopy experiments we also observed peak-to-peak longterm drifts of tens of kHz of cavity 1 with respect to the atomic resonance. This indicates that the home-built controller does not reach the 200 μ K instability achieved when testing the controller. The only difference in the test was that the on-board thermistor was used instead of the thermistor at the cavity heat shield. Thus, most probably thermoelectric voltages in the sensor connection compromise the performance. Moreover, residual gradients on the outer heat shield that change with the cooling power, might limit the stability of the average shield temperature as explained

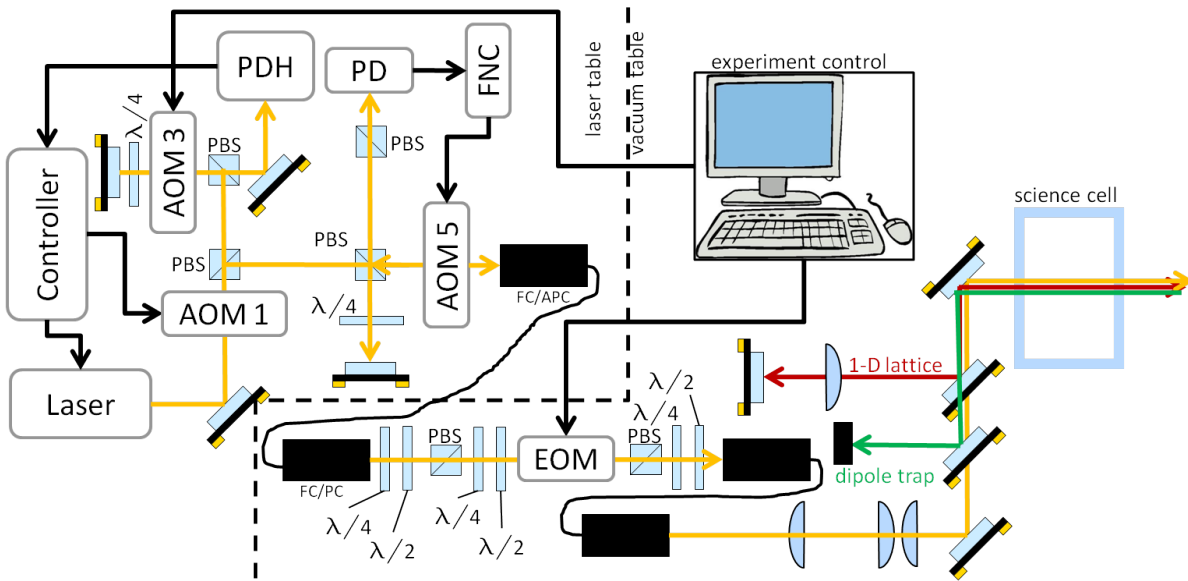


Figure 3.16: Setup for clock spectroscopy of ultracold Yb in an optical lattice. See main text for a detailed explanation.

in section 3.1.1. While the use of two thermistors at the top and the bottom of the shield should minimize this effect, the size of residual gradients and their variation is unclear. From the experience we have gained from spectroscopy experiments so far, improving the thermal drifts of the cavity is highly desirable. Therefore, either the temperature stability needs to be improved by an order of magnitude, or measures need to be taken in order to reach the zero-CTE temperature.

3.1.4 The Spectroscopy Setup

Having generated stable, narrow-band laser light at the $^1S_0 \rightarrow ^3P_0$ transition frequency, this light must be prepared for spectroscopy experiments. In practice, two things need to be taken care of. First, the light must be brought from the laser table to the ultracold atoms without adding extra phase noise. Second, a suitable modulator needs to be installed for shaping the amplitude of the spectroscopy pulse.

The setup for these two tasks is shown in fig. 3.16. From the laser table the light is sent via a 10 m long fiber to the table supporting the vacuum chamber. The phase noise caused by vibrations of the fiber is canceled, using a standard fiber noise cancellation (FNC) setup, similar to that used for the three-beam optical lattice (cf. section 2.4.2): The retro-reflection from the plane-cut rear end of the fiber is diffracted a second time by AOM 5 and is overlapped with light, split off in front of the AOM. The phase of the resulting beat note is compared with a stable DDS reference and fed to a proportional-integral controller that acts on the RF-frequency of AOM 5 to lock the phase of the beat to that of the reference.

At the vacuum chamber, an EOM is used to control the intensity of the clock light. Waveplates in front of the EOM are used to optimize the polarization for maximum extinction behind

the EOM and polarizer. An additional fiber behind the EOM is necessary to obtain good extinction ratios exceeding 10^5 . The high extinction is desirable, because the Rabi frequency is proportional to the square root of the intensity. Consequently, an extinction ratio of 10^4 allows to suppress the Rabi frequency only by a factor of 100. The second fiber has a length of 1 m and is rigidly installed on the optical table in order to minimize vibration induced phase noise, since FNC cannot be used here. Behind the second fiber, the clock laser light is focused to the position of the atomic sample and overlapped with the dipole trap and lattice beams. At the position of the atoms the $1/e^2$ -radius of the clock laser beam is $200 \mu\text{m}$. The lattice and clock laser beams hit the glass cell at a small angle of 1.4° , ensuring that the retro-reflection from the uncoated inner surface of the cell does not interfere with the incoming beam. In case of perfect perpendicular alignment, interference between the incoming beam and the 4% reflected light would create a standing wave with an intensity contrast of 20% causing a modulation of the Rabi frequency by 10%. The frequency of the spectroscopy light is controlled via AOM 3, shifting the frequency sent to the ultrastable cavity. A linear drift of the cavity frequency is canceled, by applying a frequency ramp to AOM 3 on top of the desired frequency detuning. The original idea behind using an EOM for rapid switching of the clock laser instead of an AOM was to minimize power loss, because for certain applications very large clock laser intensities are desirable. Due to the necessity of the second fiber, this argument is no longer valid. Moreover, temperature-dependent birefringence in the EOM crystal makes the maximum extinction rather sensitive to temperature drifts. Therefore, it is necessary to optimize the extinction every few hours even with the EOM put inside a hermetically sealed box for temperature isolation. Due to these two reasons, switching with an AOM is eventually preferable. We are currently changing the setup accordingly.

3.2 Lattice Spectroscopy of Single Component Fermions

While our ultimate goal is to coherently control the electronic state of an ultracold, fermionic multi-spin mixture, we first characterized our spectroscopy using a spin-polarized gas. The spectroscopy is performed as follows: As explained in section 2.5.2, we prepare a weakly degenerate spin-polarized Fermi gas by pumping the majority of the atoms into the $m_F = +5/2$ state¹⁰ prior to evaporation, leaving however an equal distribution of the remaining five spin-states present. The minority spin components then sympathetically cool the $m_F = +5/2$ -atoms during evaporation. In this way we end up with a polarized sample of $7 \dots 9 \cdot 10^4$ atoms at $T/T_F \leq 0.3$. We then adiabatically ramp up the optical lattice to values between 10 and $40 E_r$. Once the atoms are loaded into the lattice, the dipole trap is ramped down in 10ms and switched off completely to avoid the differential AC-stark shift of the dipole trap light. Held only by the

¹⁰While the ground-state spin was denoted as I in section 2.5.2 in order to make explicit that it is a purely nuclear spin, it will be denoted as F in this section to be consistent with the existing literature.

magic wavelength optical lattice, we excite the atoms on the clock transition using π -polarized light. So far, we detect only the remaining ground-state atoms after the probe laser pulse has been applied. Thus, spectral features appear as dips in the remaining ground-state fraction.

While freely moving atoms exhibit a smooth Doppler-broadened optical excitation spectrum, the confinement by the optical lattice changes the spectrum into a series of discrete peaks, corresponding to simultaneous electronic- and motional excitation to the different bands of the lattice. The spacings between these discrete excitation peaks are given by the bandgaps of the lattice, which can easily reach many kHz and are therefore well resolvable with a narrow linewidth laser. The resonance corresponding to an electronic excitation without changing the band index is called the *carrier*. The resonances corresponding to the excitation of higher or lower bands are called *blue* and *red sidebands*, respectively. The Doppler widths of the various resonances are given by the respective bandwidths in the optical lattice. Using lattice depths of a few tens of E_r , the bandwidth can easily be reduced far below 1 Hz, practically eliminating Doppler broadening. Due to the finite momentum of the clock laser photons, the coupling strengths and thus the Rabi frequencies of the carrier and the various sidebands differ from each other. As the depth of the lattice is increased, the Rabi frequency of the carrier increases while the sidebands are more and more suppressed. The regime where the carrier is the dominant transition is called the Lamb-Dicke regime. The theoretical description of optical spectroscopy in the Lamb-Dicke regime is nicely presented in [122] for ions or atoms in a single tight harmonic trap. A brief theoretical description of the optical excitation of motional states in an optical lattice is presented in appendix A of this thesis.

In order to distinguish in our experiment between the carrier and the sideband resonances, we performed spectroscopy over a wide frequency range of ~ 100 kHz using a long excitation pulse with a pulse area of $\sim 55\pi$. Using a long excitation pulse is advantageous when looking for sidebands, because as mentioned above the carrier and the various sidebands all have different Rabi frequencies. A pulse area of multiple π and a pulse duration much longer than the system's coherence time should result in an excitation fraction of 50% independent of the Rabi frequency. The atoms in the lowest band of the lattice only contribute to the blue sidebands and not to the red sidebands, leading to an imbalance between the red and blue sidebands. This imbalance should allow to identify the individual resonances. The observed sideband spectrum is shown in fig. 3.17 a). Four spectral features can be identified belonging to the first red sideband, the carrier, the first and the second blue sidebands.

The higher order sidebands are suppressed due to the reduced Rabi frequency as explained in appendix A. From the discussion in section 2.5.3, we should expect that in the measurement shown fig. 3.17 a) with $7 \cdot 10^4$ atoms in a three-dimensional lattice about 30% of the atoms occupy higher bands. This does however not agree with the strength of the red sideband in fig. 3.17 a), which is compatible with an excitation fraction of a few percent. However, as shown in appendix A quasimomentum and band-index transverse to the propagation direction of the clock laser beam cannot be changed during the excitation. Consequently, only those atoms contribute to the red sideband that are located in the regions of the second Brillouin zone along the direction of propagation of the spectroscopy laser. This is illustrated in fig. 3.17 b). As shown in the measurement of fig. 2.19 b), for $6 \cdot 10^4$ atoms about 10% of the atoms are loaded into the

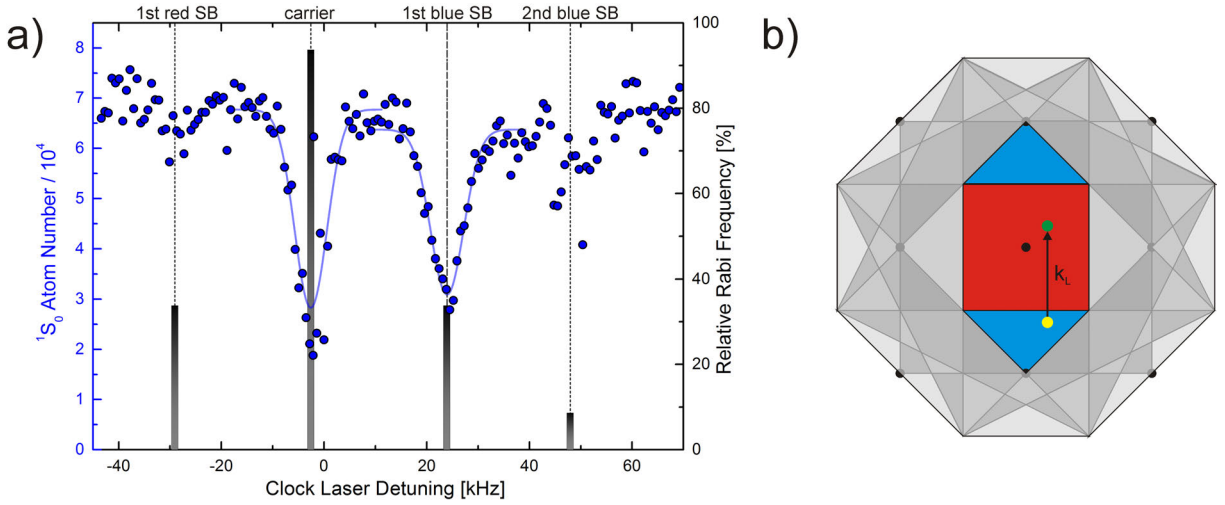


Figure 3.17: Panel a): Excitation spectrum of a spin-polarized Fermi gas on the clock transition in a three-dimensional optical lattice. Before loading the atoms into the lattice $T/T_F = 0.3$. The lattice is ramped to depths of $49E_r$ and $34E_r$ for the 1D- and 2D-lattice respectively. A large pulse area of $\sim 55\pi$ is used in order to well observe the higher order sidebands. The different Rabi frequencies of the sideband transitions, shown as bars in the figure, lead to different strengths of the observed resonances. Only those atoms located in the second Brillouin zone along the propagation direction of the clock laser contribute to the first red sideband as illustrated in panel b) for a square lattice.

second band in the direction of the 1D-lattice, which is compatible with the strength of the red sideband observed in fig. 3.17 a).

Having identified the carrier resonance in the optical lattice, we looked at Rabi oscillations of the lattice-confined atoms. Figure 3.18 a) - d) depict oscillations for different Rabi frequencies and lattice depths. For a single π -pulse, a high excitation fraction exceeding 90% is achieved. For longer pulses, the oscillations are damped towards a mean excitation of 50%. The fact that the damping occurs symmetrically towards 50% excitation indicates that it is caused by dephasing due to an inhomogeneous Rabi frequency. This indication is further strengthened by the observation that the damping depends on the Rabi frequency itself as can be seen by comparing fig. 3.18 a) and b). As the Rabi frequency is decreased from 9.4 kHz in panel a) to 1.5 kHz in panel b) the damping rate also decreases from 2.9 ms^{-1} to 0.65 ms^{-1} . In optical clock experiments, which work with thermal atoms in a one-dimensional optical lattice, such an inhomogeneity of the Rabi frequency is caused by the distribution of the atoms over many radial oscillator levels [51]. In our case, where the atoms are confined in a three-dimensional optical lattice, this effect is absent. The main reason for an inhomogeneous Rabi frequency should then be an inhomogeneous probe laser intensity. For the measurements in fig. 3.18 a) and b) we used a rather tightly focused probe laser beam with $w_0 = 61\ \mu\text{m}$. From our trap frequencies we estimate the radius of our cloud transverse to the clock laser beam to be $r \approx 15\ \mu\text{m}$ corresponding to 25% of w_0 . Figure 3.19 shows numerically calculated Rabi oscillations for an atomic ensemble equally distributed on a disc of radius r , driven by a probe laser beam

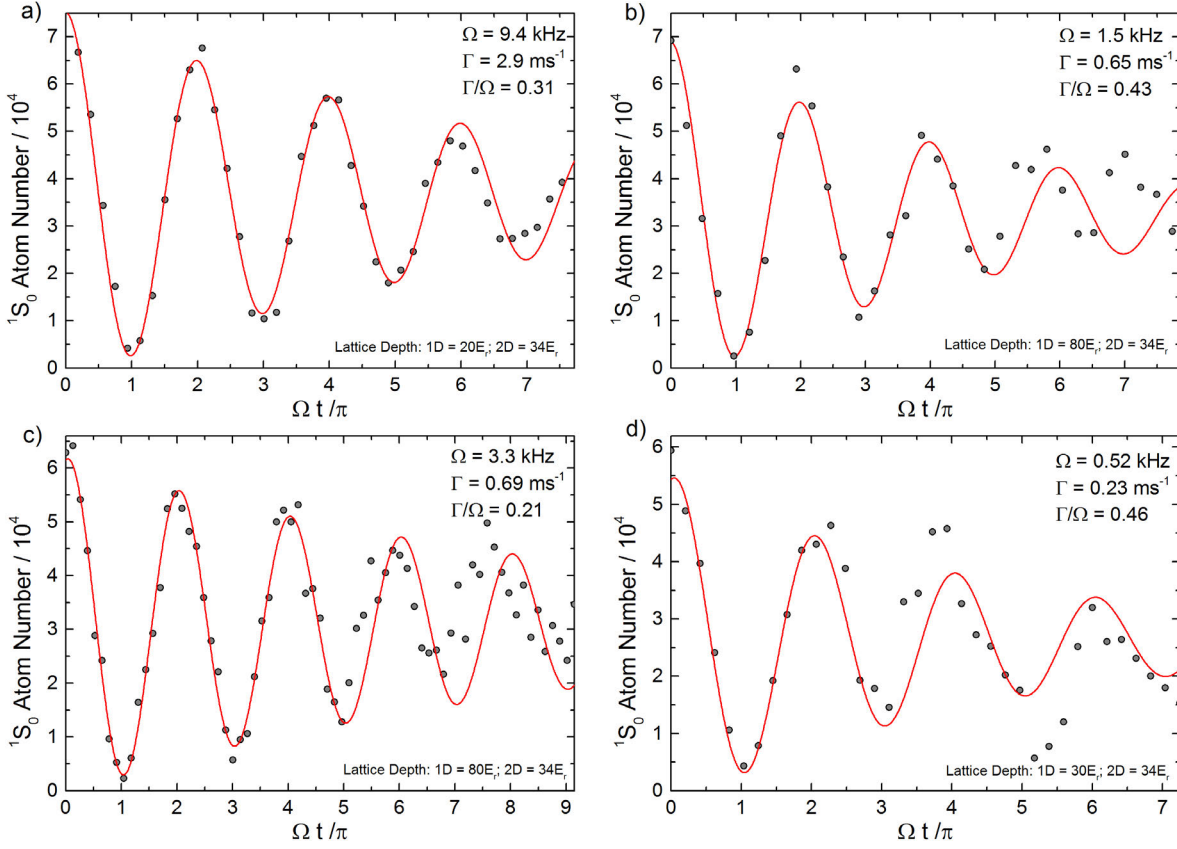


Figure 3.18: Rabi oscillations of a spin-polarized gas of ^{173}Yb in the three-dimensional optical lattice. Before loading the atoms in the lattice $T/T_F = 0.3$. The lattice is ramped within 50 ms to the depths indicated in the images. For the measurement in panel c), the lattice is initially ramped to depths of $30E_r$ and $34E_r$ for the 1D- and 2D-lattice respectively. Subsequently, the 1D-lattice is ramped to a depth of $80E_r$ within 5 ms. For the measurements in panels a) and b) a clock laser beam with a $1/e^2$ -radius of $w_0 = 61 \mu\text{m}$ was used. For panels c) and d) w_0 was increased to $200 \mu\text{m}$. All measured oscillations exhibit damping with a rate Γ . The ratio of damping and Rabi frequency Γ/Ω is almost the same for all measurements. The origin for this Rabi frequency-dependent damping is currently not understood.

with a Gaussian transverse intensity profile with a $1/e^2$ -radius w_0 , which is displaced with respect to the center of the atom cloud by x_c . Comparing the measurement to the calculation for $r/w_0 = 25\%$ and $x_c = 0$ in fig. 3.19 a), it is obvious that the size of the cloud alone does not explain the observed damping. The inhomogeneity of the Rabi frequency increases however, when the laser hits the sample off center, as shown in panel b) of fig. 3.18. A misalignment of 10% to 20% of w_0 would explain the observed damping. In order to check for a possible probe misalignment, we carefully aligned the clock laser beam for minimum damping of the Rabi oscillations using a mirror mount equipped with precision micrometer screws. However, the damping could not be reduced. Still, we increased the waist of the clock laser beam by about a factor of three from $61 \mu\text{m}$ to $200 \mu\text{m}$, which should significantly reduce the effect of the cloud size as well as a possible misalignment. The measurements in fig. 3.18 c) and d) are

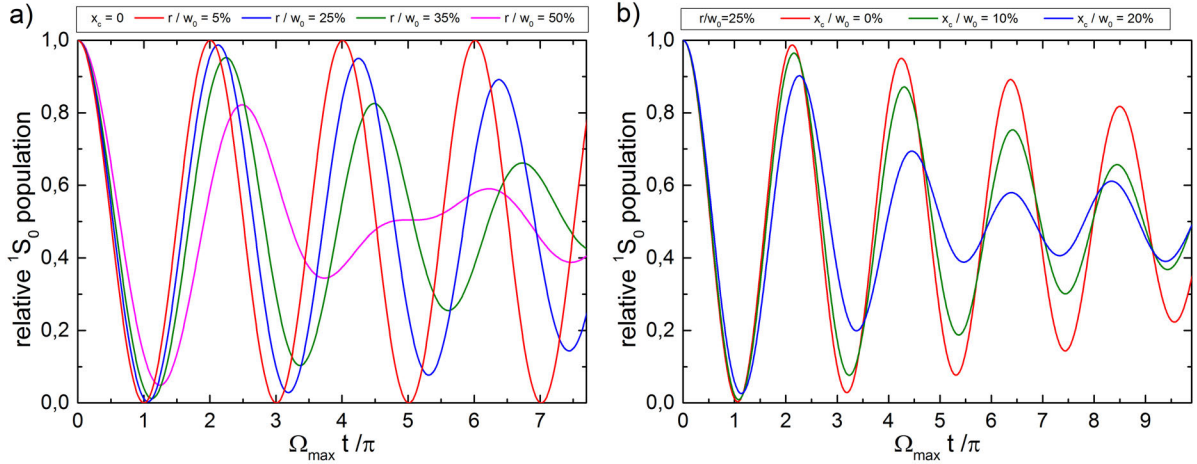


Figure 3.19: Numerical calculations of Rabi oscillations of atoms equally distributed on a disc of radius r transverse to the direction of the excitation laser beam. The intensity profile of the excitation laser is taken to be Gaussian with a $1/e^2$ -radius w_0 . In panel a) the ratio of the size of the atomic sample and the laser beam r/w_0 is varied. The oscillations exhibit significant damping for $r/w_0 > 5\%$, due to dephasing caused by the inhomogeneity of the Rabi frequency. In panel b) r/w_0 is fixed to 25% and the beam is displaced with respect to the cloud by a variable offset x_c , increasing the inhomogeneity of the Rabi frequency and thus the damping of the oscillations.

obtained with the enlarged probe beam, again after careful alignment. The fact that the Rabi frequency-dependent damping hardly changed, indicates that it is not caused by the Gaussian probe beam profile. An inhomogeneous clock laser intensity could also be due to an intensity modulation caused by the interference of the incoming probe beam with its retro-reflection off the inner glass cell surface. This is, however, avoided by a slight misalignment between the beam and the glass cell, as discussed in section 3.1.4.

Another reason for the damping could be the significant occupation of higher bands. As discussed in appendix A, atoms in the first and second band experience a different Rabi frequency on the carrier transition, causing a beating between the Rabi oscillations of atoms in the first and the second band. However, as mentioned earlier and discussed in appendix A the Rabi frequency does not depend on the full three-dimensional band-index but only on that along the direction of probe laser and 1D-lattice. The fraction of $\sim 10\%$ of the atoms that occupy higher bands along this direction cannot explain the observed damping. However, it is to be expected that the atoms in higher bands sit on doubly occupied sites together with an atom in the lowest band. Due to the different Rabi frequencies for these atoms, they are no longer indistinguishable and can interact. This considerably complicates the situation. To investigate the effect of higher bands on the Rabi oscillations of spin-polarized samples, experiments with a significantly reduced atom number should be performed. This is however beyond the scope of this work.

Figure 3.20 shows Rabi spectra taken for a polarized Fermi gas exciting the atoms with a single square-shaped π -pulse. We observe a Fourier-limited resolution down to $\Delta_{\nu, \text{FWHM}} \leq 200$ Hz with a peak excitation fraction exceeding 90%. When the Rabi frequency is reduced below a Fourier limit of about 200 Hz, significant low frequency noise appears. However, instead of

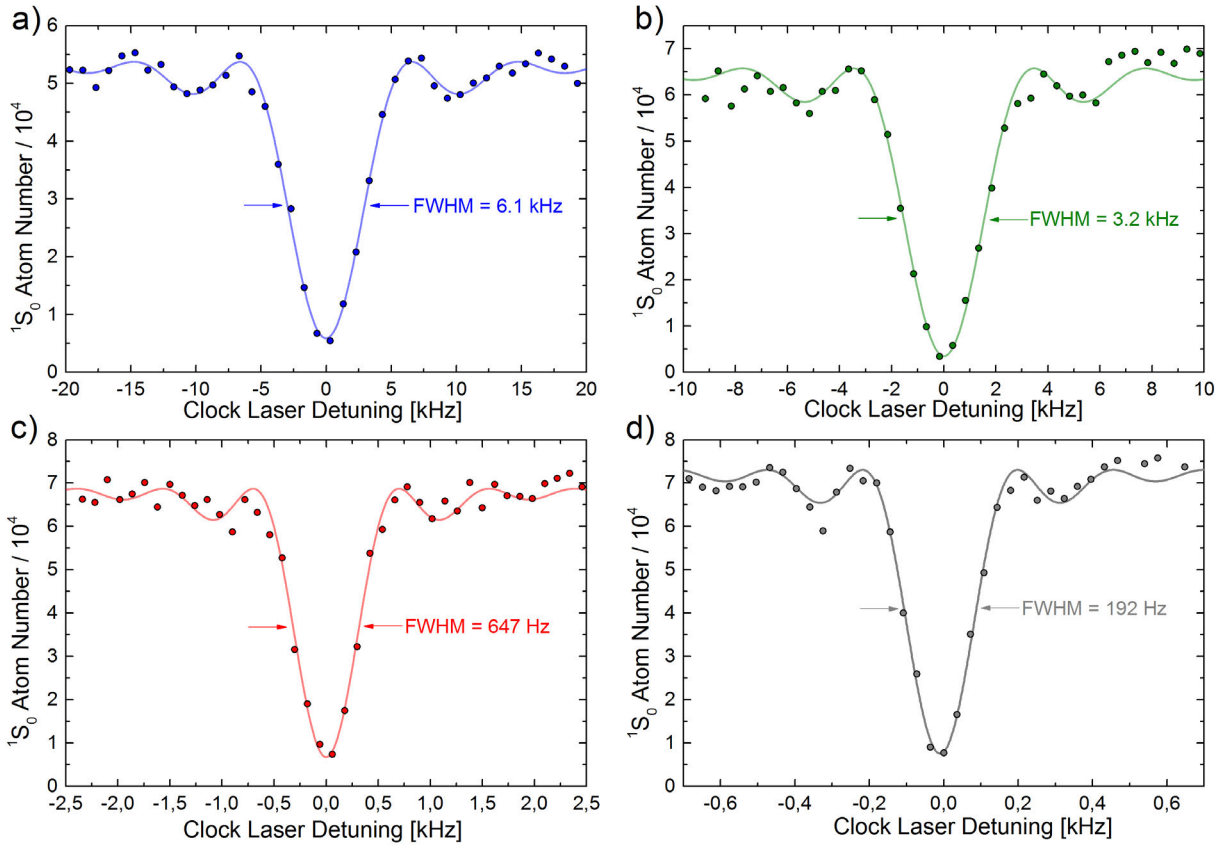
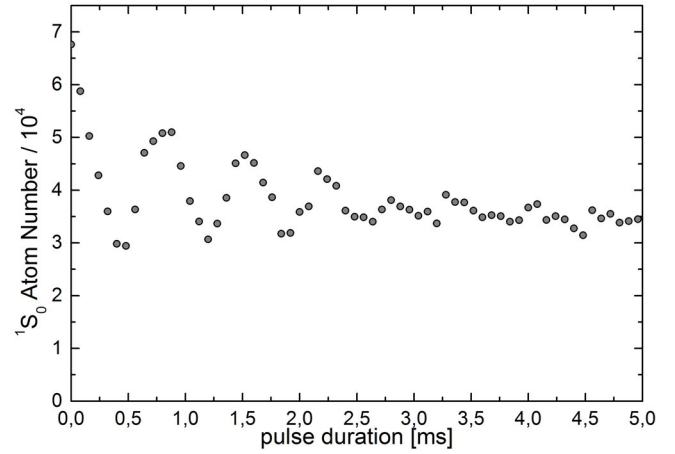


Figure 3.20: Rabi spectra of a spin-polarized gas in an optical lattice for different Rabi frequencies. The spectra a) to c) have been obtained in a three-dimensional optical lattice with depths of $40E_T$ and $33E_T$, ramped up within 50 ms. The spectrum in d) was taken for a thermal spin-polarized gas in a purely one-dimensional optical lattice with a depth of $150E_T$. The data in a) is an average over three independent spectra, while the other three spectra are single shot measurements. The observed widths of the spectra extracted from a sinc^2 -fit to the data agrees with the Fourier limit calculated from the applied Rabi frequencies within the measurement error.

a smoothly broadened spectrum, we observe strong fluctuations of the excitation fraction near resonance. This indicates that the noise responsible for this distortion is occurring at Fourier frequencies below the inverse pulse time, but above the experimental cycle time. In order to narrow down the frequency range of this noise we shortened the experimental cycle in order to reduce the dead time between subsequent spectroscopy pulses. Instead of evaporating to ultracold temperatures, we continuously switch on the one-dimensional optical lattice at a large depth of $150E_T$. After loading atoms from the MOT into the dipole trap, they are optically pumped into the $m_F = +5/2$ state. Subsequently, the atoms are evaporatively cooled to a few μK and transferred into the optical lattice by ramping the dipole trap to zero over a time of 1 s. This has the main advantage that less atoms are lost during evaporation² and the MOT loading time can be decreased from 20 s to 5 s. In total, this decreases the experimental repetition time from 30 s to 8 s. The higher repetition rate does not have any noticeable influence on the spec-

Figure 3.21: Rabi oscillations on the first blue sideband of a spin-polarized gas of ^{173}Yb in a three-dimensional optical lattice with depths of $30E_r$ and $34E_r$ for the 1D- and 2D-lattice respectively. The peak excitation fraction is limited to about 50%, because only atoms initially in the lowest band of the lattice contribute to the sideband. The asymmetric damping of the oscillations hints at loss from the excited state (see main text).



troscopic noise. Therefore, we conclude that the noise occurs on timescales between 4 ms and 10 s. The stability analysis of the spectroscopy laser presented in section 3.1.3 shows, however, that on these timescales, the laser exhibits a linewidth below 20 Hz. Thus, the limitation of the spectroscopy to linewidths of ~ 200 Hz cannot be explained by the instability of the clock laser. Currently, we believe that the main cause of this noise are Doppler shifts due to relative motion of the clock laser and lattice beams induced by air currents and vibrations at the experiment. We are presently working on making the setup more rigid and shielding it from air flow.

An interesting perspective for future experiments is the spectroscopy on higher order motional sidebands, allowing to coherently prepare metastable state atoms in higher bands of the optical lattice. In this way, one could study band relaxation, transport in higher bands or particle-hole dynamics. All these processes can be expected to be substantially influenced by the differential interaction and inelastic collisions between ground and metastable state atoms. Figure 3.21 depicts Rabi oscillations on the first blue sideband, corresponding to exciting atoms to the 3P_0 state and simultaneously promoting them to the first excited band of the lattice. Since the bands in an optical lattice are not linearly spaced, the transition frequency of the first blue sideband depends on the initial band index of the atoms. In other words, for atoms initially in the second band, the blue sideband is located at a different frequency than for atoms initially in the first band. From fig. A.2 in appendix A, one can see that for a 1D-lattice depth of $30E_r$, the two sidebands are separated by about $1.5E_r$, corresponding to 3 kHz, which is about twice the Fourier-limited resolution in fig. 3.21. Consequently, only atoms initially in the first band can be excited. The maximum excitation fraction of 50% would however correspond to a population of 50% in higher bands along the 1D-lattice direction, which is not reasonable for $7 \cdot 10^4$ atoms in a 3D-lattice, considering the estimates and measurements discussed in section 2.5.3. Also here, the interaction between atoms on doubly occupied sites initially in different bands might be important.

In contrast to the Rabi oscillations on the carrier transition shown in fig. 3.18, the damping of the oscillations on the blue sideband is asymmetric. They decay towards the level of 50%, which corresponds to the peak initial excitation fraction. This hints at loss from the excited

state, which could occur due to metastable atoms decaying back to the lowest band and colliding inelastically with ground state atoms. While this was not the focus of our work so far, it would be very interesting to explore in detail the dynamics of metastable state atoms in higher bands.

3.3 Spectroscopy of a Two-Component Gas

3.3.1 Theoretical Description of the Spectroscopy of Spin Mixtures

Narrowline spectroscopy as a preparation and detection tool for quantum many-body physics becomes most relevant when it is applied to interacting, multi-spin quantum gas mixtures in an optical lattice. In this section I want to discuss the theoretical description of the spectroscopy for the simplest case, a *two*-component gas. As long as tunneling in the lattice is relevant, the atomic gas must be treated as a true many-body system and the theory becomes difficult. The discussion here will be restricted to the regime, where the lattice is so deep that tunneling is negligible on experimental time- and energy scales. In this case the atomic ensemble can be treated as an array of isolated harmonic traps occupied by either one or two atoms in the lowest oscillator state. Consequently, the theory becomes simple and the Hamiltonian can be solved exactly. All considerations here are for fermionic ^{173}Yb . The general arguments hold, however, for other fermionic elements.

In the following I will distinguish between two experimental configurations, which I call $\pm 5/2$ -*configuration* and $(3/2)(5/2)$ -*configuration*. In the $\pm 5/2$ -configuration shown in fig. 3.22 a) the atomic gas is prepared in a mixture of the two outermost m_F -states $|m_F = \pm 5/2\rangle$ and the spectroscopy laser is π -polarized. In this case, the Clebsch-Gordan coefficients and thus the Rabi frequencies of the two transitions are equal in magnitude, but have opposite sign. Consequently, for a given length and amplitude of the spectroscopy pulse the two spin components experience the same pulse area. Moreover, there is a relatively large differential Zeeman shift of 565 Hz/G between the two transitions [107, 123], such that they can be well resolved even at small fields. In the $(3/2)(5/2)$ -configuration depicted in fig. 3.22 b) the atoms are prepared in a mixture of the $|m_F = 3/2\rangle$ and $|m_F = 5/2\rangle$ states and the spectroscopy laser is σ^+ -polarized. In this configuration only the $|m_F = 3/2\rangle$ -state is addressed by the spectroscopy laser, because the $|m_F = 5/2\rangle$ ground state obviously does not couple to σ^+ -polarized light. This makes it harder to compare the observed two-component spectra with the single-component spectra, which for reasons of optical pumping are recorded for the $|m_F = 5/2\rangle$ -state with π -polarized light as described in section 3.2. The advantage of this configuration is, however, that the excited state is a simultaneous eigenstate of the atom-atom interaction and the Zeeman shift. This makes the interpretation of the spectra much simpler, as will become clear in the course of this section.

Before discussing the Hamiltonian and the spectrum of two interacting atoms, it is useful to identify the Hilbert space of possible two-atom states the system can adopt. The relevant single-atom Hilbert space is the four-dimensional product space of the spin- and electronic subspaces. It is spanned by the basis $\{|e\rangle \otimes |\uparrow\rangle, |e\rangle \otimes |\downarrow\rangle, |g\rangle \otimes |\downarrow\rangle, |g\rangle \otimes |\uparrow\rangle\}$. $|e\rangle$ and $|g\rangle$ denote the

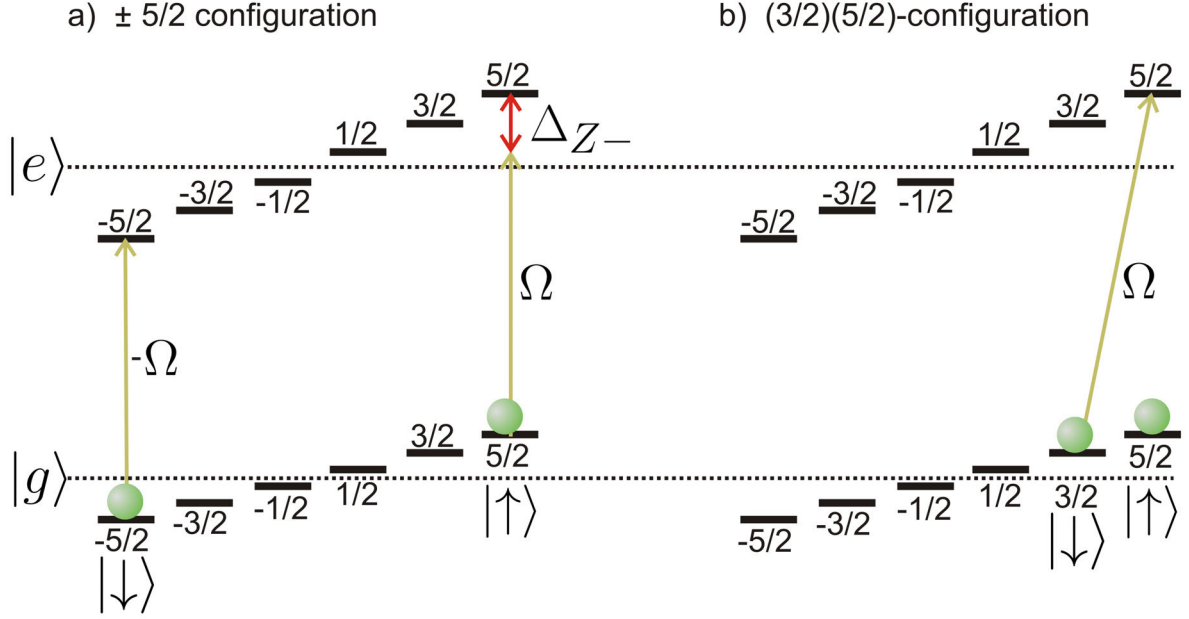


Figure 3.22: Illustration of the two spectroscopy configurations discussed in this section. In the $\pm 5/2$ -configuration shown in panel a) the atomic gas is prepared in a mixture of the two outer most m_F -states $|m_F = \pm 5/2\rangle$ and the spectroscopy laser is π -polarized. The Rabi frequencies of the two transitions have the same magnitude $|\Omega|$, but opposite sign due to their Clebsch-Gordan coefficients. Δ_{Z-} denotes the differential Zeeman shift between the transitions. In the $(3/2)(5/2)$ -configuration shown in panel b) the atoms are prepared in a mixture of the $|m_F = 3/2\rangle$ and $|m_F = 5/2\rangle$ states and the spectroscopy laser is σ^+ -polarized. In this configuration there is only one allowed transition with Rabi frequency Ω .

electronic orbital states 3P_0 and 1S_0 , respectively. $|\uparrow\rangle$ stands for the m_F -state with the larger m_F and $|\downarrow\rangle$ for that with the smaller m_F (cf. fig. 3.22). The tensor product is explicitly written here, to clarify the distinction between the electronic subspace spanned by $\{|e\rangle, |g\rangle\}$ and the m_F - or spin subspace spanned by $\{|\uparrow\rangle, |\downarrow\rangle\}$. In the later formulas it will be omitted for the sake of brevity. The tensor product of the two single-atom Hilbert spaces has 16 dimensions. However, according to the Pauli-Principle identical fermions can only be in states that are anti-symmetric with respect to particle exchange. Transforming into a (anti)-symmetrized basis, one finds that the relevant Pauli-allowed subspace of anti-symmetric states is only six-dimensional. Two basis sets of this space are

$$\begin{aligned}
 \{|b_i^{\text{int}}\rangle\} = & \{|ee\rangle |\uparrow\downarrow\rangle^-, \\
 & |eg\rangle^+ |\uparrow\downarrow\rangle^-, \\
 & |eg\rangle^- |\uparrow\uparrow\rangle, \\
 & |eg\rangle^- |\uparrow\downarrow\rangle^+, \\
 & |eg\rangle^- |\downarrow\downarrow\rangle, \\
 & |gg\rangle |\uparrow\downarrow\rangle^-\}, \tag{3.13}
 \end{aligned}$$

and

$$\begin{aligned}
\{|b_i^Z\rangle\} = & \{|ee\rangle |\uparrow\downarrow\rangle^-, \\
& \frac{1}{\sqrt{2}} (|e\uparrow g\downarrow\rangle - |g\downarrow e\uparrow\rangle), \\
& |eg\rangle^- |\uparrow\uparrow\rangle, \\
& \frac{1}{\sqrt{2}} (|g\uparrow e\downarrow\rangle - |e\downarrow g\uparrow\rangle), \\
& |eg\rangle^- |\downarrow\downarrow\rangle, \\
& |gg\rangle |\uparrow\downarrow\rangle^-\}.
\end{aligned} \tag{3.14}$$

$|eg\rangle^\pm$ denote the (anti)-symmetric superpositions $1/\sqrt{2}(|eg\rangle \pm |ge\rangle)$. In the same way $|\uparrow\downarrow\rangle^\pm = 1/\sqrt{2}(|\uparrow\downarrow\rangle \pm |\downarrow\uparrow\rangle)$. These basis sets will be important later on, because as shown in appendix B $\{|b_i^{\text{int}}\rangle\}$ is an eigenbasis of the atom-atom interaction and not of the Zeeman shift. $\{|b_i^Z\rangle\}$ on the other hand, is an eigenbasis of the Zeeman Hamiltonian and not of the atom-atom interaction.

Now I turn to the description of the Hamiltonian $\hat{\mathcal{H}}_S$ that governs the spectroscopy process. The construction of $\hat{\mathcal{H}}_S$ is in detail explained in appendix B. Here, I will only highlight those aspects that are important for the understanding of the expected spectra. The Hamiltonian consists of four contributions:

$$\hat{\mathcal{H}}_S = \underbrace{\hat{\mathcal{H}}_{\text{el}} + \hat{\mathcal{H}}_Z + \hat{\mathcal{H}}_{\text{int}}}_{\hat{\mathcal{H}}_a} + \hat{\mathcal{H}}_L. \tag{3.15}$$

$\hat{\mathcal{H}}_{\text{el}}$ is the bare electronic Hamiltonian and $\hat{\mathcal{H}}_Z$ describes the Zeeman shift due to an external magnetic field. These two Hamiltonians are known from basic atomic physics and are given in eqs. (B.16) and (B.18). $\hat{\mathcal{H}}_{\text{int}}$ contains the s-wave interaction between the two atoms. It has already been discussed in section 2.1 and is given by eq. (2.4). Since the interaction between the atoms is m_F -independent in the 1S_0 - as well as in the 3P_0 -state, $\hat{\mathcal{H}}_{\text{int}}$ is the same for both spectroscopy configurations. $\hat{\mathcal{H}}_{\text{el}}$, $\hat{\mathcal{H}}_Z$, and $\hat{\mathcal{H}}_{\text{int}}$ make up the atomic Hamiltonian $\hat{\mathcal{H}}_a$. The fourth contribution $\hat{\mathcal{H}}_L$ describes the coupling Hamiltonian between the atoms and the light field. Note that its form depends on whether the system is in the $\pm 5/2$ - or the $(3/2)(5/2)$ -configuration. Spontaneous emission can be neglected, because of the extremely long lifetime of the excited states.

Since the light field probes the energy spectrum of the atomic system $\hat{\mathcal{H}}_a$, it is instructive to first understand this atomic Hamiltonian and leave the atom-light coupling aside. The most interesting aspect of $\hat{\mathcal{H}}_a$ is that generally the atom-atom interaction $\hat{\mathcal{H}}_{\text{int}}$ and the Zeeman Hamiltonian $\hat{\mathcal{H}}_Z$ do not commute as shown in eq. (B.21). The physical mechanism behind this becomes clear by comparing the matrix representations of $\hat{\mathcal{H}}_S$ in the two different bases $\{|b_i^{\text{int}}\rangle\}$ and $\{|b_i^Z\rangle\}$ given in eqs. (B.27) and (B.36): On the one hand, the differential Zeeman shift Δ_{Z-} between the two

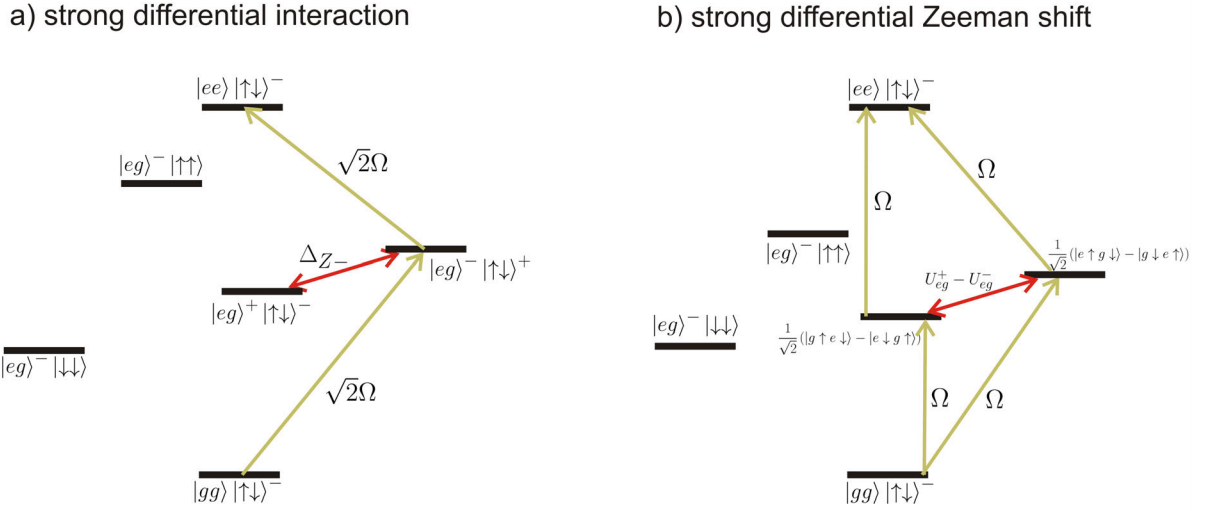


Figure 3.23: Level diagrams of the interacting two-atom system in the $\pm 5/2$ -configuration. In panel a) the differential interaction dominates over the differential Zeeman shift. In panel b) the differential Zeeman shift dominates over the differential interaction. Further explanations are given in the main text.

transitions couples the interaction eigenstates $|b_2^{\text{int}}\rangle = |eg\rangle^+ |\uparrow\downarrow\rangle^-$ and $|b_4^{\text{int}}\rangle = |eg\rangle^- |\uparrow\downarrow\rangle^+$. On the other hand, the difference of the singlet and triplet interaction $\Delta U_{eg} = U_{eg}^+ - U_{eg}^-$ couples the Zeeman eigenstates $|b_2^Z\rangle = \frac{1}{\sqrt{2}} (|e\uparrow g\downarrow\rangle - |g\downarrow e\uparrow\rangle)$ and $|b_4^Z\rangle = \frac{1}{\sqrt{2}} (|g\uparrow e\downarrow\rangle - |e\downarrow g\uparrow\rangle)$. The other four basis states are, however, identical in the two eigenbases and are simultaneous eigenstates of both $\hat{\mathcal{H}}_{\text{int}}$ and $\hat{\mathcal{H}}_Z$. This situation is schematically depicted in fig. 3.23. The energy spectrum of the coupled states is shown in fig. 3.24 a) to c) for different interaction configurations. A non-zero differential interaction ΔU_{eg} leads to an avoided crossing of the two Zeeman eigenstates, while the average interaction $\bar{U}_{eg} = (U_{eg}^+ + U_{eg}^-) / 2$ simply shifts the energy of the interacting states.

If the differential interaction dominates over the differential Zeeman shift, Δ_{Z-} can be treated in perturbation theory. Since Δ_{Z-} appears only in the off-diagonal elements of the Hamiltonian, the correction in first order perturbation theory vanishes. The leading correction is in second order perturbation theory and is given by:

$$\Delta E_{|eg\rangle^- |\uparrow\downarrow\rangle^+} = -\Delta E_{|eg\rangle^+ |\uparrow\downarrow\rangle^-} = \frac{(\Delta_{Z-})^2}{\Delta U_{eg}} \quad (3.16)$$

In the opposite case, where the differential Zeeman shift dominates over the differential interaction, it is useful to transform the perturbation to the Zeeman eigenbasis. The leading correction to the energies of the Zeeman eigenstates due to the differential interaction is again in second order perturbation theory and reads:

$$\Delta E_{\frac{1}{\sqrt{2}}(|e\uparrow g\downarrow\rangle - |g\downarrow e\uparrow\rangle)} = -\Delta E_{\frac{1}{\sqrt{2}}(|g\uparrow e\downarrow\rangle - |e\downarrow g\uparrow\rangle)} = \frac{(\Delta U_{eg})^2}{8\Delta_{Z-}} \quad (3.17)$$

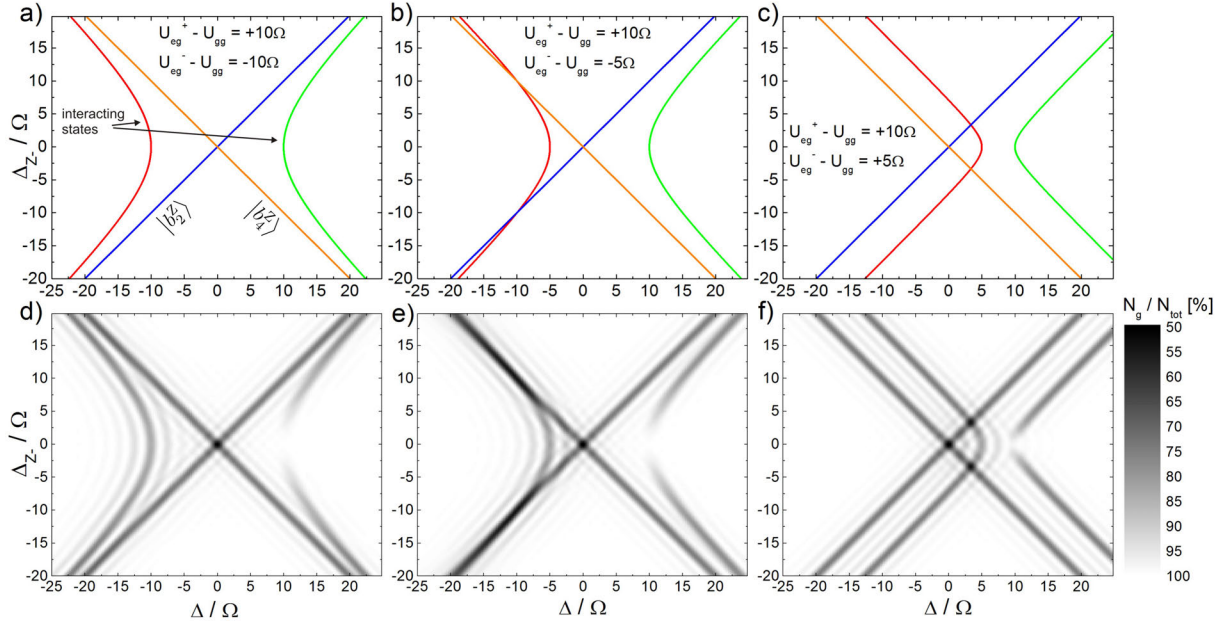


Figure 3.24: a)-c): Energies of the singly excited states of the atomic Hamiltonian $\hat{\mathcal{H}}_a$ in the $\pm 5/2$ -configuration. The vertical coordinate is the differential Zeeman shift Δz_- between the two single-atom transitions. The horizontal coordinate is the detuning Δ from the unshifted single-atom excited state. Both coordinates are given in units of the Rabi frequency used for the calculation of the excitation spectra in panels d)-f). The solid blue and orange lines represent the Zeeman eigenstates $|b_2^Z\rangle$ and $|b_4^Z\rangle$ with all interactions set to zero. The solid green and red lines represent the interacting states, which for zero magnetic field equal the interaction eigenstates $|eg\rangle^- |\uparrow\downarrow\rangle^+$ (red) and $|eg\rangle^+ |\uparrow\downarrow\rangle^-$ (green). The interaction parameters U_{eg}^\pm used for the different spectra are given in the figure. d)-f): Fraction of remaining ground state atoms N_g/N_{tot} after applying a spectroscopy pulse as a function of the laser detuning Δ from the unshifted single-atom resonance and the differential Zeeman shift Δz_- in units of the single-atom Rabi frequency Ω . U_{eg}^\pm are the same as in the corresponding plots a)-c) above. U_{ee} has been set to a very large value, such that the $|ee\rangle$ -state is not populated. The spectroscopy pulse used for these spectra is a square pulse of pulse area π for the single-atom transition. The atomic ensemble is assumed to consist of 50% singly occupied sites and 50% doubly occupied sites.

Thus, in the limit of a large differential Zeeman shift, the differential interaction ΔU_{eg} is negligible and only the average interaction $\overline{U_{eg}}$ leads to a shift of the resonance.

For spectroscopy experiments the mixing between the Zeeman- and interaction eigenstates is only relevant if the probe light couples the ground state to these mixed states. This is the case in the $\pm 5/2$ -configuration, where the atom-light coupling Hamiltonian is given by eq. (B.25) and reads:

$$\hat{\mathcal{H}}_{L,\pi} = \frac{\hbar\sqrt{2}\Omega}{2} (|eg\rangle^- |\uparrow\downarrow\rangle^+ \langle gg| \langle \uparrow\downarrow|^- - |ee\rangle |\uparrow\downarrow\rangle^- \langle eg|^- \langle \uparrow\downarrow|^+ + h.c.) \quad (3.18)$$

Two aspects of this Hamiltonian are worth mentioning: First, note that the light field does not couple to the state $|eg\rangle^+ |\uparrow\downarrow\rangle^-$. This is due to the opposite sign of the Clebsch-Gordan coefficients of the two single-atom transitions. Second, the Rabi frequency is enhanced by a

factor $\sqrt{2}$ compared to the single atom Rabi frequency, reflecting the collective character of the excitation. Having constructed the full Hamiltonian of the driven two-atom system, it is straightforward to calculate the Rabi spectrum. To do so, the Hamiltonian is diagonalized, the ground state $|gg\rangle |\uparrow\downarrow\rangle^-$ is evolved over the duration of a π -pulse and the expectation value $\langle \hat{n}_g \rangle$ of the number of g -atoms in the final state is calculated. Figure 3.24 d) - f) depicts three such spectra for different values of U_{eg}^- . For simplicity U_{ee} has been set to a very large value, such that the doubly excited state $|ee\rangle |\uparrow\downarrow\rangle^-$ cannot be populated. The case where U_{ee} is on the same order of magnitude as U_{eg}^\pm will be considered later on. The spectra are calculated for a mixture of 50% singly occupied sites and 50% doubly occupied sites, because this allows to extract the interaction induced shifts from a single spectrum. The pulse area is chosen to be π for the singly occupied sites. These spectra reproduce the spectral structure of the atomic Hamiltonian shown in fig. 3.24 a) - c). The singly occupied sites are excited, where the non-interacting Zeeman states are in resonance. The doubly occupied sites are excited at the resonances of the interacting states. However, in the region of low magnetic field where the eigenstates of the two-atom system are nearly the interaction eigenstates, only the state $|eg\rangle^- |\uparrow\downarrow\rangle^+$ is efficiently excited as mentioned above. For stronger magnetic fields, the two interaction eigenstates are mixed and the spectrum becomes more and more symmetric. Due to the $\sqrt{2}$ enhancement of the Rabi frequency for the transition to the $|eg\rangle^- |\uparrow\downarrow\rangle^+$ state the pulse area for this transition is $\pi\sqrt{2}$, which results in a lower excitation fraction and larger sinc-ripples for this transition. This is again only relevant in the low field region. In the high field region, the interacting states have a large overlap with the Zeeman eigenstates, which experience the same Rabi frequency as the non-interacting, single-atom states (cf. eqs. (B.37) and (B.38)).

When the excited state interaction shift ($U_{ee} - U_{gg}$) is on the same order of magnitude as ($U_{eg}^\pm - U_{gg}$), a situation may be achieved in which the energy of one of the $|eg\rangle$ -states lies nearly centered between the energies of the $|gg\rangle$ - and $|ee\rangle$ -state. In this case, the transitions $|gg\rangle \rightarrow |eg\rangle$ and $|eg\rangle \rightarrow |ee\rangle$ are simultaneously near resonance and the doubly excited state $|ee\rangle |\uparrow\downarrow\rangle^-$ can be populated with a single laser pulse. Figure 3.25 depicts three spectra for different ratios of $\eta = (U_{ee} - U_{gg}) / (U_{eg}^- - U_{gg})$. The values for U_{eg}^\pm are the same as in fig. 3.24 a). In panel b) of fig. 3.25 $\eta = 2$. Thus, the transitions $|gg\rangle |\uparrow\downarrow\rangle^- \rightarrow |eg\rangle^- |\uparrow\downarrow\rangle^+$ and $|eg\rangle^- |\uparrow\downarrow\rangle^+ \rightarrow |ee\rangle |\uparrow\downarrow\rangle^-$ are simultaneously on resonance for zero magnetic field. In this region both atoms on a doubly occupied site are excited and the corresponding spectral feature looks exactly as for non-interacting atoms, only that it is shifted by $U_{eg}^- - U_{gg}$. For $\eta > 2$ as in fig. 3.25 c) the energy difference between the two transitions due to the interaction needs to be compensated by the Zeeman shift in order to achieve exact simultaneous resonance and get strong double excitation. Note, however, that even in between the two points of exact Zeeman compensation a significant fraction of atoms is excited to the $|ee\rangle$ -state and a clear splitting between the peaks for single and double excitation can be observed. The spectral feature for double excitation follows a straight vertical line in the shown spectra. This is due to the absence of Zeeman shifts in the states $|gg\rangle |\uparrow\downarrow\rangle^-$ and $|ee\rangle |\uparrow\downarrow\rangle^-$. In panel a) of fig. 3.25 $\eta = 1.8$. In this case the straight line of the double excitation feature never crosses the single excitation curves and exact simultaneous resonance cannot be achieved at any magnetic field. Significant

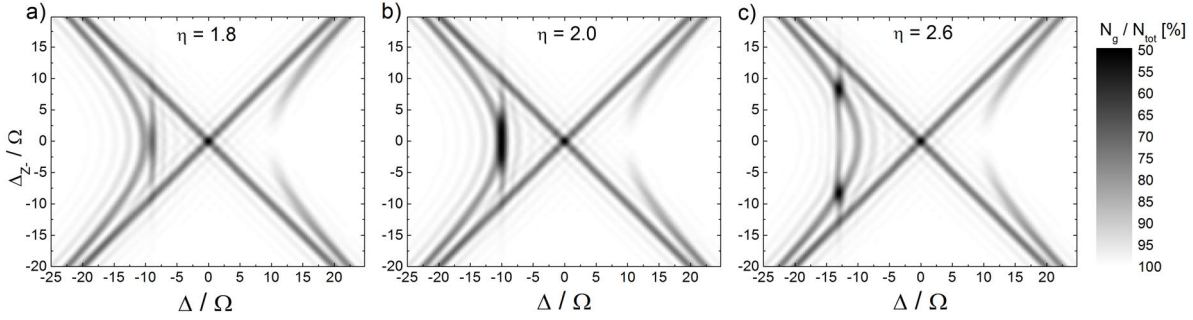


Figure 3.25: Fraction of remaining ground state atoms N_g/N_{tot} after applying a spectroscopy pulse as a function of the laser detuning Δ from the unshifted single-atom resonance and the differential Zeeman shift Δ_{z-} in units of the single-atom Rabi frequency Ω . All parameters except U_{ee} are the same as in fig. 3.24 a). In contrast to fig. 3.24, U_{ee} has been set close to U_{eg}^- , such that the $|ee\rangle$ can be populated. The ratio $\eta = (U_{ee} - U_{gg}) / (U_{eg}^\pm - U_{gg})$ changes from panel a) to c) as written in the figure.

double excitation occurs only at low fields where the single and double excitation peaks are closest. For even smaller values of η the amplitude of the double excitation peak drops very quickly to zero. On the other side of the spectrum near the state $|eg\rangle^+ |\uparrow\downarrow\rangle^-$, double excitation is hardly possible at all, even if simultaneous resonance of the $|gg\rangle |\uparrow\downarrow\rangle^- \rightarrow |eg\rangle^+ |\uparrow\downarrow\rangle^-$ and $|eg\rangle^+ |\uparrow\downarrow\rangle^- \rightarrow |ee\rangle |\uparrow\downarrow\rangle^-$ is achieved. This is because the light field does not couple to the state $|eg\rangle^+ |\uparrow\downarrow\rangle^-$, preventing double excitation at low magnetic fields. One might be tempted to think that at large magnetic fields, where a significant portion of the state $|eg\rangle^- |\uparrow\downarrow\rangle^+$ is mixed in, double excitation should become possible. However, this mixing leads to a larger overlap with the Zeeman eigenstates, which do not allow double excitation due to the differential Zeeman shift. Consequently, double excitation is always very weak on the $|eg\rangle^+$ -side of the spectrum, no matter which magnetic field is used.

These considerations lead to the following conclusions: The $\pm 5/2$ -configuration is well suited to detect the average interaction $\overline{U_{eg}}$, because it simply shifts the Zeeman eigenstates by the interaction difference $(\overline{U_{eg}} - U_{gg})$ independent of the applied magnetic field. In contrast, the differential interaction ΔU_{eg} leads to a significant shift only at small magnetic fields. At large fields this shift is reduced to a small second-order energy correction, which is given by eq. (3.17). When working in the low-field regime, one has to be aware that the transition to the singlet state $|eg\rangle^- |\uparrow\downarrow\rangle^+$ has a $\sqrt{2}$ enhanced Rabi frequency compared to the single atom Rabi frequency, while the triplet state $|eg\rangle^+ |\uparrow\downarrow\rangle^-$ does not couple to the light field at all. Direct excitation of the doubly excited state $|ee\rangle |\uparrow\downarrow\rangle^-$ is possible, if the ratio between the excited state interaction shift and the $|eg\rangle^-$ interaction shift $\eta \geq 2$. For $\eta < 2$ direct double excitation is very weak. In this case, the doubly excited state can only be reached via two subsequent spectroscopy pulses at different detunings. Altogether, the $\pm 5/2$ -configuration exhibits a rich spectral structure providing a high degree of flexibility especially for state preparation. Without any knowledge about the interactions it may however be somewhat tedious to find the right experimental parameters for the spectroscopy, since the number of expected peaks and their splittings depend strongly on the relative sizes of the different interactions.

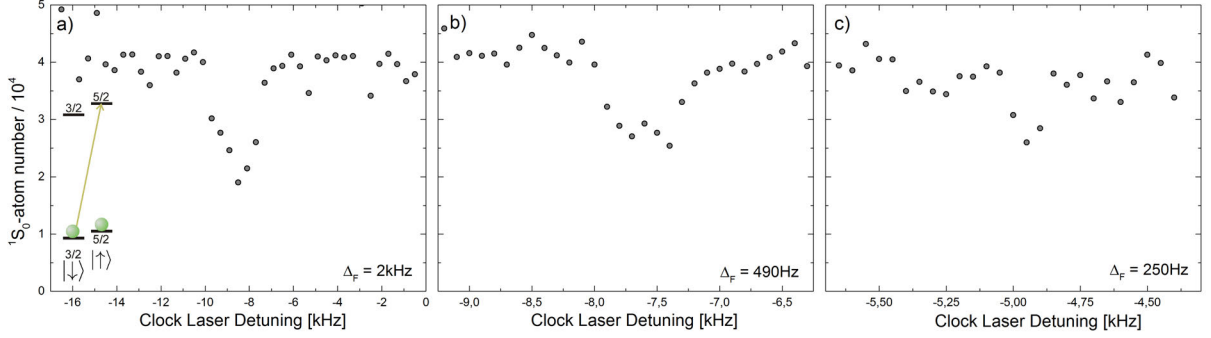


Figure 3.26: Spectra obtained in the $(3/2)(5/2)$ -configuration. A balanced mixture of the $m_F = 3/2$ and $m_F = 5/2$ -states is loaded into a three-dimensional lattice with lattice depths of $40E_T$ and $33E_T$ for the 1D- and 2D-lattice respectively. Duration and intensity of the probe pulse were adjusted such that a pulse area of π is obtained for the atoms on singly occupied sites. From a) to c) the probe intensity is reduced, resulting in a Fourier-limited resolution of $\Delta_F = 2$ kHz in a), $\Delta_F = 490$ Hz in b) and $\Delta_F = 250$, Hz in c). The fact that in panel c) the width of the resonance is below the Fourier-limited resolution probably comes from an imperfect compensation of the frequency drift of the clock laser. The detuning of the clock laser is given up to some offset.

In the $(3/2)(5/2)$ -configuration the competition between the interaction and the Zeeman shift is irrelevant and the spectra become much simpler. In this configuration $\hat{\mathcal{H}}_L$ is given by eq. (B.26). It has the form:

$$\hat{\mathcal{H}}_{L,\sigma} = -\frac{\hbar\Omega}{2} (|eg\rangle^- |\uparrow\uparrow\rangle \langle gg| \langle \uparrow\downarrow|^- + |ee\rangle |\uparrow\downarrow\rangle^- \langle eg|^- \langle \downarrow\downarrow| + h.c.) \quad (3.19)$$

From a look at the eigenbases $\{|b_i^{\text{int}}\rangle\}$ and $\{|b_i^Z\rangle\}$ it is verified that all coupled states are simultaneous eigenstates of $\hat{\mathcal{H}}_{\text{int}}$ and $\hat{\mathcal{H}}_Z$. Moreover, the Rabi frequency is the same as for non-interacting atoms. Consequently, the spectrum of a mixture of singly and doubly occupied sites only exhibits two peaks. One for the non-interacting and one for the interacting sites. They have both the same shape, because the Rabi frequencies are identical. And they are separated by the interaction difference $(U_{eg}^- - U_{gg})$. Excitation from the ground state to the doubly excited state is not possible in this configuration, because there is no common intermediate state to which both states are coupled. Thus I conclude that spectroscopy in the $(3/2)(5/2)$ -configuration is conceptually much simpler than in the $\pm 5/2$ -configuration.

3.3.2 Spectroscopy of a Two-Component Gas

In this section, I briefly describe first experiments on the spectroscopy of two-component spin mixtures that we performed in order to obtain information about the interaction properties of the metastable state atoms.

Figure 3.26 shows spectra obtained with a balanced mixture of the $m_F = 3/2$ and $m_F = 5/2$ states and σ^+ polarized probe light, realizing the $(3/2)(5/2)$ -configuration discussed in the previous section. As explained there, this configuration is sensitive to the interaction difference

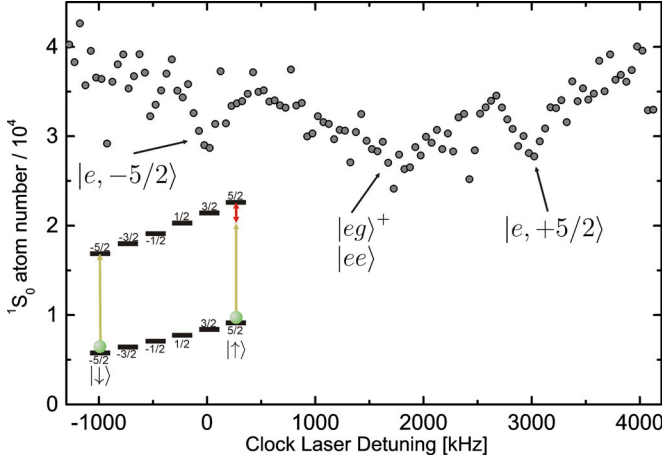


Figure 3.27: Spectrum obtained in the $\pm(5/2)$ -configuration. A balanced mixture of the $m_F = \pm 5/2$ -states is loaded into a three-dimensional lattice with lattice depths of $30E_r$ and $34E_r$ for the 1D- and 2D-lattice respectively. An excitation pulse with a duration of 2.7 ms was used, resulting in a π -pulse for atoms on singly occupied sites and a corresponding Fourier-limited resolution of 290 Hz. A homogeneous magnetic field of 5.5 G has been applied, which induces a splitting of 3.1 kHz between the single atom resonances of the $m_F = \pm 5/2$ -states. Comparing the spectrum to similar measurements from ref. [79] performed by the Munich group, the broad central peak can be attributed to $|eg\rangle^+$ and $|ee\rangle$ resonances. Details are given in the main text. The detuning of the clock laser is given with respect to the $m_F = -5/2$ -resonance.

between the ground state and the $|eg\rangle^-$ -state ($U_{eg}^- - U_{gg}$). For the spectra a) to c) the Rabi frequency is reduced in two steps, resulting in a Fourier-limited resolution between 2 kHz and 250 Hz. Within the scanned spectral range of 16 kHz no splitting is observed.

Figure 3.27 shows a spectrum in the $\pm(5/2)$ -configuration, i.e. a balanced mixture of the $m_F = \pm 5/2$ -states and a π -polarized clock laser. A homogeneous magnetic field of 5.5 G has been applied to induce a Zeeman splitting between the single-atom resonances of the two m_F -states. Here, despite the low signal to noise ratio three spectral features can be identified. From the known differential Zeeman shift of the clock transition of 113 Hz/G $\cdot m_F$ [107, 123], one can identify the peaks resulting from atoms in the $m_F = \pm 5/2$ -states on singly occupied sites. Between these two resonances, there is a broad spectral feature, which we could initially not interpret. However, when finishing this manuscript similar measurements were published by the Munich group [79], achieving a significantly better signal to noise ratio. Their measurements indicate that the broad central peak can indeed be attributed to the excitation of the $|eg\rangle^+$ -state. It consists, however, of three closely neighboring peaks: One from the excitation of the $|eg\rangle^+$ -state with both atoms in the lowest band, one from the excitation of the $|eg\rangle^+$ -state with one atom in the first and one in the second band, and a third peak corresponding to the doubly excited $|ee\rangle$ -state. Taking several spectra at different values of the magnetic field, it is possible to extract both U_{eg}^+ and U_{eg}^- by fitting the magnetic field dependent position of the $|eg\rangle^+$ resonance to the model described in section 3.3.1. In this way, the authors of ref. [79] find $a_{eg}^+ = a_{gg} + (22.7 \pm 7.3) a_0$ and $a_{eg}^- = a_{gg} + (1970 \pm 190) a_0$. The extremely large value of a_{eg}^- would lead to splittings of several tens of kHz in a three-dimensional optical lattice. This would explain the fact that we observe no splitting in the $(3/2)(5/2)$ -configuration, since we only scanned over a spectral width of 16 kHz.

While time did not permit to perform improved experiments within this thesis, our team is currently working on improving the spectroscopic resolution as well as our detection scheme.

The implementation of a repump laser on the ${}^3P_0 \rightarrow {}^3D_1$ transition at 1388 nm will allow to detect both ground- and metastable state atoms, which eliminates noise due to fluctuations of the total atom number [107]. As mentioned in section 3.2, we believe that the spectroscopic resolution is currently limited by fluctuating Doppler shifts induced by mechanical noise on the lattice- and clock laser beams. Therefore, improving the mechanical stability of these beams should lead to an improved resolution. Moreover, using a shallower dipole trap such that only the lowest band of the lattice is occupied should considerably simplify the interpretation of the observed spectra. With these improvements underway, we are optimistic that we will soon be able to coherently address the interacting two-atom states $|eg\rangle^\pm$ in the lattice.

Outlook

In this thesis a versatile apparatus for the investigation of quantum degenerate Yb has been presented. This setup allows the preparation of bosonic and fermionic ensembles in a triangular optical lattice, reaching the strongly correlated regime. The nuclear spin composition can be controlled and coherent manipulation of the electronic state has been achieved. These capabilities are a good starting point for the study of quantum many-body physics with mixtures of ground- and metastable-state Yb, realizing Hamiltonians that are not accessible with current alkali-based experiments.

Having observed first indications of 1S_0 - 3P_0 -interaction, an improved spectroscopy setup should soon enable us to prepare in a controlled way the interacting $|eg\rangle^\pm$ -states in a magic optical lattice. Once hopping between lattice sites is turned on in such a system, an interesting many-body Hamiltonian is realized, consisting of three different contributions: The Hubbard on-site interaction of ground- and metastable-state atoms U_{gg} and U_{ee} , the Kondo-exchange interaction due to the different scattering lengths of the $|eg\rangle^\pm$ -states $V_{\text{ex}} = \Delta U_{eg}/2$, and dissipation due to inelastic collisions between two metastable atoms. The competition between these processes can be expected to lead to interesting phenomena.

The next important steps will then be the realization of a state-dependent optical lattice that suppresses the tunneling of metastable-state atoms, as well as the development of efficient techniques for the preparation of 1S_0 - 3P_0 -mixtures in such a state-dependent lattice. In this way the Kondo lattice model can be realized with ultracold Yb, as has been described in the introduction and is again depicted in fig. 4.1 a).

Panel b) of the same figure schematically depicts the phase diagram of the Kondo lattice model in one dimension [25], where a relatively good theoretical understanding has already been established [29]. The general form of this phase diagram results from the competition of RKKY-type interactions between the localized metastable-state atoms (e-atoms), mediated by the mobile ground-state atoms (g-atoms), on the one hand, and the direct Kondo-exchange between the g- and e-atoms on the other hand. While the RKKY interaction induces ferromagnetic ordering of the localized atoms, the Kondo-exchange favors the formation of spin singlets of g- and e-atoms, leading to a paramagnetic state with heavy-fermion behavior of the mobile g-atoms. When the number of g-atoms per site is exactly one, i.e. at half filling, each g-atom forms a spin singlet with a localized e-atom and a so-called Kondo insulator forms. The relative strength of the RKKY- versus the Kondo-interaction depends on the ratio of exchange-coupling and hopping of g-atoms V_{ex}/J_g , as well as the number of g-atoms per lattice site n_g , as seen in fig. 4.1 b). With ultracold Yb in an optical lattice, it is straightforward to tune both these parameters by adjusting the ratio of 1S_0 and 3P_0 atoms and by varying the lattice depth. In this way it will be possible to study the phase transition between the ferromagnetic, the paramagnetic, and the

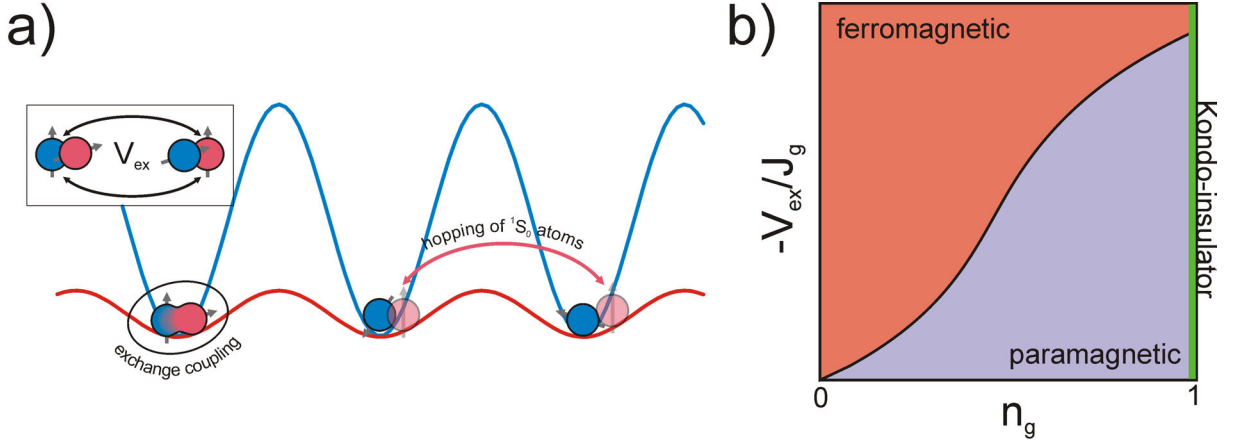


Figure 4.1: Panel a): Illustration of the Kondo lattice model realized with ultracold Yb. A mixture of ground- and metastable state atoms is loaded into a state-dependent optical lattice, where only the ground-state atoms can hop between lattice sites. The differential interaction ΔU_{eg} between the $|eg\rangle^\pm$ -states results in a direct spin-exchange interaction between e- and g-atoms. Panel b): Schematic phase diagram of the 1D Kondo lattice model according to refs. [25, 29]. The competition between RKKY-interactions and Kondo-exchange leads to a ferromagnetic and a paramagnetic phase.

Kondo insulator phase. Moreover, in an optical lattice, the dimensionality of the system can be changed by increasing the lattice depth along certain directions to very large values, freezing out the motion along these directions. Thus, optical lattice experiments allow to explore the Kondo lattice model in one dimension, where solid theoretical knowledge exists, as well as in two- and three-dimensions, where the theoretical understanding is so far rather limited. The temperatures that need to be reached in order to observe Kondo- and RKKY physics are given by $k_B T \leq J_g \exp(J_g/|V_{ex}|)$ for the Kondo- and $k_B T \leq V_{ex}^2/J_g$ for the RKKY regime [24]. For the large V_{ex} of ^{173}Yb suggested by the measurements in ref. [79] both temperatures should be much easier to achieve than the superexchange temperature necessary for the observation of magnetism in the Hubbard model.

Another type of experiments, which should be readily feasible with the current setup, exploits the dissipation of inelastic 3P_0 - 3P_0 s-wave collisions. In combination with the Pauli-blocking of s-wave collisions between identical fermions, the dissipation dynamics in 3P_0 spin-mixtures of fermionic Yb is predicted to produce highly entangled multi-particle spin states [124]. These entangled states are then completely free from s-wave collisions, which should be observable as a dramatic slow down of particle loss after the entanglement has formed.

A different direction of research of our project, which has not been described here, aims at the exploration of ultracold mixtures of Yb and Rb. The vacuum setup is already equipped with Rb-dispensers and the cooling laser setup is currently implemented. Such mixtures will open up a wide range of experimental possibilities from the use of Yb as an impurity probe for Rb-BECs [125] to the creation of open shell dipolar molecules [36].

Appendix A

Spectroscopic Excitation of Motional States

This appendix discusses the excitation of motional states in optical lattice spectroscopy experiments. The full interaction Hamiltonian of a two-level atom with states $|g\rangle$ and $|e\rangle$ and a running plane-wave electric field is given by [122]:

$$\mathcal{H}_{\text{int}} = \frac{\hbar}{2}\Omega_0 (|g\rangle \langle e| \otimes e^{-i\mathbf{k}_L\mathbf{r}} + |e\rangle \langle g| \otimes e^{i\mathbf{k}_L\mathbf{r}}) \quad (\text{A.1})$$

Here, \mathbf{k}_L is the wave-vector of the electric field. The Hamiltonian has already been transformed into the reference frame rotating at the laser frequency, and the rotating wave approximation has been applied. The factors $e^{\pm i\mathbf{k}_L\mathbf{r}}$ stemming from the running-wave nature of the electric field lead to the coupling of different momentum states. This can be seen by considering the transition matrix element for a freely moving atom. The motional eigenstates of an atom experiencing no forces are the eigenstates of the momentum operator, which are plane waves:

$$|\mathbf{k}\rangle = \frac{1}{\sqrt{V}}e^{i\mathbf{k}\mathbf{r}}, \quad (\text{A.2})$$

where V is a suitable normalization constant. The transition matrix element for an atom with initial momentum $\hbar\mathbf{k}_i$ and final momentum $\hbar\mathbf{k}_f$ is then given by:

$$\langle e, \mathbf{k}_f | \mathcal{H}_{\text{int}} | g, \mathbf{k}_i \rangle = \frac{\hbar}{2}\Omega_0 \frac{1}{V} \int e^{-i\mathbf{k}_f\mathbf{r}} e^{i\mathbf{k}_L\mathbf{r}} e^{i\mathbf{k}_i\mathbf{r}} d^3r = \frac{\hbar}{2}\Omega_0 \cdot \delta(\mathbf{k}_i + \mathbf{k}_L - \mathbf{k}_f) \quad (\text{A.3})$$

The Dirac delta function expresses the momentum conservation condition $\mathbf{k}_f = \mathbf{k}_i + \mathbf{k}_L$. Thus, when the atom is promoted to the electronically excited state $|e\rangle$, it simultaneously gets a kick due to the momentum of the absorbed photon.

If the atom is moving through a periodic lattice potential, its eigenstates are no longer plane waves, but rather the Bloch waves of the lattice, described by their quasimomentum \mathbf{q} and band-index n . The wavefunction of the state $|n, \mathbf{q}\rangle$ is then given by:

$$\psi_{n,\mathbf{q}}(\mathbf{r}) = u_{n,\mathbf{q}}(\mathbf{r}) e^{i\mathbf{q}\mathbf{r}}, \quad (\text{A.4})$$

where $u_{n,\mathbf{q}}(\mathbf{r})$ is the Bloch function. In this case the corresponding transition matrix element is given by:

$$d = \langle e, m, \mathbf{q}_f | \mathcal{H}_{\text{int}} | g, n, \mathbf{q}_i \rangle = \frac{\hbar}{2}\Omega_0 \int \psi_{m,\mathbf{q}_f}^*(\mathbf{r}) \psi_{n,\mathbf{q}_i}(\mathbf{r}) \cdot e^{i\mathbf{k}_L\mathbf{r}} d^3r \quad (\text{A.5})$$

In analogy to vibrational spectroscopy of molecules, the overlap integral in eq. (A.5) will be called the Franck-Condon factor of the transition in the following. For our experimental setup, the matrix element can be further simplified: Since our lattice is composed of a one-dimensional lattice along y and a two-dimensional triangular lattice in the x - z plane, the lattice Hamiltonian can be written as a sum of these two lattices:

$$\mathcal{H}_{\text{lat}}(\mathbf{r}) = \mathcal{H}_{1\text{D}}(y) + \mathcal{H}_{2\text{D}}(x, z) \quad (\text{A.6})$$

Consequently, the eigenstates can be written as products of the eigenstates of the 1D- and 2D-lattices:

$$\psi_{n_1, n_2, q_1, \mathbf{q}_2}(\mathbf{r}) = \psi_{n_1, q_1}(y) \cdot \psi_{n_2, \mathbf{q}_2}(x, z) \quad (\text{A.7})$$

Making use of this factorization and the fact that the excitation laser propagates along the direction of the 1D-lattice, the matrix element of eq. (A.5) simplifies to:

$$d = \frac{\hbar}{2} \Omega_0 \int \psi_{m_1, q_{1f}}^*(y) \psi_{n_1, q_{1i}}(y) e^{ik_L y} dy \int \psi_{m_2, \mathbf{q}_{2f}}^*(x, z) \psi_{n_2, \mathbf{q}_{2i}}(x, z) dx dz \quad (\text{A.8})$$

$$= \frac{\hbar}{2} \Omega_0 \delta_{m_2, n_2} \delta(\mathbf{q}_{2f} - \mathbf{q}_{2i}) \int \psi_{m_1, q_{1f}}^*(y) \psi_{n_1, q_{1i}}(y) e^{ik_L y} dy \quad (\text{A.9})$$

Here, the orthonormalization of the x - z -eigenstates has been used. The resulting delta functions express the fact that the motional state transverse to the direction of the spectroscopy laser cannot be changed during the laser excitation. In order to get further insight into the remaining Franck-Condon integral, it is useful to expand the 1D-wavefunctions according to Bloch's theorem as a sum over reciprocal 1D-lattice vectors G :

$$\psi_{n_1, q_1}(y) = \sum_G c_{n_1}(q_1 - G) e^{i(q_1 - G)y}. \quad (\text{A.10})$$

Inserting this Fourier sum into eq. (A.9), one obtains:

$$\begin{aligned} d &= \frac{\hbar}{2} \Omega_0 \delta_{m_2, n_2} \delta(\mathbf{q}_{2f} - \mathbf{q}_{2i}) \sum_{G, G'} c_{n_1}(q_{1i} - G) c_{m_1}^*(q_{1f} - G') \int e^{i(q_{1i} - G)y} e^{-i(q_{1f} - G')y} e^{ik_L y} dy \\ &= \frac{\hbar}{2} \Omega_0 \delta_{m_2, n_2} \delta(\mathbf{q}_{2f} - \mathbf{q}_{2i}) \sum_{G, G'} c_n(q_i - G) c_m^*(q_{1f} - G') \cdot \delta(q_{1i} + k_L - q_{1f} - (G - G')) \end{aligned} \quad (\text{A.11})$$

Here, the Dirac delta function under the sum expresses the conservation of quasimomentum along y , implying momentum transfer from the excitation laser to the atoms:

$$q_{1i} + k_L = q_{1f} + \tilde{G}, \quad (\text{A.12})$$

where $\tilde{G} = G - G'$. Since the quasimomenta q_{1f} and q_{1i} are restricted to the first Brillouin zone, it can easily be verified that there is only one combination of q_{1f} and \tilde{G} which fulfills eq. (A.12). Thus, the sum in eq. (A.11) depends only on q_{1i} and k_L and we can write:

$$d = \frac{\hbar}{2} \Omega_0 \cdot \alpha_{n_1, m_1}(q_{1i}, k_L) \cdot \delta_{m_2, n_2} \delta(\mathbf{q}_{2f} - \mathbf{q}_{2i}) \quad (\text{A.13})$$

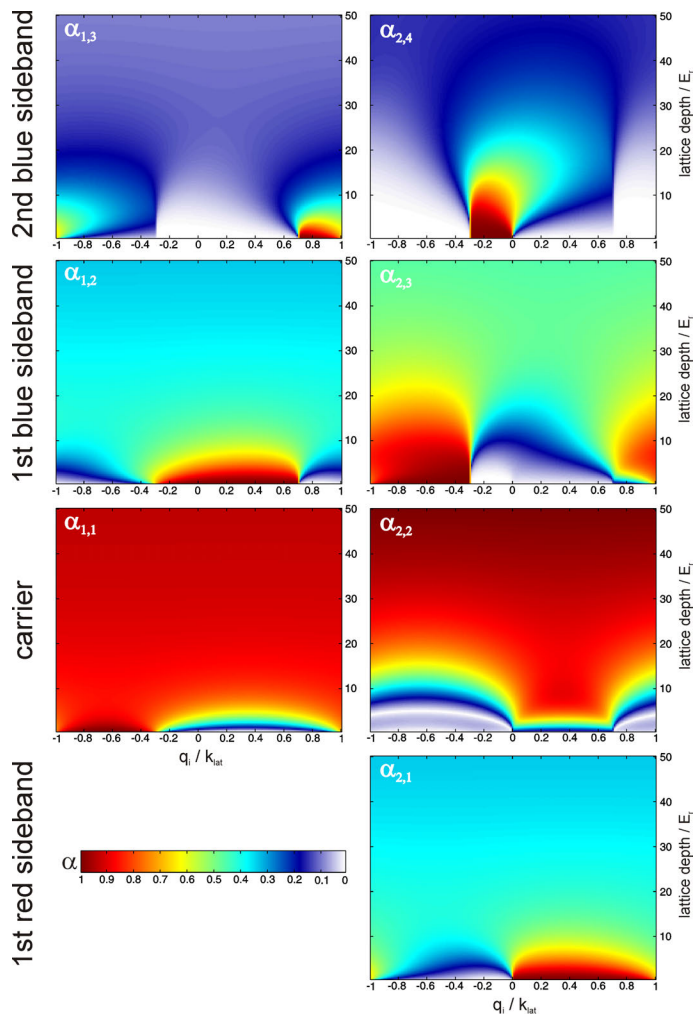


Figure A.1: Franck-Condon factors α_{n_1, m_1} for transitions between different bands in a sinusoidal optical lattice plotted as a function of the initial quasi-momentum and the lattice depth. The wavenumber of the spectroscopy laser is taken to be $k_L = 1.3k_{\text{lat}}$. A detailed explanation is given in the main text.

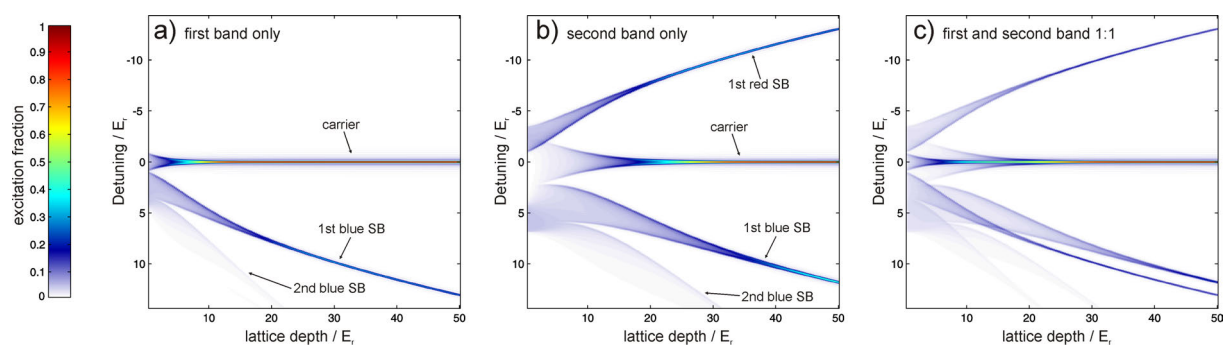


Figure A.2: Rabi spectra of atoms in a one-dimensional optical lattice with no transverse motional degrees of freedom, obtained by numerically diagonalizing the spectroscopy Hamiltonian. Panel a) depicts the spectrum obtained for an initially completely filled lowest band with no higher band population. In b) the initial state is a completely filled second band with all other bands empty. The spectrum c) is obtained when the lowest and the first excited band are initially populated. Further explanations are given in the main text.

Thus, on top of the selection rule, stating that band-index and quasimomentum are unchanged along the propagation direction transverse to the excitation laser, the matrix element contains the band- and momentum dependent Franck-Condon factor $\alpha_{n,m}(q_{1i}, k_L)$, causing a reduction of the bare Rabi frequency. Figure A.1 depicts $\alpha_{n,m}(q_{1i}, k_L)$ as a function of lattice depth for different inter- and intra-band transitions in a sinusoidal optical lattice. The lattice depth is given in units of the recoil energy with respect to the lattice laser $E_r = \hbar^2 k_{\text{lat}}^2 / 2M$, where k_{lat} is the wavenumber of the lattice laser and M is the mass of the atom. The wavenumber of the spectroscopy laser is taken to be $k_L = 1.3k_{\text{lat}}$ as is the case for the $^1S_0 \rightarrow ^3P_0$ clock transition of Yb.

For small lattice depths, there is a strong q -dependence of the Franck-Condon factors, which quickly flattens as the lattice depth increases. For large lattice depths all quasimomenta can be excited equally well, leaving only the dependence of α on the band-index. The regime of negligible q -dependence is analogous to the Lamb-Dicke regime in the spectroscopy of harmonically confined atoms or ions, since in the limit of large lattice depth each lattice site can be treated as an individual harmonic microtrap.

Having calculated the matrix elements from eq. (A.13), one can numerically diagonalize the spectroscopy Hamiltonian and calculate the excitation spectrum in the lattice. Figure A.2 shows spectra obtained for a purely one-dimensional lattice along the direction of the probe laser, neglecting the transverse dimensions. The excitation pulse has been assumed to be a square pulse of duration $\tau = \pi/\Omega_0$, i.e. a π -pulse with respect to the bare Rabi frequency. The Rabi frequency itself has been set to $\Omega_0 = 0.1E_r/\hbar$, corresponding to $2\pi \cdot 200$ Hz for Yb in a magic optical lattice. Panel a) shows the spectrum obtained for a completely occupied first band, with no higher band population. The spectrum in panel b) is obtained for the second band completely filled with no population in other bands, while in c) half the population is in the first and the other half in the second band, with both bands filled completely. The different sidebands appearing in the spectra reveal the bandstructure of the lattice. The shape of the sidebands is determined by the dispersion of the lattice and the q -dependence of the Franck-Condon factors as well as the density of states. As the lattice depth increases, the bands as well as the Franck-Condon factors flatten. Consequently, the spectral width of the sidebands decreases and the excitation becomes more homogeneous. The higher the initial band-index and the higher the order of the sideband, the more confinement is needed to achieve a sharp resonance. For a Rabi frequency of 200 Hz used here, the carrier resonance of atoms in the first band becomes Fourier limited for lattice depths above $10E_r$, while for atoms in the second band a lattice depth above $30E_r$ is necessary to achieve an equally narrow spectrum. When exciting higher bands, deeper lattices are required. The first blue sideband becomes Fourier limited above $25E_r$ for atoms in the first band and above $45E_r$ for atoms in the second band.

For future experiments, the simultaneous excitation of electronic and motional states opens up interesting possibilities. In deep lattices where the Franck-Condon factor is q -independent and the bandwidths are low, the whole atomic ensemble can be excited to a higher band, allowing to study band-relaxation processes and their dependence on interaction and dissipation of metastable-state collisions. Alternatively, in a shallow lattice one can excite the atoms in a momentum resolved way and study particle-hole dynamics and transport processes. This could

be especially interesting in a Kondo lattice scenario, where the Kondo-exchange leads to an anomalously high effective mass of the particles and so-called *heavy-fermion* behavior. This behavior should result in a dramatic slow down of mass transport in the lattice [81].

Appendix B

Derivation of the Spectroscopy Hamiltonian

In this appendix, I derive the Hamiltonian $\hat{\mathcal{H}}_S$ for two interacting fermionic atoms in the ground state of a harmonic trap driven by a classical light field. It describes the clock spectroscopy of two-component fermions in a deep optical lattice reported in section 3.3.2 and complements the theoretical discussion in section 3.3.1. $\hat{\mathcal{H}}_S$ has four contributions:

$$\hat{\mathcal{H}}_S = \underbrace{\hat{\mathcal{H}}_{\text{el}} + \hat{\mathcal{H}}_Z + \hat{\mathcal{H}}_{\text{int}}}_{\hat{\mathcal{H}}_a} + \hat{\mathcal{H}}_L. \quad (\text{B.1})$$

$\hat{\mathcal{H}}_{\text{el}}$ is the bare electronic Hamiltonian, $\hat{\mathcal{H}}_Z$ describes the Zeeman shift due to an external magnetic field, and $\hat{\mathcal{H}}_{\text{int}}$ contains the s-wave interaction between the two atoms. Together, these three contributions form the atomic Hamiltonian $\hat{\mathcal{H}}_a$. $\hat{\mathcal{H}}_L$ is the coupling Hamiltonian between the atoms and the light field. Because of the extremely long lifetime of the excited states, spontaneous emission can be neglected.

For the experiments described in section 3.3.2 two different configurations are used, which are depicted in fig. 3.22. In the $\pm 5/2$ -configuration, the atomic sample is prepared in a mixture of the $m_F = \pm 5/2$ substates of the 1S_0 ground state manifold and π -polarized light is used. In this configuration, the states $|m_F = +5/2\rangle$ and $|m_F = -5/2\rangle$ are denoted as $|\uparrow\rangle$ and $|\downarrow\rangle$, respectively. In the $(3/2)(5/2)$ -configuration, the atoms are prepared in a mixture of the $|m_F = 3/2\rangle$ and $|m_F = 5/2\rangle$ substates and the spectroscopy laser is σ^+ -polarized. In this case, the notation for the spin states is $|m_F = 3/2\rangle = |\downarrow\rangle$ and $|m_F = 5/2\rangle = |\uparrow\rangle$. The electronic states 1S_0 and 3P_0 are denoted as $|g\rangle$ and $|e\rangle$, respectively, in both configurations.

The two-atom Hilbert space has already been described in section 3.3.1. In accordance with the Pauli-Principle it includes only those states that are anti-symmetric with respect to particle exchange and is six-dimensional.

Two relevant basis sets for this space are the eigenbases of the atom-atom interaction and the Zeeman shift, which are given in eqs. (3.13) and (3.14). Here, they are written down again together with their vector representations used later on for the matrix representations of the

Hamiltonians. The interaction eigenbasis $\{|b_i^{\text{int}}\rangle\}$ is given by:

$$|ee\rangle \otimes |\uparrow\downarrow\rangle^- = \{1, 0, 0, 0, 0, 0\} = |b_1^{\text{int}}\rangle \quad (\text{B.2})$$

$$|eg\rangle^+ \otimes |\uparrow\downarrow\rangle^- = \{0, 1, 0, 0, 0, 0\} = |b_2^{\text{int}}\rangle \quad (\text{B.3})$$

$$|eg\rangle^- \otimes |\uparrow\uparrow\rangle = \{0, 0, 1, 0, 0, 0\} = |b_3^{\text{int}}\rangle \quad (\text{B.4})$$

$$|eg\rangle^- \otimes |\uparrow\downarrow\rangle^+ = \{0, 0, 0, 1, 0, 0\} = |b_4^{\text{int}}\rangle \quad (\text{B.5})$$

$$|eg\rangle^- \otimes |\downarrow\downarrow\rangle = \{0, 0, 0, 0, 1, 0\} = |b_5^{\text{int}}\rangle \quad (\text{B.6})$$

$$|gg\rangle \otimes |\uparrow\downarrow\rangle^- = \{0, 0, 0, 0, 0, 1\} = |b_6^{\text{int}}\rangle, \quad (\text{B.7})$$

and the Zeeman eigenbasis $\{|b_i^Z\rangle\}$ by:

$$|ee\rangle \otimes |\uparrow\downarrow\rangle^- = \{1, 0, 0, 0, 0, 0\} = |b_1^Z\rangle \quad (\text{B.8})$$

$$\frac{1}{\sqrt{2}} (|e \uparrow g \downarrow\rangle - |g \downarrow e \uparrow\rangle) = \{0, 1, 0, 0, 0, 0\} = |b_2^Z\rangle \quad (\text{B.9})$$

$$|eg\rangle^- \otimes |\uparrow\uparrow\rangle = \{0, 0, 1, 0, 0, 0\} = |b_3^Z\rangle \quad (\text{B.10})$$

$$\frac{1}{\sqrt{2}} (|g \uparrow e \downarrow\rangle - |e \downarrow g \uparrow\rangle) = \{0, 0, 0, 1, 0, 0\} = |b_4^Z\rangle \quad (\text{B.11})$$

$$|eg\rangle^- \otimes |\downarrow\downarrow\rangle = \{0, 0, 0, 0, 1, 0\} = |b_5^Z\rangle \quad (\text{B.12})$$

$$|gg\rangle \otimes |\uparrow\downarrow\rangle^- = \{0, 0, 0, 0, 0, 1\} = |b_6^Z\rangle, \quad (\text{B.13})$$

$|eg\rangle^\pm = 1/\sqrt{2} (|eg\rangle \pm |ge\rangle)$ denote the eg -singlet and -triplet states, respectively. Analogously, $|\uparrow\downarrow\rangle^\pm$ denote the $\uparrow\downarrow$ -singlet and -triplet states. It will become clear later on that $\{|b_i^{\text{int}}\rangle\}$ and $\{|b_i^Z\rangle\}$ are indeed eigenbases to $\hat{\mathcal{H}}_{\text{int}}$ and $\hat{\mathcal{H}}_Z$.

In the reference frame rotating at the laser frequency, the electronic Hamiltonian for a single atom is spin independent and reads:

$$\hat{\mathcal{H}}_{\text{el},1} = \frac{\hbar\Delta}{2} (|g\rangle\langle g| - |e\rangle\langle e|), \quad (\text{B.14})$$

where $\Delta = \omega_L - \omega_a$ is the detuning of the laser frequency from the atomic transition. From this elementary Hamiltonian the full two-atom Hamiltonian, including spin is given by the tensor product:

$$\hat{\mathcal{H}}_{\text{el}} = \left(\hat{\mathcal{H}}_{\text{el},1}^{(1)} \otimes \mathbb{1}_{\uparrow\downarrow}^{(1)} \right) \otimes \mathbb{1}^{(2)} + \mathbb{1}^{(1)} \otimes \left(\hat{\mathcal{H}}_{\text{el},1}^{(2)} \otimes \mathbb{1}_{\uparrow\downarrow}^{(2)} \right) \quad (\text{B.15})$$

$$= \frac{\hbar\Delta}{2} (|gg\rangle|\uparrow\downarrow\rangle^- \langle gg| \langle\uparrow\downarrow|^- - |ee\rangle|\uparrow\downarrow\rangle^- \langle ee| \langle\uparrow\downarrow|^-), \quad (\text{B.16})$$

where the upper index (1, 2) denotes atom 1 and atom 2, respectively.

The Zeeman Hamiltonian acts on the combined spin and electronic space of each atom. For a single atom it has the form:

$$\begin{aligned} \hat{\mathcal{H}}_{Z,1} = & \hbar(\Delta_{Z,g\downarrow} |g, \downarrow\rangle \langle g, \downarrow| + \Delta_{Z,g\uparrow} |g, \uparrow\rangle \langle g, \uparrow| \\ & + \Delta_{Z,e\downarrow} |e, \downarrow\rangle \langle e, \downarrow| + \Delta_{Z,e\uparrow} |e, \uparrow\rangle \langle e, \uparrow|) \end{aligned} \quad (\text{B.17})$$

The combined two-atom Zeeman Hamiltonian is then:

$$\hat{\mathcal{H}}_Z = \hat{\mathcal{H}}_{Z,1}^{(1)} \otimes \mathbb{1}^{(2)} + \mathbb{1}^{(1)} \otimes \hat{\mathcal{H}}_{Z,1}^{(2)} \quad (\text{B.18})$$

Multiplying out the tensor product and diagonalizing the Hamiltonian, one finds that $\{|b_i^Z\rangle\}$ is indeed the eigenbasis of $\hat{\mathcal{H}}_Z$:

$$\begin{aligned} \hat{\mathcal{H}}_Z = & (\Delta_{Z,e\uparrow} + \Delta_{Z,e\downarrow}) |b_1^Z\rangle \langle b_1^Z| + (\Delta_{Z,e\uparrow} + \Delta_{Z,g\downarrow}) |b_2^Z\rangle \langle b_2^Z| \\ & + (\Delta_{Z,e\uparrow} + \Delta_{Z,g\uparrow}) |b_3^Z\rangle \langle b_3^Z| + (\Delta_{Z,e\downarrow} + \Delta_{Z,g\uparrow}) |b_4^Z\rangle \langle b_4^Z| \\ & + (\Delta_{Z,e\downarrow} + \Delta_{Z,g\downarrow}) |b_5^Z\rangle \langle b_5^Z| + (\Delta_{Z,g\uparrow} + \Delta_{Z,g\downarrow}) |b_6^Z\rangle \langle b_6^Z| \end{aligned} \quad (\text{B.19})$$

The interaction between ground- and metastable state Yb atoms has already been discussed in section 2.1. The interaction Hamiltonian is spin independent and is given by eq. (2.4). I write it here again for completeness:

$$\begin{aligned} \hat{\mathcal{H}}_{\text{int}} = & (U_{ee} |ee\rangle \langle ee| + U_{eg}^+ |eg\rangle^+ \langle eg|^+ + U_{eg}^- |eg\rangle^- \langle eg|^+ + U_{gg} |gg\rangle \langle gg|) \\ & \otimes \mathbb{1}_{\uparrow\downarrow}^{(1)} \otimes \mathbb{1}_{\uparrow\downarrow}^{(2)}. \end{aligned} \quad (\text{B.20})$$

Since the interaction is spin independent it is immediately clear that $\{|b_i^{\text{int}}\rangle\}$ is an eigenbasis of $\hat{\mathcal{H}}_{\text{int}}$.

The commutator of $\hat{\mathcal{H}}_{\text{int}}$ and $\hat{\mathcal{H}}_Z$ is given by:

$$\begin{aligned} [\hat{\mathcal{H}}_Z, \hat{\mathcal{H}}_{\text{int}}] = & \frac{1}{2} \Delta U_{eg} \Delta_{Z-} |b_2^Z\rangle \langle b_4^Z| \\ & - \frac{1}{2} \Delta U_{eg} \Delta_{Z-} |b_4^Z\rangle \langle b_2^Z|, \end{aligned} \quad (\text{B.21})$$

where $\Delta_{Z-} = (\Delta_{Z,e\downarrow} - \Delta_{Z,e\uparrow} - \Delta_{Z,g\downarrow} + \Delta_{Z,g\uparrow})$ is the differential Zeeman shift between the two transitions and $\Delta U_{eg} = (U_{eg}^+ - U_{eg}^-)$ is the difference between the interaction energies of the eg -singlet and -triplet states. This shows that in the presence of a non-zero magnetic field and at the same time a non-zero differential interaction ΔU_{eg} , neither $\{|b_i^{\text{int}}\rangle\}$ nor $\{|b_i^Z\rangle\}$ diagonalize the two-atom Hamiltonian $\hat{\mathcal{H}}_a$. This complicates the interpretation of the observed spectra in the $\pm 5/2$ -configuration as is explained in section 3.3.1.

The last contribution to the spectroscopy Hamiltonian is the atom-light interaction that is captured in $\hat{\mathcal{H}}_L$. The form of $\hat{\mathcal{H}}_L$ depends on the polarization of the spectroscopy laser, as well as on the particular m_F -levels chosen as $|\uparrow\rangle$ and $|\downarrow\rangle$. For a single atom in the $\pm 5/2$ -configuration it has the form (see e.g. [126]):

$$\hat{\mathcal{H}}_{L1,\pi} = \frac{\hbar\Omega}{2} (|g\uparrow\rangle \langle e\uparrow| - |g\downarrow\rangle \langle e\downarrow|) + h.c. \quad (\text{B.22})$$

Here, $\hat{\mathcal{H}}_L$ has been transformed into the reference frame rotating at the laser frequency, as was already done with the electronic Hamiltonian in eq. (B.14). Moreover, the rotating wave

approximation has been applied to eliminate the fast oscillating terms. Ω is the Rabi frequency of the $|g \uparrow\rangle \rightarrow |e \uparrow\rangle$ transition. The minus sign in eq. (B.22) is due to the opposite sign of the Clebsch-Gordan coefficients of the $m_F = +5/2$ and $m_F = -5/2$ transitions.

In the $(3/2)(5/2)$ -configuration, the atom-light coupling Hamiltonian for a single atom is given by:

$$\hat{\mathcal{H}}_{L1,\sigma} = \frac{\hbar\Omega}{2} |g \downarrow\rangle \langle e \uparrow| + h.c. \quad (\text{B.23})$$

Since the $|m_F = 5/2\rangle$ state does not couple to σ_+ -polarized light, there is only one Rabi frequency in $\hat{\mathcal{H}}_{L,\sigma}$. The atom-light coupling Hamiltonian for two atoms is again constructed from the single-atom Hamiltonians by a sum of tensor products:

$$\hat{\mathcal{H}}_{L,\pi,\sigma} = \hat{\mathcal{H}}_{L1,\pi,\sigma}^{(1)} \otimes \mathbb{1}^{(2)} + \mathbb{1}^{(1)} \otimes \hat{\mathcal{H}}_{L1,\pi,\sigma}^{(2)} \quad (\text{B.24})$$

Evaluating eq. (B.24) for the two configurations one finds:

$$\hat{\mathcal{H}}_{L,\pi} = \frac{\hbar\sqrt{2}\Omega}{2} (|eg\rangle^- |\uparrow\downarrow\rangle^+ \langle gg| \langle \uparrow\downarrow\rangle^- - |ee\rangle |\uparrow\downarrow\rangle^- \langle eg|^- \langle \uparrow\downarrow\rangle^+ + h.c.) \quad (\text{B.25})$$

$$\hat{\mathcal{H}}_{L,\sigma} = -\frac{\hbar\Omega}{2} (|eg\rangle^- |\uparrow\uparrow\rangle \langle gg| \langle \uparrow\downarrow\rangle^- + |ee\rangle |\uparrow\downarrow\rangle^- \langle eg|^- \langle \downarrow\downarrow\rangle + h.c.) \quad (\text{B.26})$$

The complete spectroscopy Hamiltonian $\hat{\mathcal{H}}_S$ is now obtained by summing up eqs. (B.16), (B.19), (B.20) and (B.24). A good overview over the Hamiltonian is obtained by writing down its matrix representation. For the $(3/2)(5/2)$ -configuration using the interaction basis $\{|b_i^{\text{int}}\rangle\}$ the Hamiltonian matrix reads:

$$\mathcal{H}_{S,\sigma}^{\text{int}}/\hbar = \begin{pmatrix} U_{ee} - \Delta + \Delta_{Z,e+} & 0 & 0 & 0 & -\frac{\Omega}{2} & 0 \\ 0 & U_{eg}^+ + \Delta_{Z,+} & 0 & \Delta_{Z,-} & 0 & 0 \\ 0 & 0 & U_{eg}^- + \Delta_{Z,\uparrow+} & 0 & 0 & -\frac{\Omega}{2} \\ 0 & \Delta_{Z,-} & 0 & U_{eg}^- + \Delta_{Z,+} & 0 & 0 \\ -\frac{\Omega}{2} & 0 & 0 & 0 & U_{eg}^- + \Delta_{Z,\downarrow+} & 0 \\ 0 & 0 & -\frac{\Omega}{2} & 0 & 0 & \Delta + \Delta_{Z,g+} + U_{gg} \end{pmatrix}. \quad (\text{B.27})$$

The different sums of Zeeman shifts have been abbreviated as follows:

$$\Delta_{Z,+} = \frac{1}{2} (\Delta_{Z,e\uparrow} + \Delta_{Z,e\downarrow} + \Delta_{Z,g\uparrow} + \Delta_{Z,g\downarrow}) \quad (\text{B.28})$$

$$\Delta_{Z,-} = \frac{1}{2} (\Delta_{Z,e\uparrow} - \Delta_{Z,e\downarrow} - \Delta_{Z,g\uparrow} + \Delta_{Z,g\downarrow}) \quad (\text{B.29})$$

$$\Delta_{Z,e+} = \Delta_{Z,e\uparrow} + \Delta_{Z,e\downarrow} \quad (\text{B.30})$$

$$\Delta_{Z,g+} = \Delta_{Z,e\uparrow} + \Delta_{Z,e\downarrow} \quad (\text{B.31})$$

$$\Delta_{Z,\uparrow+} = \Delta_{Z,e\uparrow} + \Delta_{Z,g\uparrow} \quad (\text{B.32})$$

$$\Delta_{Z,\downarrow+} = \Delta_{Z,e\downarrow} + \Delta_{Z,g\downarrow} \quad (\text{B.33})$$

$$\Delta_{Z,\uparrow\downarrow} = \Delta_{Z,e\uparrow} + \Delta_{Z,g\downarrow} \quad (\text{B.34})$$

$$\Delta_{Z,\downarrow\uparrow} = \Delta_{Z,e\downarrow} + \Delta_{Z,g\uparrow} \quad (\text{B.35})$$

Alternatively the Zeeman basis $\{|b_i^Z\rangle\}$ can be used and one obtains:

$$\mathcal{H}_{S,\sigma}^Z/\hbar = \begin{pmatrix} U_{ee} - \Delta + \Delta_{Z,e+} & 0 & 0 & 0 & -\frac{\Omega}{2} & 0 \\ 0 & \overline{U_{eg}} + \Delta_{Z,\uparrow\downarrow} & 0 & \frac{\Delta U_{eg}}{2} & 0 & 0 \\ 0 & 0 & U_{eg}^- + \Delta_{Z,\uparrow+} & 0 & 0 & -\frac{\Omega}{2} \\ 0 & \frac{\Delta U_{eg}}{2} & 0 & \overline{U_{eg}} + \Delta_{Z,\downarrow\uparrow} & 0 & 0 \\ -\frac{\Omega}{2} & 0 & 0 & 0 & U_{eg}^- + \Delta_{Z,\downarrow+} & 0 \\ 0 & 0 & -\frac{\Omega}{2} & 0 & 0 & \Delta + \Delta_{Z,g+} + U_{gg} \end{pmatrix}, \quad (\text{B.36})$$

where $\Delta U_{eg} = U_{eg}^+ - U_{eg}^-$ and $\overline{U_{eg}} = (U_{eg}^+ + U_{eg}^-)/2$ are abbreviations for the differential and the average interaction of the eg -states. In the $\pm 5/2$ -configuration the Hamiltonian matrix in the interaction basis is given by:

$$\mathcal{H}_{S,\pi}^{\text{int}}/\hbar = \begin{pmatrix} -\Delta + U_{ee} & 0 & 0 & -\frac{\Omega}{\sqrt{2}} & 0 & 0 \\ 0 & U_{eg}^+ & 0 & \Delta_{Z-} & 0 & 0 \\ 0 & 0 & U_{eg}^- + \Delta_{Z+} & 0 & 0 & 0 \\ -\frac{\Omega}{\sqrt{2}} & \Delta_{Z-} & 0 & U_{eg}^- & 0 & \frac{\Omega}{\sqrt{2}} \\ 0 & 0 & 0 & 0 & U_{eg}^- - \Delta_{Z+} & 0 \\ 0 & 0 & 0 & \frac{\Omega}{\sqrt{2}} & 0 & \Delta + U_{gg} \end{pmatrix}. \quad (\text{B.37})$$

Here, in addition to the abbreviations of eqs. (B.28) to (B.33) it was used that in the $\pm 5/2$ -configuration $\Delta_{Z,g\uparrow} = -\Delta_{Z,g\downarrow}$ and $\Delta_{Z,e\uparrow} = -\Delta_{Z,e\downarrow}$. In the Zeeman basis this Hamiltonian is given by:

$$\mathcal{H}_{S,\pi}^Z/\hbar = \begin{pmatrix} -\Delta + U_{ee} & -\frac{\Omega}{2} & 0 & \frac{\Omega}{2} & 0 & 0 \\ -\frac{\Omega}{2} & \overline{U}_{eg} + \Delta_{Z-} & 0 & \frac{\Delta U_{eg}}{2} & 0 & \frac{\Omega}{2} \\ 0 & 0 & U_{eg}^- + \Delta_{Z+} & 0 & 0 & 0 \\ \frac{\Omega}{2} & \frac{\Delta U_{eg}}{2} & 0 & \overline{U}_{eg} - \Delta_{Z-} & 0 & -\frac{\Omega}{2} \\ 0 & 0 & 0 & 0 & U_{eg}^- - \Delta_{Z+} & 0 \\ 0 & \frac{\Omega}{2} & 0 & -\frac{\Omega}{2} & 0 & \Delta + U_{gg} \end{pmatrix} \quad (\text{B.38})$$

Appendix C

Yb Term Diagram

Bibliography

- [1] Sören Dörscher, Alexander Thobe, Bastian Hundt, André Kochanke, Rodolphe Le Targat, Patrick Windpassinger, Christoph Becker, and Klaus Sengstock, *Creation of quantum-degenerate gases of ytterbium in a compact 2D-/3D-magneto-optical trap setup*, Review of Scientific Instruments **84**, 043109 (2013)
- [2] Patrick A. Lee, Naoto Nagaosa, and Xiao-Gang Wen, *Doping a Mott insulator: Physics of high-temperature superconductivity*, Rev. Mod. Phys. **78**, 17–85 (2006)
- [3] Leon Balents, *Spin liquids in frustrated magnets*, Nature **464**, 199–208 (2010)
- [4] C.W.J. Beenakker, *Search for Majorana Fermions in Superconductors*, Annual Review of Condensed Matter Physics **4**, 113–136 (2013)
- [5] D. Jaksch, C. Bruder, J. I. Cirac, C. W. Gardiner, and P. Zoller, *Cold Bosonic Atoms in Optical Lattices*, Phys. Rev. Lett. **81**, 3108–3111 (1998)
- [6] Cheng Chin, Rudolf Grimm, Paul Julienne, and Eite Tiesinga, *Feshbach resonances in ultracold gases*, Rev. Mod. Phys. **82**, 1225–1286 (2010)
- [7] Immanuel Bloch, *Ultracold quantum gases in optical lattices*, Nat Phys **1**, 23–30 (2005)
- [8] Markus Greiner, Olaf Mandel, Tilman Esslinger, Theodor W. Hänsch, and Immanuel Bloch, *Quantum phase transition from a superfluid to a Mott insulator in a gas of ultracold atoms*, Nature **415**, 39–44 (2002)
- [9] Robert Jördens, Niels Strohmaier, Kenneth Günter, Henning Moritz, and Tilman Esslinger, *A Mott insulator of fermionic atoms in an optical lattice*, Nature **455**, 204–207 (2008)
- [10] U. Schneider, L. Hackermüller, S. Will, Th Best, I. Bloch, T. A. Costi, R. W. Helmes, D. Rasch, and A. Rosch, *Metallic and Insulating Phases of Repulsively Interacting Fermions in a 3D Optical Lattice*, Science **322**, 1520–1525 (2008)
- [11] Qijin Chen, Jelena Stajic, Shina Tan, and K. Levin, *BCS–BEC crossover: From high temperature superconductors to ultracold superfluids*, Physics Reports **412**, 1–88 (2005)
- [12] Stefano Giorgini, Lev P. Pitaevskii, and Sandro Stringari, *Theory of ultracold atomic Fermi gases*, Rev. Mod. Phys. **80**, 1215–1274 (2008)

- [13] N. Navon, S. Nascimbène, F. Chevy, and C. Salomon, *The Equation of State of a Low-Temperature Fermi Gas with Tunable Interactions*, *Science* **328**, 729–732 (2010)
- [14] P. Soltan-Panahi, J. Struck, P. Hauke, A. Bick, W. Plenkers, G. Meineke, C. Becker, P. Windpassinger, M. Lewenstein, and K. Sengstock, *Multi-component quantum gases in spin-dependent hexagonal lattices*, *Nat Phys* **7**, 434–440 (2011)
- [15] Gyu-Boong Jo, Jennie Guzman, Claire K. Thomas, Pavan Hosur, Ashvin Vishwanath, and Dan M. Stamper-Kurn, *Ultracold Atoms in a Tunable Optical Kagome Lattice*, *Phys. Rev. Lett.* **108**, 045305 (2012)
- [16] Waseem S. Bakr, Jonathon I. Gillen, Amy Peng, Simon Fölling, and Markus Greiner, *A quantum gas microscope for detecting single atoms in a Hubbard-regime optical lattice*, *Nature* **462**, 74–77 (2009)
- [17] Jacob F. Sherson, Christof Weitenberg, Manuel Endres, Marc Cheneau, Immanuel Bloch, and Stefan Kuhr, *Single-atom-resolved fluorescence imaging of an atomic Mott insulator*, *Nature* **467**, 68–72 (2010)
- [18] Y.-J. Lin, R. L. Compton, K. Jiménez-García, J. V. Porto, and I. B. Spielman, *Synthetic magnetic fields for ultracold neutral atoms*, *Nature* **462**, 628–632 (2009)
- [19] Axel Griesmaier, Jörg Werner, Sven Hensler, Jürgen Stuhler, and Tilman Pfau, *Bose-Einstein Condensation of Chromium*, *Phys. Rev. Lett.* **94**, 160401 (2005)
- [20] Mingwu Lu, Nathaniel Q. Burdick, Seo Ho Youn, and Benjamin L. Lev, *Strongly Dipolar Bose-Einstein Condensate of Dysprosium*, *Phys. Rev. Lett.* **107**, 190401 (2011)
- [21] K. Aikawa, A. Frisch, M. Mark, S. Baier, A. Rietzler, R. Grimm, and F. Ferlaino, *Bose-Einstein Condensation of Erbium*, *Phys. Rev. Lett.* **108**, 210401 (2012)
- [22] T. Lahaye, C. Menotti, L. Santos, M. Lewenstein, and T. Pfau, *The physics of dipolar bosonic quantum gases*, *Rep. Prog. Phys.* **72**, 126401 (2009)
- [23] Masao Takamoto, Feng-Lei Hong, Ryoichi Higashi, and Hidetoshi Katori, *An optical lattice clock*, *Nature* **435**, 321–324 (2005)
- [24] A. V. Gorshkov, M. Hermele, V. Gurarie, C. Xu, P. S. Julienne, J. Ye, P. Zoller, E. Demler, M. D. Lukin, and A. M. Rey, *Two-orbital $SU(N)$ magnetism with ultracold alkaline-earth atoms*, *Nat Phys* **6**, 289–295 (2010)
- [25] Michael Foss-Feig, Michael Hermele, and Ana Maria Rey, *Probing the Kondo lattice model with alkaline-earth-metal atoms*, *Phys. Rev. A* **81**, 051603 (2010)
- [26] Andrew J. Daley, Martin M. Boyd, Jun Ye, and Peter Zoller, *Quantum Computing with Alkaline-Earth-Metal Atoms*, *Phys. Rev. Lett.* **101**, 170504–4 (2008)

- [27] A. V. Gorshkov, A. M. Rey, A. J. Daley, M. M. Boyd, J. Ye, P. Zoller, and M. D. Lukin, *Alkaline-Earth-Metal Atoms as Few-Qubit Quantum Registers*, Phys. Rev. Lett. **102**, 110503–4 (2009)
- [28] K. Shibata, S. Kato, A. Yamaguchi, S. Uetake, and Y. Takahashi, *A scalable quantum computer with ultranarrow optical transition of ultracold neutral atoms in an optical lattice*, Appl. Phys. B **97**, 753–758 (2009)
- [29] Hirokazu Tsunetsugu, Manfred Sigrist, and Kazuo Ueda, *The ground-state phase diagram of the one-dimensional Kondo lattice model*, Rev. Mod. Phys. **69**, 809 (1997)
- [30] Fabrice Gerbier and Jean Dalibard, *Gauge fields for ultracold atoms in optical superlattices*, New J. Phys. **12**, 033007 (2010)
- [31] Jean Dalibard, Fabrice Gerbier, Gediminas Juzeliunas, and Patrik Ohberg, *Colloquium: Artificial gauge potentials for neutral atoms*, Rev. Mod. Phys. **83**, 1523–1543 (2011)
- [32] D. J. Thouless, M. Kohmoto, M. P. Nightingale, and M. den Nijs, *Quantized Hall Conductance in a Two-Dimensional Periodic Potential*, Phys. Rev. Lett. **49**, 405–408 (1982)
- [33] Hirokazu Miyake, Georgios A. Siviloglou, Colin J. Kennedy, William Cody Burton, and Wolfgang Ketterle, *Realizing the Harper Hamiltonian with Laser-Assisted Tunneling in Optical Lattices*, Phys. Rev. Lett. **111**, 185302 (2013)
- [34] M. Aidelsburger, M. Atala, M. Lohse, J. T. Barreiro, B. Paredes, and I. Bloch, *Realization of the Hofstadter Hamiltonian with Ultracold Atoms in Optical Lattices*, Phys. Rev. Lett. **111**, 185301 (2013)
- [35] Michael Hermele, Victor Gurarie, and Ana Maria Rey, *Mott Insulators of Ultracold Fermionic Alkaline Earth Atoms: Underconstrained Magnetism and Chiral Spin Liquid*, Phys. Rev. Lett. **103**, 135301 (2009)
- [36] Daniel A. Brue and Jeremy M. Hutson, *Prospects of forming ultracold molecules in 2Σ states by magnetoassociation of alkali-metal atoms with Yb*, Phys. Rev. A **87**, 052709 (2013)
- [37] Yosuke Takasu, Kenichi Maki, Kaduki Komori, Tetsushi Takano, Kazuhito Honda, Mitsutaka Kumakura, Tsutomu Yabuzaki, and Yoshiro Takahashi, *Spin-Singlet Bose-Einstein Condensation of Two-Electron Atoms*, Phys. Rev. Lett. **91**, 040404 (2003)
- [38] Seiji Sugawa, Kensuke Inaba, Shintaro Taie, Rekishu Yamazaki, Makoto Yamashita, and Yoshiro Takahashi, *Interaction and filling-induced quantum phases of dual Mott insulators of bosons and fermions*, Nat Phys **7**, 642–648 (2011)

- [39] Shintaro Taie, Rekishu Yamazaki, Seiji Sugawa, and Yoshiro Takahashi, *An $SU(6)$ Mott insulator of an atomic Fermi gas realized by large-spin Pomeranchuk cooling*, *Nat Phys* **8**, 825–830 (2012)
- [40] Sebastian Kraft, Felix Vogt, Oliver Appel, Fritz Riehle, and Uwe Sterr, *Bose-Einstein Condensation of Alkaline Earth Atoms: $Ca40$* , *Phys. Rev. Lett.* **103**, 130401 (2009)
- [41] Simon Stellmer, Meng Khoon Tey, Bo Huang, Rudolf Grimm, and Florian Schreck, *Bose-Einstein Condensation of Strontium*, *Phys. Rev. Lett.* **103**, 200401 (2009)
- [42] K. Dieckmann, R. J. C. Spreeuw, M. Weidemüller, and J. T. M. Walraven, *Two-dimensional magneto-optical trap as a source of slow atoms*, *Phys. Rev. A* **58**, 3891 (1998)
- [43] C. Ospelkaus, S. Ospelkaus, K. Sengstock, and K. Bongs, *Interaction-Driven Dynamics of $K40$ - $Rb87$ Fermion-Boson Gas Mixtures in the Large-Particle-Number Limit*, *Phys. Rev. Lett.* **96**, 020401 (2006)
- [44] S. Mejri, J. J. McFerran, L. Yi, Y. Le Coq, and S. Bize, *Ultraviolet laser spectroscopy of neutral mercury in a one-dimensional optical lattice*, *Phys. Rev. A* **84**, 032507 (2011)
- [45] T. G. Tiecke, S. D. Gensemer, A. Ludewig, and J. T. M. Walraven, *High-flux two-dimensional magneto-optical-trap source for cold lithium atoms*, *Phys. Rev. A* **80**, 013409 (2009)
- [46] T. Kuwamoto, K. Honda, Y. Takahashi, and T. Yabuzaki, *Magneto-optical trapping of Yb atoms using an intercombination transition*, *Phys. Rev. A* **60**, R745 (1999)
- [47] K. Honda, Y. Takahashi, T. Kuwamoto, M. Fujimoto, K. Toyoda, K. Ishikawa, and T. Yabuzaki, *Magneto-optical trapping of Yb atoms and a limit on the branching ratio of the $1P1$ state*, *Phys. Rev. A* **59**, R934 (1999)
- [48] Zhao Peng-Yi, Xiong Zhuan-Xian, Liang Jie, He Ling-Xiang, and Lu Bao-Long, *Magneto-Optical Trapping of Ytterbium Atoms with a 398.9 nm Laser*, *Chinese Phys. Lett.* **25**, 3631 (2008)
- [49] U. D. Rapol, A. Krishna, A. Wasan, and V. Natarajan, *Laser cooling and trapping of Yb from a thermal source*, *Eur. Phys. J. D* **29**, 409–414 (2004)
- [50] Takashi Mukaiyama, Hidetoshi Katori, Tetsuya Ido, Ying Li, and Makoto Kuwata-Gonokami, *Recoil-Limited Laser Cooling of $Sr87$ Atoms near the Fermi Temperature*, *Phys. Rev. Lett.* **90**, 113002 (2003)
- [51] Martin M. Boyd, *High Precision Spectroscopy of Strontium in an Optical Lattice: Towards a New Standard for Frequency and Time*, Ph.D. thesis, University of Colorado, Boulder (2007)

- [52] Sören E. Dörscher, *Creation of ytterbium quantum gases with a compact 2D-/3D-MOT setup*, Ph.D. thesis, Universität Hamburg, Hamburg (2013)
- [53] Hans Kessler, *Setting up a blue laser system as light source for a Ytterbium 2D-MOT*, Diplomarbeit, Universität Hamburg, Hamburg (2011)
- [54] Jürgen Appel, Andrew MacRae, and A. I. Lvovsky, *A versatile digital GHz phase lock for external cavity diode lasers*, *Meas. Sci. Technol.* **20**, 055302 (2009)
- [55] Anders H. Hansen, Alexander Khramov, William H. Dowd, Alan O. Jamison, Vladyslav V. Ivanov, and Subhadeep Gupta, *Quantum degenerate mixture of ytterbium and lithium atoms*, *Phys. Rev. A* **84**, 011606 (2011)
- [56] Sven Tassy, *Sympathetische Kühlung von Ytterbium mit Rubidium*, Ph.D. thesis, Heinrich-Heine-Universität, Düsseldorf (2007)
- [57] Anders H. Hansen, Alexander Y. Khramov, William H. Dowd, Alan O. Jamison, Benjamin Plotkin-Swing, Richard J. Roy, and Subhadeep Gupta, *Production of quantum-degenerate mixtures of ytterbium and lithium with controllable interspecies overlap*, *Phys. Rev. A* **87**, 013615 (2013)
- [58] B. Zimmermann, T. Müller, J. Meineke, T. Esslinger, and H. Moritz, *High-resolution imaging of ultracold fermions in microscopically tailored optical potentials*, *New J. Phys.* **13**, 043007 (2011)
- [59] Thomas E. Barrett, Samuel W. Dapore-Schwartz, Mark D. Ray, and Gregory P. Lafyatis, *Slowing atoms with σ -polarized light*, *Phys. Rev. Lett.* **67**, 3483–3486 (1991)
- [60] Yoshiro Takahashi, *private communication*
- [61] Christopher Pethick and Henrik Smith, *Bose-Einstein Condensation in Dilute Gases*, Cambridge University Press (2002)
- [62] Paul S. Julienne, *Ultra-Cold Collisions of Atoms and Molecules*, in *Scattering, Two-Volume Set: Scattering and inverse scattering in Pure and Applied Science*, volume 2, 1043–1067, Academic Press (2001)
- [63] Yuki Kawaguchi and Masahito Ueda, *Spinor Bose-Einstein condensates*, *Physics Reports* **520**, 253–381 (2012)
- [64] F. H. Mies, W. J. Stevens, and M. Krauss, *Model calculation of the electronic structure and spectroscopy of Hg₂*, *Journal of Molecular Spectroscopy* **72**, 303–331 (1978)
- [65] Masaaki Kitagawa, Katsunari Enomoto, Kentaro Kasa, Yoshiro Takahashi, Roman Ciuryło, Pascal Naidon, and Paul S. Julienne, *Two-color photoassociation spectroscopy of ytterbium atoms and the precise determinations of s-wave scattering lengths*, *Phys. Rev. A* **77**, 012719 (2008)

- [66] Takeshi Fukuhara, Yosuke Takasu, Mitsutaka Kumakura, and Yoshiro Takahashi, *Degenerate Fermi Gases of Ytterbium*, Phys. Rev. Lett. **98**, 030401 (2007)
- [67] T. Fukuhara, Y. Takasu, S. Sugawa, and Y. Takahashi, *Quantum Degenerate Fermi Gases of Ytterbium Atoms*, J Low Temp Phys **148**, 441–445 (2007)
- [68] Takeshi Fukuhara, Seiji Sugawa, and Yoshiro Takahashi, *Bose-Einstein condensation of an ytterbium isotope*, Phys. Rev. A **76**, 051604 (2007)
- [69] Seiji Sugawa, Rekishu Yamazaki, Shintaro Taie, and Yoshiro Takahashi, *Bose-Einstein condensate in gases of rare atomic species*, Phys. Rev. A **84**, 011610 (2011)
- [70] Yixuan Wang and Michael Dolg, *Pseudopotential study of the ground and excited states of Yb2*, Theor Chem Acc **100**, 124–133 (1998)
- [71] J. P. Pique, F. Hartmann, R. Bacis, S. Churassy, and J. B. Koffend, *Hyperfine-Induced Ungerade-Gerade Symmetry Breaking in a Homonuclear Diatomic Molecule near a Dissociation Limit: I2127 at the P322-P122 Limit*, Phys. Rev. Lett. **52**, 267–270 (1984)
- [72] Gerhard Herzberg, *Spectra of diatomic molecules*, Van Nostrand (1950)
- [73] D. Jaksch and P. Zoller, *The cold atom Hubbard toolbox*, Annals of Physics **315**, 52–79 (2005)
- [74] M. J. Martin, M. Bishof, M. D. Swallows, X. Zhang, C. Benko, J. von Stecher, A. V. Gorshkov, A. M. Rey, and Jun Ye, *A Quantum Many-Body Spin System in an Optical Lattice Clock*, Science **341**, 632–636 (2013)
- [75] X. Zhang, M. Bishof, S. L. Bromley, C. V. Kraus, M. S. Safronova, P. Zoller, A. M. Rey, and J. Ye, *Direct observation of SU(N) orbital magnetism*, arXiv:1403.2964 (2014)
- [76] N. D. Lemke, J. von Stecher, J. A. Sherman, A. M. Rey, C. W. Oates, and A. D. Ludlow, *p-Wave Cold Collisions in an Optical Lattice Clock*, Phys. Rev. Lett. **107**, 103902 (2011)
- [77] Bishof, M. Martin, M. Swallows, C. Benko, Y. Lin, G. Quéméner, A. Rey, and J. Ye, *Inelastic collisions and density-dependent excitation suppression in a Sr87 optical lattice clock*, Physical Review A **84**, 052716/1–6 (2011)
- [78] Ch. Lisdat, J. S. R. Vellore Winfred, T. Middelmann, F. Riehle, and U. Sterr, *Collisional Losses, Decoherence, and Frequency Shifts in Optical Lattice Clocks with Bosons*, Phys. Rev. Lett. **103**, 090801 (2009)
- [79] F. Scazza, C. Hofrichter, M. Höfer, P. C. De Groot, I. Bloch, and S. Fölling, *Observation of two-orbital spin-exchange interactions with ultracold SU(N)-symmetric fermions*, arXiv:1403.4761 (2014)

- [80] Y. N. Martinez de Escobar, P. G. Mickelson, P. Pellegrini, S. B. Nagel, A. Traverso, M. Yan, R. Côté, and T. C. Killian, *Two-photon photoassociative spectroscopy of ultracold Sr88*, Phys. Rev. A **78**, 062708 (2008)
- [81] Michael Foss-Feig, Michael Hermele, Victor Gurarie, and Ana Maria Rey, *Heavy fermions in an optical lattice*, Phys. Rev. A **82**, 053624 (2010)
- [82] Z. W Barber, J. E Stalnaker, N. D Lemke, N. Poli, C. W Oates, T. M Fortier, S. A Diddams, L. Hollberg, C. W Hoyt, A. V Taichenachev, and V. I Yudin, *Optical Lattice Induced Light Shifts in an Yb Atomic Clock*, Phys. Rev. Lett. **100**, 103002 (2008)
- [83] V A Dzuba and A Derevianko, *Dynamic polarizabilities and related properties of clock states of the ytterbium atom*, Journal of Physics B: Atomic, Molecular and Optical Physics **43**, 074011 (2010)
- [84] Rudolf Grimm, Matthias Weidemüller, and Yurii B. Ovchinnikov, *Optical Dipole Traps for Neutral Atoms*, in *Advances In Atomic, Molecular, and Optical Physics*, volume 42, 95–170, Elsevier (2000)
- [85] F. Baumer, F. Münchow, A. Görlitz, S. E. Maxwell, P. S. Julienne, and E. Tiesinga, *Spatial separation in a thermal mixture of ultracold Yb174 and Rb87 atoms*, Phys. Rev. A **83**, 040702 (2011)
- [86] P. W. H. Pinkse, A. Mosk, M. Weidemüller, M. W. Reynolds, T. W. Hijmans, and J. T. M. Walraven, *One-dimensional evaporative cooling of magnetically trapped atomic hydrogen*, Phys. Rev. A **57**, 4747–4760 (1998)
- [87] E. L. Surkov, J. T. M. Walraven, and G. V. Shlyapnikov, *Collisionless motion and evaporative cooling of atoms in magnetic traps*, Phys. Rev. A **53**, 3403–3408 (1996)
- [88] J. Söding, D. Guéry-Odelin, P. Desbiolles, F. Chevy, H. Inamori, and J. Dalibard, *Three-body decay of a rubidium Bose–Einstein condensate*, Appl Phys B **69**, 257–261 (1999)
- [89] Christoph Becker, *Multi component Bose-Einstein Condensates*, Ph.D. thesis, Universität Hamburg, Hamburg (2008)
- [90] J. Struck, C. Ölschläger, R. Le Targat, P. Soltan-Panahi, A. Eckardt, M. Lewenstein, P. Windpassinger, and K. Sengstock, *Quantum Simulation of Frustrated Classical Magnetism in Triangular Optical Lattices*, Science **333**, 996–999 (2011)
- [91] J. Struck, M. Weinberg, C. Ölschläger, P. Windpassinger, J. Simonet, K. Sengstock, R. Höppner, P. Hauke, A. Eckardt, M. Lewenstein, and L. Mathey, *Engineering Ising-XY spin-models in a triangular lattice using tunable artificial gauge fields*, Nat Phys **9**, 738–743 (2013)

- [92] Julian Struck, *Artificial Gauge Fields in Driven Optical Lattices*, Ph.D. thesis, Universität Hamburg, Hamburg (2013)
- [93] B. DeMarco, C. Lannert, S. Vishveshwara, and T.-C. Wei, *Structure and stability of Mott-insulator shells of bosons trapped in an optical lattice*, Phys. Rev. A **71**, 063601 (2005)
- [94] Dirk-Sören Lühmann, Ole Jürgensen, and Klaus Sengstock, *Multi-orbital and density-induced tunneling of bosons in optical lattices*, New J. Phys. **14**, 033021 (2012)
- [95] M. J. Holland, B. DeMarco, and D. S. Jin, *Evaporative cooling of a two-component degenerate Fermi gas*, Phys. Rev. A **61**, 053610 (2000)
- [96] Brian DeMarco, *Quantum Behavior of an Atomic Fermi Gas*, Ph.D. thesis, University of Colorado, Boulder (2001)
- [97] R. J. Cook, *Theory of Atomic Motion in a Resonant Electromagnetic Wave*, Phys. Rev. Lett. **41**, 1788–1791 (1978)
- [98] T. Sleator, T. Pfau, V. Balykin, O. Carnal, and J. Mlynek, *Experimental demonstration of the optical Stern-Gerlach effect*, Phys. Rev. Lett. **68**, 1996–1999 (1992)
- [99] Shintaro Taie, Yosuke Takasu, Seiji Sugawa, Rekishu Yamazaki, Takuya Tsujimoto, Ryo Murakami, and Yoshiro Takahashi, *Realization of a $SU(2) \times SU(6)$ System of Fermions in a Cold Atomic Gas*, Phys. Rev. Lett. **105**, 190401 (2010)
- [100] Simon Stellmer, Rudolf Grimm, and Florian Schreck, *Detection and manipulation of nuclear spin states in fermionic strontium*, Phys. Rev. A **84**, 043611 (2011)
- [101] Markus Greiner, Immanuel Bloch, Olaf Mandel, Theodor W. Hänsch, and Tilman Esslinger, *Exploring Phase Coherence in a 2D Lattice of Bose-Einstein Condensates*, Phys. Rev. Lett. **87**, 160405 (2001)
- [102] Michael Köhl, Henning Moritz, Thilo Stöferle, Kenneth Günter, and Tilman Esslinger, *Fermionic Atoms in a Three Dimensional Optical Lattice: Observing Fermi Surfaces, Dynamics, and Interactions*, Phys. Rev. Lett. **94**, 080403 (2005)
- [103] P. B. Blakie, A. Bezett, and P. Buonsante, *Degenerate Fermi gas in a combined harmonic-lattice potential*, Phys. Rev. A **75**, 063609 (2007)
- [104] L. Viverit, C. Menotti, T. Calarco, and A. Smerzi, *Efficient and Robust Initialization of a Qubit Register with Fermionic Atoms*, Phys. Rev. Lett. **93**, 110401 (2004)
- [105] V. Ruuska and P. Törmä, *Quantum transport of non-interacting Fermi gas in an optical lattice combined with harmonic trapping*, New J. Phys. **6**, 59 (2004)

- [106] Shinya Kato, Seiji Sugawa, Kosuke Shibata, Ryuta Yamamoto, and Yoshiro Takahashi, *Control of Resonant Interaction between Electronic Ground and Excited States*, Phys. Rev. Lett. **110**, 173201 (2013)
- [107] Zeb Barber, *Ytterbium Optical Lattice Clock*, Ph.D. thesis, University of Colorado, Boulder (2007)
- [108] J. Alnis, A. Matveev, N. Kolachevsky, Th. Udem, and T. W. Hänsch, *Subhertz linewidth diode lasers by stabilization to vibrationally and thermally compensated ultralow-expansion glass Fabry-Pérot cavities*, Phys. Rev. A **77**, 053809 (2008)
- [109] Mark Notcutt, Long-Sheng Ma, Jun Ye, and John L. Hall, *Simple and compact 1-Hz laser system via an improved mounting configuration of a reference cavity*, Opt. Lett. **30**, 1815–1817 (2005)
- [110] H. Stoehr, F. Mensing, J. Helmcke, and U. Sterr, *Diode laser with 1 Hz linewidth*, Opt. Lett. **31**, 736–738 (2006)
- [111] B. C. Young, F. C. Cruz, W. M. Itano, and J. C. Bergquist, *Visible Lasers with Subhertz Linewidths*, Phys. Rev. Lett. **82**, 3799–3802 (1999)
- [112] Thomas Rützel, *Conceptual Design and Setup of a Highly Stable Laser for Precision Measurements on Ultracold Quantum Gases*, Diplomarbeit, Universität Hamburg, Hamburg (2010)
- [113] P. K. Madhavan Unni, M. K. Gunasekaran, and A. Kumar, *$\pm 30 \mu\text{K}$ temperature controller from 25 to 103 °C: Study and analysis*, Review of Scientific Instruments **74**, 231–242 (2003)
- [114] G. Rempe, R. Lalezari, R. J. Thompson, and H. J. Kimble, *Measurement of ultralow losses in an optical interferometer*, Opt. Lett. **17**, 363–365 (1992)
- [115] Igor Dotsenko, *Single atoms on demand for cavity QED experiments*, Ph.D. thesis, Rheinische Friedrich-Wilhelms-Universität Bonn, Bonn (2007)
- [116] Gianni Di Domenico, Stéphane Schilt, and Pierre Thomann, *Simple approach to the relation between laser frequency noise and laser line shape*, Appl. Opt. **49**, 4801–4807 (2010)
- [117] A. L. Schawlow and C. H. Townes, *Infrared and Optical Masers*, Phys. Rev. **112**, 1940–1949 (1958)
- [118] R. W. P. Drever, J. L. Hall, F. V. Kowalski, J. Hough, G. M. Ford, A. J. Munley, and H. Ward, *Laser phase and frequency stabilization using an optical resonator*, Appl. Phys. B **31**, 97–105 (1983)

-
- [119] Eric D. Black, *An introduction to Pound–Drever–Hall laser frequency stabilization*, American Journal of Physics **69**, 79–87 (2001)
- [120] S. Dilwali and G. Soundra Pandian, *Transfer function of thermal FM, FSK step response and the dip in the FM response of laser diodes*, Optical and Quantum Electronics **24**, 661–676 (1992)
- [121] Hardo Stoehr, *Diodenlaser mit Hertz-Linienbreite für ein optisches Calcium Frenquenznormal*, Ph.D. thesis, Universität Hannover, Hannover (2005)
- [122] D. Leibfried, R. Blatt, C. Monroe, and D. Wineland, *Quantum dynamics of single trapped ions*, Rev. Mod. Phys. **75**, 281–324 (2003)
- [123] Sergey G. Porsev, Andrei Derevianko, and E. N. Fortson, *Possibility of an optical clock using the $6\ 1S_0 - 6\ 3P_0$ transition in $171, 173\text{Yb}$ atoms held in an optical lattice*, Phys. Rev. A **69**, 021403 (2004)
- [124] Michael Foss-Feig, Andrew J. Daley, James K. Thompson, and Ana Maria Rey, *Steady-State Many-Body Entanglement of Hot Reactive Fermions*, Phys. Rev. Lett. **109**, 230501 (2012)
- [125] David C. Roberts and Sergio Rica, *Impurity Crystal in a Bose-Einstein Condensate*, Phys. Rev. Lett. **102**, 025301 (2009)
- [126] Rodney Loudon, *The Quantum Theory of Light*, Oxford University Press (2000)

Danksagung

Diese Arbeit hätte ohne die Unterstützung vieler engagierter Menschen nicht entstehen können. Allen voran möchte ich mich bei meinen langjährigen Laborkollegen Sören Dörscher, Bastian Hundt und André Kochanke bedanken. Vielen Dank für Euren unermüdlichen Einsatz und die angenehme Atmosphäre im Labor.

Ein besonderer Dank gilt auch meinem Doktorvater Prof. Dr. Klaus Sengstock, dessen Tür für Fragen und Probleme aller Art immer offen stand. In zahlreichen Gesprächen hast Du mich immer wieder motiviert und die Begeisterung für Physik neu geweckt.

Dr. Christoph Becker hat mir während der gesamten Zeit am Yb-Projekt unzählige Fragen zu kalten Quantengasen beantwortet und wichtige physikalische Anstöße gegeben. Vielen Dank, auch für Deine entspannte Art und die unvergleichliche Fähigkeit, mit einem guten Spruch jede noch so schwierige Situation aufzulockern.

Bei Prof. Dr. Henning Moritz bedanke ich mich für die Übernahme des Zweitgutachtens meiner Dissertation.

Neben den schon genannten haben noch viele andere tatkräftig zum Gelingen des Projekts beigetragen: Prof. Dr. Patrick Windpassinger, Dr. Rodolphe LeTargat, Thomas Pohnert, Thomas Rützel, Jan Carstens, Hans Kessler, Niels Petersen und Anna Skottke. Danke Euch allen.

Reinhard Mielk hat mit großem Einsatz und Sachverstand bei der Lösung aller denkbaren technischen Probleme geholfen: Vom Ausfall der Klimaanlage, über das Wickeln der MOT-Spulen, bis hin zum Transport der Vakuum-Apparatur.

Vielen Dank auch an die gesamte Forschungsgruppe für die freundschaftliche Zusammenarbeit und die gute Atmosphäre.

Ganz besonders bedanke ich mich bei meiner Familie. Meine Eltern Regina und Bernhard haben mich mein Leben lang bei allem unterstützt, was ich mir vorgenommen habe. Mit Rat und Tat, Geduld und Verständnis. Auch meiner Schwester Katharina gilt ein herzlicher Dank.

Schließlich möchte ich mich bei meiner Freundin Therese bedanken, ohne deren fröhliche und liebevolle Art diese Arbeit nicht entstanden wäre. Danke!